

Intrusion Detection System and Corrective Actions in Modern Power Systems

BY

AHMAD KHAN

B.Sc., Qatar University, 2014

M.Sc., Qatar University, 2017

THESIS

Submitted as partial fulfillment of the requirements
for the degree of Doctor of Philosophy in Electrical and Computer Engineering
in the Graduate College of the
University of Illinois Chicago, 2023
Chicago, Illinois

Defense Committee:

Mohammad Shadmand, Chair and Advisor

Sudip Mazumder

Danilo Erricolo

Mesrob Ohannessian

George Amariuca, Kansas State University

Dedicated to my Mother and Father

ACKNOWLEDGEMENTS

First and foremost, I would like to express my gratitude to my Ph.D. Advisor Professor Mohammad Shadmand for his wisdom, patience, encouragement, and unconditional and continuous technical support, his guidance was the most crucial assets that led me to accomplish this Ph.D. dissertation successfully.

I would also like to thank my Ph.D. committee members, Professor Sudip Mazumder, Professor Danilo Erricolo, Professor Mesrob Ohannessian, and Professor George Amariuca, for all their guidance through this process; your discussion, guidance, and feedback have been helpful.

In addition, I would like to extend my gratitude to Professor Haitham Abu-Rub, Professor Sertac Bayhan, and all my colleagues at Texas A&M University at Qatar and Smart Grid Center. I greatly appreciate all your support over the years.

I would like to thank all my research colleagues in Intelligent Power Electronics at Grid Edge (IPEG) Research Laboratory at University of Illinois Chicago (UIC), You all have brilliantly supported me during these years. I am very thankful to all of you.

Very special thanks go to my colleague in IPEG lab, friend, and neighbor Dr. Mohsen Hosseinzadehtaher for his remarkable support during the Ph.D. years. Your support is appreciated greatly and will not be forgotten.

Finally, I need to express my deepest thanks to my beautiful wife Mariam Khan and my beautiful daughter Roz Khan for loving me, supporting me, encouraging me, and giving me the energy to accomplish this Ph.D. dissertation successfully. In addition, I would like to express my thanks also to my father, mother, sisters, and brothers. I have gotten support,

ACKNOWLEDGEMENTS (Continued)

encouragement, and love from all of you all the time. I believe without your remarkable support during these years, I could not accomplish this success.

AK

PREFACE

This dissertation is an original intellectual product of the author, Ahmad Khan. All the work presented here was conducted in the Intelligent Power Electronics at Grid Edge (IPEG) Research Laboratory at University of Illinois Chicago.

The results of our research have been previously published as journal, conference, workshop articles in:

- IEEE Access, 2022
- IEEE Open Journal of Industrial Electronics Society, 2020
- IEEE Industrial Electronics Magazine, 2020
- 21st IFAC 2020 World Congress, 2020
- IEEE Energy Conversion Congress and Exposition (ECCE, 2020)
- IEEE 12th International Symposium on Power Electronics for Distributed Generation Systems (PEDG, 2021)
- IEEE 22nd Workshop on Control and Modelling of Power Electronics (COMPEL, 2021)
- 2021 IEEE Industry Applications Society Annual Meeting (IAS, 2021)
- 2019 IEEE Power and Energy Conference at Illinois (PECI, 2019)
- IEEE CyberPELS, 2020

The copyright permissions for reusing the published materials are given in the Appendix.

Ahmad Khan
November 4, 2022

CONTRIBUTION OF AUTHORS

Major parts of the results and discussions in this dissertation are taken from my published or submitted papers with permission from the journals that allow re-publication in thesis. Below, the contributions of all the co-authors are listed:

Authors' contributions in IEEE Access 2022: A. Khan and M. Shadmand conceived the main idea. A. Khan led the investigations and conducted the analytical analysis, technical results, and write-up. S. Mazumder contributed to review the write-up of the manuscript.

Authors' contributions in IEEE Open Journal Industrial Electronics Society 2020: A. Khan and M. Shadmand conceived the main idea. A. Khan led the investigations and conducted the analytical analysis, technical results, and write-up. S. Bayhan and H. Abu-Rub contributed to review the write-up of the manuscript.

Authors' contributions in IEEE Industrial Electronics Magazine 2020: A. Khan, M. Hosseinzadehtaher and M. Shadmand conceived the main idea. A. Khan and M. Hosseinzadehtaher led the investigations and conducted the analytical analysis, technical results. M. Hosseinzadehtaher contributed to the write-up of manuscript and drawing some figures. S. Bayhan and H. Abu-Rub contributed to the concept of the write-up of the manuscript.

Authors' contributions in 21st IFAC 2020 World Congress 2020: A. Khan, M. Hosseinzadehtaher and M. Shadmand conceived the main idea and A. Khan led the investigations and conducted the analytical analysis, technical results, and write-up of the manuscript.

CONTRIBUTION OF AUTHORS (Continued)

Authors' contributions in IEEE Energy Conversion Congress and Exposition (ECCE 2020): A. Khan, and M. Shadmand conceived the main idea and A. Khan led the investigations and conducted the analytical analysis, technical results, and write-up. M. Easley, M. Hosseinzadehtaher, H. Abu-Rub, and P. Fajri contributed to some part of write-up of manuscript.

Authors' contributions in IEEE Energy Conversion Congress and Exposition (ECCE 2020): A. Khan, and M. Shadmand conceived the main idea and A. Khan led the investigations and conducted the analytical analysis, technical results, and write-up. M. Hosseinzadehtaher, M. Easley, and H. Abu-Rub contributed to some part of write-up of manuscript.

Authors' contributions in IEEE 12th International Symposium on Power Electronics for Distributed Generation Systems (PEDG 2021): A. Khan, M. Hosseinzadehtaher and M. Shadmand conceived the main idea and A. Khan, led the investigations, and conducted the analytical analysis, technical results, and write-up. S. Mazumder contributed to review the write-up of the manuscript.

Authors' contributions in IEEE 22nd Workshop on Control and Modelling of Power Electronics (COMPEL 2021): A. Khan and M. Shadmand conceived the main idea. A. Khan led the investigations and conducted the analytical analysis, technical results, and write-up.

CONTRIBUTION OF AUTHORS (Continued)

Authors' contributions in 2021 IEEE Industry Applications Society Annual Meeting

(IAS 2021): A. Khan, and M. Shadmand conceived the main idea. A. Khan led the investigations and conducted the analytical analysis, technical results, and write-up. M. Hosseinzadehtaher, and A. Fard contributed to the analytical analysis, technical results, write-up and drawing some figures.

Authors' contributions in IEEE Power and Energy Conference at Illinois (PECI

2019): A. Khan, and M. Shadmand conceived the main idea. A. Khan led the investigations and conducted the analytical analysis, technical results, and write-up. H. Abu-Rub contributed to review the write-up of the manuscript.

Authors' contributions in IEEE CyberPELS 2020:

A. Khan, M. Hosseinzadehtaher, and M. Shadmand conceived the main idea. A. Khan led the investigations and conducted the analytical analysis, technical results, and write-up. D. Saleem, and H. Abu-Rub contributed to review the write-up of the manuscript.

TABLE OF CONTENTS

CHAPTER	PAGE
1. INTRODUCTION.....	1
1.1. The New Energy Paradigm	2
1.2. Power Electronics Dominated Grid Characteristics.....	5
1.3. Concept of Stability, Categorization, and Vulnerabilities of Power Electronics Dominated Grid.....	9
1.3.1. Concept of Stability.....	9
1.3.2. Stability Categorization and Vulnerabilities	11
1.4. Small-Perturbation and Large-Perturbation Instabilities.....	16
1.5. Research Roadmap and Open Research Questions in the Power Electronics Dominated Grid.....	18
1.5.1. Frequency Control.....	18
1.5.2. Voltage Control	19
1.5.3. Heterogeneity	20
1.5.4. Cybersecurity Vulnerability	21
1.5.5. Synchronverter and coherence enforcement potentials in the power electronics dominated grid	22
1.6. Conclusion	24
2. PRIMARY CURRENT CONTROL DEVELOPMENT.....	26
2.1. Phase Locked Loop (PLL) Limitations	27
2.2. Mathematical Modeling, Controller Design, and Control Stability of the Developed PLL-less Grid-Following Inverter Control.....	28
2.2.1. Mathematical Modelling	28
2.2.2. Control Design	31
2.2.3. Control Stability	32
2.3. Weak Grid and Point of Common Coupling Voltage Steady State Stability.....	34
2.3.1. Resistive Weak Grid Consideration	34
2.3.2. Inductive Weak Grid Consideration.....	35
2.4. Validating Results on PLL-less Grid-Following Inverter Control.....	36
2.5. PLL-less Grid-following Inverter Control Adaptive to Frequency.....	45
2.5.1. Mathematical Modeling with Frequency Adaptation Inclusion.....	45
2.5.2. Frequency Adaptation PLL-less Grid-Following Inverter Control Validations	46
2.6. Conclusion.....	50
3. GRID-FOLLOWING INVERTER CONTROL WITH ACTIVE POWER DECOUPLING CONTROL FOR FUTURE POWER ELECTRONICS-DOMINATED GRID DC LINK VOLTAGE STABILITY IMPROVEMENT	51
3.1. Nanogrid Main Interfacing Grid-Following Inverter with Active Power Decoupling Capability	52

TABLE OF CONTENTS (Continued)

<u>CHAPTER</u>	<u>PAGE</u>
3.1.1. Origin of Power Ripples.....	57
3.1.2. Power Ripple Mitigation Principle.....	60
3.1.3. Power Ripple Mitigation Automation and Practical Considerations	63
3.1.4. Stabilization.....	68
3.1.5. Validations.....	75
3.2. PLL-less Grid-Following Control with Active Power Decoupling Control.....	82
3.3. PLL-less Grid-Following Control with Active Power Decoupling Control with Variable Frequency Operation	92
3.4. Conclusion.....	98
4. STABILITY BOUND IDENTIFICATION	100
4.1. Voltage Stability in the Power Electronics-Dominated Grid	101
4.1.1. New Energy Paradigm Voltage Stability	101
4.1.2. Impact of Prosumers Grid-Feeding Inverter’s Active Power Set-Point Change on the Local PCC Voltage	104
4.1.3. Voltage Stability Bound Derivations	106
4.1.4. Voltage Stability Bound Validation	114
4.2. Online Voltage Stability Identification from Local PCC terminals	115
4.2.1. Online Voltage Stability Linkage to Cyber Security.....	115
4.2.2. Nearby Prosumers’ Set-Points Variation Impact on a Specific Targeted ith Prosumer Point of Common Coupling Bus Voltage.....	117
4.2.3. Real-Time Observation of Nearby Prosumers’ Set-Points Variation at a Targeted i th Prosumer Point of Common Coupling Bus	120
4.2.4. On-Line Voltage Stability Bound Identification Validations.....	122
4.3. Cybersecurity Linkage to Stability Bounds.....	129
4.3.1. Cybersecurity in the New Energy Paradigm	129
4.3.2. Cyber-Attack Hypothesis, Normal Operation Region Derivation, and Cybersecurity Analytics.....	133
4.3.3. Validation of the Derived Operation Regions.....	137
4.4. Conclusion.....	140
5. INTRUSION DETECTION SYSTEM	141
5.1. Future Power Grid and Cyber Threats	142
5.2. Multi-Layer Controlled PEDG Network Understudy	146
5.2.1. List of Symbols Used in this Chapter.....	146
5.2.2. Preliminary Considerations	148
5.3. Safe Operation Region Derivations and Intrusion Scenario	150
5.3.1. Intrusion and Malicious PQ Set-Points Impact	150
5.3.2. Safe Operation Region “i.e., Morphism 2”	153
5.3.3. Graphical Example of Morphism 2 Derivation.....	158

TABLE OF CONTENTS (Continued)

<u>CHAPTER</u>	<u>PAGE</u>
5.4. Cyber Intrusion Detection System and Situational Awareness Improvement Based on Morphism 1 And Morphism 2.....	161
5.5. Validation on Intrusion Detection System Performance.....	163
5.5.1. Malicious Cyber-Attack Scenario I.....	164
5.5.2. Malicious Cyber-Attack Scenario II.....	166
5.6. Mathematical Background and Proofs.....	168
5.6.1. Stability of the i^{th} Grid-Feeding Inverter Primary Layer Used for DEGs In The Single-Phase PEDG (Time Separation Proof).....	168
5.6.2. Implication of L_2 Norm $\text{Im}\{\ v_{PCC}\ _2\}$ in Unstable PEDG Conditions Induced By Cyber Intruder Set-Points.....	173
5.6.3. Morphism Terminology Linked to Safe Operation Region.....	173
5.6.4. Proof On L_2 Norm Non-Zero Imaginary Value Indicates That the Set-Point Requested From The Upper Layer Belongs To Unstable Operation Region (UOR).....	175
5.6.5. The Two Point Impedance Theory Used in <i>Morphism 2</i> Analysis.....	180
5.7. Conclusion.....	182
6. CORRECTIVE ACTION POST CYBERATTACK OPERATION BASED ON CONSENSUS DYNAMICS CONTROL.....	184
6.1. Post-Attack Operation.....	184
6.2. Background about Consensus Dynamics Control in Power Systems.....	184
6.3. Event-Triggered Consensus Distributed Control Scheme Formulation.....	189
6.4. Validations Scenario with Stability Analysis.....	191
6.4.1. Validation Scenario 1: Two GFLIs in Radial Network with Cyber Layer Layout of Figure 6.2(a).....	191
6.4.2. Validation Scenario 2: Five GFLIs in Radial Network with Cyber Layer Layout Figure 6.2(b).....	196
6.4.3. Validation Scenario 3: Two GFLIs in Radial Network with Reverse Coupling Dynamics $P - V$ and $Q - f$ with Cyber Layer Layout Figure 6.2(c).....	198
6.4.4. Validation Scenario 4: Distribution Feeder with 42 GFLIs in a Reverse Coupling Dynamics $P - V$ and $Q - f$ with Cyber Layer Layout Figure 6.2(d).....	201
6.4.5. Validation Scenario 5: Distribution Network in Ring Configuration with 42 GFLIs in a Reverse Coupling Dynamics $P - V$ and $Q - f$ with Cyber Layer Layout of Figure 6.2(e).....	205
6.5. Conclusion.....	206
7. CONCLUSIONS.....	207
8. APPENDIX.....	209

TABLE OF CONTENTS (Continued)

<u>CHAPTER</u>		<u>PAGE</u>
9. REFERENCES.....		218
VITA.....		236

LIST OF TABLES

<u>TABLE</u>	<u>PAGE</u>
I. SUMMARY OF THE POWER ELECTRONICS DOMINATED GRID STABILITY WITH ORIGIN AND EFFECTS	17
II. GRID FORMING TECHNOLOGIES, OPERATION PRINCIPLE ANALOGY, STATE OF MATURITY, RESEARCH TREND AND REFERENCES	21
III. PLL-LESS GRID-FOLLOWING INVERTER CONTROL RATINGS	36
IV. ADAPTIVE FREQUENCY PLL-LESS GRID-FOLLOWING INVERTER CONTROL	46
V. SUMMARY OF POWER RIPPLE MITIGATION TECHNIQUES	54
VI. NANOGRID DETAILS	76
VII. DIFFERENTIAL BUCK CONVERTER WITH PLL-LESS GRID-FOLLOWING CURRENT CONTROL RATINGS	88
VIII. VARIABLE FREQUENCY ACTIVE RECTIFIER RATINGS	93
IX. INDIVIDUAL GRID-FEEDING INVERTER RATINGS	113
X. INDIVIDUAL GRID-FEEDING INVERTER DEGS RATINGS	164

LIST OF FIGURES

<u>FIGURE</u>	<u>PAGE</u>
1.1. Generic example of power electronics dominated grid exemplifying the three level control hierarchy.....	2
1.2. Analogy of manual weighing instrument with the degree of coupling between active power demand, reactive power demand, frequency, and voltage: (a) bulk power system follows P - f and Q - V , and (b) power electronics dominated grid follows P - f & V and Q - V & f	5
1.3. Equal area criterion for stability indicating the impact of inertia (H) on the critical clearing time (t_{cct}).	6
1.4. Illustration of inertia concept with pendulums in equilibrium conditions: (a) bulk power system and (b) power electronics dominated grid.....	7
1.5. Power electronics dominated grid stability categorization with root cause and resulting phenomena.....	8
1.6. Illustration of the effect of the short circuit fault location on the size of the instability	15
1.7. New stability challenges that power electronics dominated grid introduced in comparison with the time scale	24
2.1. PLL issue related to its contribution to the output impedance of the GFLI that is negative damping.	28
2.2. PLL issue related to having high impedance after the point of common coupling terminals in weak grid connections for GFLI.	29
2.3: Developed PLL-less single control loop active and reactive power control for single phase GFLI.....	30
2.4: Proposed controller dynamic performance in tracking the commanded PQ set-point references.....	37
2.5: Steady state PCC current and voltage waveforms in Figure 2.4 before the commanded PQ set-point references are changed at instant 2 sec.....	37
2.6: Transient PCC current and voltage waveforms in Figure 2.4 at the instant the commanded PQ set-point references are changed.....	38

LIST OF FIGURES (Continued)

<u>FIGURE</u>	<u>PAGE</u>
2.7: Steady state PCC current and voltage waveforms in Figure 2.4 after the commanded PQ set-point references are changed at instant 2 sec.....	38
2.8: Verification of inequality (2.34) with commanded PQ set-point references variation in weak resistive grid connection.	40
2.9: Initial steady state stable PCC current and voltage waveforms when the command PQ set-point references are satisfying inequality (2.34) in Figure 2.8.....	40
2.10: Transient PCC current and voltage waveforms when transiting from stable to unstable operation induced by violation of inequality (2.34) at instant 2 sec in Figure 2.8.....	41
2.11: Transient PCC current and voltage waveforms when the stable operation is induced by satisfying inequality (2.34) at instant 3 sec in Figure 2.8.....	41
2.12: Final steady state stable PCC current and voltage waveforms when the command PQ set-point references are satisfying inequality (2.34) at instant 3 sec in Figure 2.8.	41
2.13: Verification of inequality (2.38) with commanded PQ set-points references variation in weak inductive grid connection.....	42
2.14: Initial steady state stable PCC current and voltage waveforms when the command PQ set-point references are satisfying inequality (2.38) in Figure 2.13.	42
2.15: Transient PCC current and voltage waveforms when transiting from stable to unstable operation induced by violation of inequality (2.38) at instant 2 sec in Figure 2.13.....	43
2.16: Transient PCC current and voltage waveforms when the stable operation is induced by satisfying inequality (2.38) at instant 4 sec in Figure 2.13.....	43
2.17: Final steady state stable PCC current and voltage waveforms when the command PQ set-point references are satisfying inequality (2.38) at instant 4 sec in Figure 2.13. ...	43
2.18. Variable frequency second order generalized integrator (VF-SOGI).....	44
2.19. PLL-less GFLI adaptive to frequency changes.....	44
2.20. Scenario 1: Performance of the frequency adaptive PLL-less grid-following inverter control with frequency variations.....	47

LIST OF FIGURES (Continued)

<u>FIGURE</u>	<u>PAGE</u>
2.21. Scenario 2: Performance of the frequency adaptive PLL-less grid-following inverter control with frequency variations and active power set-point change	48
2.22. Scenario 3: Performance of the frequency adaptive PLL-less grid-following inverter control with frequency variations, active power set-point change, reactive power set-point change.	49
3.1. Nanogrid architecture.....	53
3.2. The proposed SSC with zero-sequence control mode in a nanogrid.	55
3.3. Modified pulse width modulator to accommodate controlling the zero-sequence operation mode of the SSC.....	55
3.4. Equivalent circuit of the SSC in the active power transferring mode.....	56
3.5. Equivalent circuit of the SSC zero-sequence operation mode (point of common coupling loop is in open circuit condition).....	57
3.6. Model for stability analysis.....	66
3.7. Bode plot of $G_3(s)$ indicating instability in the APT mode.....	67
3.8. Bode plot of $G_6(s)$ indicating instability in the 0-Seq mode.....	68
3.9. (a) Pole zero plot of $G_{APT}(s)$ with varying K_{APT} from 0 to 0.045 indicating stability improvement with gain increase and (b) $G_{APT}(s)$ bode plot indicating stability with K_{APT} of 0.045.....	70
3.10. (a) Pole zero plot of $G_{0-Seq}(s)$ with varying K_{0-Seq} from 0 to 0.015 indicating stability improvement with gain increase and (b) $G_{0-Seq}(s)$ bode plot indicating stability with K_{0-Seq} of 0.015.....	73
3.11. Impact of the proposed stabilizer approach on a 500V/5kW nanogrid with 50 μ F DC link capacitor (Note that, the different DC voltages have different offsets as the following: $v_{DC1}^{Offset} = 0$, $v_{DC2}^{Offset} = -750V$, $v_{DC3}^{Offset} = -950V$, and $v_{Bat}^{Offset} = -90V$).	78

LIST OF FIGURES (Continued)

<u>FIGURE</u>	<u>PAGE</u>
3.12. Impact of the proposed zero-sequence mode control on a 500V/5kW nanogrid with 50 μ F DC link capacitor (Note that, the different DC voltages have different offsets as the following: $v_{DC1}^{Offset} = 0$, $v_{DC2}^{Offset} = -750V$, $v_{DC3}^{Offset} = -950V$, and $v_{Bat}^{Offset} = -90V$).....	79
3.13. Proposed zero-sequence mode control with 10% load increase in 500V/5kW nanogrid with 50 μ F DC link capacitor.....	80
3.14. Proposed zero-sequence mode control with filter capacitors mismatch with $\gamma = 2$ in a 500V/5kW nanogrid with 50 μ F DC link capacitor.....	82
3.15: Proposed decoupled single loop active and reactive power control without utilizing PLL for the differential buck converter.....	86
3.16: Performance of the proposed controller for the differential buck converter: Duration (1) active CM control with 2 kW absorption at unity power factor operation, duration (2) active CM control with 4 kW absorption at unity power factor operation, duration (3) active CM control with 4 kW absorption and 2 kVar injection, and duration (4) deactivated CM control (i.e. no active power decoupling control) with 4 kW absorption and 2 kVar injection	89
3.17. Variable frequency proportional resonance controller (VF-PR).	90
3.18. Active rectifier for variable frequency operation with active power decoupling capability.	91
3.19. (a) Variable frequency decoupled direct active and reactive power control, (b) variable frequency active power decoupling control, and (c) variable frequency control modulation indices. (VF-SOGI: variable frequency second order generalized integrator, VF-PR: variable frequency proportional resonance controller)	91
3.20. Scenario I: (a) without variable frequency active power decoupling control, and (b) with variable frequency active power decoupling control.	95
3.21. Scenario II: (a) without variable frequency active power decoupling control, and (b) with variable frequency active power decoupling control.	95
3.22. Scenario III: (a) without variable frequency active power decoupling control, and (b) with variable frequency active power decoupling control.	96

LIST OF FIGURES (Continued)

<u>FIGURE</u>	<u>PAGE</u>
4.1. Futuristic PEDG illustrating the i^{th} PCC bus equivalent: original network.	102
4.2. Futuristic PEDG illustrating the i^{th} PCC bus equivalent: switch level equivalent.....	103
4.3. Futuristic PEDG illustrating the i^{th} PCC bus equivalent: reduced circuit representation.	105
4.4. Futuristic PEDG illustrating the i^{th} PCC bus equivalent: controller representation for the i^{th} local PCC bus.	106
4.5. Impact of active power reversal on grid-edge network voltage: (a) internal PCC bus 2, internal PCC bus 3, PEDG network example.....	107
4.6. Stability bound prediction by observing the value of $\partial P_{PCC2}/\partial v_{PCC3} $	109
4.7. Stability bound prediction by observing the imaginary part of $\partial P_{PCC2}/\partial v_{PCC3} $	113
4.8. Validation of the derived mathematical voltage stability bounds.....	114
4.9. Virtual power plant concept as a power electronics-dominated grid.....	115
4.10. Virtual power plant cyber-layer from the perspective of i^{th} prosumer point of common coupling bus.	116
4.11. Online observation of the grid voltage (v_{g1}) seen at i^{th} prosumers point of common coupling bus for online real-time stability boundary identification.	121
4.12. Scenario I: duration (1) 5 kW with 0 kVar, duration (2) grid voltage sag, duration (3) 2.5 kW with 0 kVar, duration (4) 8 kW with 0 kVar, duration (5) 8 kW with 2.5 kVar, and (6) 8 kW with -2.5 kVar.	122
4.13. Scenario I online stability boundary identification: (a) stability boundary for duration (1), (b) stability boundary for durations (2), (3), (4), and (c) stability boundary for durations (5) and (6).	123
4.14. Scenario I real-time stability boundary identification, the simulation set-up showing the targeted prosumer point of common coupling bus.	123

LIST OF FIGURES (Continued)

<u>FIGURE</u>	<u>PAGE</u>
4.15. Scenario II targeted prosumer point of common coupling bus at 2.5 kW with 0 kVar: duration (1) nearby inverter 10 kW with 0 kVAR, duration (2) nearby inverter 5 kW with 0 kVAR, and duration (3) nearby inverter -5 kW with 0 kVar	124
4.16. Scenario II real-time stability boundary identification: (a) stability boundary for duration (1), (b) stability boundary for duration (2), and (c) stability boundary for duration (3).	125
4.17. Scenario II real-time stability boundary identification: (a) simulation set-up showing the targeted prosumer point of common coupling bus, and (b) alternative simulation to validate the estimated value of v_{gl}	125
4.18. Scenario III real-time stability boundary identification 13 prosumers point of common coupling bus virtual power plant.	126
4.19. Scenario III real-time stability boundary identification, simulation set-up showing the targeted prosumer point of common coupling bus.	128
4.20. Scenario III online stability boundary identification 13 prosumers point of common coupling bus virtual power plant: real-time movement of the stability bound on the P - V curves at v_{PCC} (The arrow indicates time progression in scenario III from 0.1 sec to 0.5 sec in Figure 4.60).	128
4.21. VPP concept illustration as a power electronics-dominated grid	129
4.22. Primary control layout considered for DEGs detailing the cybersecurity analytics and switch level depiction.	130
4.23. (a) VPP general network, (b) illustrating the i^{th} local PCC bus equivalent circuit at the secondary control layer time scale.	131
4.24. Example of N DEGs VPP for Thévenin voltage closed form derivation	132
4.25. Normal operation region of the whole network	133
4.26. Cyber-attack scenario I without activating the proposed cybersecurity analytics system	138
4.27. Cyber-attack scenario II with activating the proposed cybersecurity analytics system	138

LIST OF FIGURES (Continued)

<u>FIGURE</u>	<u>PAGE</u>
5.1. Multi-layered controlled PEDG concept extended to the grid edge with unobservable single-phase DEGs in grid-feeding mode of operation.	149
5.2. Grid-feeding primary control layer considered for DEGs in the PEDG: inverter structure.	149
5.3. Grid-feeding primary control layer considered for DEGs in the PEDG: controller structure with measurements, nonlinear coordinate the transformation illustration, and the intrusion detection system.	151
5.4. General PEDG network, illustrating the i th local PCC terminals equivalent circuit. .	151
5.5. Four bus single-phase PEDG considered for illustrating the operation regions graphically in scenario I.	152
5.6. Eight bus single-phase PEDG example and the Thevenin impedance of PCC2.	154
5.7. Eight bus single-phase PEDG example with the correction for Thevenin voltage on superposition theory to obtain PCC2.....	155
5.8. Operation regions of (a) PCC 1, (b) PCC 2, (c) PCC 3, and (d) SOR and SNOR of the four PCC bus single-phase PEDG for scenario I.	156
5.9. Scenario I effectiveness using the identified real-time operation regions for intrusion detection in PEDG of Figure 5.74.	163
5.10. Seven bus single phase PEDG for scenario II	164
5.11. Scenario II for the seven bus single-phase PEDG shown in Figure 5.79 the PEDG operator is utilizing the operation regions after detecting anomalous voltage at PCC2 and PCC3.....	165
5.12. Seven bus single phase PEDG for scenario II operation regions.....	166
5.13. Stability margin observation from the developed generalized P - V curves at local PCC bus 3 ($\ V_{PCC3}\ _2$) (i.e., Morphism 2) showing that the after the stability margin the structure of Morphism 2 is not sustained from \mathbb{R}^{2N} to \mathbb{R}	176
5.14. Stability margin prediction by observing the real and imaginary parts of $\partial P_{PCC2} / \partial \ V_{PCC3}\ _2$	179

LIST OF FIGURES (Continued)

<u>FIGURE</u>	<u>PAGE</u>
6.1. Multi-layered controlled PEDG with stealthy attacker compromising the secondary control layer and showing that the GFLs are distributing the active and reactive power reference generated from correcting the main PEDG PCC bus voltage and frequency through a specific mesh graph.....	185
6.2. Consensus dynamics control cyber layers layout tested in this chapter: (a) scenario 1, (b) scenario 2, (c) scenario 3, (d) scenario 4, and (e) scenario 5.....	186
6.3. $P - f$ and $Q - v$ coupling dynamics upper grid modelling for the scenarios testing the consensus dynamics control.	187
6.4. $P - v$ and $Q - f$ coupling dynamics upper grid modelling for the scenarios testing the consensus dynamics control.	188
6.5. Current control of the GFLs used in the consensus dynamics control validation scenarios.	190
6.6. Range of consensus gain k_Q that guarantees BIBO stability.....	193
6.7. Range of consensus gain k_Q that guarantees BIBO stability that produce oscillatory behavior.	193
6.8. Scenario 1 the proposed distributed control performance under random disturbances in resistive radial PEDG with GFLI ₁ at PCC bus 1 and GFLI ₂ at PCC bus 2 with capacities of 20 kVA: (a) control is activated, and (b) control is deactivated. [frequency base is 60 Hz, voltage base is 171 V, active and reactive power base is 20 kVA].....	194
6.9. Scenario 2 the proposed distributed control performance under random disturbances in resistive radial PEDG with five GFLI with the capacities of 20 kVA: (a) control is activated, and (b) control is deactivated. [Frequency base is 60 Hz, voltage base is 171 V, active and reactive power base is 20 kVA].....	195
6.10. Scenario 3 the proposed distributed control performance under random disturbances in resistive radial PEDG reverse coupling dynamics $P - V$ and $Q - f$ with GFLI ₁ at PCC bus 1 and GFLI ₂ at PCC bus 2 with capacities of 20 kVA: (a) control is activated, and (b) control is deactivated. [frequency base is 60 Hz, voltage base is 171 V, active and reactive power base is 20 kVA].....	196

LIST OF FIGURES (Continued)

<u>FIGURE</u>		<u>PAGE</u>
6.11.	Scenario 4 the proposed distributed control performance under random disturbances in distribution feeder with 42 GFLIs in a reverse coupling dynamics $P - V$ and $Q - f$ with GFLI _i at PCC bus i and GFLI _{i+1} at PCC bus $i+1$ with capacities of 20 kVA: (a) frequency at main PCC bus, and (b) voltage of the main PCC bus. [frequency base is 60 Hz, voltage base is 171 V].....	198
6.12.	Scenario 4 the proposed distributed control performance under random disturbances in distribution feeder with 42 GFLIs in a reverse coupling dynamics such as $P - V$ and $Q - f$ with GFLI _i at PCC bus i and GFLI _{i+1} at PCC bus $i+1$ with capacities of 20 kVA: (a) internal PCC bus GFLI active power from bus number 1 to 10, and (b) internal PCC bus GFLI active power from bus number 11 to 20, (c) internal PCC bus GFLI active power from bus number 21 to 30, and (d) internal PCC bus GFLI active power from bus number 31 to 42. [Active power base is 20 kVA]	199
6.13.	Scenario 4 the proposed distributed control performance under random disturbances in distribution feeder with 42 GFLIs in a reverse coupling dynamics such as $P - V$ and $Q - f$ with GFLI _i at PCC bus i and GFLI _{i+1} at PCC bus $i+1$ with capacities of 20 kVA: (a) internal PCC bus GFLI reactive power from bus number 1 to 10, and (b) internal PCC bus GFLI reactive power from bus number 11 to 20, (c) internal PCC bus GFLI reactive power from bus number 21 to 30, and (d) internal PCC bus GFLI reactive power from bus number 31 to 42. [Reactive power base is 20 kVA]	199
6.14.	Scenario 4 the post-attack operation without the proposed distributed control performance under random disturbances in distribution feeder with 42 GFLIs in a reverse coupling dynamics $P - V$ and $Q - f$ network with GFLI _i at PCC bus i and GFLI _{i+1} at PCC bus $i+1$ with capacities of 20 kVA: (a) frequency at main PCC bus, and (b) voltage of the main PCC bus. [Frequency base is 60 Hz, voltage base is 171 V]	200
6.15.	Scenario 4 the post-attack operation without the proposed distributed control performance under random disturbances in distribution feeder with 42 GFLIs in a reverse coupling dynamics such as $P - V$ and $Q - f$ with GFLI _i at PCC bus i and GFLI _{i+1} at PCC bus $i+1$ with capacities of 20 kVA: (a) internal PCC bus GFLI active power from bus number 1 to 10, and (b) internal PCC bus GFLI active power from bus number 11 to 20, (c) internal PCC bus GFLI active power from bus number 21 to 30, and (d) internal PCC bus GFLI active power from bus number 31 to 42. [Active power base is 20 kVA]	202

LIST OF FIGURES (Continued)

<u>FIGURE</u>		<u>PAGE</u>
6.16.	Scenario 4 the post-attack operation without the proposed distributed control performance under random disturbances in distribution feeder with 42 GFLIs in a reverse coupling dynamics such as $P - V$ and $Q - f$ with GFLI _{<i>i</i>} at PCC bus <i>i</i> and GFLI _{<i>i</i>+1} at PCC bus <i>i</i> +1 with capacities of 20 kVA: (a) internal PCC bus GFLI reactive power from bus number 1 to 10, and (b) internal PCC bus GFLI reactive power from bus number 11 to 20, (c) internal PCC bus GFLI reactive power from bus number 21 to 30, and (d) internal PCC bus GFLI reactive power from bus number 31 to 42. [Reactive power base is 20 kVA].....	202
6.17.	Scenario 5 the proposed distributed control performance under random disturbances in distribution network in ring configuration with 42 GFLIs in a reverse coupling dynamics $P - V$ and $Q - f$ network with GFLIs of 20 kVA and the cyber layer is as Figure 6.2(e): (a) frequency at main PCC bus, and (b) voltage of the main PCC bus. [frequency base is 60 Hz, voltage base is 171 V]	203
6.18.	Scenario 5 the post-attack operation without the proposed distributed control performance under random disturbances in distribution network in ring configuration with 42 GFLIs in a reverse coupling dynamics $P - V$ and $Q - f$ network with GFLIs of 20 kVA and the cyber layer is as Figure 6.2(e): (a) frequency at main PCC bus, and (b) voltage of the main PCC bus. [frequency base is 60 Hz, voltage base is 171 V].	204

LIST OF ABBREVIATIONS

APT	Active Power Transferring Mode
CM	Common Mode
DEG	Distributed Energy Generator
DM	Differential Mode
GFLI	Grid Following Inverter
IDS	Intrusion Detection System
PCC	Point of Common Coupling
PEDG	Power Electronics-Dominated Grid
PI	Proportional Integral
PLL	Phase Locked Loop
PR	Proportional Resonance
PV	Photovoltaic
SCR	Short Circuit Ratio
SNOR	Stable/Normal Operation Region
SOGI	Second Order Generalized Integrator
SOR	Safe Operation Region
SSC	Solid State Converter
UOR	Unstable Operation Region
VPP	Virtual Power Plant

SUMMARY

The futuristic energy paradigm implicates high penetration of renewable based generation through embracing distributed energy generators (DEGs). At the grid edge, grid-feeding inverters are the prevailing type of DEGs. In this mode of operation, the DEGs are following the inertial response of the network and their capabilities is confined in injecting/absorbing current into/from their local point of common coupling bus. Henceforth, real-time system level coordination is crucial to assure the optimal utilization of DEGs that are potentially installed behind the meters. Thereby, concepts such as the power electronics-dominated grid (PEDG) with multi-layer control layout are used as an effective solution enabling DEGs efficient utilization. However, this futuristic power grid is anticipated to be vulnerable to malicious cyberattacks due to the dispersed generation nature. In this dissertation, an intrusion detection system (IDS) is developed to prevent malicious set-points assigned to the primary control layer by an intruder breaching into the secondary control layer. This IDS is based on a derived operation region identification framework. Precisely, each point of common coupling bus is described with a non-linear multi-dimensional manifold where the network DEGs set-points are appearing as the domain variables constructing the feasible voltage co-domain. The IDS is equipped at the primary control layer of each DEG, once an anomalous point of common coupling voltage is detected, the IDS authenticates the set-point with the developed operation regions to decide if an intrusion occurred or not. Then, after the intrusion is detected, the IDS perform a corrective action to regain normal operation. This corrective action is based on consensus dynamics control that assures the normal operation of the PEDG in post-attack operation.

SUMMARY (Continued)

Additionally, in this dissertation, a single-loop direct decoupled active and reactive power control without phase-locked-loop (PLL) requirement for grid-following inverters with adaptation to frequency deviations is developed. This developed control is proven to be asymptotically exponentially stable with Lyapunov theory. This proposed control is used as the main primary control for the network DEGs to avoid instabilities correlated with PLL synchronization usage.

Chapter 1

1. Introduction

Part of this chapter, including figures and text are based on my following papers:

© 2018-2022 IEEE

- A. Khan, M. Hosseinzadehtaher, M. B. Shadmand, S. Bayhan and H. Abu-Rub, "On the Stability of the Power Electronics-Dominated Grid: A New Energy Paradigm," *IEEE Industrial Electronics Magazine*, vol. 14, no. 4, pp. 65-78, Dec. 2020.

1.1. The New Energy Paradigm

The current energy network is going through a modernization phase by an escalating penetration of renewable energy resources and energy storage systems [1]. In fact, the wind energy installation is projected to reach 903 GW by 2023 [2]. Likewise, photovoltaic (PV) energy integration will reach 1296 GW in 2023 [3]. As well as, the global deployment of energy storage systems is anticipated to be 2500 MW by 2023 [4]. Meaning that, this new energy paradigm is transforming the current energy network from being reliant on synchronous generators to power electronics based power generation [5-7]. This is recently termed as the power-electronics-dominated-grid (PEDG) (see Figure 1.1) [7].

The power electronic converters in PEDG are employed in PV systems, wind farms, battery banks, high voltage DC (HVDC), multi-terminal DC (MTDC), micro-grids, nanogrids, etc. Furthermore, PEDG can be interconnected to a larger upper network through point of common coupling. This larger power network could be another stronger

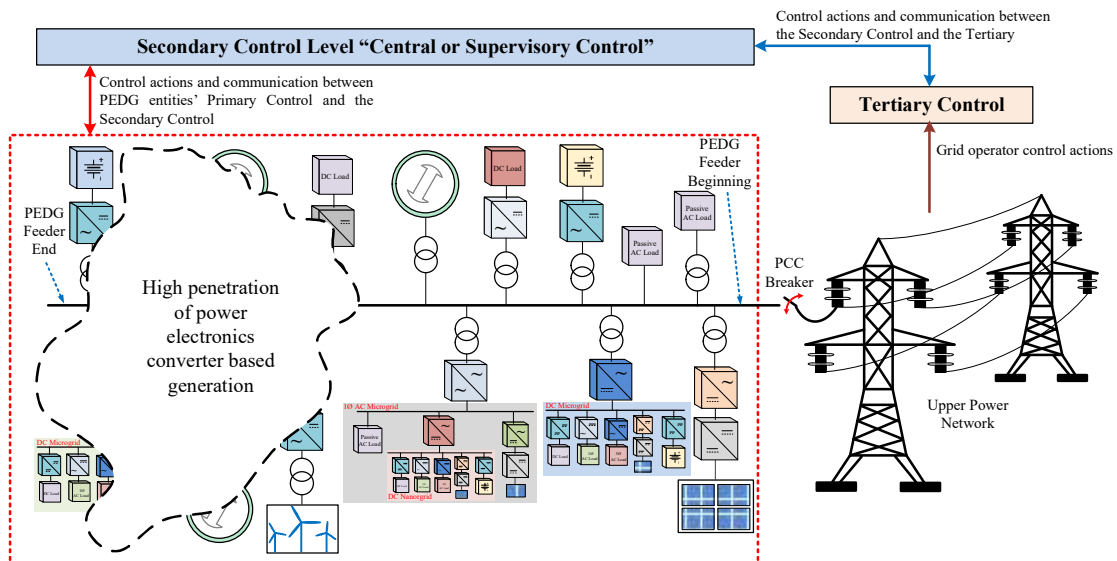


Figure 1.1. Generic example of power electronics dominated grid exemplifying the three level control hierarchy.

PEDG or a cluster of synchronized PEDGs. In a single PEDG three level of controls is required: (i) primary control, (ii) secondary control, and (iii) tertiary control [8]. The primary control is associated with each individual power electronic interface. The secondary control level is responsible of managing the different energy generation assets by assuring optimal and reliable operation. Furthermore, the secondary control communication level is observing and controlling the meters, relays, and breakers. The role of the tertiary control is like the secondary control role, but on a larger scale. In more details, the tertiary control ensures operational optimality and reliability from the perspective of the upper power network requirements or other synchronized PEDGs. The secondary and tertiary control layers may have communication interactions based on the aggregation defined by operators. Essentially, the main functionalities of these three level controls collectively are: sustaining the frequency and voltage in their acceptable levels, achieve balanced demand and power supply, seamless transition between operation modes, accomplish economic dispatch, and achieve demand side management.

The stability topic is majorly associated to control level that possess fastest dynamics. In such hierarchy, the primary level is the fastest control responsible for voltage/frequency control, islanding detection, and active/reactive power allocation. However, the stability study in conditions where the PEDG is connected to a larger power network is so far limited to the stability of a single or multiple power generation assets, motors, or loads. Examples of such instabilities are termed as harmonic instabilities or harmonic resonance [7, 9]. These instabilities are triggered by exciting the parallel or series resonance of the converter's filter itself or resonance with neighboring converters' filters or resonance with

the parasitic elements in the network [10]. Another type of such instabilities are those coupled with the phase-locked-loop (PLL) which are the negative damping. Particularly, the negative damping is observed in the low frequency spectrum range with PLL dynamics contribution to the inverter q-axis output impedance [11-13], while the negative damping is created in the d-axis at the low frequency spectrum range by the outer DC link control of an active rectifier feeding a constant power load [14]. The necessity of synchronous reference frame transformation (i.e., from abc components to dq-axis components) is to convert sinusoidal signals into dc signals that are easily controlled through conventional linear control theory [15]. Consequently, voltage and frequency stability in grid-connected PEDG is governed by the stability of the upper stronger power network. Thus, the operation of the PEDG in such mode is limited to active power exchange and ancillary services.

Islanded PEDGs are anticipated to enhance the resiliency of the future energy network [16, 17]. In the islanded operation of PEDGs, the frequency and voltage are no longer supported by the upper power network. Thereby, the individual energy resources in the PEDG are required to sustain the voltage and frequency in their satisfactory ranges. Nevertheless, the PEDG's primary control in standalone mode highly varies depending on the control approach adopted for the energy assets. For instance, the behavior of synchronous machines is different compared to the droop controlled inverters [18]. Precisely, for synchronous machines the frequency and voltage are controlled through the governor and the field current control loop, respectively [19]. In contrast, in islanded PEDG the network's inverters rely on rapid control loops for voltage, current, and PLL. In other

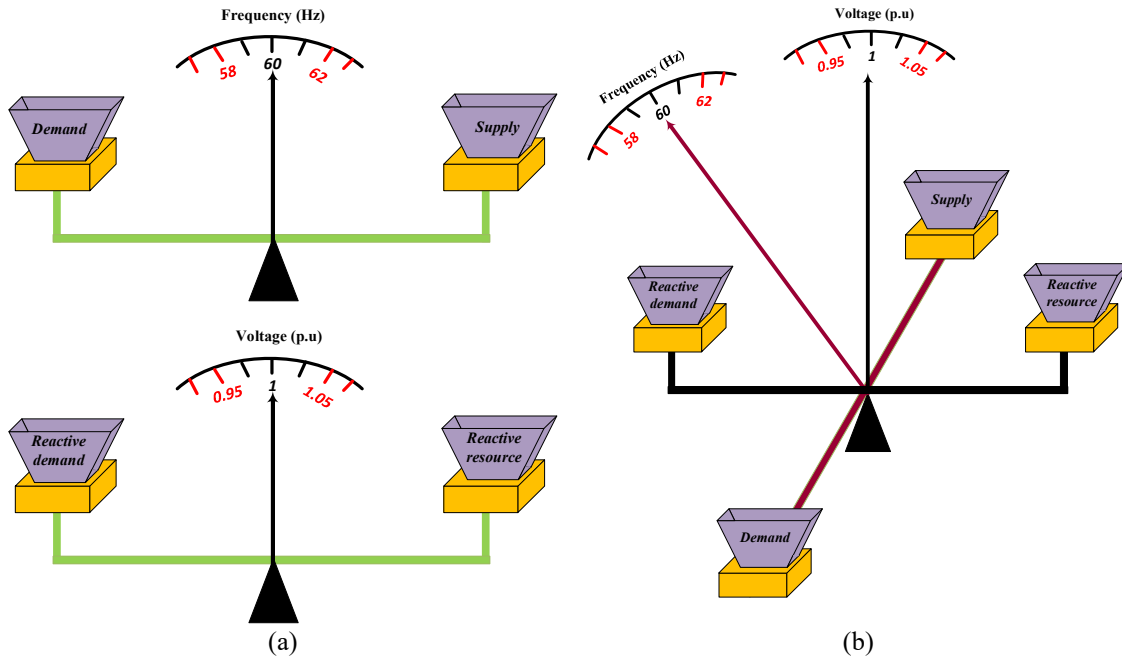


Figure 1.2. Analogy of manual weighing instrument with the degree of coupling between active power demand, reactive power demand, frequency, and voltage: (a) bulk power system follows $P - f$ and $Q - V$, and (b) power electronics dominated grid follows $P - f$ & V and $Q - V$ & f .

words, PEDG has low mechanical inertia and rapid and multi-time scale dynamics [20], not forgetting the dominant stochastic generation nature of PEDG's energy assets. Given these distinctive characteristics, the stability concept, vulnerabilities, and categorization of PEDG should be reassessed.

1.2. Power Electronics Dominated Grid Characteristics

The power generation at the point of the load in PEDG results in shorter feeders and smaller reactance to resistance ratio (X/R) in comparison to the traditional bulk power system [21]. Consequently, the mathematical representation of PEDG's voltage, frequency, bus angles, active power flow, and reactive power flow dynamics is significantly different compared to bulk power systems. Figure 1.2 demonstrates a comparison between the bulk

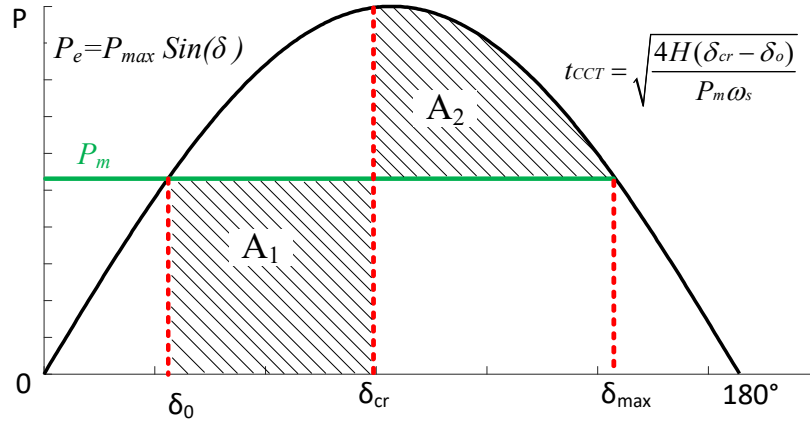


Figure 1.3. Equal area criterion for stability indicating the impact of inertia (H) on the critical clearing time (t_{CCT}).

power system and the PEDG regarding the degree of coupling between active power demand, reactive power demand, frequency and voltage by analogy of the manual weighing instrument. Specifically, in bulk power system the balance between active power demand/supply impact only frequency while reactive power demand/supply impact voltage (see Figure 1.2(a)). Whereas, in the PEDG active power demand/supply balance is coupled to both frequency and voltage (see Figure 1.2(b)). Similarly, the reactive power demand/supply balance is also coupled to both voltage and frequency (see Figure 1.2(b)). Additionally, the proximity between loads and generation units in PEDG makes the network more sensitive to the stochastic nature of renewable energy resources or any existing uncertainties. Furthermore, balancing the demand and supply in PEDG is challenging due to the dominant intermittent nature of the PEDG energy resources [22, 23]. Combining that challenge with the bidirectional power flow feature of the PEDG, the PEDG entails complex control and protection coordination among the network's prosumers.

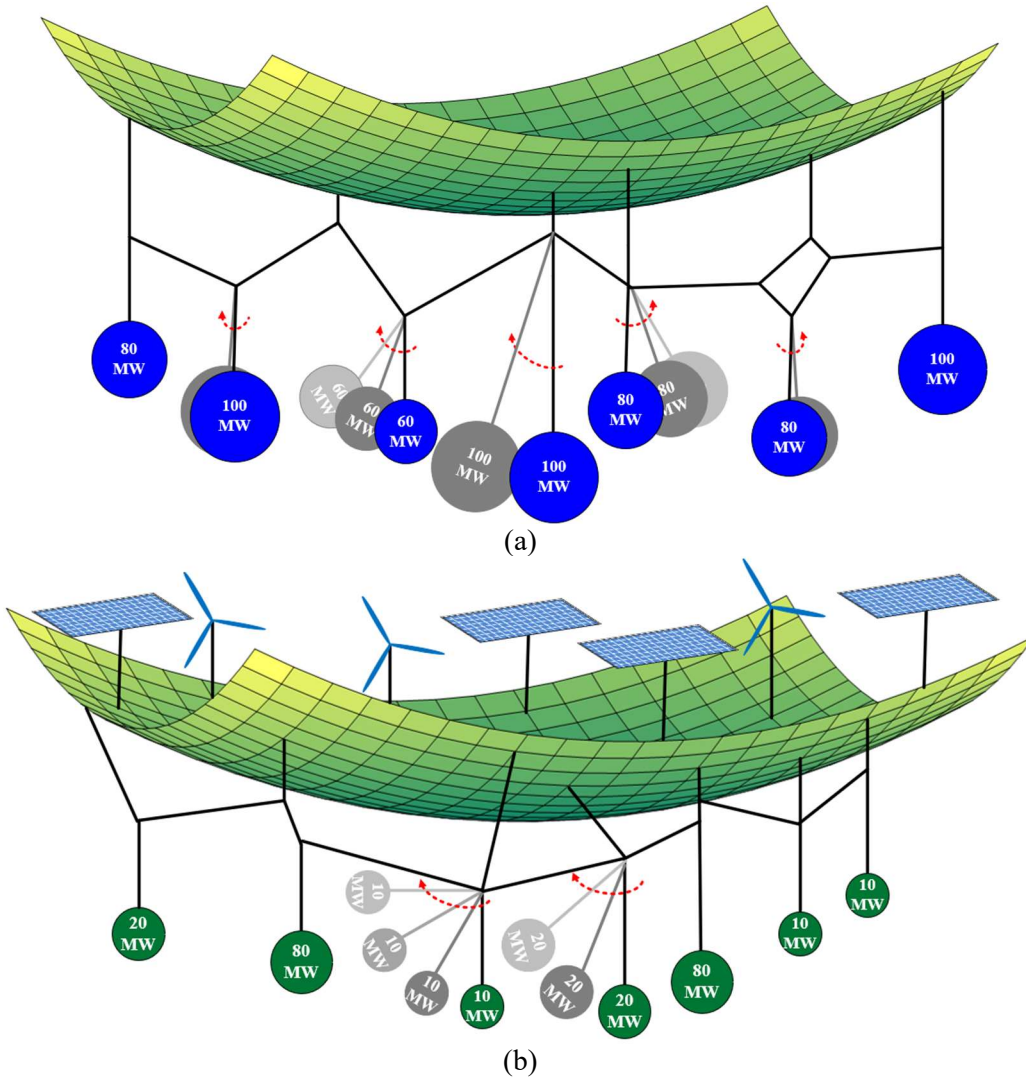


Figure 1.4. Illustration of inertia concept with pendulums in equilibrium conditions: (a) bulk power system and (b) power electronics dominated grid

With the expectation that the number of synchronous machines will be lesser in PEDG compared to static power electronics based generators, this will have a substantial impact on the system's overall inertia. Specifically, the PEDG inertia is significantly lower compared to the bulk interconnected power system. The low inertia problem of PEDG is severe with the low short circuit capacity of the network. Precisely, slight deviations in the

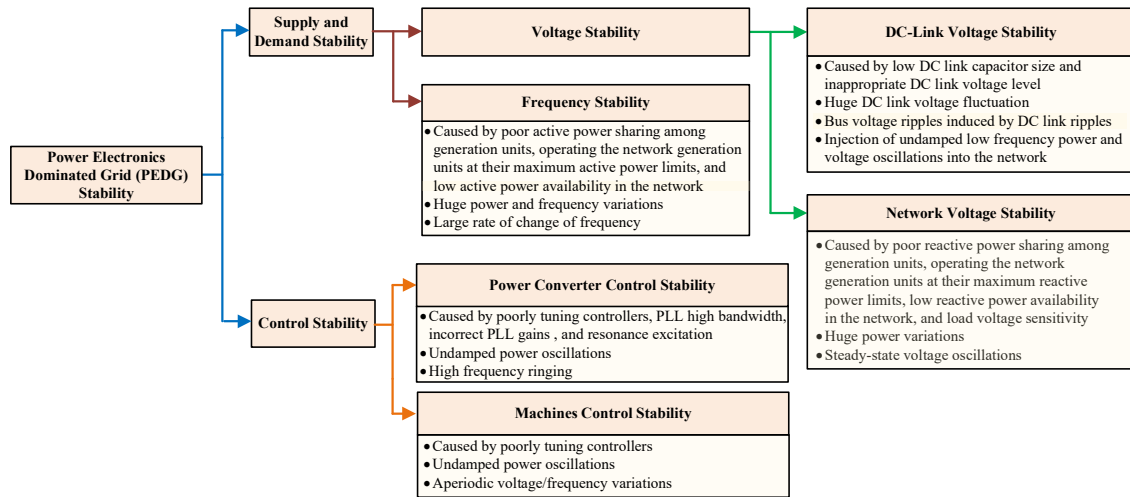


Figure 1.5. Power electronics dominated grid stability categorization with root cause and resulting phenomena.

PEDG architecture due to any intentional load or generator disconnection would have a drastic effect on the voltage and frequency. In fact, from protection perspective, the low inertia characteristic results in decreasing drastically the critical clearing time (t_{CCT}). As a result, fault clearance in the PEDG paradigm requires very fast relays. However, even if fast relays were deployed, the actual fault clearance will be slowed down due to the slow dynamics of the mechanical circuit breakers. Moreover, t_{CCT} is derived from the equal area criteria that is depicted in Figure 1.3. The analogy of the hanging pendulums network in Figure 1.4 illustrates the inertia comparison between the bulk power system and the futuristic PEDG paradigm. Specifically, the traditional grid is represented by heavy pendulums that are in a certain stable equilibrium point (see Figure 1.4(a)). If a disturbance occurs, such as external force impacting one of the pendulums in Figure 1.4(a), a significant number of other pendulums start to oscillate and eventually reaching to an equilibrium; since the pendulums are heavy in the traditional power system (representing bulk power

generation) these oscillations are damped quickly. However, when the same scenario is considered on the light pendulums that represent the low inertia PEDG network in Figure 1.4(b); drastic oscillations occur that takes longer time to damp. In fact, this indicates that the possibility to reach an instable equilibrium (i.e., network collapse) is higher in the PEDG paradigm compared to the bulk power system given the same size of the disturbance. This is due to the low inertia of the PEDG network. Furthermore, the mixture of synchronous machines with inverter based generations results in a combination of large and small time constants. This might force inverter based generation units to unintentionally shutdown during perturbation in the system parameters.

It is expected that PEDG is inherently unbalanced given the intermittent generation nature if not properly controlled. The three phase system could reach to severe unbalance conditions and destabilize the system if PEDG does not utilize the full capability of smart devices to provide corrective actions. Thus, the traditional stability analysis techniques are not sufficient to study the accurate dynamics of the PEDG paradigm.

1.3. Concept of Stability, Categorization, and Vulnerabilities of Power Electronics Dominated Grid

1.3.1. Concept of Stability

Take an example of a PEDG that is operating in equilibrium point. This means all network state variables are sustaining their operational constraints. Specifically, voltages and the frequency are in their appropriate values in steady-state. This network is stable if its state variables - after the network is being subjected to disturbance - reach to new steady-

state levels that are also sustaining the operational constraints and without intentional load shedding. However, in the PEDG paradigm loads can participate as controllable energy assets [24] and the operator has the liberty to prioritize certain load feeders over the rest of the network loads. For instance, feeders that are delivering power to critical loads such as hospitals and airports must have the highest priority in PEDG. Therefore, unlike bulk power system, the intentional load shedding of the critical loads renders the network to be unstable by the concept considered in this chapter; since in such situations the PEDG is no longer accomplishing its main objective to ensure energy services for critical infrastructures.

The disturbance in the operation of PEDG is categorized into small or large. The disturbance on a power network is defined as an external input that is resultant from load variations, element failures, or intentional and nonintentional operation mode changes or set-point adjustments. Fortunately, small disturbances can be captured by the linearized state space models and hence such disturbances are classified as small-signal perturbations. On the other hand, the large disturbances cannot be captured by the linearized state space models. Examples of such large disturbances are: generations assets loss, short-circuit faults, nonintentional transition from non-islanded to islanded mode of operation. Additionally, both large and small disturbances are further subcategorized into short and long term. For instance, small variations of loads in a heavy loaded network might trigger undamped power oscillations in the long term. In contrary, unbalanced power sharing among power generation assets excites power resonance phenomena that build up rapidly in short term.

1.3.2. Stability Categorization and Vulnerabilities

Given the distinctive characteristics of PEDG illustrated in subsection 1.2, the high portion of stability issues in the PEDG paradigm are related to frequency due to the intrinsic low inertia nature of the network. The voltage and transient instabilities that are dominant in the bulk power system are not expected to occur frequently in the islanded PEDG. This indicates the need for a light shedding on vulnerabilities for PEDG stability. Furthermore, stability of a power network is often classified based on: (i) magnitude of the disturbance causing instability, (ii) duration of the instability, (iii) physical root-cause of the instability, (iv) components caused or involved in the instability, (v) instability analysis approach, and (vi) instability trajectory and prediction approach. Categorizing stability in the PEDG paradigm according to the established stability concept is not simple, as PEDG variables dynamics are strongly coupled. In more details, any instability phenomena in a PEDG will result in oscillations in all the variables. In other words, it would be hard to distinguish voltage instability from frequency instability in a PEDG. Hence, the most logical categorization for instability in the PEDG is based on the origin of the instability, see Figure 1.5.

1.3.2.1. Demand and Supply Stability

Demand and supply balance stability is concerned about attaining the power generation and the required power demand equilibrium with assuring the optimal power sharing among the network energy resources assets. Poor power sharing among multiple energy generation assets, loss of energy generation assets, and unintentional load loss are examples that might originate a demand and supply instability issue. The demand and supply stability is divided into: (1.3.2.1.1) voltage and (1.3.2.1.2) frequency stability.

1.3.2.1.1. Voltage Stability:

Due to short feeder in PEDG, it is expected that voltage collapse is minimal. Often, a voltage collapse occurs due to insufficient reactive power and load recovery procedure. Furthermore, the key factors that influence voltage instability in PEDG are power limits of the distributed generation units and the sensitivity of the network loads to supplied voltages. These two factors make the small steady-state voltage oscillation to be considered as voltage instabilities. In fact, a potential unexpected delay in voltage recovery after fault clearance might cause a significant voltage drop in the PEDG. In such conditions, the PEDG network motor loads experience motor stall phenomena; since they are absorbing huge amounts of reactive power to assure re-magnetization. This leads to voltage instability and voltage sensitive loads disconnection because of the lack in reactive power availability in the network. Therefore, managing reactive power sharing among the PEDG energy generation assets is critical to voltage stability but challenging to achieve.

The difficulty of reactive power management is that it is linked to the short length of the network feeders. Precisely, any variations in the generation busses result immediately on other busses in the network. Additionally, in the PEDG paradigm, it is expected that the voltage of busses is dominantly controlled by the power converters associated with the generation units. This is a challenging aspect as the coordination between the different $Q - V$ droop curves of the generation units becomes difficult. In fact, any mismatch in these $Q - V$ droop curves might trigger large voltage fluctuations that are originated from the huge reactive power circulation among the energy generation units. Even though, if such mismatch problem in $Q - V$ droop curves is tackled, it is not likely that optimal reactive

power flow sharing in the PEDG network will be accomplished. This is because in a PEDG paradigm the network has a low X/R ratio that makes the reactive power flow dynamics coupled both with the frequency and the voltage. In other word, the $Q - V$ droop curves are no longer describing the reactive power flow dynamics accurately in the PEDG network.

Due to the multi-stage nature of the power electronics converters in the PEDG, often a DC link is required to buffer any instantaneous voltage ripples generated by the unbalanced nature of the PEDG paradigm [25]. With such requirement, DC links in the PEDG also enforce another type of voltage instability [26-28]. These instabilities are majorly linked to the size of the DC link capacitor and the voltage level on the DC link. For instance, insufficient DC link capacitance will result in undamped power ripples of twice the nominal network frequency [29]. Therefore, small reactive power demand increments for inverters operating at their maximum capacity will result in excess voltage ripples across their DC links that will inevitably reflect in the active and reactive power supplied into the network. Similarly, failure to maintain the appropriate voltage level on the DC link capacitor either impacts the balance between the injected and absorbed instantaneous power or forces the inverter to operate in nonlinear operation region. Consequently, injecting undamped low order power and voltage oscillation into the PEDG network. The root-cause of short-term voltage instability is related to rapid variations in the active and reactive power sharing. On contrary, operating at the maximum capacity of the generation units creates the long-term voltage instabilities; this condition is affecting the steady-state operation gradually. The large disturbance voltage instability originates from abrupt change in the demand such as a

generation loss, while small disturbance voltage instability is associated with gradual change in the demand of a network operating near its maximum capacity.

1.3.2.1.2. Frequency Stability:

The low inertia nature of a PEDG make frequency regulation a crucial challenge. In fact, even with an adequate power reserve existence, such frequency instability issues in low inertia systems cannot be recovered. Furthermore, in the PEDG paradigm the $P - f$ droop relation does not express the dynamics of the system accurately, since PEDG feeders' short length and low X/R ratio make a strong coupling between frequency dynamics with active power flow as well as voltage dynamics. Any voltage variations at the generation busses reflects instantaneously on the network loads, which indirectly affect the system demand and supply (i.e., system frequency) due to voltage sensitive loads tripping. Furthermore, frequency instabilities originate from various reasons, such as an unexpected huge demand increase without enough generation reserve availability. In such case, the frequency will decrease abruptly resulting in a blackout that is triggered by the protection relays [30]. Another root-cause of frequency instability in the PEDG paradigm is when there is poor power sharing among the network energy assets. This could result in small perturbation instability for durations ranging from seconds to minutes [31]. The duration of the frequency instability (i.e., short or long term) is linked to the time that the frequency protection relay is activated. Also, frequency instabilities in PEDG are extended to steady-state operation. For example, for a network operating at its maximum capacity, small variations in the demand might trigger frequency protection relays, which is considered as a long-term frequency instability. On contrary, this long-term frequency instability problem is tackled

by controlling the governor in power system. However, such mechanism is irrelevant to the PEDG paradigm.

1.3.2.2. Control Stability

Stability issues from system controllers' point of view are of two types: (1.3.2.2.1) power converters control stability, (1.3.2.2.2) machines control stability.

1.3.2.2.1. Power Converters Control Stability:

The inner control loops of the different power converters originate small perturbation instabilities in the PEDG paradigm. Furthermore, in terms of the instability frequency range, the outer power control loops are responsible on low frequency fluctuation instabilities, while high frequency type instability fluctuations are generated by the

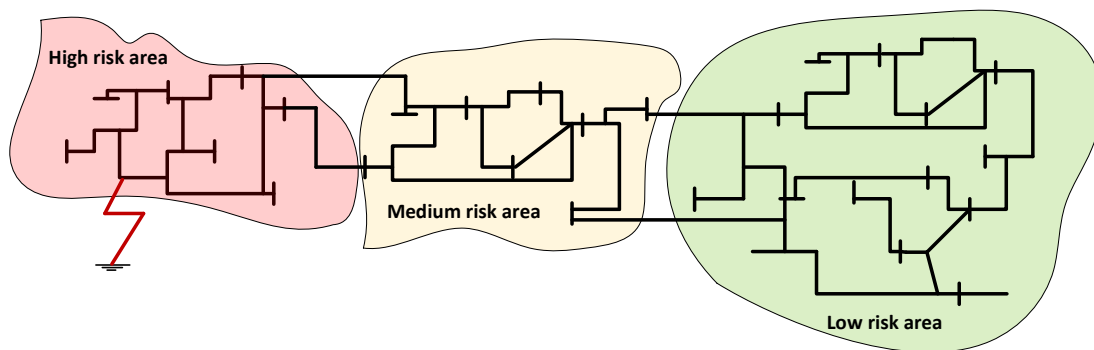


Figure 1.6. Illustration of the effect of the short circuit fault location on the size of the instability

interaction of the inner and outer control loops. Another control related element that might trigger resonance effects in the PEDG is the high frequency switching of the power converter modulators. In fact, with the proximity of generation units and loads property, it is more likely that mutli-resonance excitation, due to control actions, occurs in the PEDG

compared to the bulk power system [32]. Moreover, as instabilities are induced by the PLL controller in grid-connected mode; in the islanded PEDG paradigm the PLL controller gains are vulnerable which might lead to instabilities in the system. Recent literature recommended decreasing the bandwidth of the PLL controller to eliminate the voltage instabilities that is caused by the negative damping at the low range of frequencies with high bandwidth PLL controllers [4, 13, 27, 33-35]. Nevertheless, low bandwidth PLLs rises another instability which is particularly related to heavy loaded PEDG.

1.3.2.2.2. Machines Control Stability:

In PEDG a phenomenon such as synchronous generators' rotors acceleration during faults to remain synchronized with the network is not likely to happen, due to the low X/R ratio. Nevertheless, the rotor angle deceleration phenomena might occur if a short circuit fault happens at the end of the feeder; the reason is the resistive nature of PEDG. Moreover, instabilities associated with undamped or aperiodic oscillations of synchronous generators' rotor angle are not expected to occur in the PEDG paradigm. This is because the issues of synchronous generators low damping torque or low synchronization torque are tackled by properly tuned governors and exciters in the PEDG paradigm. Hence, instabilities of electric machines in the PEDG are originated by improperly tuned controllers.

1.4. Small-Perturbation and Large-Perturbation Instabilities

The origin of small-perturbation instabilities is majorly linked to the low damping availability for critical eigenvalues of the network. Small-perturbation instabilities can be captured by the linearized state-space model of the network. However, the duration of the small-perturbation instabilities is due to the root cause of the instabilities, disturbance

Table 1. Summary of the power electronics dominated grid stability with origin and effects

Category	1. Supply and Demand Stability		2. Control Stability		
Subcategory	1.1. Frequency Stability	1.2. Voltage Stability		2.1. Power Converters Control Stability	2.2. Machines Control stability
Sub subcategory		1.2.1. DC link Voltage Stability	1.2.2. Network Voltage Stability		
Origin	<ul style="list-style-type: none"> - Poor active power sharing among generation units - Operating the generation units at their maximum active power limits - Low active power availability in the network 	<ul style="list-style-type: none"> -Low DC link capacitor size - Inappropriate DC link voltage level 	<ul style="list-style-type: none"> - Poor reactive power sharing among generation units - Operating the generation units at their maximum reactive power limits - Low reactive power availability in the network 	<ul style="list-style-type: none"> -Poorly tuning controllers - PLL high bandwidth -Incorrect PLL gains - Resonance excitation 	<ul style="list-style-type: none"> -Poorly tuning controllers
Effect	<ul style="list-style-type: none"> - Huge power and frequency variations - Large rate of change of frequency 	<ul style="list-style-type: none"> - Huge DC -link voltage fluctuation - Bus voltage ripples induced by DC link ripples - Injection of undamped low frequency power and voltage oscillations in to the network 	<ul style="list-style-type: none"> -Huge power variations -Steady-state voltage oscillations 	<ul style="list-style-type: none"> - Undamped power oscillations -High frequency ringing 	<ul style="list-style-type: none"> - Undamped power oscillations -Aperiodic voltage/frequency variations

magnitude, inherent nature of the network. For instance, undamped power oscillations are witnessed when poor power sharing among multiple distributed generation occurs; this power oscillations grows quickly violating the operation constrains of the network in short term. On the contrary, small demand and supply change in a heavy loaded network rises undamped power oscillations that take long time to violate the operational constraints. Instabilities that

cannot be captured by the linearized state-space model of the network are considered as large-perturbation instabilities. Large-perturbation instabilities originate from amount and location of short-circuit faults, unintentional transition from non-islanded to islanded mode of operation, and generation units' loss. The relative size of the instability is illustrated in Figure 1.6. Specifically, the area near to the location of the short-circuit fault (i.e., the red color area in Figure 1.6) experiences large-perturbation instability. Whereas areas far from the location of the fault might witness small-perturbation instability such as the green area in Figure 1.6. However, the difficulty in the PEDG paradigm is to determine the boundary where the small-perturbation is equal to large-perturbation instability. In other words, validating to how much extent the linearized state-space models can represent the system accurately which is shown by yellow area in Figure 1.6. Regarding large-perturbation instability time frame, large perturbation instability is always a short-term phenomenon. For instance, unplanned islanding makes the system rapidly unstable due to drastic large variations in the frequency and the voltage. Finally, the categorization provided in Figure 1.5 is summarized in Table 1 indicating the origin of the instability with its effects on the network parameters.

1.5. Research Roadmap and Open Research Questions in the Power Electronics Dominated Grid

1.5.1. Frequency Control

Automatic Frequency Control in the PEDG: The need for automatic frequency control is necessary for compensating the lack in the inertia. This new requirement for automatic frequency control at the edge of the grid multiple questions arise as follows: (i) Which kind

of measurement are needed to achieve this automatic frequency control at the distribution level, (ii) should be a communication among each distributed generation unit or each distributed generation unit communicate with the system operator only, (iii) what type of communication infrastructure is required, is it peer-peer, centralized, aggregators, bandwidth, latency, etc., (iv) can the frequency limit specified by the standards be loosened in the PEDG paradigm.

Active Power Control: The control of active power is basically curtailment of the available energy production by operating the system below the maximum power point. In traditional power system, power curtailment does not sacrifice the available energy but in PEDG the renewable energy is sacrificed; as the loss for renewable energy-based system is considering the system when not operating at the maximum available power as a loss [14]. Hence, it is necessary to validate, develop, and investigate control approaches to support grid frequency and voltage by the power electronics converters with or without storage.

1.5.2. Voltage Control

Loss of Reactive Power: In PEDG the compensation of reactive power loss by the automatic voltage control of traditional synchronous generators is replaced by local voltage/Var control at the edge of the grid by the power electronics converters. The critical questions here are what is the impact of moving the voltage control from generation side in the bulk power system to thousands inverters at the distribution level and how they will impact the voltage stability in PEDG.

1.5.3. Heterogeneity

The heterogeneous nature of PEDG results in unexpected events that may cause synchronization failure, instability, and eventually blackouts of various sizes. Thus, the open research questions coupled with heterogeneity of the PEDG paradigm includes: (i) feasible penetration level of power electronics-based generation without jeopardizing the power grid stability; (ii) impact of grid-following versus grid-forming inverters on the system stability; (iii) assessing the PEDG vulnerability to frequency deviation and restoration given the fact that higher inertia-based generation is minimal; (iv) feasibility to design the controllers in PEDG to avoid undesired interactions between grid-following inverters, grid-forming inverters, and synchronous generators; (v) feasibility of leveraging the classical power system stabilizers (PSS) in PEDG but at the grid-edge. Another concern that is related to the system heterogeneity is regarding the geographical distribution of the generation entities in the PEDG paradigm. How does the PEDG paradigm network topology influence the distributed voltage/Var control stability; especially, with the mixture of small portion synchronous generators with power converters in various control modes. Specifically, that in grid-following mode the inverter replicates the instantaneous inertial response of synchronous machines with a delay and perform sub-optimally on the time scales of interest [16]. On the other hand, in grid-forming mode the inverter mimics the behavior of synchronous machines in black-start capability, load sharing, load drooping, inertial response, and multi-layer frequency and voltage regulation [36]. Moreover, the main reported grid-forming controls are: (i) droop control that mimic synchronous machines speed droop [37], (ii) virtual synchronous machines or so-called the

Table 2. Grid Forming technologies, operation principle analogy, state of maturity, research trend and references

Technology	Operation Principle Analogy	State of Maturity	Research Trend	References
Droop Control	Mimic speed droop of synchronous machines	In the market	Low	[37], [39]
Synchronverter	Speed droop with inertia emulation through swing equation of synchronous machines	Started	High	[20-22, 40-43]
Virtual Oscillator Control	Synchronizing mechanism of Liénard-type oscillators	Not started	Medium	[44-47]
Matching Control	Structural similarity between DC link voltage to synchronous machines frequency behavior	Not started	High	[38, 48-50]

synchronverters that are an extension of the droop control but with additional inertia emulation utilizing the swing equation [21], (iii) matching control that relates structural similarities between the converter control to a synchronous machines; which are based on the observation that the DC link voltage is similar to synchronous machines frequency indicating power imbalance [38], (iv) virtual oscillator control that mimic the synchronizing mechanism of Liénard-type oscillators that globally synchronize a fully converter based network [44-46]. Furthermore, based on the number of publications in the literature related to grid forming technologies the state of maturity, the research trend and references are illustrated in Table 2.

1.5.4. Cybersecurity Vulnerability

In the PEDG paradigm, the number of remote-control capabilities that utilizes information communication technologies is high compared to the bulk power system. Initially, the notion of using more intelligent devices in the PEDG paradigm might appear appealing [37], as the network controllability and observability increases, which also

indirectly impacts the network efficiency and reliability positively. However, this large integration of intelligent devices in the PEDG paradigm brings cybersecurity vulnerability [51]. These cyber-attacks are ranging from simple thefts and consumer loads damage to high impacts that leads to shutdown, cascaded failures and large blackouts that impact the energy market operation [52].

Intelligent cyber-physical attacks on the PEDG network are targeting the physical layer to violate the network stability limits by appearing as normal network uncertainties or even remain undetected until a server interruption in the system - stealthy attacks. Given the PEDG paradigm multi-time scale nature, this dictates the detection of cyber-attacks in a very short duration to avoid serious consequences on the PEDG operation. To summarize, the PEDG paradigm is more vulnerable to cyber-attacks compared to traditional bulk power system. Thus, proactive intrusion detection mechanisms and corrective control actions are required to enable cyber-secure PEDG.

1.5.5. Synchronverter and coherence enforcement potentials in the power electronics dominated grid

As the control diversity of a network increases, as in the PEDG paradigm, the network characteristics might be tunable by individual controllers. For instance, droop control grid forming inverters can be leveraged to change the inherent characteristics of the network from being high resistive to highly inductive through virtual impedance emulation. Such alteration if possible is crucial as it makes sure that the energy network is following the conventional $P - f$ and $Q - V$ droop curves, which is an essential research need for the PEDG. Moreover, theories such as coherency enforcement are leveraged in investigating

the possibility to enforce $P - f$ and $Q - V$ droop on a resistive network [53, 54]. Another research and application trend that is expected to happen is the adoption of large amount of self-synchronized synchronverters i.e., virtual synchronous machines with no dedicated PLL [21, 22, 40, 55-59]. In fact, [60] demonstrated a field implementation synchronverters that seamlessly transition from grid-connected mode to islanded mode without PLL. Also, all necessary functionalities are achieved without communication links [40] – minimizing the cybersecurity vulnerability of PEDG. With these two possibilities, it might be possible that the PEDG paradigm will be enforced to follow conventional power system behavior; thus, application of the well-establish power system stability theory might be applicable for the PEDG paradigm. However, this is still an open question that needs to be verified and implemented in practice.

Figure 1.7 illustrates some of the open research stability challenges that are comparable to bulk power system stability. For instance, how the angle stability will be impacted with mixture of synchronverter, non-inertia emulating grid-forming inverters, grid-following and conventional synchronous generators. The investigation of this issue is crucial as the transition from the bulk power system to the PEDG paradigm will not happen instantaneously. Furthermore, another concern in this futuristic grid is in what way power converters terminal voltage and DC link voltage fast controllers contribute to voltage dynamic stability. In other words, can they play the role of machines exciters. Furthermore, how the network voltage stability will be impacted by the PEDG distributed voltage/var control and what is the impact of these measurements at the grid edge. Similarly, can the new paradigm generation behave the same as governors and support system frequency.

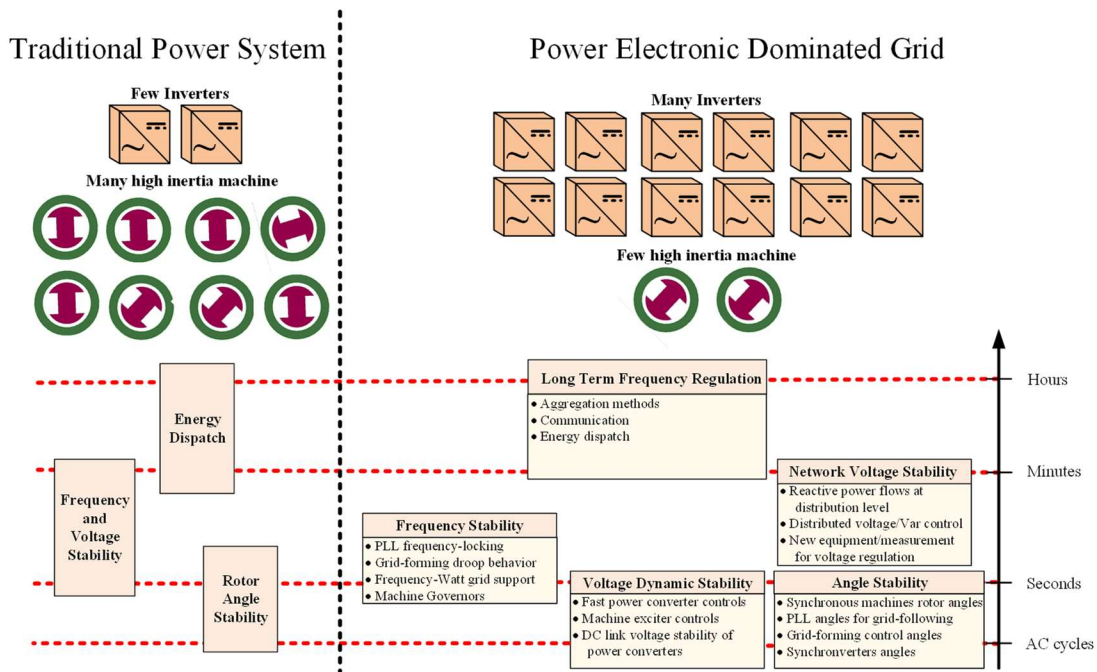


Figure 1.7. New stability challenges that power electronics dominated grid introduced in comparison with the time scale

Finally, what will happen to long-term frequency regulation issues. For instance, how optimal energy dispatch and unit commitment problems should be solved, what are the aggregation methods, and which type of communication infrastructure is needed.

1.6. Conclusion

This chapter presented detailed stability concepts, categorization, and open research questions for the power electronic dominated grid (PEDG) paradigm. The distinct characteristic of the PEDG network, low inertia, stochastic generation, proximity of generation units and loads, low X/R ratio, short feeders, etc., made the acceptable dynamic operation and the stability limits of the PEDG different compared to traditional power system. For example, stability in the PEDG paradigm cannot be classified by frequency or

voltage instability; this is due to the strong coupling between these dynamics. In more details, any instability phenomena in a PEDG will result in oscillations in all the variables. Hence, the most logical categorization for instability in the PEDG paradigm is based on the origin of the instability. Specifically, the stability of PEDG is categorized into two major parts: (1) supply and demand stability and (2) control stability. The supply demand stability covers frequency and voltage stability. While the control stability includes power converters control and machines control stability. Such instabilities have negative effect on the PEDG paradigm network such as: huge power and frequency variations, large rate of change of frequency, huge DC link voltage fluctuation, bus voltage ripples induced by DC link ripples, injection of undamped low frequency power and voltage oscillation into the network, steady-state voltage oscillations, high frequency ringing, and aperiodic voltage and frequency variations. Moreover, since the transition from the bulk power system to the PEDG paradigm will not happen instantaneously; various open research questions arise that are mainly focused on moving necessary functionality of the bulk power system to the grid edge with thousands of inverters in different operation modes i.e., grid-following mode, non-inertia grid-forming mode, synchronverters mode, etc. These questions are discussed in detail in the research roadmap section with the level of maturity of each technology.

Chapter 2

2. Primary Current Control Development

Part of this chapter, including figures and text are based on my following papers:

© 2018-2022 IEEE

- A. Khan, M. Hosseinzadehtaher, M. B. Shadmand, "Single Stage PLL-less Decoupled Active and Reactive Power Control for Weak Grid Interactive Inverters", *IFAC-PapersOnLine*, vol. 53, no, 2, pp. 12390-12395, 2020

- A. Khan, M. Easley, M. Hosseinzadehtaher, M. B. Shadmand, H. Abu-Rub and P. Fajri, "PLL-less Active and Reactive Power Controller for Grid-Following Inverter," *2020 IEEE Energy Conversion Congress and Exposition (ECCE)*, pp. 4322-4328, 2020

- A. Khan, M. Hosseinzadehtaher, A. Y. Fard and M. B. Shadmand, "Active Power Decoupling Control for Rectifiers with Variable Frequency Supply for More Electric Aircraft," *2021 IEEE Industry Applications Society Annual Meeting (IAS)*, pp. 1-8, 2021

2.1. Phase Locked Loop (PLL) Limitations

One of the crucial parts of the current control for grid-following inverters (GFLIs) that ensures synchronization with the utility grid terminals is the phase-locked-loop (PLL) [15, 61, 62]. Recent literature revealed that PLL influences the small-signal stability of GFLIs [4, 22, 40, 63]. Precisely, a negative admittance increment is observed at the low range of the frequency spectrum of the inverter output impedance [13, 64] (see Figure 2.1 for illustration). According to [65], the range of this negative admittance is linked to the bandwidth of the PLL, and it has been revealed that a low bandwidth PLL will guarantee current control robustness. Yet, a low bandwidth PLL sacrifices the dynamic performance of the GFLI. In fact, with a properly designed low bandwidth PLL, enforcing the GFLI to remain stable under weak grid conditions is challenging as depicted in Figure 2.2. Thereby, providing a control approach for GFLI without a PLL utilizations enhances the stability of the inverter when interacting with a weak grid [66].

In this chapter, a PLL-less single control loop direct active and reactive power (PQ) control for single-phase GFLIs is developed. The control single stage structure reduces the effort required in tuning the controller gains compared to the typical dual-loop cascaded PQ control methodology [67, 68]. This control approach enables point of common coupling (PCC) current synchronization without the deployment of a PLL. This removes concerns of instabilities that might arise due to PLL non-linear nature and weak grid's large line impedance seen after the PCC negative influence [69, 70]. Furthermore, to assure the GFLI capability in tracking the PQ set-points with weak resistive or inductive grid connections, PQ steady state stability bounds associated to PCC voltage are derived in this chapter.

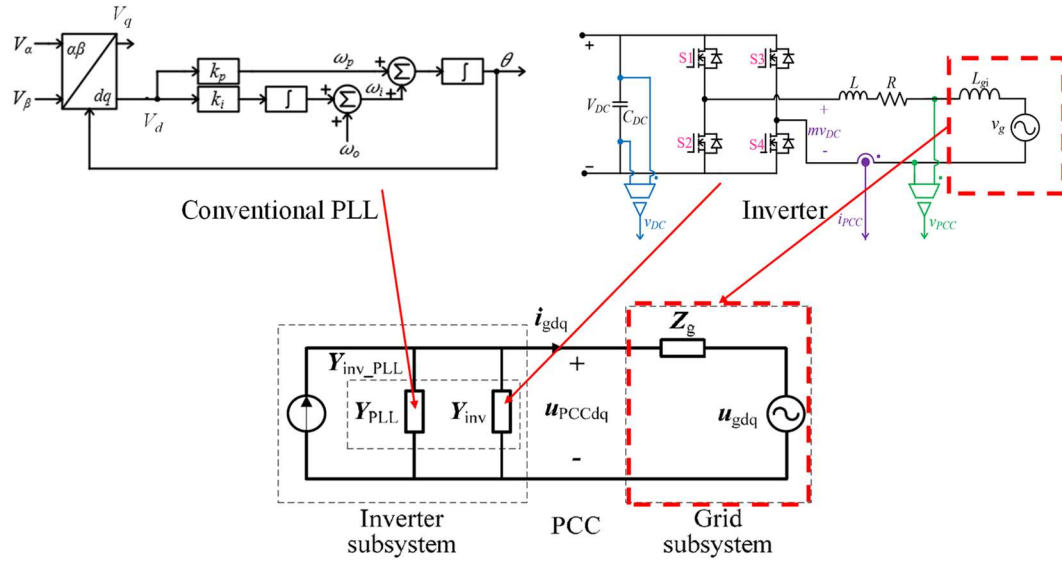


Figure 2.1. PLL issue related to its contribution to the output impedance of the GFLI that is negative damping.

These bounds assure that the fundamental component of the point of common coupling (PCC) voltage is available for the correct operation of the GFLI. In addition, this chapter develops an improved GFLI control with no PLL requirement to accommodate current control that is adaptive to frequency.

2.2. Mathematical Modeling, Controller Design, and Control Stability of the Developed PLL-less Grid-Following Inverter Control

2.2.1. Mathematical Modelling

Consider the single-phase GFLI that is connected to a weak grid in Figure 2.3. The active power (P) and reactive power (Q) injected into the grid can be measured by utilizing the second order generalized integrator (SOGI) that was developed in [71] and presented as (2.1) and (2.2), respectively. The SOGI has a harmonic filtering capability that makes

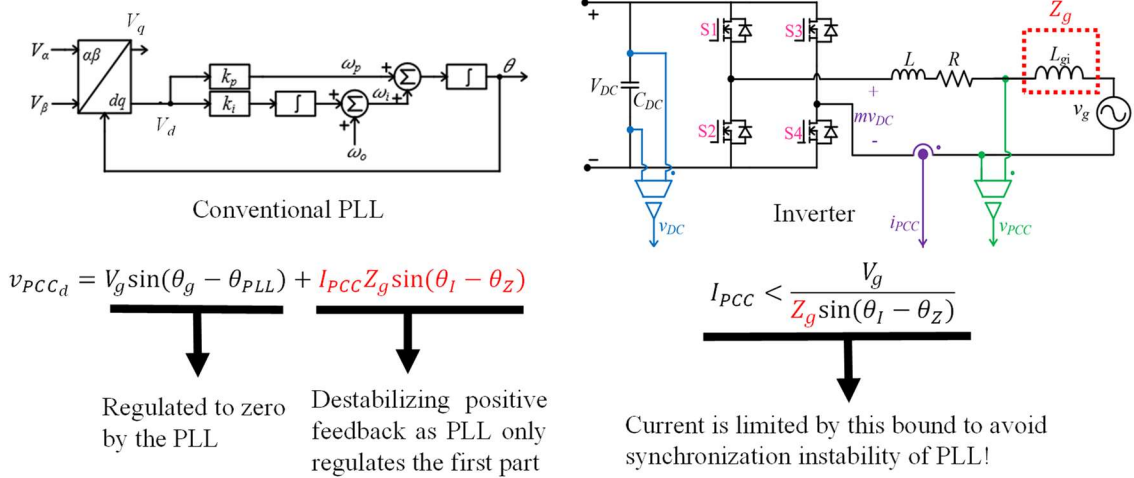


Figure 2.2. PLL issue related to having high impedance after the point of common coupling terminals in weak grid connections for GFLI.

the measurements robust to distortion imposed by weak grid conditions [72, 73].

$$P = \frac{1}{2} i_{PCC}^\alpha v_{PCC}^\alpha + \frac{1}{2} i_{PCC}^\beta v_{PCC}^\beta \quad (2.1)$$

$$Q = \frac{1}{2} i_{PCC}^\alpha v_{PCC}^\beta - \frac{1}{2} i_{PCC}^\beta v_{PCC}^\alpha \quad (2.2)$$

By differentiating equations (2.1) and (2.2) with respect to time, the state-space model that includes active and reactive power as state variables can be determined,

$$\frac{dP}{dt} = \frac{1}{2} v_{PCC}^\alpha \frac{di_{PCC}^\alpha}{dt} + \frac{1}{2} i_{PCC}^\alpha \frac{dv_{PCC}^\alpha}{dt} + \frac{1}{2} v_{PCC}^\beta \frac{di_{PCC}^\beta}{dt} + \frac{1}{2} i_{PCC}^\beta \frac{dv_{PCC}^\beta}{dt} \quad (2.3)$$

$$\frac{dQ}{dt} = \frac{1}{2} v_{PCC}^\beta \frac{di_{PCC}^\alpha}{dt} + \frac{1}{2} i_{PCC}^\alpha \frac{dv_{PCC}^\beta}{dt} - \frac{1}{2} v_{PCC}^\alpha \frac{di_{PCC}^\beta}{dt} - \frac{1}{2} i_{PCC}^\beta \frac{dv_{PCC}^\alpha}{dt} \quad (2.4)$$

Furthermore, the expression for the derivatives with respect to time of the stationary reference frame PCC currents i_{PCC}^α and i_{PCC}^β in (2.3) and (2.4) are deduced by applying Kirchhoff's voltage law at the loop of common coupling depicted in Figure 2.3. Hence, the PCC currents derivatives are as (2.5) and (2.6).

$$\frac{di_{PCC}^\alpha}{dt} = \frac{v_{DC}}{L} m_\alpha - \frac{1}{L} v_{PCC}^\alpha - \frac{R}{L} i_{PCC}^\alpha \quad (2.5)$$

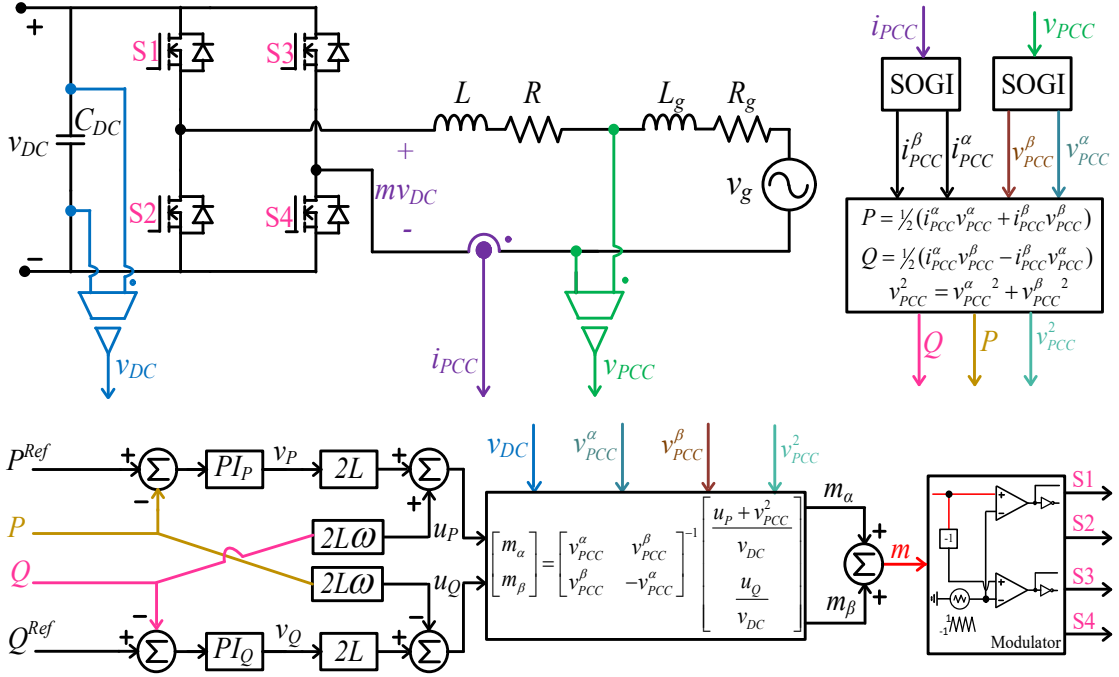


Figure 2.3: Developed PLL-less single control loop active and reactive power control for single phase GFLI.

$$\frac{di_{PCC}^\beta}{dt} = \frac{v_{DC}}{L} m_\beta - \frac{1}{L} v_{PCC}^\beta - \frac{R}{L} i_{PCC}^\beta \quad (2.6)$$

where m_α and m_β are stationary reference frame modulation indices, L is the filter inductance, and R is the filter stray resistance. Similarly, expression of the derivatives of the stationary reference PCC voltages v_{PCC}^α and v_{PCC}^β in equations (2.3) and (2.4) are given as (2.7) and (2.8).

$$\frac{dv_{PCC}^\alpha}{dt} = -\omega v_{PCC}^\beta \quad (2.7)$$

$$\frac{dv_{PCC}^\beta}{dt} = \omega v_{PCC}^\alpha \quad (2.8)$$

where ω is the angular frequency of the network. Therefore, substituting (2.5), (2.6), (2.7) and (2.8) into (2.3) and (2.4) results in the time varying multi input multiple output (MIMO) state-space system given by (2.9) and (2.10). The system is time varying because

the stationary reference modulation indices m_α and m_β are multiplied by the PCC voltages.

In addition, this MIMO state space control inputs are coupled in both states.

$$\frac{dP}{dt} = -\frac{RP}{L} - \omega Q + \frac{1}{2L} (m_\alpha v_{DC} v_{PCC}^\alpha + m_\beta v_{DC} v_{PCC}^\beta - v_{PCC}^2) \quad (2.9)$$

$$\frac{dQ}{dt} = -\frac{RQ}{L} + \omega P + \frac{1}{2L} (m_\alpha v_{DC} v_{PCC}^\beta - m_\beta v_{DC} v_{PCC}^\alpha) \quad (2.10)$$

where v_{PCC} is the norm of v_{PCC}^α and v_{PCC}^β .

2.2.2. Control Design

If the two inputs are defined as (2.11) and (2.12); the state-space in (2.9) and (2.10) transforms into a simple linear time invariant (LTI) MIMO state-space as (2.13) and (2.14).

$$u_p = m_\alpha v_{DC} v_{PCC}^\alpha + m_\beta v_{DC} v_{PCC}^\beta - v_{PCC}^2 \quad (2.11)$$

$$u_Q = m_\alpha v_{DC} v_{PCC}^\beta - m_\beta v_{DC} v_{PCC}^\alpha \quad (2.12)$$

$$\frac{dP}{dt} = -\frac{R}{L} P - \omega Q + \frac{1}{2L} u_p \quad (2.13)$$

$$\frac{dQ}{dt} = -\frac{R}{L} Q + \omega P + \frac{1}{2L} u_Q \quad (2.14)$$

Now, consider the error on the instantaneous active and reactive power as (2.15) and (2.16),

$$e_p = P_{Ref} - P \quad (2.15)$$

$$e_Q = Q_{Ref} - Q \quad (2.16)$$

where P_{Ref} is the reference commanded active power and Q_{Ref} is the reference commanded reactive power. Moreover, the cancellation of the coupling terms in (2.13) and (2.14) is achieved by taking the following control law that includes feedback and feedforward as (2.17) and (2.18).

$$u_p = \underbrace{2L\omega Q}_{\text{Feedforward}} + \underbrace{2Lv_p}_{\text{Feedback}} \quad (2.17)$$

$$u_Q = \underbrace{-2L\omega P}_{\text{Feedforward}} + \underbrace{2Lv_Q}_{\text{Feedback}} \quad (2.18)$$

The feedback term v_p in (2.17) is obtained with a Proportional Integral (PI) controller as (2.19) that tracks the desired active power reference.

$$v_p = K_{pp}e_p + K_{pi} \int_0^t e_p(\tau) d\tau \quad (2.19)$$

Similarly, the feedback term v_Q in (2.18) is deduced with a PI controller as (2.20), this PI controller assures tracking the desired reactive power reference.

$$v_Q = K_{Qp}e_Q + K_{Qi} \int_0^t e_Q(\tau) d\tau \quad (2.20)$$

Moreover, substituting (2.19) into (2.17) and then placing the resulting expression into (2.13) yields the error dynamics of the active power that is given by (2.21).

$$\frac{de_p}{dt} = -\left(K_{pp} + \frac{R}{L}\right)e_p - K_{pi} \int_0^t e_p(\tau) d\tau \quad (2.21)$$

Likewise, inserting (2.20) into (2.18) and then substituting the resulting expression into (2.14) yields the error dynamics of the reactive power as (2.22).

$$\frac{de_Q}{dt} = -\left(K_{Qp} + \frac{R}{L}\right)e_Q - K_{Qi} \int_0^t e_Q(\tau) d\tau \quad (2.22)$$

2.2.3. Control Stability

The active and reactive power error dynamics in (2.21) and (2.22) indicate that if the controller gains K_{pp} , K_{pi} , K_{Qp} and K_{Qi} are positive, the primary control layer is exponentially globally asymptotically stable. This is proved by linear quadratic Lyapunov stability theorem as follows, (2.21) and (2.22) are expressed by the state-space (2.23).

$$\begin{aligned} \frac{dX}{dt} &= AX \\ X &\in \mathbb{R}^4, A \in \mathbb{R}^{4 \times 4} \\ X &= \begin{bmatrix} e_p & \frac{de_p}{dt} & e_Q & \frac{de_Q}{dt} \end{bmatrix}^T \\ A &= \begin{bmatrix} 0 & 1 & 0 & 0 \\ -K_{pi} & -\left(K_{ppi} + \frac{R}{L}\right) & 0 & 0 \\ 0 & 0 & 0 & 1 \\ 0 & 0 & -K_{Qi} & -\left(K_{Qpi} + \frac{R}{L}\right) \end{bmatrix} \end{aligned} \quad (2.23)$$

Then, to prove the stability of the closed loop control, the selection a positive definite matrix symmetrical matrix ($Q \in \mathbb{R}^{4 \times 4}$), results in a positive definite symmetrical matrix ($P \in \mathbb{R}^{4 \times 4}$) for satisfying the (2.24).

$$PA + A^T P + Q = 0 \quad (2.24)$$

To show this, the selection of $Q = I^{4 \times 4}$ ($I^{4 \times 4}$ is the identity matrix with dimension of 4×4) which is positive definite symmetrical matrix. The solution of (2.24) will be as given in (2.25).

$$P = \begin{bmatrix} \Theta_{11} & \Theta_{12} & 0 & 0 \\ -\Theta_{12} & \Theta_{22} & 0 & 0 \\ 0 & 0 & \Lambda_{11} & \Lambda_{12} \\ 0 & 0 & -\Lambda_{12} & \Lambda_{22} \end{bmatrix}$$

$$\Theta_{11} = K_{P_i}^2 + \left(K_{P_p} + \frac{R}{L}\right)^2 + K_{P_i}, \Theta_{12} = \frac{1}{2K_{P_i}}, \Theta_{22} = \frac{1}{K_{P_i} \left(K_{P_p} + \frac{R}{L}\right)} - 1, \quad (2.25)$$

$$\Lambda_{11} = K_{Q_i}^2 + \left(K_{Q_p} + \frac{R}{L}\right)^2 + K_{Q_i}, \Lambda_{12} = \frac{1}{2K_{Q_i}}, \Lambda_{22} = \frac{1}{K_{Q_i} \left(K_{Q_p} + \frac{R}{L}\right)} - 1$$

If the parameters K_{P_p} , K_{P_i} , K_{Q_p} and K_{Q_i} are designed respecting the conditions shown in (2.26),

$$K_{P_p} + \frac{R}{L} > 0, K_{P_i} > 0, K_{Q_p} + \frac{R}{L} > 0, K_{Q_i} > 0 \quad (2.26)$$

Then, $P > 0$ (i.e., positive definite matrix since all leading minors and the determinant are positive). Therefore, the equilibrium point $(0,0,0,0)$ is globally exponentially asymptotically stable. Hence, converging to the error dynamics to the equilibrium point $(0,0,0,0)$ means the original system is converging to $(P_{Ref}, 0, Q_{Ref}, 0)$ as $t \rightarrow \infty$. The Lyapunov candidate energy function is mathematically described in (2.27).

$$V(X) = X^T P X, \quad \frac{dV(X)}{dX} = X^T (PA + A^T P) X$$

$$\because A < 0, P > 0 \quad (2.27)$$

$$\therefore V(X) > 0, \quad \frac{dV(X)}{dX} < 0$$

To retrieve the original system inputs which are the inverter stationary reference modulation indices m_α and m_β ,

$$\begin{bmatrix} m_\alpha \\ m_\beta \end{bmatrix} = \frac{1}{v_{PCC}^2} \begin{bmatrix} v_{PCC}^\alpha & v_{PCC}^\beta \\ v_{PCC}^\beta & -v_{PCC}^\alpha \end{bmatrix} \begin{bmatrix} \frac{u_P + v_{PCC}^2}{v_{DC}} \\ \frac{u_Q}{v_{DC}} \end{bmatrix} \quad (2.28)$$

v_{PCC}^2 in (2.28) is the square of the L_2 norm of v_{PCC} . In network stable conditions $v_{PCC}^2 \in \mathbb{R}$, since v_{PCC} is well-posed and the signals v_{PCC}^α and v_{PCC}^β are always orthogonal. Finally, the modulation index that controls the single-phase GFLI is given as (2.29).

$$m = [1 \quad 1] \begin{bmatrix} m_\alpha \\ m_\beta \end{bmatrix} \quad (2.29)$$

The overall controller structure of the developed single loop PLL-less PQ control for single phase GFLIs is illustrated in Figure 2.3.

2.3. Weak Grid and Point of Common Coupling Voltage Steady State Stability

2.3.1. Resistive Weak Grid Consideration

The power flow between the PCC terminals and the weak resistive grid in steady state stable operation is expressed by (2.30) and (2.31).

$$P_{Ref} \triangleq P = \frac{V_{PCC}^2}{R_g} - \frac{V_{PCC} V_g}{R_g} \cos(\delta) \quad (2.30)$$

$$Q_{Ref} \triangleq Q = \frac{V_{PCC} V_g}{R_g} \sin(\delta) \quad (2.31)$$

where the V_{PCC} is the magnitude of the PCC voltage, V_g is the magnitude of the grid voltage, δ is the power angle at the PCC bus, and R_g is the resistive weak grid resistance.

Furthermore, by combining (2.30) and (2.31) through cancelling the power angle from both equations; the PCC voltage magnitude is given by,

$$V_{PCC} = \sqrt{\frac{(V_g^2 + 4R_g P_{Ref})^2}{4} - 4R_g^2 (P_{Ref}^2 + Q_{Ref}^2) + \frac{V_g^2 + 4R_g P_{Ref}}{2}} \quad (2.32)$$

Evidently, from (2.32) the steady state PCC voltage magnitude has a valid solution if the term under the root is a positive value. Otherwise, the PCC voltage fundamental component magnitude will be an imaginary value. In such conditions, the GFLI will be incapable of tracking the commanded PQ set-point. Hence, the inverter will gradually converge to an unstable equilibrium point. Furthermore, the theoretical condition to assure that the GFLI is in normal operation is given by,

$$\frac{V_g^4}{16R_g^2} + \frac{V_g^2}{2R_g} P_{Ref} - P_{Ref}^2 - Q_{Ref}^2 \geq 0 \quad (2.33)$$

Moreover, the active power is limited by the available energy. While, the reactive power is controlled to sustain the condition in (2.33). Thus, the amount of the reactive power required to avoid unstable steady state voltage conditions is as (2.34).

$$Q_{Ref}^2 \leq \frac{V_g^4}{16R_g^2} + \frac{V_g^2}{2R_g} P_{Ref} - P_{Ref}^2 \quad (2.34)$$

2.3.2. Inductive Weak Grid Consideration

In the case of the inductive weak grid, the power flow is expressed by (2.35) and (2.36).

$$P_{Ref} \triangleq P = \frac{V_{PCC} V_g}{\omega L_g} \sin(\delta) \quad (2.35)$$

$$Q_{Ref} \triangleq Q = \frac{V_{PCC}^2}{\omega L_g} - \frac{V_{PCC} V_g}{\omega L_g} \cos(\delta) \quad (2.36)$$

In this case, the PCC voltage steady state magnitude is as given in (2.37),

Table 3. PLL-less Grid-Following Inverter Control Ratings

Parameter	Symbol	Value
Rated Power	P_{Rated}	30 kW
Switching Frequency	f_{sw}	10 kHz
Nominal Grid Frequency	ω	376.8 rad/sec
Grid Voltage Peak	V_g	$120\sqrt{2}$ V
DC-Bus Voltage	V_{DC}	420 V
DC-link Capacitor	C_{DC}	2 mF
Filter Inductor	L	0.5 mH
Filter Inductor Resistance	R	0.05 Ω
Weak Inductive Grid Inductor	L_g	1 mH
Weak Resistive Grid Resistor	R_g	1 Ω

$$V_{PCC} = \sqrt{\sqrt{\frac{(V_g^2 + 4\omega L_g Q_{Ref})^2}{4} - 4\omega^2 L_g^2 (Q_{Ref}^2 + P_{Ref}^2)} + \frac{V_g^2 + 4\omega L_g Q_{Ref}}{2}} \quad (2.37)$$

Thus, the amount of reactive power required for stable PCC voltage conditions with weak inductive grids is given by (2.38).

$$Q_{Ref} \geq \frac{2\omega L_g P_{Ref}^2}{V_g^2} - \frac{V_g^2}{8\omega L_g} \quad (2.38)$$

Thereby, to inject a specific amount of available active power (P_{Ref}); the GFLI must supply a reactive power (Q_{Ref}) according to the inequality expressed in (2.38).

2.4. Validating Results on PLL-less Grid-Following Inverter Control

The theoretical analysis is verified by simulation in PSIM software. A 30 kW GFLI is implemented with the component values given in Table 3. Additionally, the subsection is subdivided into three; (2.4.1) validates the performance of the proposed control in tracking the commanded PQ set- point references. (2.4.2) is dedicated to a scenario in which the GFLI is operating with resistive weak grid. (2.4.1) examines a scenario where a GFLI is operating with inductive weak grid. Both scenarios discussed in subsections (2.3.1) and (2.3.2) verify the inequality conditions that guarantee the PCC steady state voltage stability.

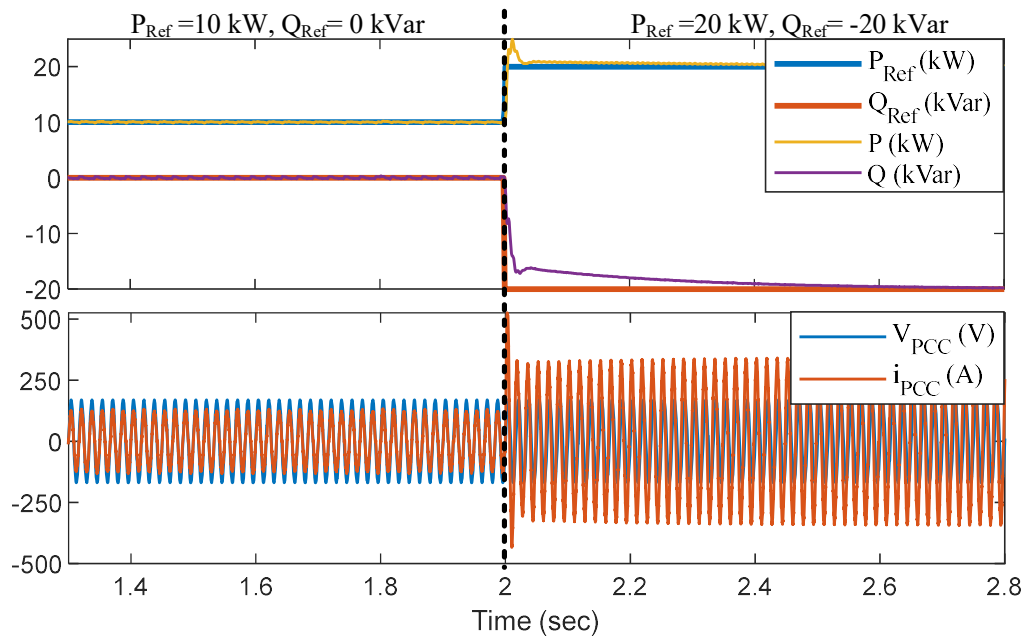


Figure 2.4: Proposed controller dynamic performance in tracking the commanded PQ set-point references.

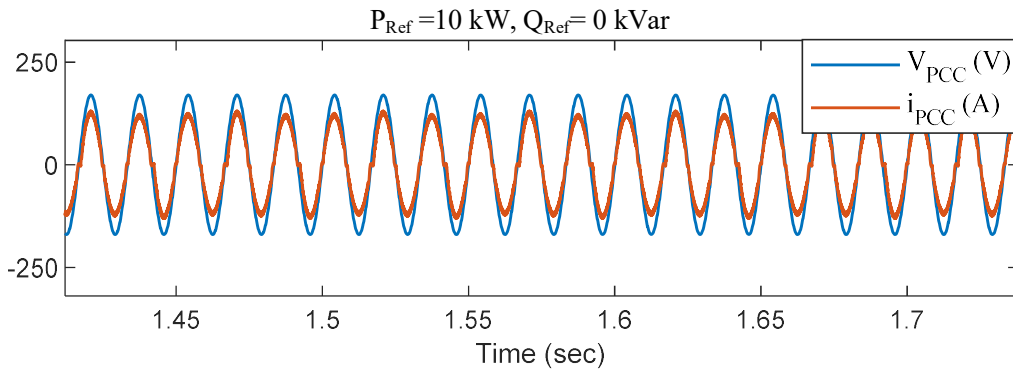


Figure 2.5: Steady state PCC current and voltage waveforms in Figure 2.4 before the commanded PQ set-point references are changed at instant 2 sec.

2.4.1. Controller Dynamic

The dynamic performance of the proposed PLL-less single-loop controller is depicted in Figure 2.4. As evident in Figure 2.4, the controller is tracking the required commanded

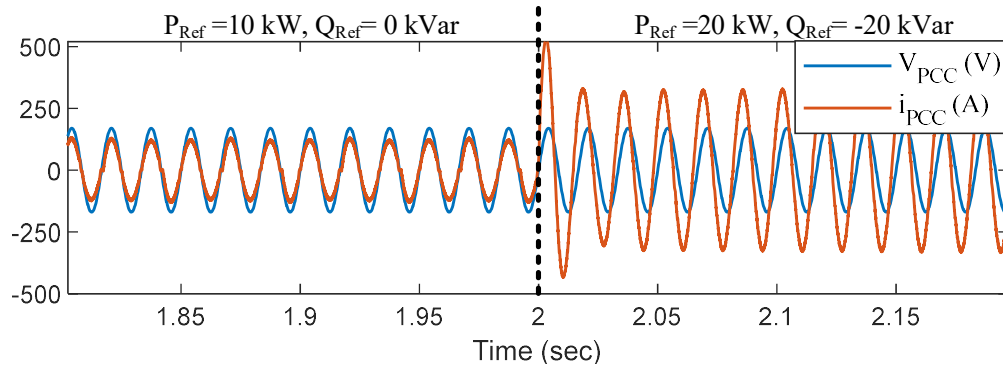


Figure 2.6: Transient PCC current and voltage waveforms in Figure 2.4 at the instant the commanded PQ set-point references are changed.

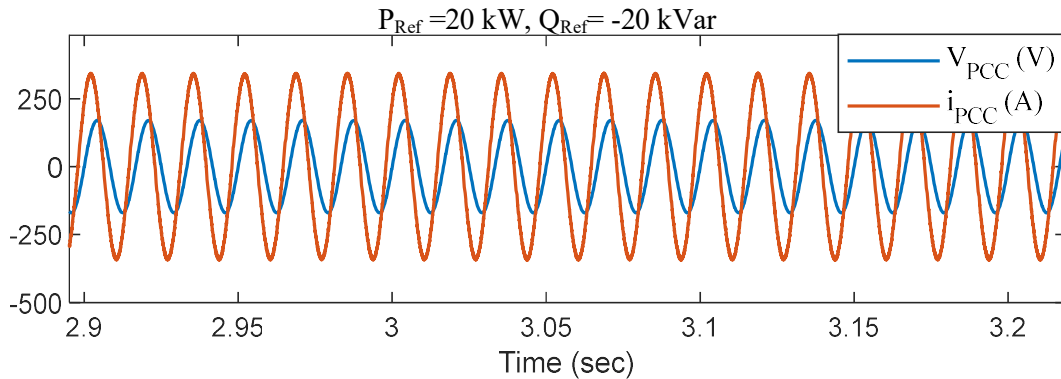


Figure 2.7: Steady state PCC current and voltage waveforms in Figure 2.4 after the commanded PQ set-point references are changed at instant 2 sec.

PQ set-point references accurately. In addition, the injected PCC current is sinusoidal. In this scenario, the GFLI is initially injecting 10 kW at unity power factor (see Figure 2.4 before instant 2 sec and Figure 2.5). Then, at time instant 2 sec the commanded PQ set-points are changed to 20 kW and -20 kVar. At this instant, the GFLI tries to adjust the amount of the injected active and reactive power as seen in Figure 2.4 and Figure 2.6. After 0.6 sec duration the injected active and reactive power of the inverter converge to the commanded PQ set-points as seen in Figure 2.4 after time instant 2.6 sec and Figure 2.7. Note that, in this scenario the grid has no impedance (i.e., stiff grid connection).

2.4.2. Weak Resistive Grid Connection

The previous scenario validated the developed theory in achieving grid-current synchronization without the need for a PLL in stiff grid conditions. However, the main motivation behind PLL-less controls is to guarantee control robustness especially in weak grid conditions. As the GFLI might witness unstable operation given that the commanded PQ set-point references may violating certain bounds. If these bounds are violated, the GFLI will be incapable of tracking the commanded PQ set-point references due to the absence of the fundamental component of the PCC voltage. Furthermore, in this scenario, the GFLI is simulated considering a grid resistance of 1Ω . This means that the grid is very weak with a SCR of 0.48. Initially, the GFLI is operating at unity power factor with 10 kW active power injection (see Figure 2.8 before instant 2 sec). This initial operating point is not violating the inequality (2.34) since the PCC current and voltage are sinusoidal without distortion as seen in Figure 2.9. Then, at time instant 2 sec the commanded reactive power set-point reference is adjusted to -10 kVar such that the inequality (2.34) is not satisfied. Directly the GFLI operation collapses as it is incapable of tracking the commanded PQ set-point references (see Figure 2.8 after 2 sec and Figure 2.10). The reason for this operation collapse is the absence of the PCC voltage fundamental component. Then at time instant 3 sec, the commanded PQ set-point references are adjusted to not violate inequality (2.34). Hence, the GFLI gradually regains the normal operation in less than 1 sec (see Figure 2.8 after instant 3 sec, Figure 2.11 and Figure 2.12).

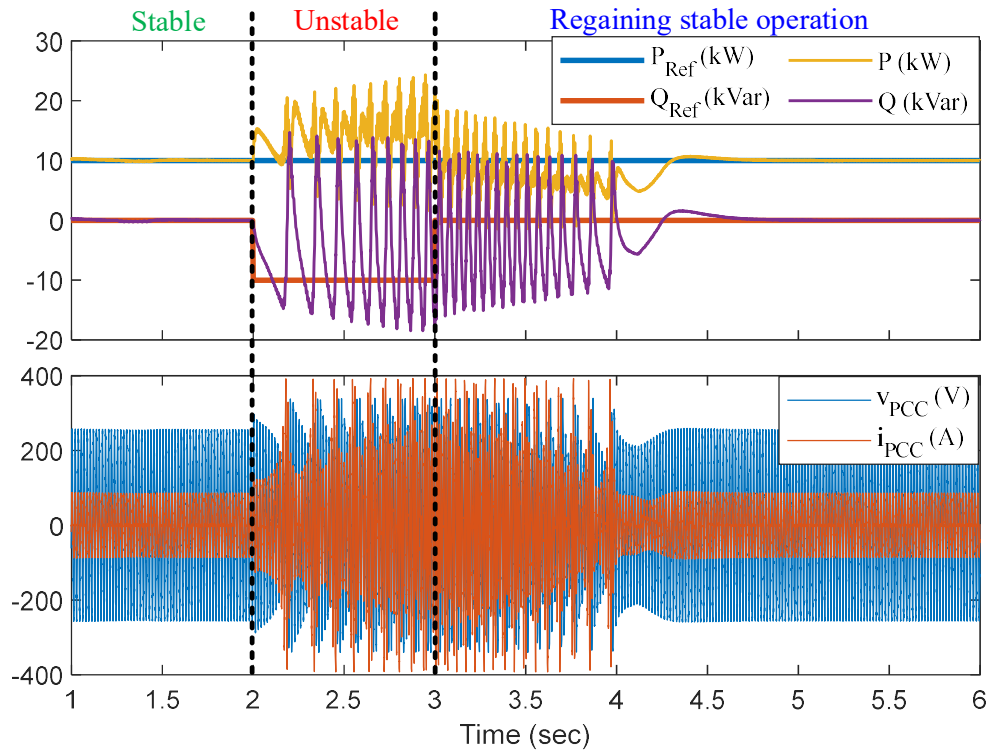


Figure 2.8: Verification of inequality (2.34) with commanded PQ set-point references variation in weak resistive grid connection.

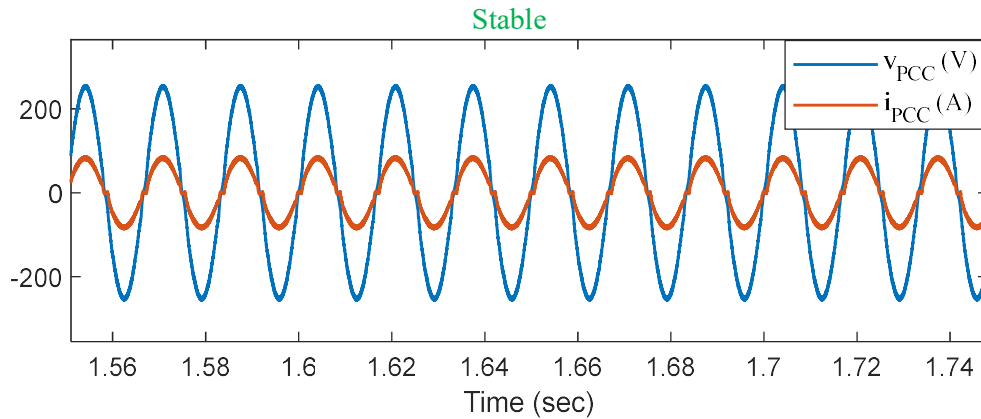


Figure 2.9: Initial steady state stable PCC current and voltage waveforms when the command PQ set-point references are satisfying inequality (2.34) in Figure 2.8.

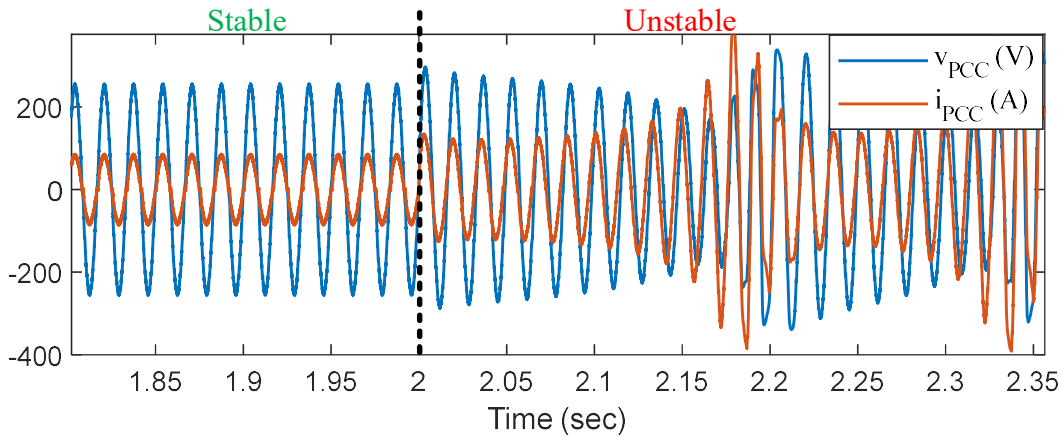


Figure 2.10: Transient PCC current and voltage waveforms when transiting from stable to unstable operation induced by violation of inequality (2.34) at instant 2 sec in Figure 2.8.

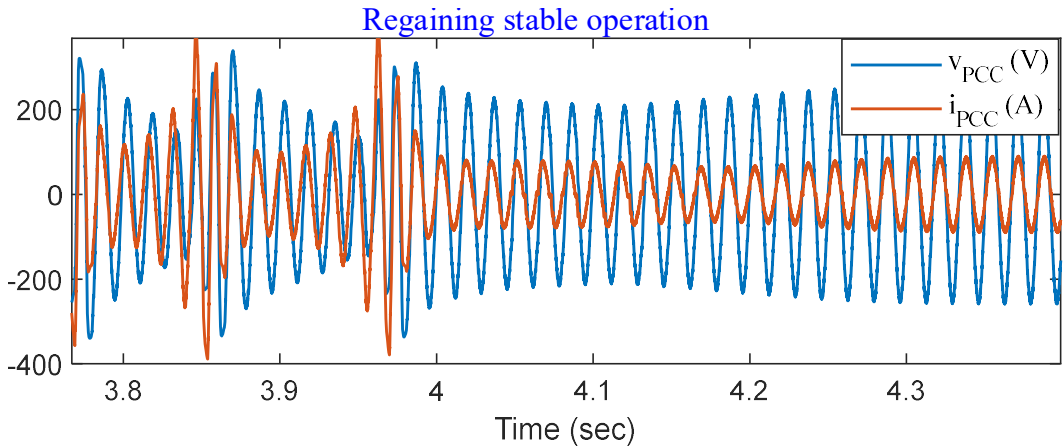


Figure 2.11: Transient PCC current and voltage waveforms when the stable operation is induced by satisfying inequality (2.34) at instant 3 sec in Figure 2.8.

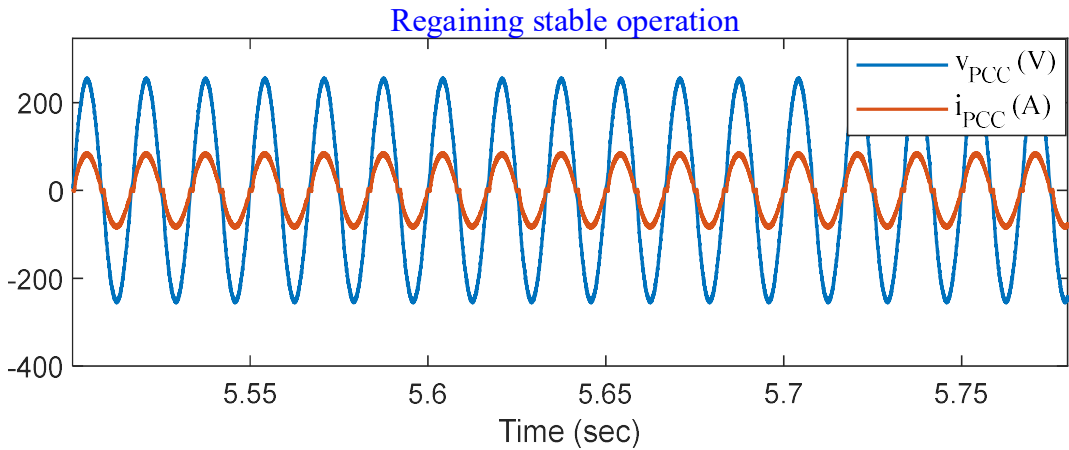


Figure 2.12: Final steady state stable PCC current and voltage waveforms when the command PQ set-point references are satisfying inequality (2.34) at instant 3 sec in Figure 2.8.

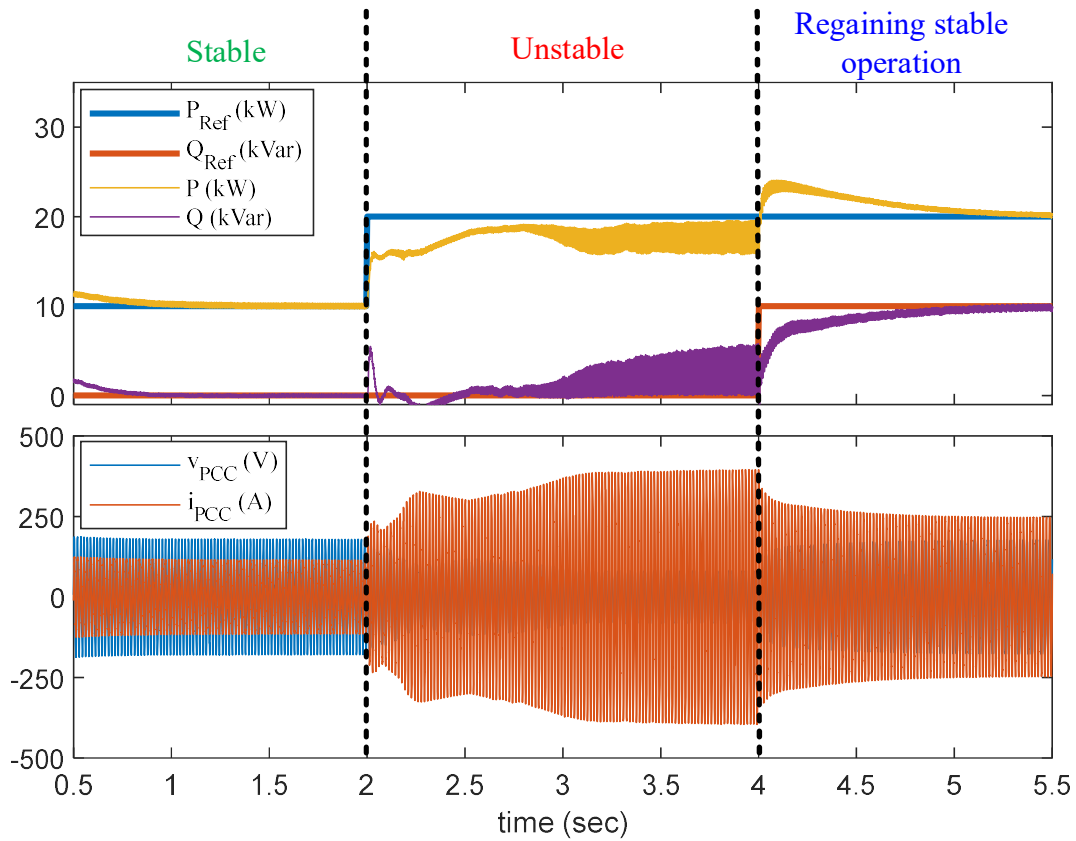


Figure 2.13: Verification of inequality (2.38) with commanded PQ set-points references variation in weak inductive grid connection.

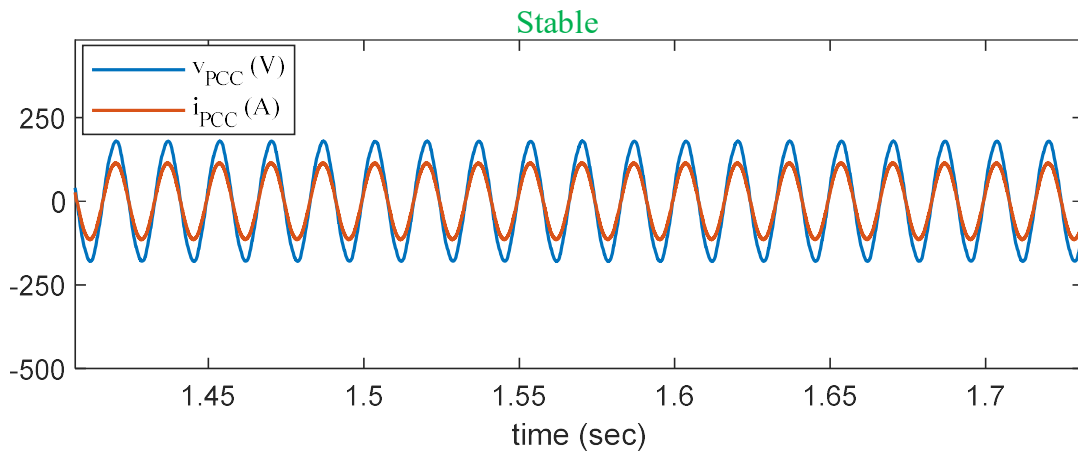


Figure 2.14: Initial steady state stable PCC current and voltage waveforms when the command PQ set-point references are satisfying inequality (2.38) in Figure 2.13.

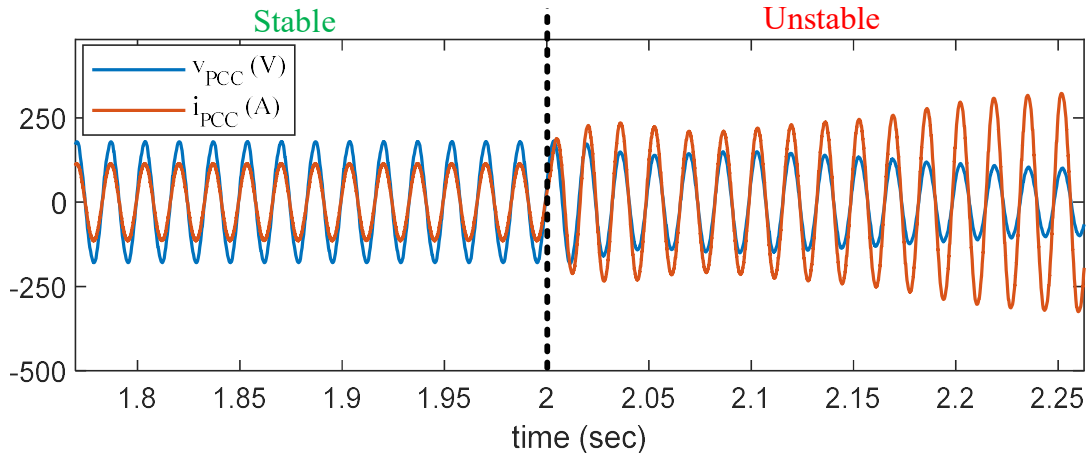


Figure 2.15: Transient PCC current and voltage waveforms when transiting from stable to unstable operation induced by violation of inequality (2.38) at instant 2 sec in Figure 2.13.

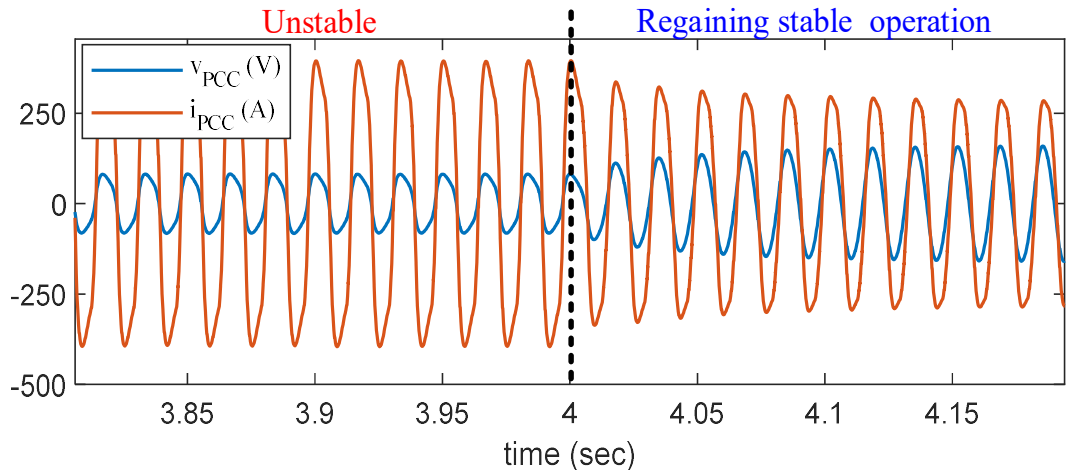


Figure 2.16: Transient PCC current and voltage waveforms when the stable operation is induced by satisfying inequality (2.38) at instant 4 sec in Figure 2.13.

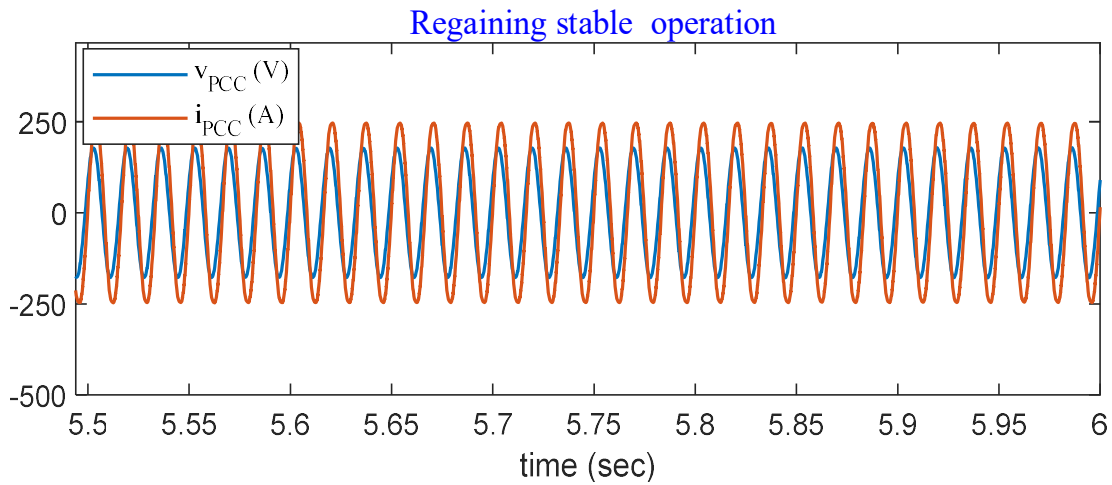


Figure 2.17: Final steady state stable PCC current and voltage waveforms when the command PQ set-point references are satisfying inequality (2.38) at instant 4 sec in Figure 2.13.

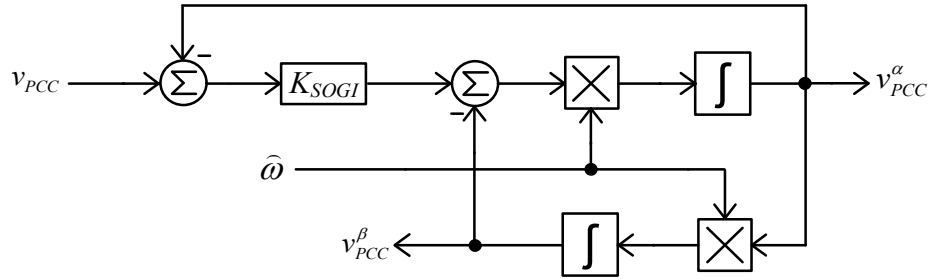


Figure 2.18. Variable frequency second order generalized integrator (VF-SOGI).

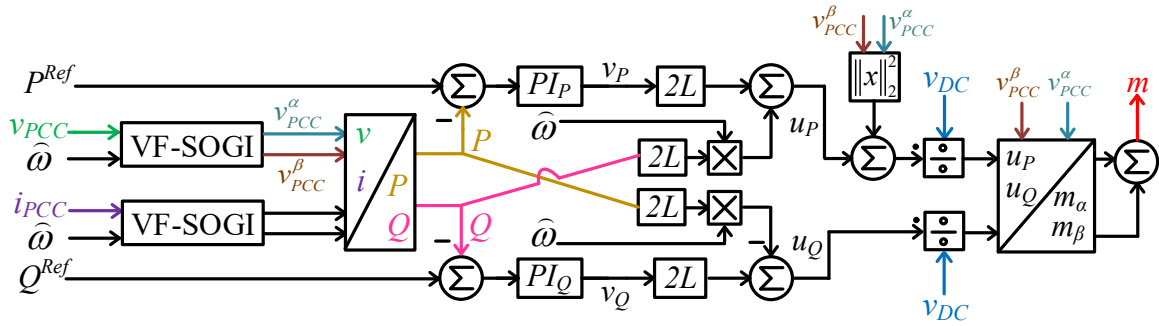


Figure 2.19. PLL-less GFLI adaptive to frequency changes.

2.4.3. Weak Inductive Grid Connection

This scenario is considering a weak inductive grid with a SCR of 1.27. The grid inductance is 1 mH. The GFLI is initially operating stably (i.e., no violation of inequality (2.38)) with the PQ operation set-point references set to 10 kW at unity power factor (see Figure 2.13 before instant 2 sec and Figure 2.14). Then, at instant 2 sec the commanded PQ set-points are adjusted to 20 kW at unity power factor to violate inequality (2.38). The inverter gradually fails in tracking the command PQ set-point references as evident in Figure 2.13 after instant 2 sec. This also is manifested in the non-sinusoidal behavior of fundamental component of the PCC current and voltage in Figure 2.15 after instant 2 sec. Nevertheless, to further validate the inequality (2.38), the commanded reactive power set-point is adjusted to 20 kVar at instant 4 sec to sustain inequality (2.38) (see Figure 2.13

and Figure 2.16). This new set-point results in gradual stable operation of the GFLI in less than 0.5 seconds. In fact, the fundamental component of the PCC current and voltage are seen regaining their sinusoidal waveform shape as shown in Figure 2.16 and Figure 2.17.

2.5. PLL-less Grid-following Inverter Control Adaptive to Frequency

2.5.1. Mathematical Modeling with Frequency Adaptation Inclusion

The beauty of the theory developed about how PLL-less GFLI control can be deployed is extended to include adaptive feature to changes in the frequency of the network. The beauty of this theory is embedded in the fact that frequency estimation is always simpler than phase estimation. Thereby, the PLL-less feature makes extension to frequency adaptation in the current control simpler. Therefore, conventional fixed frequency second order generalized integrator (SOGI) can be extended to adaptive frequency operation by considering the estimation of the frequency ($\hat{\omega}$) as depicted in Figure 2.18. The state space of the adaptive frequency second order generalized integrator is given in (2.39).

$$\begin{aligned} \frac{dx}{dt} &= Ax + Bu, \quad y = Cx \\ x &\in \mathbb{R}^4, u \in \mathbb{R}, y \in \mathbb{R}^2, A \in \mathbb{R}^{4 \times 4}, B \in \mathbb{R}^{4 \times 1}, C \in \mathbb{R}^{2 \times 4} \\ x &= \left[v_{PCC}^\alpha(\hat{\omega}) \quad \frac{dv_{PCC}^\alpha(\hat{\omega})}{dt} \quad v_{PCC}^\beta(\hat{\omega}) \quad \frac{dv_{PCC}^\beta(\hat{\omega})}{dt} \right]^T, \quad u = v_{PCC}(\hat{\omega}), y = [v_{PCC}^\alpha(\hat{\omega}) \quad v_{PCC}^\beta(\hat{\omega})]^T \\ A &= \begin{bmatrix} 0 & 1 & 0 & 0 \\ -\hat{\omega}^2 & -K_{SOGI}\hat{\omega}^2 & 0 & 0 \\ 0 & 0 & 0 & 1 \\ 0 & 0 & -\hat{\omega}^2 & -K_{SOGI}\hat{\omega}^2 \end{bmatrix}, \quad B = \begin{bmatrix} 0 \\ 1 \\ 0 \\ 1 \end{bmatrix} \\ C &= \begin{bmatrix} 0 & K_{SOGI}\hat{\omega} & 0 & 0 \\ 0 & 0 & K_{SOGI}\hat{\omega}^2 & 0 \end{bmatrix} \end{aligned} \quad (2.39)$$

where K_{SOGI} is the gain of the adaptive frequency SOGI, v_{PCC} is the point of common coupling voltage, $v_{PCC}^\alpha(\omega)$ is the alpha component of the point of common coupling

Table 4. Adaptive Frequency PLL-less Grid-Following Inverter Control

Parameter	Symbol	Value
Rated Power	S_{Rated}	20 kVA
Switching Frequency	f_{sw}	10 kHz
AC Bus Voltage	V_g	120V
Maximum Frequency	ω_{Max}	1884 rad/s
DC Bus Voltage	V_{DC}	500 V
DC link Capacitor	C_{DC}	500 μ F
Filter Inductor	L	0.25 mH
Filter Inductor Resistance	R	0.05 Ω
Filter Capacitor	C	60 μ F

voltage, and $v_{PCC}^\beta(\omega)$ is the beta component of the point of common coupling voltage. This adaptive frequency SOGI, without loss of generality, at any specific frequency, $P(\omega)$ and $Q(\omega)$ at the PCC can be obtained with the variable frequency SOGI developed. Then, using the same methodology in the previous subsection, the state space of the PLL-less GFLI control with adaptive frequency consideration is shown in (2.40).

$$\begin{bmatrix} \frac{dP(\hat{\omega})}{dt} \\ \frac{dQ(\hat{\omega})}{dt} \end{bmatrix} = \begin{bmatrix} -\frac{R}{L} & -\hat{\omega} \\ \hat{\omega} & -\frac{R}{L} \end{bmatrix} \begin{bmatrix} P(\hat{\omega}) \\ Q(\hat{\omega}) \end{bmatrix} + \frac{1}{2L} \begin{bmatrix} m_\alpha(\hat{\omega})v_{DC}v_{PCC}^\alpha(\hat{\omega}) + m_\beta(\hat{\omega})v_{DC}v_{PCC}^\beta(\hat{\omega}) - \|v_{PCC}(\hat{\omega})\|_2^2 \\ m_\alpha(\hat{\omega})v_{DC}v_{PCC}^\beta(\hat{\omega}) - m_\beta(\hat{\omega})v_{DC}v_{PCC}^\alpha(\hat{\omega}) \end{bmatrix} \quad (2.40)$$

Thereby, this system can be controlled with the same methodology explained in the previous subsection with adaptation to the frequency deviations. The control structure for this adaptive PLL-less GFLI control is depicted in Figure 2.19.

2.5.2. Frequency Adaptation PLL-less Grid-Following Inverter Control Validations

The theoretical analysis is verified by simulation of an adaptive frequency single-phase GFLI control with the ratings depicted in Table 4. Three scenarios are simulated. The first scenario is validating the performance of the adaptive frequency PLL-less GFLI control during sudden changes in the AC supply frequency. The second scenario is validating the operation of the adaptive frequency PLL-less GFLI control with active power set-points

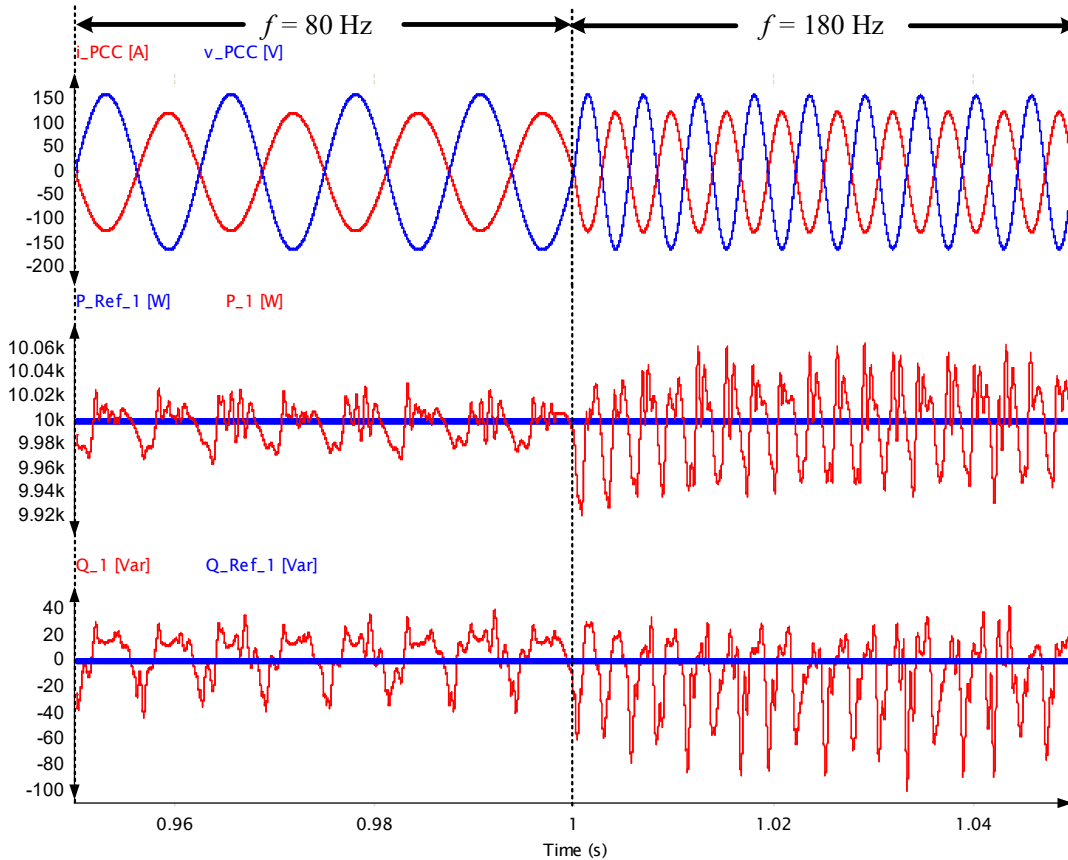


Figure 2.20. Scenario 1: Performance of the frequency adaptive PLL-less grid-following inverter control with frequency variations.

and frequency variations under unity power factor operation. The third scenario is validating the performance of the PLL-less GFLI control with frequency variations, and active and reactive set-points variations.

Scenario 1 is depicted in Figure 2.20. Particularly, in this scenario a dynamical variation in the frequency of the AC supply occurs at time instant 1 s in Figure 2.20. This is depicting the performance of the adaptive frequency PLL-less GFLI control. Initially, in Figure 2.20 the AC supply operating frequency is 80 Hz with the active power exchange of 10 kW at unity power factor. After time instant 1 s, the AC supply frequency is changed to 180 Hz

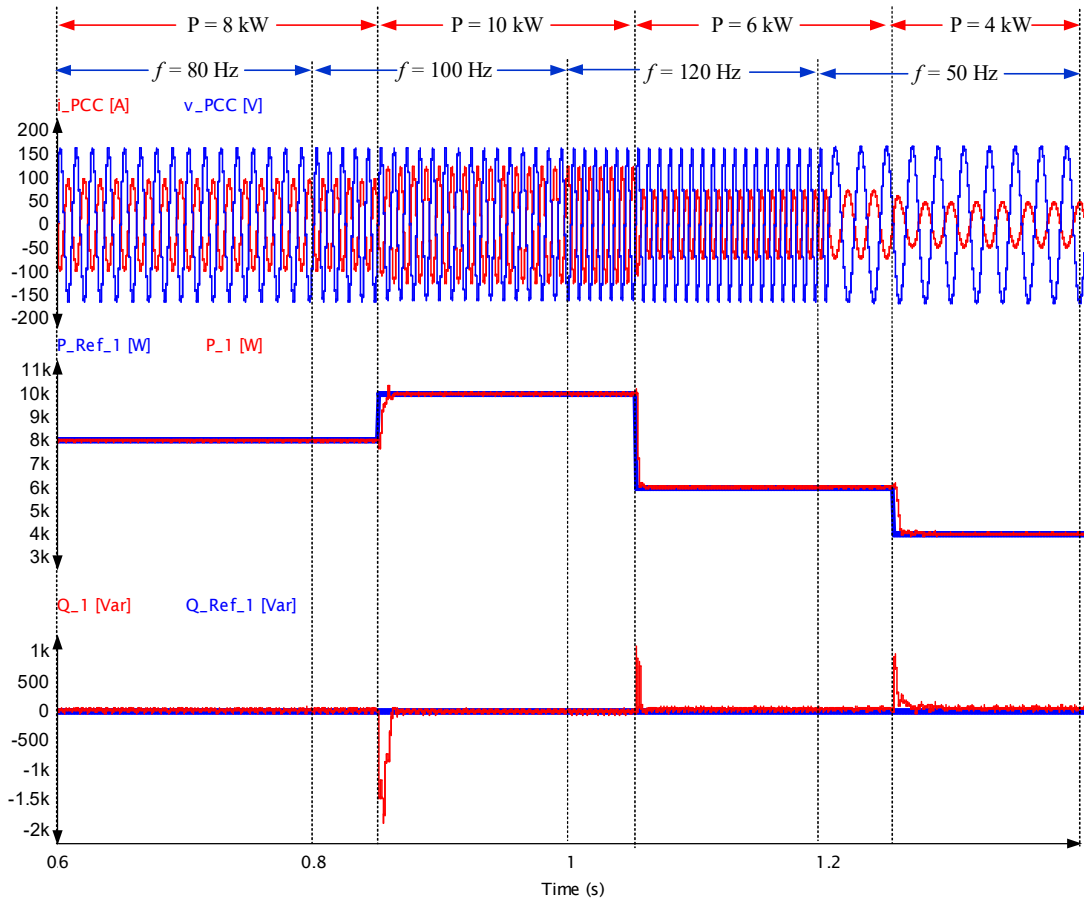


Figure 2.21. Scenario 2: Performance of the frequency adaptive PLL-less grid-following inverter control with frequency variations and active power set-point change

in Figure 2.20. The PLL-less GFLI control is performing well even with supply frequency variations and tracking the set-points (see Figure 2.20).

Scenario 2 is validating the performance of the adaptive frequency GFLI control with active power set-points dynamic changes at unity power factor operation (see. Figure 2.21). Moreover, initially the inverter is operating with 80 Hz, 8 kW at unity power factor (see Figure 2.21 before 0.8 s). Then, at 0.8 s in Figure 2.21 the AC supply frequency is increased to 100 Hz. After that, at 0.85 s the active power set-point is increased to 10 kW in Figure 2.21. At time instant 1 s in Figure 2.21 the frequency is increase to 120 Hz and after 1.05

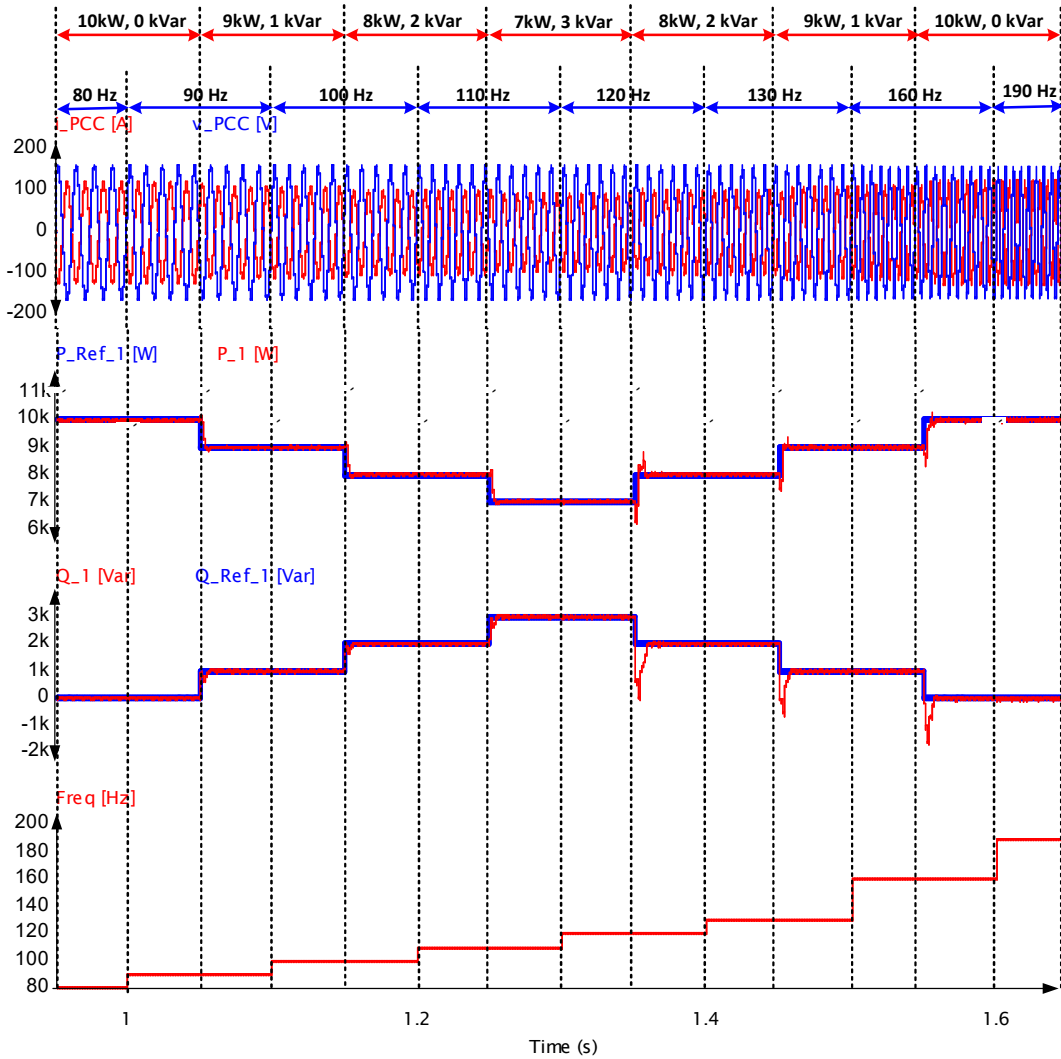


Figure 2.22. Scenario 3: Performance of the frequency adaptive PLL-less grid-following inverter control with frequency variations, active power set-point change, reactive power set-point change.

s the active power set-point is decreased to 6 kW. Then, at 1.2 s the frequency is decreased to 50 Hz in Figure 2.21. Finally, the active power set-point is moved to 4 kW. In this scenario that the adaptive frequency GFLI PLL-less current control is capability of operating the inverter in unity power factor with tracking the commanded active power set-point reference.

The scenario 3, which is depicted in Figure 2.22, is validation of operating the adaptive frequency PLL-less GFLI control under variations in the AC supply frequency, active power set-point reference, and reactive power set-point reference. Evidently, in scenario 3 in Figure 2.22, the adaptive frequency PLL-less GFLI control is capability of operating the inverter with tracking the active and reactive power set-point references accurately.

2.6. Conclusion

The first section of this chapter provided a GFLI control with no PLL requirement with single loop structure. The stability and control design were also investigated and validated with multiple operation scenarios. In addition, in the first section, steady-state voltage stability bounds also were investigated for analyzing the operation of the GFLI without PLL requirement. Then, the second section of this chapter, utilized the beauty of not requiring PLL for synchronization to accommodate GFLI control with active and reactive power tracking with frequency adaption.

Chapter 3

3. Grid-Following Inverter Control with Active Power Decoupling Control for Future Power Electronics-Dominated Grid DC Link Voltage Stability Improvement

Part of this chapter, including figures and text are based on my following papers:

© 2018-2022 IEEE

- A. Khan, M. B. Shadmand, S. Bayhan and H. Abu-Rub, "A Power Ripple Compensator for DC Nanogrids via a Solid-State Converter," *IEEE Open Journal of the Industrial Electronics Society*, vol. 1, pp. 311-325, 2020

- A. Khan, M. B. Shadmand and H. Abu-Rub, "Active Power Decoupling Control Scheme for Distorted Grids," *2019 IEEE Power and Energy Conference at Illinois (PECI)*, pp. 1-7, 2019

- A. Khan, M. Hosseinzadehtaher, M. Easley, M. B. Shadmand and H. Abu-Rub, "Decoupled Active and Reactive Power Control without PLL Requirement for Differential Buck Converter," *2020 IEEE Energy Conversion Congress and Exposition (ECCE)*, pp. 4994-4999, 2020

- A. Khan, M. Hosseinzadehtaher, A. Y. Fard and M. B. Shadmand, "Active Power Decoupling Control for Rectifiers with Variable Frequency Supply for More Electric Aircraft," *2021 IEEE Industry Applications Society Annual Meeting (IAS)*, pp. 1-8, 2021

3.1. Nanogrid Main Interfacing Grid-Following Inverter with Active Power Decoupling Capability

Given the nature of photovoltaic (PV), energy storage systems (ESS), electric vehicles (EV), etc., nanogrids have risen as attractive, efficient and reliable solutions for their interconnection [74, 75]. Furthermore, the nanogrid is interfaced with the utility grid via a solid state converter (SSC) [76]. This SSC is the main nanogrid energy control unit that is communicating with the upper network and managing the nanogrid elements, this SSC is a grid-following inverter (GFLI) [77]. However, when the SSC operates, a 2nd order harmonic voltage ripple inevitably is superimposed on the DC bus voltage. This voltage ripple originates from the nature of single-phase AC systems [78]. The instantaneous power exchanged between the utility network and the nanogrid is oscillating at twice the utility grid frequency [79, 80]. Furthermore, due to the limited output impedance of distributed energy resources' converters and point of load converters, the 2nd order power harmonic causes large current and voltage fluctuations at the resource and load sides of these converters [81]. These fluctuations are undesirable, as they shorten the lifetime of batteries, fuel cells, and loads [82-84]. Suppressing the 2nd order harmonic voltage is possible by passive or active methods [85]. The passive methodology is simply to increase the DC bus capacitance. This approach is not recommended as realizing high capacitance is only attained by short lifetime electrolytic capacitors (e-caps) [27, 86]. In fact, roughly 60% of power electronic devices failure are due to the use of e-caps [87]. On the other hand, most of the active solutions are combination of hardware with control schemes utilization. An example of these ripple buffering solutions is the various active power decoupling

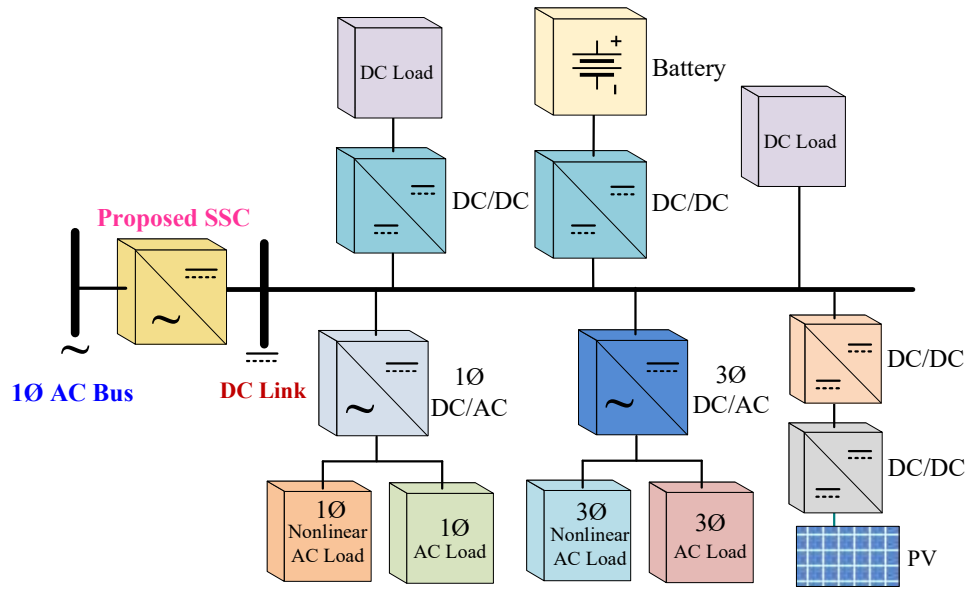


Figure 3.1. Nanogrid architecture.

circuitries [88-94]. These technologies are summarized in Table 5 with emphasizing on the principle of the approach and highlighting the main features and the drawbacks. Table 5 clustered these existing solutions into six groups: (I) AC link based, (II) center trap transformer based, (III) series compensation, (IV) parallel compensation, (V) parallel compensation with shared control, and (VI) control dependent compensation. Even though, these active power decoupling solutions are effective; the requirement for additional power switches and energy storage devices decrease the reliability of the entire nanogrid system for the methods in clusters (I) – (IV) in Table 5. While, the control dependent compensation methods (i.e., cluster (VI) in Table 5) are not robust to system parameters mismatch, and operation setpoint variations. This makes their operation even further problematic with non-ideal conditions or nanogrid operation change such as load increase or decrease, etc. As the power ripple are not solely originated from the main AC node; linear and non-linear

AC loads in the nanogrid contribute to the bus voltage ripple in a different manner. In fact, the AC node non-ideality will produce voltage ripple at higher order harmonics and not only at 2nd order harmonic.

Table 5. Summary of Power Ripple Mitigation Techniques

Cluster	Minimization Technique	Features	Drawbacks
I	AC-Link [95]	<ul style="list-style-type: none"> - Eliminate the dc link capacitor - Ripple mitigation is independent of other elements 	<ul style="list-style-type: none"> - Eight additional switches needed - Additional capacitor and inductor - Used for low frequency switching application - Needs a high frequency transformer
II	Center Tap Transformer [96]	<ul style="list-style-type: none"> - Used in several kilowatt application 	<ul style="list-style-type: none"> - Additional inductor and capacitor are needed. - Ripple mitigation depend on the other elements - Center tap transformer is required
III	Series Compensation [97]	<ul style="list-style-type: none"> - General solution that is applicable on current source network. - Ripple mitigation is independent of other elements. - Used in kilowatt power ratings. - Ripple mitigation does not impact the DC bus utilization. - Ripple mitigation does not introduce current stress 	<ul style="list-style-type: none"> - Four additional switches needed. - Two capacitors and one inductor are needed. - The dc link of the series converter requires a large capacitor or an additional power source.
IV	Parallel Compensation	Quasi-Resonant Control [98] <ul style="list-style-type: none"> - No impact on the DC bus utilization - No additional current stress 	<ul style="list-style-type: none"> - Cascaded DC/DC converter is required - Suitable for low power applications - Require high bandwidth control for the DC/DC converter that compensates the ripple.
		Three legs [99-101] <ul style="list-style-type: none"> - Independent ripple mitigation control of other elements - Used for several hundred watts to several kilowatts. 	<ul style="list-style-type: none"> - Two additional switches required - Additional capacitors and an inductor - Voltage balancing issue between the power mitigation circuit capacitors with the half-bridge type.
		Four legs [102] <ul style="list-style-type: none"> - Independent ripple mitigation control of other elements - Used for several kilowatt applications 	<ul style="list-style-type: none"> -Needs four additional switches -Additional one inductor and capacitor
V	Parallel Compensation with Shared Control	H-Bridge [103, 104] <ul style="list-style-type: none"> - Used for several kilowatt applications 	<ul style="list-style-type: none"> - One or two additional capacitors needed. - One inductor is needed. - The control of the ripple is shared with the control of the other elements. - Ripple mitigation control reference requires computation.
		Three legs [105, 106] <ul style="list-style-type: none"> - Used for several kilowatt applications 	<ul style="list-style-type: none"> - Two additional switches - Additional inductor is needed - Additional capacitor is needed - Ripple mitigation control reference requires computation. - General solution that is applicable on current source network.
VI	Control Dependent Compensation [107-110]	<ul style="list-style-type: none"> - Used for less than one kilowatt applications - No additional switches 	<ul style="list-style-type: none"> - The control of the ripple is shared with the control of the other elements. - Ripple compensation control is not autonomous. - Ripple compensation does not consider other low order harmonics generated by nonlinear loads, linear loads, and grid distortion. - Ripple control is not robust to parameters and load variations - Stabilization scheme is not discussed
	Proposed Solution	<ul style="list-style-type: none"> - No additional switches - No additional capacitor or inductors needed the filter structures is similar to non-isolated application - Autonomous ripple mitigation control 	<ul style="list-style-type: none"> - Stabilization scheme required - The control of the ripple is shared with the control of the other elements

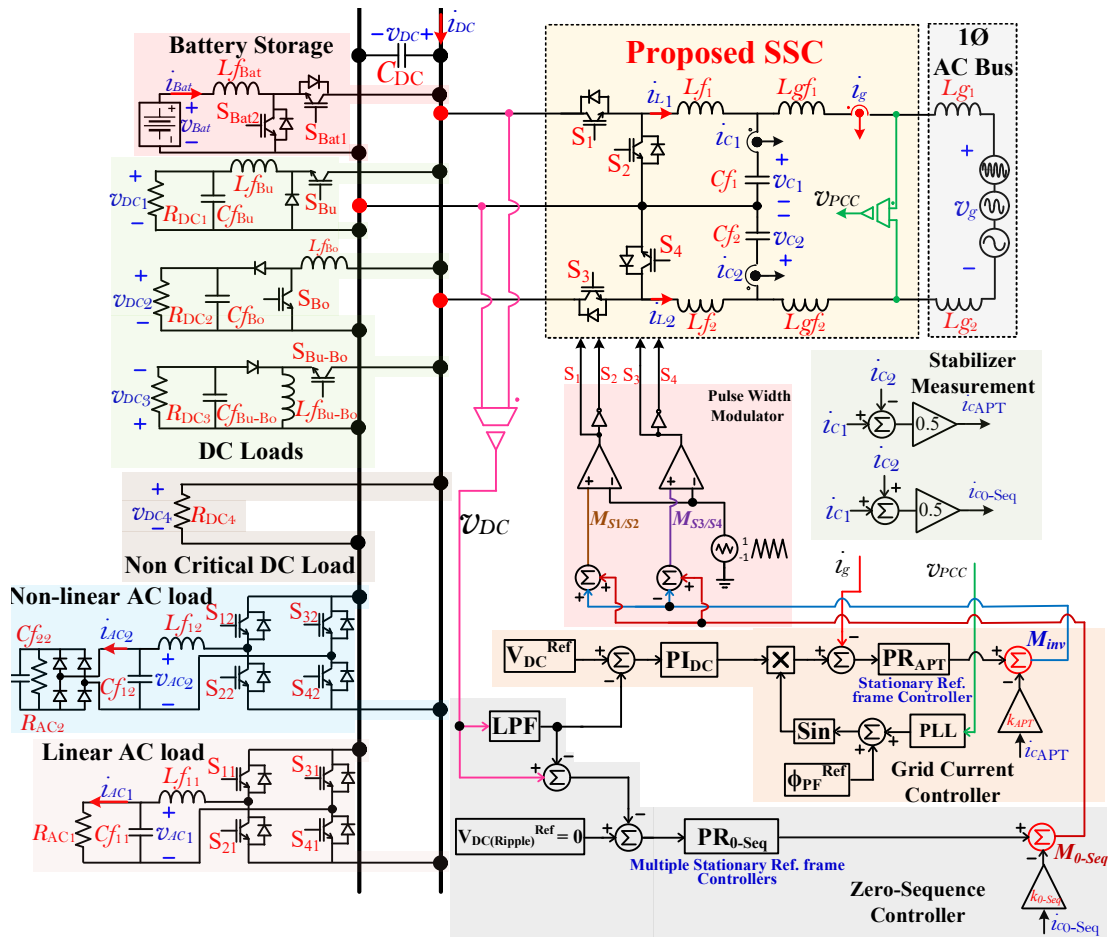


Figure 3.2. The proposed SSC with zero-sequence control mode in a nanogrid.

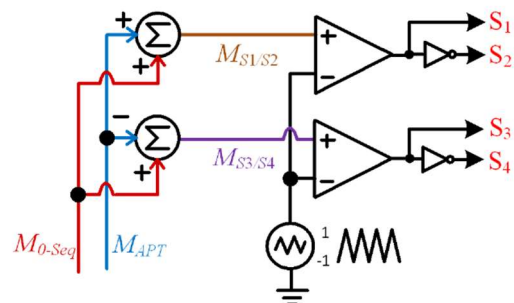


Figure 3.3. Modified pulse width modulator to accommodate controlling the zero-sequence operation mode of the SSC.

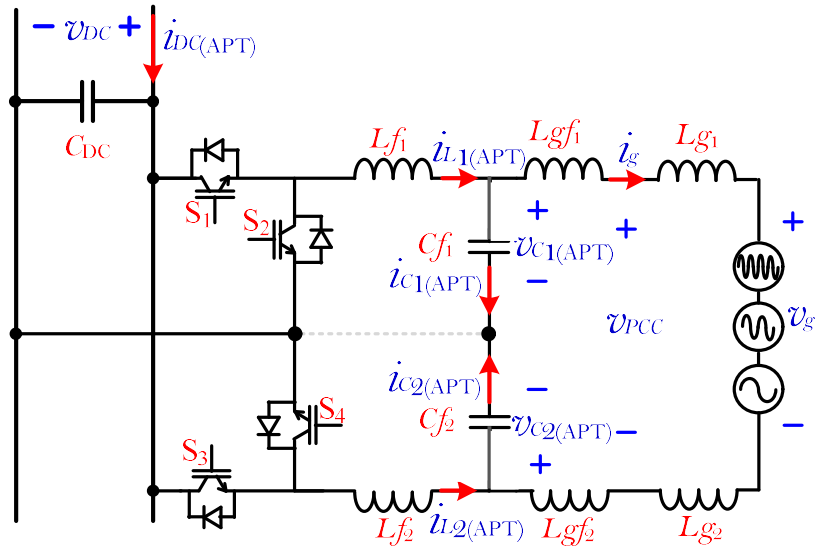


Figure 3.4. Equivalent circuit of the SSC in the active power transferring mode.

This chapter provides analysis on the origins of the DC bus voltage ripple in a nanogrid. Then, the working principle of the proposed SSC will be presented. The proposed SSC has the capability to absorb the ripple without deploying additional components and is robust to system parameters and operation setpoint variations. The proposed approach considers ripple mitigation due to non-ideal AC node voltage, linear and non-linear loads. The main aim is to reduce the DC bus capacitance requirement and utilize the commercially available long lifetime low capacitance film capacitors as energy buffer at DC-link in the nanogrid. The proposed methodology enables achieving a highly reliable nanogrid without e-caps utilization. The low frequency ripple are solely absorbed by the zero-sequence operation mode control of the proposed SSC.

The nanogrid in Figure 3.1 is rated at 500V/5kW. This nanogrid is considered as low voltage network that has DC loads and sources and single-phase AC loads and sources. The loads are controlled in output voltage control mode and sources are controlled in input

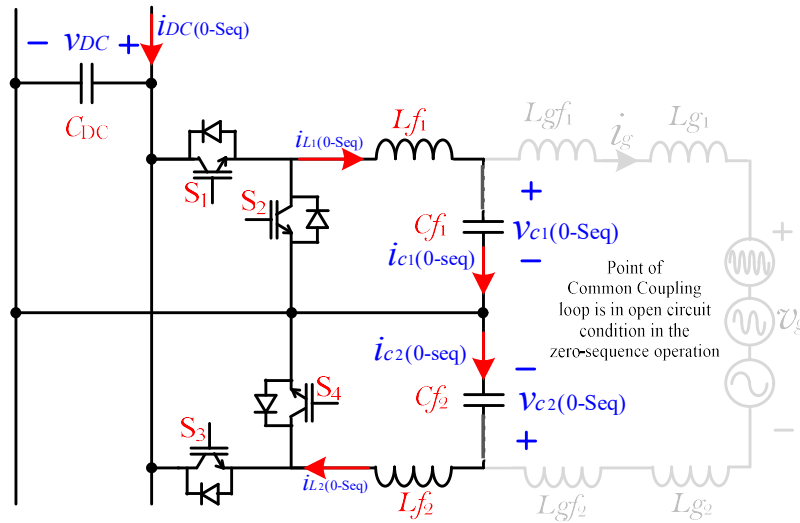


Figure 3.5. Equivalent circuit of the SSC zero-sequence operation mode (point of common coupling loop is in open circuit condition).

current control mode. Furthermore, since the operation and control of the subsystems are well established in the literature [111-117]; there will be no further emphasis on their control and operation. The focus of this section will be the SSC depicted in Figure 3.1 that governs power exchange between the DC bus and the single-phase AC node. This converter is in current control mode with regulating the main DC bus voltage. The focus of this work will be the SSC zero-sequence operation mode control that absorbs the power ripple.

3.1.1. Origin of Power Ripples

Consider the harmonically distorted AC node that is linked to the nanogrid through the proposed SSC (see Figure 3.1); this system is equivalent to a grid connected bi-directional DC/AC converter with an *LCL* filter. The AC node voltage at the point of common coupling (PCC) is expressed as (3.1).

$$v_{PCC}(t) = V_{PCC_0} + \sum_{n=1,2,3,\dots}^{n^{th}} V_{PCC_n} \cos(n\omega_0 t + \theta_n) \quad (3.1)$$

where t is time, $v_{PCC}(t)$ is the instantaneous PCC voltage, n is the order of the harmonic, V_{PCC_n} is peak of the n^{th} harmonic component of the PCC voltage, ω_0 is the angular frequency of the network, and θ_n is the initial phase of the n^{th} PCC voltage harmonic component. Due to the AC node voltage distortion, the current drawn is polluted with odd harmonics, even harmonics and a DC component:

$$i_g(t) = I_{g_0} + \sum_{n=1,2,3,\dots}^{n^{th}} I_{g_n} \cos(n\omega_0 t + \varphi_n) \quad (3.2)$$

where $i_g(t)$ is the instantaneous grid current, I_{g_n} is the peak of the n^{th} harmonic component of the grid current, and φ_n is the initial phase of the n^{th} grid current harmonic. Then, the instantaneous power exchange at the PCC. is computed from (3.1) and (3.2) by multiplication. The expression for the instantaneous power consists of a DC term and multiple sinusoids with constant coefficients at integer order harmonics. The instantaneous power can be expressed in simplified form:

$$p_{PCC}(t) = P_{PCC} + \tilde{p}_{PCC}(\omega_0 t, 2\omega_0 t, 3\omega_0 t, \dots, 2n\omega_0 t) \quad (3.3)$$

where $p_{PCC}(t)$ is the instantaneous power, P_{PCC} is the average power (i.e, the DC term) and $\tilde{p}_{PCC}(\omega_0 t, 2\omega_0 t, 3\omega_0 t, \dots, 2n\omega_0 t)$ is the power ripple (i.e., the AC term). Thus, considering an AC node voltage distorted to n^{th} harmonics and a DC component; the resultant power ripple in the system are from 1st to $2n^{th}$ harmonic.

Other potential sources of low frequency power ripple are the nanogrid AC loads. For linear RL loads the generated power ripple are as ideal single-phase AC systems, thus only a 2nd order harmonic power ripple is generated (3.4).

$$p_{AC_1}(t) = P_{AC_1} + \tilde{p}_{AC_1}(2\omega_0 t) \quad (3.4)$$

Where $p_{AC_1}(t)$ is the instantaneous power of the linear load, P_{AC_1} is the average power of the linear load, and $\tilde{p}_{AC_1}(2\omega_0 t)$ is the power ripple of the linear load. On the other hand, non-linear AC loads are rich source of harmonics. For instance, diode rectifier with RC loads makes a pulsed shaped current drawn from the inverter at the AC side. This happens when the diode rectifier DC output is greater than the absolute value of the AC bridge output. According to [118], the spectrum of both the inverter AC output voltage and the current contain significant odd harmonics until the 9th harmonic. Thus, the AC output voltage and the AC output current of non-linear loads are approximated by,

$$v_{AC_2}(t) = \sum_{n \in \text{odd}}^{9^{\text{th}}} V_{AC_n} \cos(n\omega_0 t + \theta_n) \quad (3.5)$$

$$i_{AC_2}(t) = \sum_{n \in \text{odd}}^{9^{\text{th}}} I_{AC_n} \cos(n\omega_0 t + \phi_n) \quad (3.6)$$

where $v_{AC_2}(t)$ is the instantaneous voltage of the non-linear load, V_{AC_n} is the n^{th} harmonic component peak of the non-linear load, $i_{AC_2}(t)$ is the instantaneous current of the non-linear load, and I_{AC_n} is the n^{th} harmonics component peak of the non-linear load current. As a result, the power ripple that appears in the instantaneous power expression in (3.7) for non-linear AC loads starts from the 2nd harmonic to the 18th harmonic.

$$p_{AC_2}(t) = P_{AC_2} + \tilde{p}_{AC_2}(2\omega_0 t, 4\omega_0 t, \dots, 18\omega_0 t) \quad (3.7)$$

where $p_{AC_2}(t)$ is the instantaneous power of the non-linear load, P_{AC_2} is the average power of the non-linear load, and $\tilde{p}_{AC_2}(2\omega_0 t, 4\omega_0 t, \dots, 18\omega_0 t)$ is the power ripple of the non-linear load.

The total power ripple that appears on the DC bus will be the summation of all ripples that were generated at the AC side of different AC loads and the main grid AC node given by (3.8).

$$P_{total}(t) = P_{PCC} + P_{AC_1} + P_{AC_2} + \dots + P_{AC_j} + \tilde{p}_{PCC} + \tilde{p}_{AC_1} + \tilde{p}_{AC_2} + \dots + \tilde{p}_{AC_j} \quad (3.8)$$

where $p_{total}(t)$ is the instantaneous power of the nanogrid, and j is the index representing linear and non-linear loads in the nanogrid. However, a complication might arise if the AC loads have a different operation frequency than the main AC node nominal frequency. Nevertheless, nanogrid AC loads are rated to the nominal grid frequency or an integer multiple of the grid frequency; this makes the power ripple generated in such situations also a higher integer multiple of the main grid fundamental frequency. In other words, the power ripple spectrum will contain orthogonal components; hence, (3.8) is simplified as (3.9).

$$P_{total}(t) = P_{total} + \tilde{p}_{total}(\omega_0 t, 2\omega_0 t, 3\omega_0 t, \dots, 2n\omega_0 t) \quad (3.9)$$

where P_{total} is the average of the total power exchanged between the nanogrid and main AC bus, $\tilde{p}_{total}(\omega_0 t, 2\omega_0 t, 3\omega_0 t, \dots, 2n\omega_0 t)$ is the power ripple of the nanogrid.

3.1.2. Power Ripple Mitigation Principle

The structure of the SSC in Figure 3.2 allows utilizing the zero-sequence operation mode of the SSC independently of the active power transferring mode. If S_1/S_2 modulation index ($m_{S_1/S_2}(t)$) and S_3/S_4 modulation index ($m_{S_3/S_4}(t)$) are controlled through the active power transferring mode modulation index ($m_{APT}(t)$) and the zero-sequence modulation index ($m_{0-seq}(t)$) as the following (see Figure 3.3),

$$m_{S_1/S_2}(t) = m_{0-seq}(t) + m_{APT}(t) \quad (3.10)$$

$$m_{S3/S4}(t) = m_{0-seq}(t) - m_{APT}(t) \quad (3.11)$$

the two filter capacitors C_{f1} and C_{f2} voltages $v_{C1}(t)$ and $v_{C2}(t)$ relative to the two modulation indices and the DC link voltage (V_{DC}) will be as:

$$v_{C1}(t) = \frac{V_{DC} (m_{0-seq}(t) + m_{APT}(t) + 1)}{2} \quad (3.12)$$

$$v_{C2}(t) = \frac{V_{DC} (m_{0-seq}(t) - m_{APT}(t) + 1)}{2} \quad (3.13)$$

From (3.12) and (3.13) by subtraction; (3.14) is deduced that is representing the active power transferring mode capacitor voltage component $v_{C_{APT}}(t)$.

$$v_{C_{APT}}(t) = v_{C1}(t) - v_{C2}(t) = V_{DC} m_{APT}(t) \quad (3.14)$$

Equation (3.14) indicates that the active power transferring mode modulation index ($m_{APT}(t)$) is independent of the zero-sequence modulation index ($m_{0-seq}(t)$). Actually, the equivalent circuit of the active power transferring mode in Figure 3.4 does not contain any zero-sequence components. Therefore, $m_{APT}(t)$ can be used to control the active power exchanged. Likewise, from (3.12) and (3.13) by summation; (3.15) is deduced that is representing the zero-sequence mode capacitor voltage component $v_{C_{0-seq}}(t)$.

$$v_{C_{0-seq}}(t) = v_{C1}(t) + v_{C2}(t) = V_{DC} m_{0-seq}(t) + V_{DC} \quad (3.15)$$

Equation (3.15) shows that the modulation scheme in Figure 3.2, makes the zero-sequence mode operation to be influenced only by the imposed zero-sequence modulation index ($m_{0-seq}(t)$). In fact, the zero-sequence operation mode equivalent circuit is in open circuit conditions at the PCC (see Figure 3.5). Furthermore, next subsection discusses the methodology of using the zero-sequence component imposed for power ripple mitigation. For actively absorbing the power ripple, the SSC topology makes the filter capacitors voltages at the loop of PCC in Figure 3.2 to be as (3.16) and (3.17).

$$v_{C1}(t) = \frac{V_{DC} + v_{PCC}(t)}{2} \quad (3.16)$$

$$v_{C2}(t) = \frac{V_{DC} - v_{PCC}(t)}{2} \quad (3.17)$$

If a zero-sequence voltage component ($v_{C0-Seq}(t)$) is superimposed on the two filter capacitors by the zero-sequence modulation index as (3.18) and (3.19) such that the instantaneous power at the PCC loop is equal to the negative of the power ripple as (3.20); the power ripple will be successfully mitigated.

$$v_{C1}(t) = \frac{V_{DC} + v_{PCC}(t) + v_{C0-Seq}(t)}{2} \quad (3.18)$$

$$v_{C2}(t) = \frac{V_{DC} - v_{PCC}(t) + v_{C0-Seq}(t)}{2} \quad (3.19)$$

$$i_{C1}(t)v_{C1}(t) + i_{C2}(t)v_{C2}(t) = -\tilde{p}_{total}(\omega_0 t, 2\omega_0 t, 3\omega_0 t, \dots, 2n\omega_0 t) \quad (3.20)$$

where $i_{C1}(t)$ and $i_{C2}(t)$ are the instantaneous current of the AC filter capacitors.

Accordingly, the minimum capacitance required to accomplish a DC bus with negligible ripple will be reduced. This injected zero-sequence voltage ($v_{0-seq}(t)$) into the filter capacitors can be estimated by finding the closed form solution of (3.20). In more details, (3.20) is rewritten as (3.21) in relation to the filter capacitors with the assumption that the AC filter capacitors are equal (i.e. $C_{f1} = C_{f2} = C_f$).

$$C_f \frac{dv_{C1}(t)}{dt} v_{C1}(t) + C_f \frac{dv_{C2}(t)}{dt} v_{C2}(t) = -\tilde{p}_{total}(\omega_0 t, 2\omega_0 t, 3\omega_0 t, \dots, 2n\omega_0 t) \quad (3.21)$$

Further, since each capacitor voltage is multiplied by its derivative term in (3.21); (3.21) can be written in terms of the derivative of the square of each capacitor voltage as (3.22).

$$\frac{dv_{C1}^2(t)}{dt} + \frac{dv_{C2}^2(t)}{dt} = -\frac{2\tilde{p}_{total}(\omega_0 t, 2\omega_0 t, 3\omega_0 t, \dots, 2n\omega_0 t)}{C_f} \quad (3.22)$$

Inserting (3.18) and (3.19) into (3.22) results in (3.23).

$$\frac{d\left(V_{DC} + v_{C_0-seq}(t)\right)^2}{dt} + \frac{dv_{PCC}^2(t)}{dt} = -\frac{4\tilde{p}_{total}(\omega_0 t, 2\omega_0 t, 3\omega_0 t, \dots, 2n\omega_0 t)}{C_f} \quad (3.23)$$

From (3.23), the closed form solution for the required injected zero-sequence voltage is given by,

$$v_{C_0-seq}(t) = -V_{DC} + \sqrt{-\int \frac{4\tilde{p}_{total}(\omega_0 t, 2\omega_0 t, 3\omega_0 t, \dots, 2n\omega_0 t)}{C_f} dt - v_{PCC}^2(t) + A} \quad (3.24)$$

where the term $\tilde{p}_{total}(\omega_0 t, 2\omega_0 t, 3\omega_0 t, \dots, 2n\omega_0 t)$ has an anti-derivative expressed by elementary functions; since $\tilde{p}_{total}(\omega_0 t, 2\omega_0 t, 3\omega_0 t, \dots, 2n\omega_0 t)$ consists of multiple sinusoidal terms at different harmonics with constant coefficients. Also, the constant (A) is generated by the indefinite integration.

Nonetheless, realizing (3.24) is challenging as the zero-sequence voltage required for the power ripple mitigation needs heavy computations. Then, the closed form solution for $v_{C_0-seq}(t)$ in (3.24) depends on system parameters and this is for the unrealistic assumption that the filter capacitors C_{f1} and C_{f2} are perfectly equal. Next subsection discusses practical considerations regarding the power ripple mitigation scheme.

3.1.3. Power Ripple Mitigation Automation and Practical Considerations

3.1.3.1. Automation

Power balancing between the AC side and the DC side of the SSC highlighted in Figure 3.2 can be used to make the control scheme autonomous. The power ripple that are generated can be regarded as artificial voltage ripple or current ripple generated by the loads and the sources connected at the DC bus of the nanogrid. Then by power balancing, the instantaneous DC current $i_{DC}(t)$ generated by the nanogrid is given by (3.25).

$$i_{DC}(t) = \underbrace{\frac{P_{total}}{V_{DC}}}_{I_{DC}} + \underbrace{\frac{\tilde{p}_{total}(\omega_0 t, 2\omega_0 t, 3\omega_0 t, \dots, 2n\omega_0 t)}{V_{DC}}}_{\tilde{i}_{DC}(t)} \quad (3.25)$$

where I_{DC} is the averaged DC current generated by the nanogrid, $\tilde{i}_{DC}(t)$ is the current ripple generated by the nanogrid. In (3.25) the AC component $\tilde{i}_{DC}(t)$ flows in the DC link capacitor. Therefore, this DC current ripple in (3.26) is related to the DC bus voltage ripple as (3.26).

$$\tilde{v}_{DC}(t) = \frac{1}{C_{DC}} \int \tilde{i}_{DC}(t) dt = \frac{1}{C_{DC} V_{DC}} \int \tilde{p}_{total}(\omega_0 t, 2\omega_0 t, 3\omega_0 t, \dots, 2n\omega_0 t) dt \quad (3.26)$$

where $\tilde{v}_{DC}(t)$ is the instantaneous voltage ripple imposed on the nanogrid bus, and C_{DC} is the small capacitor that used in the nanogrid after the ripple compensation by the proposed control. This capacitor C_{DC} is designed according to the switching requirement. In other words, after successful low frequency ripple abortion the DC link capacitor is designed considering other nanogrid high frequency filtering requirement. Utilizing (3.26) instead of (3.25) reduces the number of sensors that are needed for the control scheme; as the DC bus voltage is already sensed for regulating the DC link voltage. Hence, instead of estimating the required zero-sequence voltage that needs to be injected into the filter capacitors by (3.24); considering the DC bus voltage ripple as the controller feedback is more effective. As this eliminates the extra computation required to generate the zero-sequence mode controller reference.

The previous analysis considered the SSC filter components with matched components. In other words, the filter inductors L_{f1} and L_{f2} are equal, the inductors L_{gf1} and L_{gf2} equivalent, the AC node stray inductors L_{g1} and L_{g2} are identical, and the AC filter capacitors C_{f1} and C_{f2} are equal. Practically this is not true; it is only a good assumption

for simplifying the initial design. However, since the SSC at the PCC is in open circuit conditions in the zero-sequence operation mode (see Figure 3.5); the grid-side filter inductors and the grid stray impedances do not influence the zero-sequence operation mode. Likewise, the converter-side filter inductors L_{f1} and L_{f2} also do not affect the power ripple mitigation scheme; as the ripple will be trapped in the filter capacitors before transferring to the converter-side. The main issue is filter capacitors C_{f1} and C_{f2} mismatch; as they are the location of the power ripple absorption. To see the impact of a mismatch, the previous equation (3.20) needs to be solved but considering a certain degree of mismatch termed as (γ). Meaning that, the filter capacitors are $C_{f1} = C_f$ and $C_{f2} = \gamma C_f$. Therefore, (3.20) can be revised as (3.27).

$$\frac{dv_{C1}^2(t)}{dt} + \gamma \frac{dv_{C2}^2(t)}{dt} = -\frac{2\tilde{p}_{total}(\omega_0 t, 2\omega_0 t, 3\omega_0 t, \dots, 2n\omega_0 t)}{C_f} \quad (3.27)$$

Inserting (3.18) and (3.19) into (3.27) results in (3.28):

$$\frac{d\left(V_{DC} + v_{C_{0-Seq}}(t)\right)^2}{dt} + \frac{dv_{PCC}^2(t)}{dt} + 2\frac{1-\gamma}{1+\gamma} \frac{d\left(v_{PCC}(t)\left(V_{DC} + v_{C_{0-Seq}}(t)\right)\right)}{dt} = -\frac{8\tilde{p}_{total}(\omega_0 t, 2\omega_0 t, 3\omega_0 t, \dots, 2n\omega_0 t)}{(1+\gamma)C_f} \quad (3.28)$$

Then, the close form solution for the required injected zero-sequence voltage for the ripple mitigation in case of mismatched filter capacitors is given by (3.29).

$$v_{C_{0-Seq}}(t) = -V_{DC} + \frac{\gamma-1}{\gamma+1} v_{PCC}(t) + \sqrt{\left(\frac{1-\gamma^2}{1+\gamma} - 1\right) v_{PCC}^2(t) - \int \frac{8\tilde{p}_{total}(\omega_0 t, 2\omega_0 t, 3\omega_0 t, \dots, 2n\omega_0 t)}{(1+\gamma)C_f} dt + A} \quad (3.29)$$

Then, the closed form solution (3.29) depicts that with a mismatch of γ the zero-sequence voltage injected for power ripple minimization is completely different compared to (3.24). Thus, if the capacitor voltages are directly controlled; the mismatch will produce further complications. Also, the mismatch factor γ must be known prior to control activation.

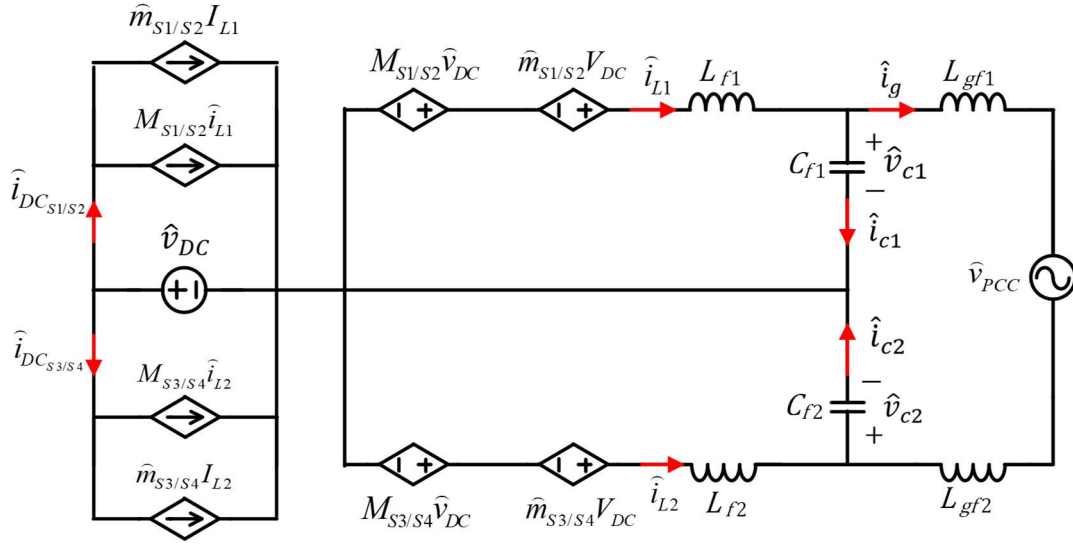


Figure 3.6. Model for stability analysis.

Nevertheless, the autonomous approach explained in previous subsection would solve this complication.

3.1.3.2. Practical Considerations

The minimum DC bus voltage and the filter capacitors are linked to the range of the linear operation of the SSC. This is because the SSC is of buck type and the location of the ripple decoupling is at the AC filter capacitors. Hence, to avoid operation of the SSC in the non-linear modulation region. The filter capacitors voltages in (3.18) and (3.19) must not go below zero level at any instant. The minimum of the capacitors' voltages is as (3.30).

$$\inf(v_{Ci}) = \inf(\frac{1}{2}v_{DC}(t)) - \sup(\frac{1}{2}v_{PCC}(t)) - \sup(\frac{1}{2}v_{C_{0-seq}}(t)) \quad (3.30)$$

Setting $\inf[v_{Ci}]$ in (3.30) to zero results in the minimum DC bus voltage obtained to avoid over modulation occurrence as (3.31).

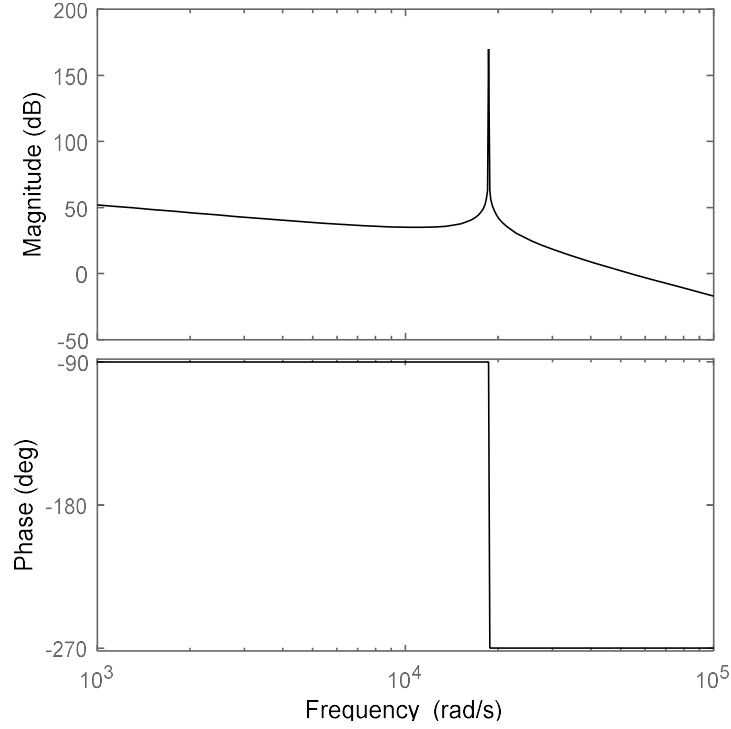


Figure 3.7. Bode plot of $G_3(s)$ indicating instability in the APT mode.

$$\begin{aligned}
 V_{DC}^{Ref} &\geq V_{DC_{min}} \\
 V_{DC_{min}} &= \inf(v_{DC}(t)) \\
 V_{DC_{min}} &= \frac{\sup\left(\left(\frac{2\gamma}{\gamma+1}\right)v_{PCC}(t)\right)}{2} + \frac{\sup\left(\sqrt{v_{PCC}(t)^2\left(\frac{1-\gamma^2}{1+\gamma}-1\right)-\int\frac{8\tilde{P}_{total}(\omega t, 2\omega t, 3\omega t, \dots, 2n\omega t)}{(1+\gamma)C_f}dt+A}}{2}\right)}{2} \quad (3.31)
 \end{aligned}$$

where V_{DC}^{Ref} is the DC bus reference voltage. Thereby, (3.31) is the design equation for selecting the nominal DC bus voltage level and the filter capacitors value with assuming a predefined maximum filter capacitors mismatch factor (γ). Then, the size of the DC link capacitor (C_{DC}) required for the nanogrid will be only for decoupling the high frequency ripple generated by the switching actions of the power electronics devices.

After the value of the filter capacitors and the DC bus voltage are selected; the filter inductors (L_{f1}) and (L_{f2}) and the AC side filter inductors (L_{gf}) and (L_{gf2}) are designed to

keep the filter resonance frequency (ω_{APT}) in the range of $10\omega_0 < \omega_{APT} < \frac{1}{2}\omega_{SW}$, where ω_{APT} is the resonance frequency of the active power transferring mode, and ω_{SW} is the switching angular frequency. However, the filter resonance frequency range constraint must be achieved with targeting the required allowable grid current ripple for the filter inductors and the harmonic suppression around the switching frequency for grid filter inductors. These design considerations are reported in [119], [120].

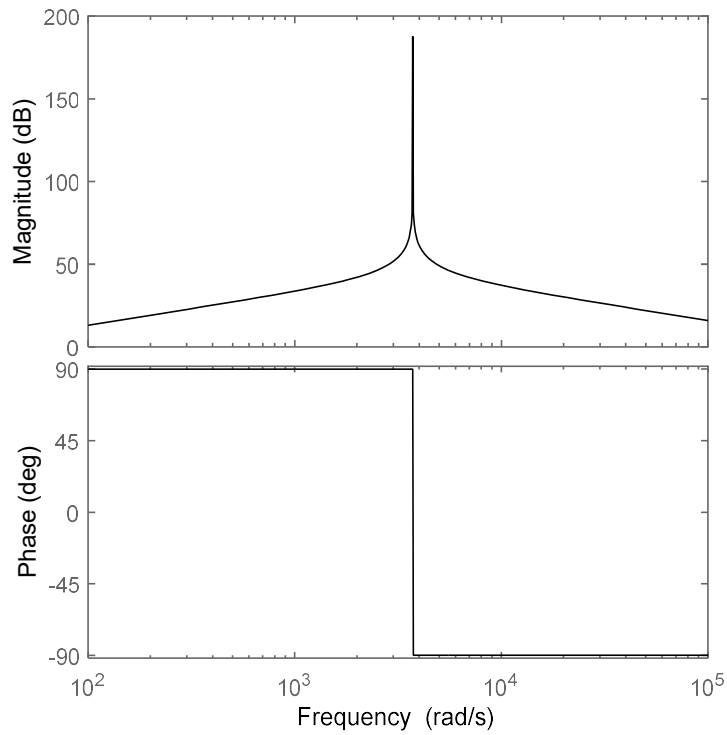


Figure 3.8. Bode plot of $G_6(s)$ indicating instability in the 0-Seq mode.

3.1.4. Stabilization

3.1.4.1. Stability Investigation

The model of the SSC is shown in Figure 3.6. This model is utilized to study the stability of the nanogrid. The switches S1 and S2 are operating with the modulation index (3.32).

$$M_{S1/S2} = M_{APT} + M_{0-Seq} \quad (3.32)$$

Whereas, switches S3 and S4 are operating with the large signal model modulation index given in (3.33).

$$M_{S3/S4} = 1 - M_{APT} + M_{0-Seq} \quad (3.33)$$

Applying small-signal perturbation analysis on the large signal modulation indices given in (3.32) and (3.33) results in (3.34) and (3.35).

$$\hat{m}_{S1/S2} = \hat{m}_{APT} + \hat{m}_{0-Seq} \quad (3.34)$$

$$\hat{m}_{S3/S4} = -\hat{m}_{APT} + \hat{m}_{0-Seq} \quad (3.35)$$

The symbol $\hat{\cdot}$ denotes the perturbed average value of the concerned parameter. Thereby, the S1/S2 has the small signal dynamics of (3.36) and (3.37).

$$(\hat{m}_{APT} + \hat{m}_{0-Seq})V_{DC} = sL_{f1}\hat{i}_{L1} + \hat{v}_{C1} \quad (3.36)$$

$$\hat{i}_{C1} = sC_{f1}\hat{v}_{C1} = \hat{i}_{L1} - \hat{i}_g \quad (3.37)$$

where \hat{i}_{L1} is inductor L_{f1} current, and \hat{i}_{C1} is capacitor C_{f1} current. Similarly, S3/S4 has the small signal dynamics of (3.38) and (3.39).

$$(-\hat{m}_{APT} + \hat{m}_{0-Seq})V_{DC} = sL_{f2}\hat{i}_{L2} + \hat{v}_{C2} \quad (3.38)$$

$$\hat{i}_{C2} = sC_{f2}\hat{v}_{C2} = \hat{i}_{L2} + \hat{i}_g \quad (3.39)$$

where \hat{i}_{L2} is inductor L_{f2} current, and \hat{i}_{C2} is capacitor C_{f2} current. Then, applying KVL at the AC output loop the grid current in relation to the SSC dynamics is given in (3.40).

$$s(L_{gf1} + L_{gf2})\hat{i}_g + \hat{v}_{PCC} = \hat{v}_{C1} - \hat{v}_{C2} \quad (3.40)$$

Then, combining (3.37) and (3.36) results in (3.41).

$$(\hat{m}_{APT} + \hat{m}_{0-Seq})V_{DC} = sL_{f1}\hat{i}_g + \hat{v}_{C1}(L_{f1}C_{f1} + 1) \quad (3.41)$$

Also, combining (3.39) and (3.38) results in (3.42).

$$(-\hat{m}_{APT} + \hat{m}_{0-Seq})V_{DC} = -sL_{f2}\hat{i}_g + \hat{v}_{C2}(L_{f2}C_{f2} + 1) \quad (3.42)$$

The output/input transfer function between the filter capacitors zero-sequence voltage component and the zero-sequence small-signal modulation index is obtained by summing of (3.41) and (3.42). This output/input transfer function is expressed in (3.43).

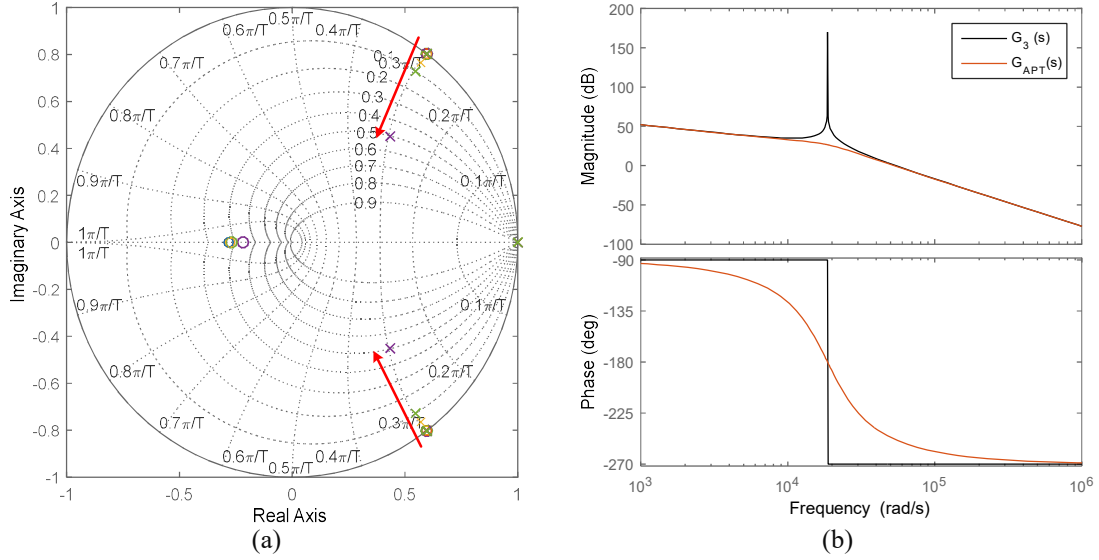


Figure 3.9. (a) Pole zero plot of $G_{APT}(s)$ with varying K_{APT} from 0 to 0.045 indicating stability improvement with gain increase and (b) $G_{APT}(s)$ bode plot indicating stability with K_{APT} of 0.045.

$$G_1(s) = \frac{\hat{v}_{C_{0-Seq}}}{\hat{m}_{0-Seq}} = \frac{V_{DC}}{s^2 L_f C_f + 1}, L_{f1} = L_{f2} = L_f, C_{f1} = C_{f2} = C_f, L_{gf1} = L_{gf2} = L_{gf} \quad (3.43)$$

Similarly, the output/input transfer function between the filter capacitors active power

Transferring mode voltage component and the active power transferring mode modulation index is obtained by subtracting (3.42) from (3.41) and combining the resultant with (3.40).

This output/input transfer function is illustrated in (3.44).

$$G_2(s) = \frac{\hat{v}_{C_{APT}}}{\hat{m}_{APT}} \Big|_{\hat{v}_{PCC}=0} = \frac{L_{gf} V_{DC}}{s^2 L_f C_f L_{gf} + L_f + L_{gf}} \quad (3.44)$$

Furthermore, the output/input transfer function between the injected/absorbed grid current is expressed in (3.45). (3.45) is obtained by combining (3.40) and (3.44).

$$G_3(s) = \frac{\hat{i}_g}{\hat{m}_{APT}} \Big|_{\hat{v}_{PCC}=0} = \frac{V_{DC}}{s^3 L_f C_f L_{gf} + s(L_f + L_{gf})} \quad (3.45)$$

Designing the controller for the active power transferring mode based on (3.45) indicates that the system has a stability problem. Specifically, the output/input transfer function in (3.45) has a resonance peak at (3.46).

$$\omega_{APT} = \sqrt{\frac{L_f + L_{gf}}{L_f C_f L_{gf}}} \quad (3.46)$$

This active power transferring mode resonance frequency (ω_{APT}) might jeopardize the operation of nanogrid. In fact, the bode plot of the transfer function (3.45) in Figure 3.7 shows that there is a sudden -180° phase crossing for gains above 0 dB.

To study the stability of the zero-sequence control, the transfer function that describes the relation between the converter-side inductor current to the zero-sequence modulation index is derived by addition of (3.37) and (3.39). This transfer function is expressed in (3.47).

$$G_4(s) = \frac{\hat{i}_{L_{0-Seq}}}{\hat{m}_{0-Seq}} = \frac{sC_f V_{DC}}{s^2 L_f C_f + 1} \quad (3.47)$$

where $\hat{i}_{L_{0-Seq}}$ is the zero-sequence mode current of the converter-side filter inductors.

Moreover, another transfer function is obtained by subtraction of (3.39) from (3.37). This obtained transfer function relates the converter-side inductors active power transferring mode component ($\hat{i}_{L_{ATP}}$) to the active power transferring mode modulation index as (3.48).

$$G_5(s) = \frac{\hat{i}_{L_{ATP}}}{\hat{m}_{ATP}} = \frac{V_{DC}(s^2 L_f C_f + 1)}{s^3 L_f C_f L_{gf} + s(L_f + L_{gf})} \quad (3.48)$$

To derive the expression that relates the nanogrid current to the two modulation indices; combining the DC current that flows in S1/S2 (3.49) and S3/S4 (3.50) would be helpful.

$$i_{DC_{S1/S2}} = (\hat{m}_{APT} + \hat{m}_{0-Seq})I_{L1} + (M_{APT} + M_{0-Seq})\hat{i}_{L1} \quad (3.49)$$

$$i_{DC_{S3/S4}} = (-\hat{m}_{APT} + \hat{m}_{0-Seq})I_{L2} + (1 - M_{APT} + M_{0-Seq})\hat{i}_{L2} \quad (3.50)$$

where $i_{DC_{S1/S2}}$ is the DC current flowing in S1/S2 switches, $i_{DC_{S3/S4}}$ is the DC current flowing in S3/S4 switches, I_{L1} is the average current of the inductor L_{f1} , and I_{L2} is the

average current of the inductor L_{f2} . Therefore, summation of (3.49) and (3.50) obtains the total nanogrid current as (3.51).

$$i_{DC} = (2M_{0-Seq} + 1)\hat{i}_{L_{0-Seq}} + \hat{m}_{0-Seq}I_{L_{0-Seq}} + (2M_{APT} + 1)\hat{i}_{L_{APT}} + \hat{m}_{APT}I_{L_{APT}} \quad (3.51)$$

where $I_{L_{0-Seq}}$ is the average zero-sequence mode current of the converter-side filter inductors, and $I_{L_{APT}}$ is the average of the active power transferring mode current of the converter-side filter inductors. Thereby, the nanogrid current to the zero-sequence modulation index transfer function is obtained by combining (3.51) with (3.48) and (3.47) as given by (3.52).

$$G_6(s) = \frac{\hat{i}_{DC}}{\hat{m}_{0-Seq}} = \frac{sC_f V_{DC} (2M_{0-Seq} + 1)}{s^2 L_f C_f + 1} + I_{0-Seq} \quad (3.52)$$

Then, the zero-sequence control plant is constructed as (3.53).

$$G_7(s) = \frac{\hat{v}_{DC_{Ripple}}}{\hat{m}_{0-Seq}} = \left(\frac{sC_f V_{DC} (2M_{0-Seq} + 1)}{s^2 L_f C_f + 1} + I_{0-Seq} \right) \left(\frac{1 - LPF(s)}{sC_{DC}} \right) \quad (3.53)$$

where $\hat{v}_{DC_{Ripple}}$ is the voltage ripple of the nanogrid, and $LPF(s)$ is a low pass filter used in extracting the ripple as shown in the overall controller in Figure 3.2. Notice that designing the zero-sequence operation mode controller based on the transfer function (3.52) and (3.53) is not recommended. This is because this system is unstable due to the resonance at (3.54).

$$\omega_{0-Seq} = \sqrt{\frac{1}{L_f C_f}} \quad (3.54)$$

This zero-sequence mode resonance ω_{0-Seq} might jeopardize the operation of nanogrid. In fact, the bode plot of the in Figure 3.8 shows that there is a sudden -180° phase transition for gains above 0 dB.

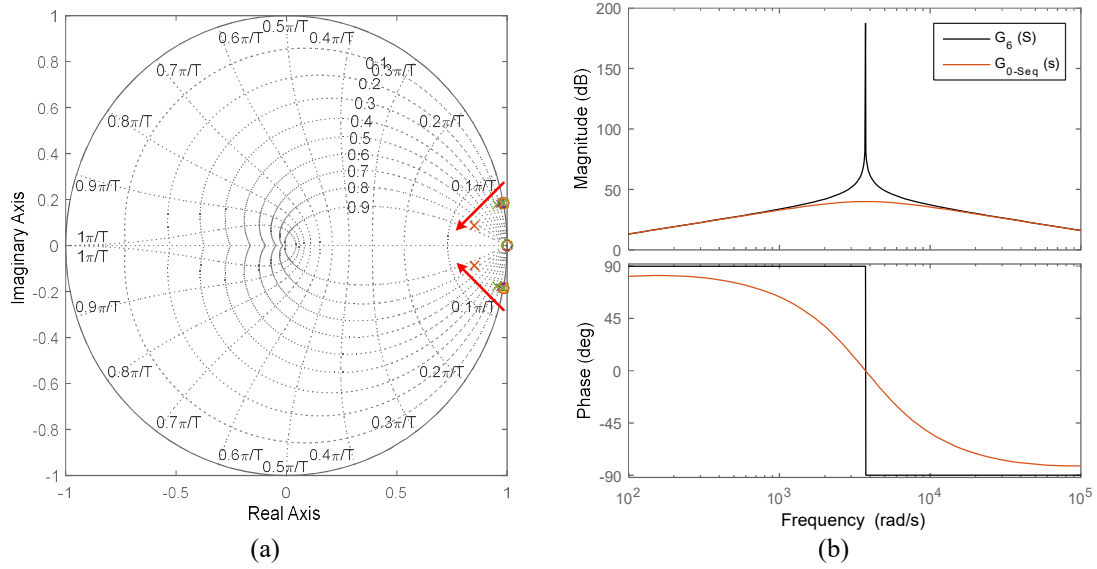


Figure 3.10. (a) Pole zero plot of $G_{0-Seq}(s)$ with varying K_{0-Seq} from 0 to 0.015 indicating stability improvement with gain increase and (b) $G_{0-Seq}(s)$ bode plot indicating stability with K_{0-Seq} of 0.015.

3.1.4.2. Stabilization Scheme

To stabilize the nanogrid, alternative plants must be derived. This is done through utilizing the filter capacitors zero-sequence and active power transferring current components. Thereby, the output/input transfer function between the filter capacitor active power transferring mode current (\hat{i}_{CAPT}) component and the zero-sequence modulation sequence is obtained by subtracting (3.39) from (3.37) then combining the resultant in (3.44) as given by (3.55).

$$G_8(s) = \frac{\hat{i}_{CAPT}}{\hat{m}_{APT}} \Big|_{\hat{v}_{PCC}=0} = \frac{sC_f L_{gf} V_{DC}}{s^2 L_f C_f L_{gf} + L_f + L_{gf}} \quad (3.55)$$

The transfer function (3.55) is used in implementing a virtual damping resistor in-parallel with the filter capacitor in the active power transferring mode operation. This is done through feeding back the capacitor current active power transferring mode component in the control loop with a specific damping gain (k_{APT}). Furthermore, and additional transfer

function is required to convert the filter capacitor active power transferring mode current into the grid-current, which is given by (3.56).

$$G_9(s) = \left. \frac{\hat{i}_g}{\hat{i}_{C_{APT}}} \right|_{\hat{v}_{PCC}=0} = \frac{1}{s^2 C_f L_{gf}} \quad (3.56)$$

(3.56) is deduced by division of (3.45) by (3.55). Therefore, the alternative active power transferring mode plant with active stabilizing capability is given in (3.57).

$$G_{APT}(s) = \frac{G_d(s)G_8(s)G_9(s)}{1 + k_{APT}G_d(s)G_8(s)} \quad (3.57)$$

where $G_d(s)$ is delay of $1.5T_{sw}$ ($T_{sw} = 2\pi/\omega_{sw}$) that is modeled by Pade approximation as (3.58).

$$G_d(s) = e^{-1.5sT_{sw}} \approx \frac{1 - 0.75T_{sw}s + 0.1875T_{sw}^2s^2}{1 + 0.75T_{sw}s + 0.1875T_{sw}^2s^2} \quad (3.58)$$

The stabilization capability of the alternative active power transferring plant in (3.57) is observable by varying the gain k_{APT} . Particularly, as the gain k_{APT} increases the pair of the unstable poles are pushed inside the unit circle in Figure 3.9(a). In fact, the -180° phase crossing for gain above 0 dB disappears (see Figure 3.9(b)).

The zero-sequence alternative plant that has stabilizing capability is composed of two transfer functions. The first transfer function is the output/input relation between the filter capacitors zero-sequence current ($\hat{i}_{C_{0-Seq}}$) and the zero-sequence modulation index (3.59).

$$G_{10}(s) = \frac{\hat{i}_{C_{0-Seq}}}{\hat{m}_{0-Seq}} = \frac{sC_f V_{DC}}{s^2 L_f C_f + 1} \quad (3.59)$$

(3.59) is the transfer function (3.47). The second transfer function is the output/input relation between the nanogrid current to the filter capacitors zero-sequence current component. This transfer function is derived by dividing (3.52) by (3.59) as (3.60).

$$G_{11}(s) = \frac{\hat{i}_{DC}}{\hat{i}_{C_{0-Seq}}} = I_{0-Seq} \frac{s^2 L_f C_f + 1}{s C_f V_{DC}} + 2M_{0-Seq} + 1 \quad (3.60)$$

Therefore, the alternative zero-sequence mode plant with active stabilizing capability is given in (3.61).

$$G_{0-Seq}(s) = \left(\frac{G_d(s)G_{10}(s)G_{11}(s)}{1 + k_{0-Seq}G_d(s)G_{10}(s)} \right) \left(\frac{1 - LPF(s)}{sC_{DC}} \right) \quad (3.61)$$

The stabilization capability of the alternative zero-sequence plant in (3.61) is observable by varying the gain k_{0-Seq} . Particularly, as the gain k_{0-Seq} increases the pair of the unstable poles are pushed inside the unit circle (see Figure 3.10(a)). In fact, the -180° phase crossing for gain above 0 dB disappears (see Figure 3.10 (b)).

3.1.5. Validations

The proposed SSC zero-sequence control scheme (see Figure 3.2) theoretical analysis are verified by implementing a 500V/5kW nanogrid in Typhoon HIL simulator. The details of the nanogrid loads, sources and components are listed in Table 6. The considered nanogrid, has a low DC bus capacitance. The total DC bus capacitance is only 50 μ F; which is realizable with the commercially available reliable film capacitors. Accordingly, the anticipated theoretical DC bus voltage ripple with such ratings are around 200V_{pp}. In addition, the grid AC node voltage that is feeding the DC bus is given by (3.62).

$$v_g(t) = 120\sqrt{2} \cos(2\pi 50t) + 1.5\sqrt{2} \cos(2\pi 100t + \frac{\pi}{9}) + 3.5\sqrt{2} \cos(2\pi 150t + \frac{2\pi}{9}) + 2.5\sqrt{2} \cos(2\pi 200t + \frac{5\pi}{18}) + 1.5\sqrt{2} \cos(2\pi 250t + \frac{\pi}{2}) \quad (3.62)$$

From (3.62), the low frequency voltage ripple that will appear on the DC bus are from the 1st harmonic till the 10th harmonic. Also, the linear AC load in the nanogrid is operating with a nominal frequency of quintuple the AC node main frequency. Thereby, generating voltage ripple at the 10th harmonic. Similarly, the non-linear AC load operates at an

Table 6. Nanogrid Details

DC bus	DC link capacitor	C_{DC}	50 μ F
	DC bus voltage	V_{DC}	500 V
	Nanogrid power	P_{DC}	5 kW
AC node	Fundamental frequency	f_0	50 Hz
	Fundamental voltage	V_{g1}	169.7 V
	Parasitic inductors	$L_{g1} = L_{g2} = L_g$	0.05 mH
SSC	Converter-side inductors	$L_{f1} = L_{f2} = L_f$	1.2 mH
	Filter capacitors	$C_{f1} = C_{f2} = C_f$	60 μ F
	AC bus-side inductors	$L_{gf1} = L_{gf2} = L_{gf}$	0.1 mH
	Switching frequency	f_{sw}	20 kHz
Loads and sources	Buck DC load		500 W @ 250 V
	Boost DC load		500 W @ 1 kV
	Buck-Boost DC load		500 W @ 1.2 kV
	Direct connected DC load		750 W @ 500 V
	Linear AC load		750 W @ 156 V _{RMS} /250Hz
	Non-linear AC load		500 W @ 71 V _{RMS} /180Hz
	Battery bank converter		1500 W @ 340 V

operating frequency of triple the AC node main frequency. Hence, the significant voltage ripple generated due to the non-linear load are higher even order multiples of the 3rd harmonic. The proposed controller considers each of the aforementioned harmonics for the ripple compensation.

3.1.5.1. Nanogrid Stabilization

The impact of the proposed nanogrid stabilization scheme is illustrated in Figure 3.11. It is obvious in Figure 3.11 before time instant 0.5 sec the nanogrid is stable; as no ringing is observed before time instant 0.5 sec. This is due to the two gains that appears in the alternative control plants (i.e., k_{APT} in (3.57) and k_{0-Seq} in (3.61)). Furthermore, at the instant that the zero-sequence stabilization gain is deactivated the nanogrid main DC bus voltage starts to ring thereby impact all the nanogrid elements (see Figure 3.11 after 0.5 sec). Furthermore, similar ringing behavior is seen on the injected grid current when the active power transferring mode stabilization gain is deactivated in Figure 3.11 after time instant

0.8 sec. Therefore, this result emphasizes on the importance of the stabilization approach for the correct operation of the nanogrid.

3.1.5.2. Impact of The Proposed Zero-Sequence Control

The impact of the proposed zero-sequence control on the size of the DC link capacitor is depicted in Figure 3.12. Particularly, before time instant 0.5 sec when the zero-sequence mode control is activated the DC bus voltage (v_{DC}) ripple are only 2% of the nominal DC bus voltage. The voltage ripple are absorbed by the zero-sequence mode voltage injected into the two filter capacitors voltages (v_{C1} and v_{C2}). The positive effect of the proposed zero-sequence control is evident on all loads and sources in the nanogrid; as no voltage ripple are observed in Figure 3.12 before time instant 0.5 sec. Conversely, in Figure 3.12 after time instant 0.5 sec the DC bus oscillates with $200V_{pp}$; thereby, impacting all source and loads in the nanogrid. A clear evidence that the zero- sequence mode control is deactivated after time instant 0.5 sec in Figure 3.12 is that the filter capacitors no longer contain a zero-sequence voltage. In such case i.e., without the proposed zero-sequence control mode only increasing the DC link capacitance to 1mF would absorb the voltage ripple. However, this will impact the reliability of the system as 1mF capacitor is only available as an e-caps.

3.1.5.3. Nanogrid Load Increase

The proposed SSC with the zero-sequence control mode is tested with load increase in Figure 3.13. Specifically, in Figure 3.13 after time instant 0.5 sec the nanogrid load is increased by 500 W (i.e., 10% load increase). The zero-sequence controller responses

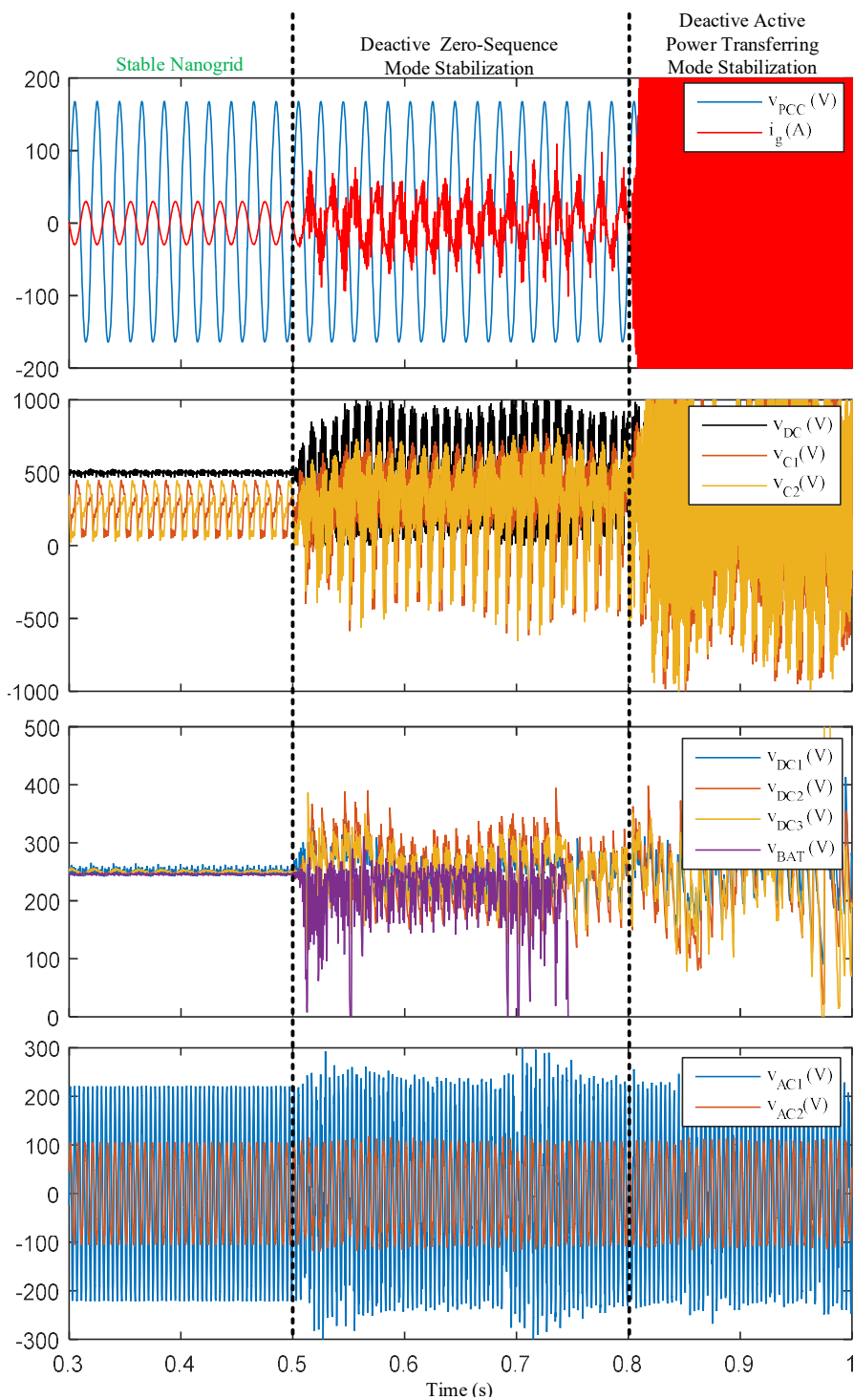


Figure 3.11. Impact of the proposed stabilizer approach on a 500V/5kW nanogrid with 50 μ F DC link capacitor (Note that, the different DC voltages have different offsets as the following: $v_{DC1}^{Offset} = 0$, $v_{DC2}^{Offset} = -750$ V, $v_{DC3}^{Offset} = -950$ V, and $v_{Bat}^{Offset} = -90$ V).

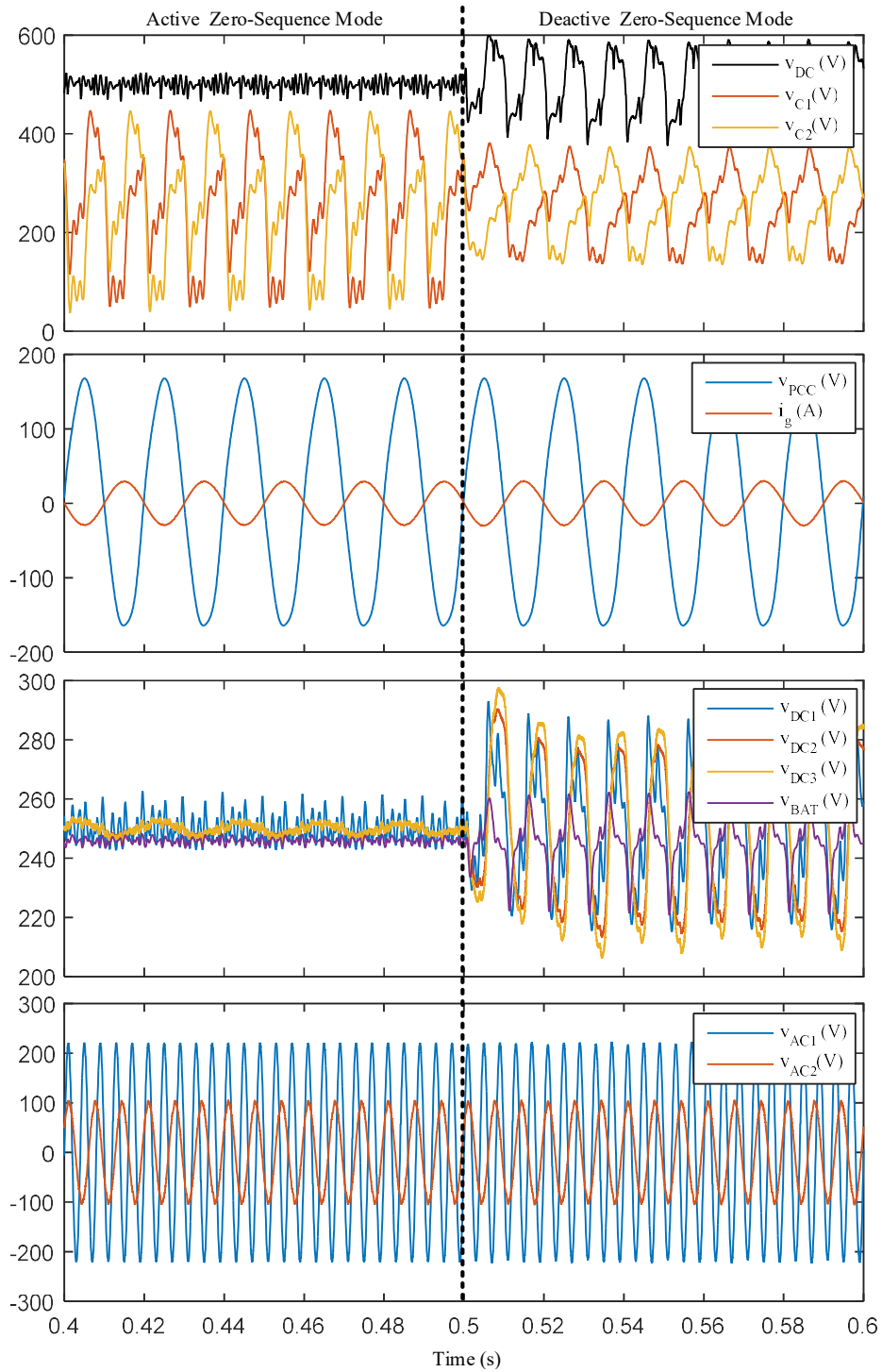


Figure 3.12. Impact of the proposed zero-sequence mode control on a 500V/5kW nanogrid with 50 μ F DC link capacitor (Note that, the different DC voltages have different offsets as the following: $v_{DC1}^{Offset} = 0$, $v_{DC2}^{Offset} = -750$ V, $v_{DC3}^{Offset} = -950$ V, and $v_{Bat}^{Offset} = -90$ V).

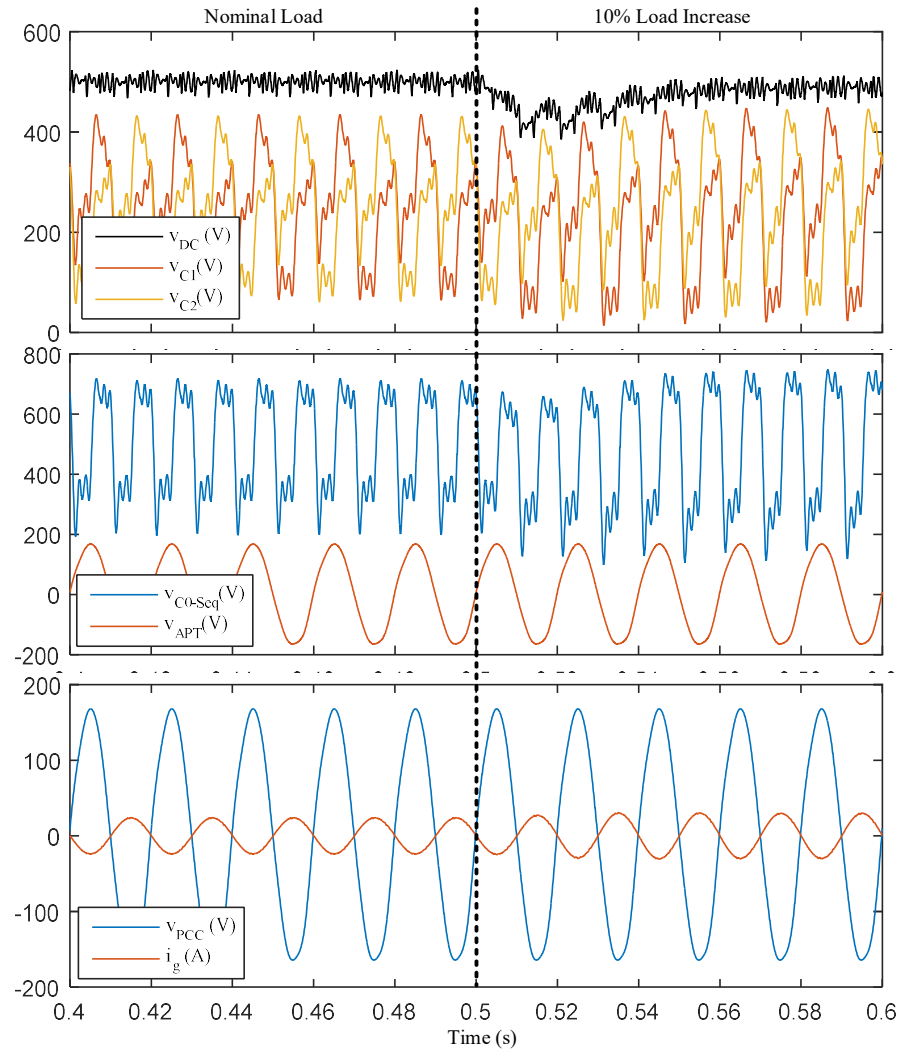


Figure 3.13. Proposed zero-sequence mode control with 10% load increase in 500V/5kW nanogrid with 50 μ F DC link capacitor.

autonomously to this load increase by increasing the amount of the zero-sequence voltage in the filter capacitor voltage to absorb the excess voltage ripple imposed on the nanogrid main bus. The system will operate well with a load increase as long as the condition in (3.31) is not violated. If (3.31) is violated the DC link voltage must be boosted to avoid over-modulation occurrence. Furthermore, it is clear that the active power transferring

mode is not affected by the proposed zero-sequence control; as the active power transferring mode component in the filter capacitors ($v_{C_{APT}}$) in Figure 3.13 is not affected by the variations in the zero-sequence voltage. These results validate the independent operation of the proposed zero-sequence control of the active power transferring mode. In fact, the active power transferring mode component in the filter capacitor ($v_{C_{APT}}$) is equal to the v_{PCC} .

3.1.5.4. Performance With Filter Components Mismatch

Figure 3.14 depicts the effect of filter capacitors mismatch. Specifically, the one of the two filter capacitors is set to twice the nominal value in Figure 3.14. It is obvious that when there is a mismatch between the two filter capacitors the zero-sequence component in the two filter capacitors is no longer symmetrical (see Figure 3.14 v_{C1} maximum and minimum peaks are different than v_{C2}). However, the proposed zero-sequence controller adapts autonomously to this mismatch without the requirement for adjusting the controller gains or prior knowledge about the degree of mismatch. These results validate equation (3.28) showing that any filter capacitors mismatch occurrence results in changing the required zero-sequence voltage required for voltage ripple absorption which is a complication if the filter capacitor voltages are directly controlled for ripple mitigation. Also, the mismatch in the filter capacitors does not affect the active power transferring mode operation; as the active power transferring mode voltage of the filter capacitors ($v_{C_{APT}}$) remains unchanged and equal to the v_{PCC} in Figure 3.14.

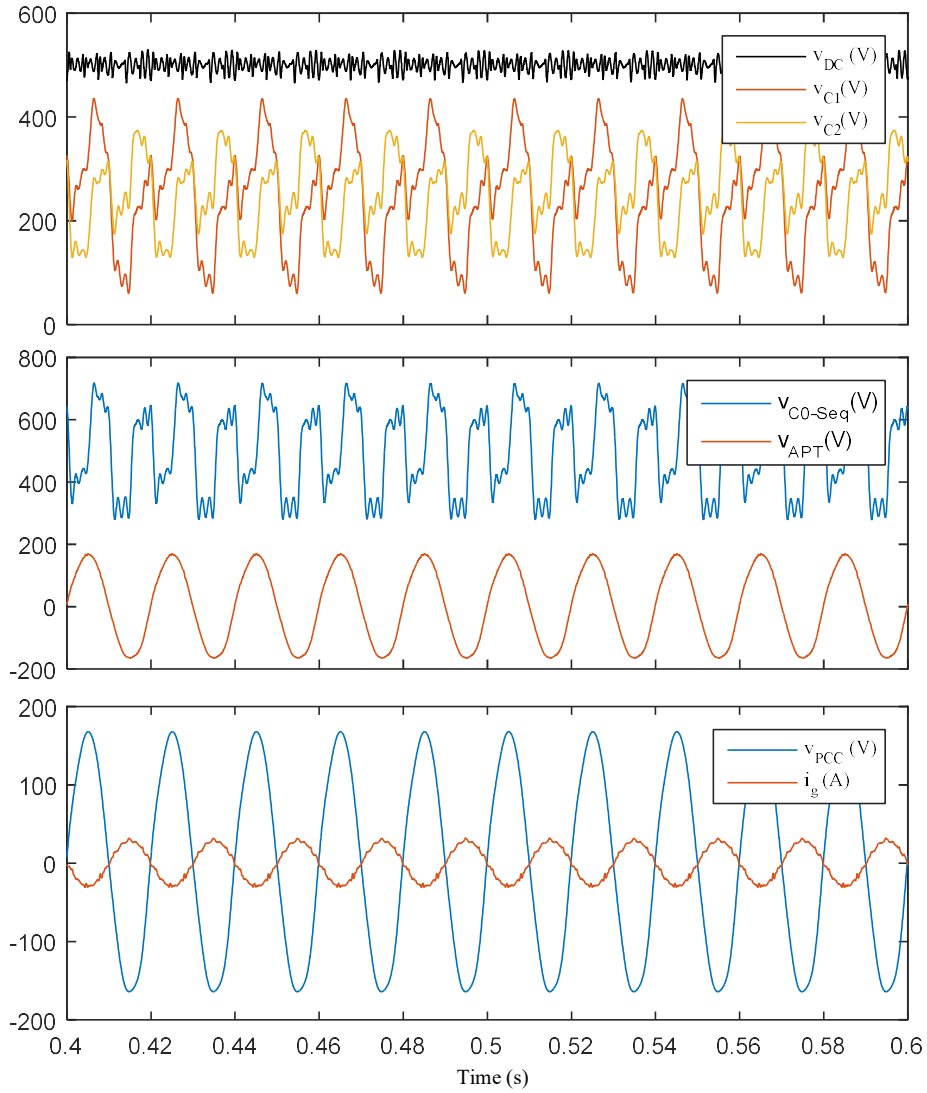


Figure 3.14. Proposed zero-sequence mode control with filter capacitors mismatch with $\gamma = 2$ in a 500V/5kW nanogrid with 50 μ F DC link capacitor.

3.2. PLL-less Grid-Following Control with Active Power Decoupling

Control

Unlike the three-phase system instantaneous power, single-phase system instantaneous power comprises of an average zero frequency component with a substantial double line

frequency ripple component [121]. This double line frequency power ripple component appears as a double line frequency voltage ripple component superimposed on the DC-link voltage. In fact, to realize a low ripple DC-link voltage, often a huge decoupling electrolytic capacitor must be installed in-parallel to the DC-link, which is often considered by power electronics experts as the main source of power converter failures [86]. Consequently, numerous methods were introduced in academia and industry to actively decrease the bulky input capacitance requirement of single-phase systems [122, 123]. All these methods are termed in the literature as active power decoupling controls. Furthermore, the articles [91, 92, 105, 124, 125] are the major survey papers about these active solutions that aim to reduce the size of the decoupling capacitor required for DC linking. The principle of these techniques is to divert this double line frequency voltage ripple component from the DC side of the converter by utilizing additional auxiliary active switches and energy storage elements.

An evolving active power decoupling control was introduced by Serban in [109] for uninterruptible power supply (UPS) applications. This active double line frequency ripple mitigation approach depends on the CM operation of the power converter with slightly modifying the output *LCL* filter architecture. Serban converter in [109], was later used in [107] for grid-connected applications with an inner converter-side current control loop. While, the d-axis reference current is obtained from the outer DC-link control loop. Then, authors of [126] realized that Serban converter consists of two bi-directional buck converters that are connected in a differential manner with the grid in non-islanded

applications or the AC load in islanded applications. Therefore, this converter is termed in the literature as the “Differential Buck Converter” (see Figure 3.15).

The authors of [126], utilized this differential connection notion to improve the double line frequency ripple mitigation approach. Specifically, by balancing the instantaneous power exchanged between the AC and DC side of the differential converter; the double line frequency ripple component is regarded as artificial CM current ripple generated from the DC source. Hence, using stationary reference frame controller tuned at twice the grid frequency, this CM ripple current can be regulated to zero. This reduces the computation burden and makes the control scheme autonomous, as there is no need to calculate the CM control loop reference. The same authors investigated the resonance phenomena in both the CM and the DM plants [126]. Reference [126] concluded that the *LCL* resonance always occurs in the DM plant for grid-side control and it does not occur for converter-side control. In fact, it always necessitates a stabilization scheme in absence of passive damping by physical resistors. On the other hand, the CM plant possesses an *LC* resonance that is severe when the components of the filter are symmetrical. Additionally, [127] extended the differential buck converter performance in non-islanded operation when there is a realistic storage capacitors mismatch. Mismatched output filter capacitors suppress the CM resonance. Nonetheless, the DC-link voltage is superimposed by odd order grid frequency harmonics instead of only even order grid frequency harmonics. Lastly, the same authors of [127], presented the effect of using the differential buck converter with non-linear loads in [128]. Their conclusion is that the DC-link voltage is contaminated with higher order even grid frequency harmonics with non-linear loads [128]. Furthermore, [129] extended

the operation of the differential buck converter when operating with distorted AC grids. Specifically, the authors suggested to use multiple stationary reference frame controllers tuned from the fundamental grid frequency to twice the high multiple of the fundamental frequency that exist in the distorted grid spectrum.

Therefore, there is no direct active and reactive power control for the differential buck converter in the literature. All existing controls are using the cascaded dual loop control for the DM operation. Specifically, an outer DC bus regulation loop that derives the d-axis reference current for the inner fast current control loop. While, the CM control loop is utilizing multiple stationary reference frame controllers at even order grid frequency harmonics to mitigate the DC-bus ripple. The main challenge with these controls is that the active and reactive power injection/absorption cannot be controlled directly. Also, complex tuning process is needed for obtaining the appropriate controller gains. Additionally, PLL induced instabilities are highly probable with the existing dual loop control. Especially, if the differential buck converter is connected to a weak grid [10].

Therefore, this subsection proposes a single control loop direct active and reactive power control for the differential buck converters. The proposed controller's single stage structure reduces the effort in tuning the controller's gains compared to the conventional dual loop cascaded active and reactive power control methodology [67, 68]. The proposed control approach enables PCC current synchronization without the utilization of a PLL (i.e., PLL-less). Hence, avoiding instabilities that might arise due to PLL controller's non-linear nature and weak grid's large line impedance negative influence on the PCC voltage [69, 70].

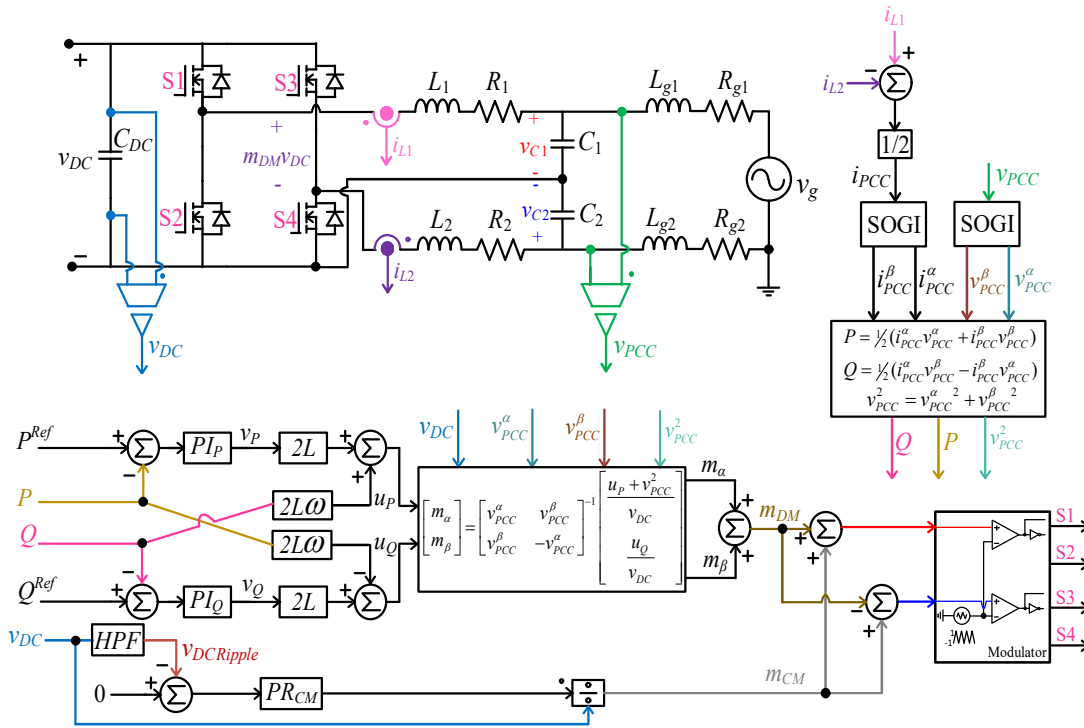


Figure 3.15: Proposed decoupled single loop active and reactive power control without utilizing PLL for the differential buck converter

Considering the differential converter that is connected to a weak grid in Figure 3.15. The active power (P) and reactive power (Q) injected/absorbed into/from the grid can be measured by using the second order generalized integrator (SOGI) that was introduced by [71] as (3.63) and (3.64), respectively. SOGI has unique harmonic filtering capability that makes the measurements robust to distortion imposed by weak grid conditions [72, 73].

$$P = \frac{(i_{L1}^{\alpha} - i_{L2}^{\alpha})(v_{C1}^{\alpha} - v_{C2}^{\alpha})}{6} + \frac{(i_{L1}^{\beta} - i_{L2}^{\beta})(v_{C1}^{\beta} - v_{C2}^{\beta})}{6} \quad (3.63)$$

$$Q = \frac{(i_{L1}^{\alpha} - i_{L2}^{\alpha})(v_{C1}^{\beta} - v_{C2}^{\beta})}{6} - \frac{(i_{L1}^{\beta} - i_{L2}^{\beta})(v_{C1}^{\alpha} - v_{C2}^{\alpha})}{6} \quad (3.64)$$

where

$$i_{PCC}^{\alpha} = \frac{i_{L1}^{\alpha} - i_{L2}^{\alpha}}{2}, i_{PCC}^{\beta} = \frac{i_{L1}^{\beta} - i_{L2}^{\beta}}{2}, v_{PCC}^{\alpha} = \frac{v_{C1}^{\alpha} - v_{C2}^{\alpha}}{2}, v_{PCC}^{\beta} = \frac{v_{C1}^{\beta} - v_{C2}^{\beta}}{2}$$

The same modeling logic yields similar PQ state-space with direct PQ control capability on the DM current as Chapter 2 derivations as seen in Figure 3.15.

For actively absorbing the double line frequency power ripple, the topology of the differential converter in Figure 3.15 makes the filter capacitors' voltages at the loop of PCC to be as (3.65) and (3.66).

$$v_{C1}(t) = \frac{V_{DC} + v_{PCC}(t)}{2} \quad (3.65)$$

$$v_{C2}(t) = \frac{V_{DC} - v_{PCC}(t)}{2} \quad (3.66)$$

If a CM voltage component ($v_{CM}(t)$) is superimposed on the two filter capacitors by the CM modulation index as (3.67) and (3.68) such that the instantaneous power at the PCC loop is equal to the negative of the double line frequency power ripple as (3.69); the double line frequency power ripple will be successfully mitigated.

$$v_{C1}(t) = \frac{V_{DC} + v_{PCC}(t)}{2} + v_{CM}(t) \quad (3.67)$$

$$v_{C2}(t) = \frac{V_{DC} - v_{PCC}(t)}{2} + v_{CM}(t) \quad (3.68)$$

$$p_{C1}(t) + p_{C2}(t) = -\tilde{p}_{2\omega_o}(t) \quad (3.69)$$

Accordingly, the minimum capacitance required to accomplish a DC-link with negligible ripple will be reduced. This injected CM voltage ($v_{CM}(t)$) into the filter capacitors can be estimated by finding the closed form solution of (3.69). In more details, (3.69) is rewritten as (3.70) in relation to the filter capacitors with the assumption that the AC filter capacitors are equal (i.e., $C_1 = C_2 = C$).

$$C \frac{dv_{C1}(t)}{dt} v_{C1}(t) + C \frac{dv_{C2}(t)}{dt} v_{C2}(t) = -\tilde{p}_{2\omega_o}(t) \quad (3.70)$$

Further, since each capacitor voltage is multiplied by its derivative term in (3.70); it can be rewritten in terms of the derivative of the square of each capacitor voltage as (3.71).

$$\frac{dv_{C1}^2(t)}{dt} + \frac{dv_{C2}^2(t)}{dt} = -\frac{2\tilde{p}_{2\omega_o}(t)}{C} \quad (3.71)$$

Inserting (3.67) and (3.68) into (3.71) results in (3.72).

Table 7. Differential buck converter with PLL-less grid-following current control ratings

Parameter	Symbol	Value
Rated Power	P_{Rated}	5 kW
Switching Frequency	f_{sw}	10 kHz
Nominal Grid Frequency	ω	376.8 rad/sec
Grid Voltage Peak	V_g	$120\sqrt{2}$ V
DC-Bus Voltage	V_{DC}	450-600 V
DC-link Capacitor	C_{DC}	50 μ F
Filter Inductor	$L = L_1 + L_2$	2 mH
Filter Capacitor	$C = C_1 = C_2$	50 μ F
Filter Inductor Resistance	$R = R_1 + R_2$	0.05 Ω
Weak Grid Resistor	$R_g = R_{g1} + R_{g2}$	0.5 Ω
Weak Grid Inductor	$L_g = L_{g1} + L_{g2}$	0.1 mH
DC load	R_{DC}	125 Ω

$$\frac{d(V_{DC} + v_{CM}(t))^2}{dt} + \frac{dv_{PCC}^2(t)}{dt} = -\frac{4\tilde{p}_{2\omega_o}(t)}{C} \quad (3.72)$$

From (3.72), the closed form solution for the required injected CM voltage is given by,

$$v_{CM}(t) = -V_{DC} + \sqrt{-\int \frac{4\tilde{p}_{2\omega_o}(t)}{C} dt - v_{PCC}^2(t) + A} \quad (3.73)$$

where the term $\tilde{p}_{2\omega_o}(t)$ has an anti-derivative expressed by elementary functions; since $\tilde{p}_{2\omega_o}(t)$ is decomposed of sinusoidal function with constant coefficient. Also, the constant (A) is generated by the indefinite integration. Nevertheless, power balancing between the AC side and the DC side of the inverter can be used to achieve active 2nd order harmonic power ripple mitigation. The power ripple that are generated can be regarded as artificial voltage ripple or current ripple generated by the DC side. Then, by power balancing, the DC current $i_{DC}(t)$ is given in (3.74).

$$i_{DC}(t) = \frac{P_{Total}}{V_{DC}} + \frac{\tilde{p}_{2\omega_o}(t)}{V_{DC}} \quad (3.74)$$

In (3.74) the AC component $\tilde{i}_{DC}(t)$ flows in the DC link capacitor. Therefore, this DC current ripple in (3.74) is related to the DC bus voltage ripple as (3.75).

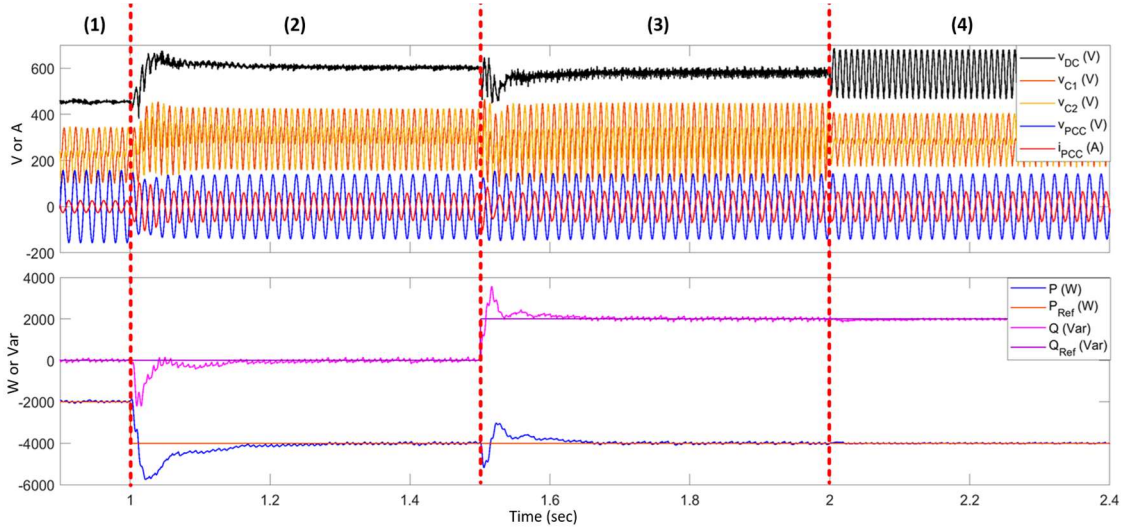


Figure 3.16: Performance of the proposed controller for the differential buck converter: Duration (1) active CM control with 2 kW absorption at unity power factor operation, duration (2) active CM control with 4 kW absorption at unity power factor operation, duration (3) active CM control with 4 kW absorption and 2 kVar injection, and duration (4) deactivated CM control (i.e. no active power decoupling control) with 4 kW absorption and 2 kVar injection

$$\tilde{v}_{DC}(t) = \frac{1}{C_{DC}} \int \tilde{i}_{DC}(t) dt = \frac{1}{C_{DC}V_{DC}} \int \tilde{p}_{2\omega_b}(t) dt \quad (3.75)$$

Hence, instead of controlling the CM voltage that needs to be injected into the filter capacitors to achieve power ripple decoupling; considering the DC bus voltage ripple as the controller feedback achieves similar purpose. The control transfer function for the CM power decoupling loop is as (3.76); the procedure to obtain this transfer function is obtained following conventional average modelling that is found in the section 1 of this chapter [70].

$$\frac{\tilde{v}_{DC}(s)}{\tilde{m}_{CM}(s)} = \frac{HPF(s)}{sC_{DC}} \left(\frac{(2M_{CM} + 1)(C_1 + C_2)V_{DC}}{s^2L(C_1 + C_2) + 1} + I_{DC_{CM}} \right) \quad (3.76)$$

The overall controller structure of the proposed PLL-less decoupled active and reactive power control for the differential buck converter is depicted in Figure 3.15.

The theory developed is verified by implementing a 5 kW grid-connected differential buck converter in PSIM software. This converter is operating in rectifier mode and connected to a weak grid. The system rating is depicted in Table 7. Notice that, the DC-

link capacitor is undersize to only 50 μF ; such a small DC decoupling capacitor means that without any power decoupling control the DC-link voltage ripple is around 200 Vpp. The classical solution to buffer this voltage ripple is to increase the size of the DC link capacitor. However, large decoupling capacitors are often available commercially as unreliable electrolytic type capacitors, which is not desirable.

Firstly, to assess the performance of the proposed control; key waveforms are observed. These key waveforms are P^{Ref} , Q^{Ref} , P , Q , v_{c_1} , v_{c_2} , i_{PCC} , v_{PCC} , and v_{DC} . The methodology of measuring these waveforms is depicted in Figure 3.15. The proposed PLL-less control for the differential buck converter is tracking accurately the commanded active and reactive set-points as evident in Figure 3.16. Specifically, it is obvious from the different operation set-points in Figure 3.16, always the error between the commanded active and reactive power references and the measurements are zero. Also, the CM power decoupling control is absorbing the double line frequency power ripples successful; as there is no DC-link voltage ripple at twice the grid frequency (see durations (1), (2) and (3) in Figure 3.16). This is achieved with a 50 μF decoupling capacitor. The ripple is absorbed by the CM voltage injected into the filter capacitors voltages v_{c_1} and v_{c_2} (see durations (1), (2) and (3) in Figure 3.16). The impact of deactivating the active double line frequency power ripple

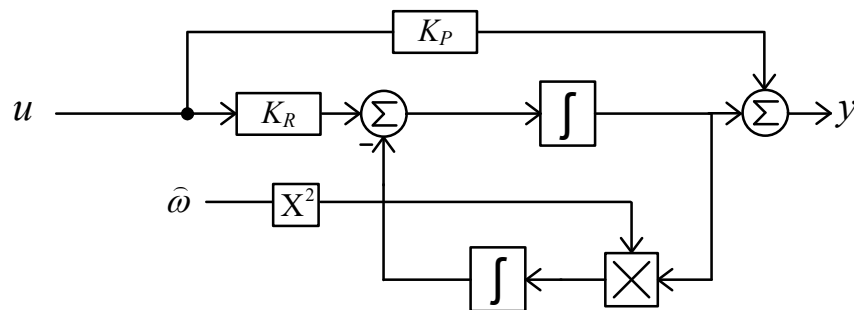


Figure 3.17. Variable frequency proportional resonance controller (VF-PR).

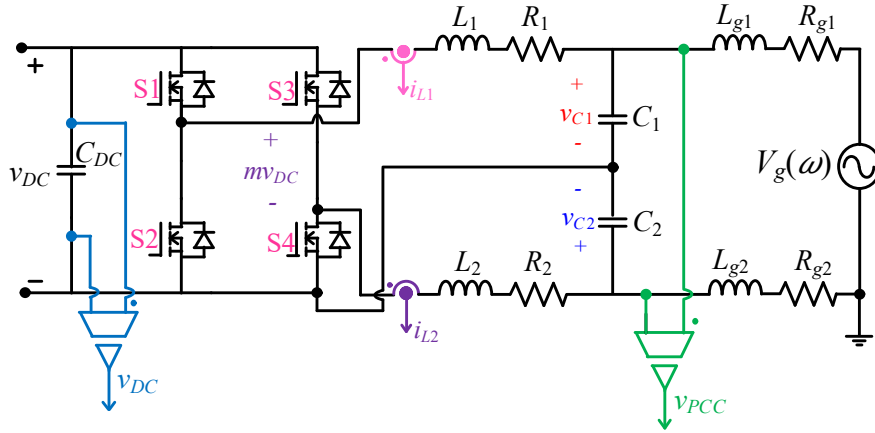


Figure 3.18. Active rectifier for variable frequency operation with active power decoupling capability.

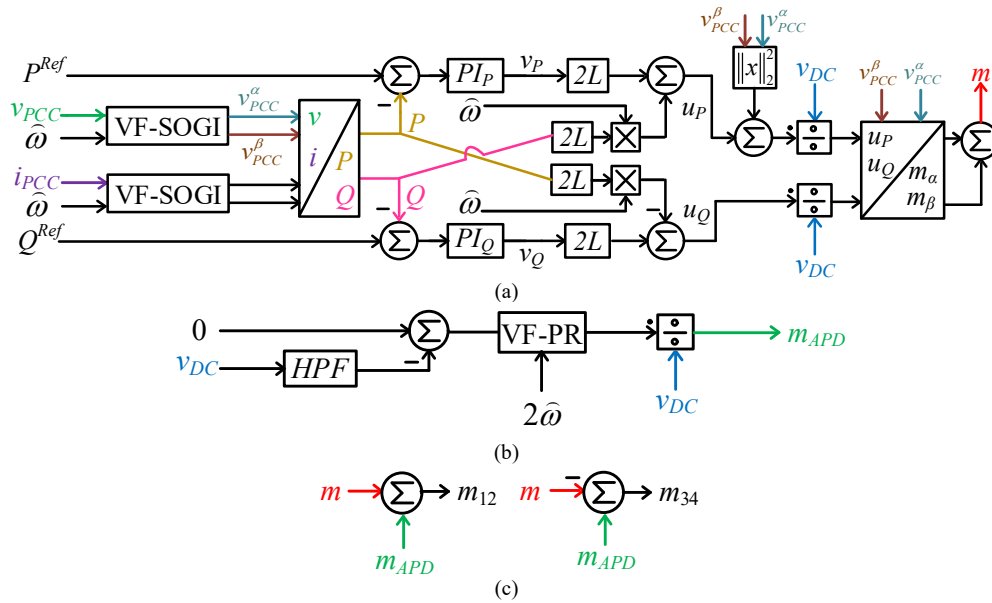


Figure 3.19. (a) Variable frequency decoupled direct active and reactive power control, (b) variable frequency active power decoupling control, and (c) variable frequency control modulation indices. (VF-SOGI: variable frequency second order generalized integrator, VF-PR: variable frequency proportional resonance controller)

mitigation control is evident in duration (4) in Figure 3.16. Specifically, the ripple on the DC-link bus are around 200 V_{pp} without CM control. The results show that the control

proposed achieves active and reactive power control without PLL requirement and reduce the DC link capacitor 50 times.

3.3. PLL-less Grid-Following Control with Active Power Decoupling Control with Variable Frequency Operation

The conventional fixed frequency SOGI can be extended to variable frequency operation by considering the estimation of the AC bus frequency ($\hat{\omega}$) as depicted for adaptation to frequency in Figure 2.18. Here, the concept used in developing the variable frequency SOGI is used to construct the variable frequency proportional resonance controller as depicted in Figure 3.17. This variable frequency proportional resonance (PR) controller is used for the active power decoupling control. The state-space of the variable frequency PR controller is given in (3.77).

$$\begin{aligned} \frac{dx}{dt} &= Ax + Bu, \quad y = Cx + Du \\ x &\in \mathbb{R}^2, u \in \mathbb{R}, y \in \mathbb{R}, A \in \mathbb{R}^{2 \times 2}, B \in \mathbb{R}^{2 \times 1}, C \in \mathbb{R}^{1 \times 2}, D \in \mathbb{R} \\ A &= \begin{bmatrix} 0 & 1 \\ -\hat{\omega}^2 & 0 \end{bmatrix}, B = \begin{bmatrix} 0 \\ 1 \end{bmatrix}, C = [0 \quad K_R], D = K_p \end{aligned} \quad (3.77)$$

where K_R is the resonance gain of the variable frequency proportional resonance controller, and K_p is the proportional gain of the variable frequency proportional resonance controller.

Without loss of generality, at any specific frequency, $P(\omega)$ and $Q(\omega)$ at the point of common coupling of the converter shown in Figure. 3.18 can be obtained with the variable frequency SOGI developed in Figure 2.18 as (3.78) and (3.79).

$$P(\hat{\omega}) = \frac{(i_{L1}^\alpha(\hat{\omega}) - i_{L2}^\alpha(\hat{\omega}))(v_{C1}^\alpha(\hat{\omega}) - v_{C2}^\alpha(\hat{\omega}))}{6} + \frac{(i_{L1}^\beta(\hat{\omega}) - i_{L2}^\beta(\hat{\omega}))(v_{C1}^\beta(\hat{\omega}) - v_{C2}^\beta(\hat{\omega}))}{6} \quad (3.78)$$

$$Q(\hat{\omega}) = \frac{(i_{L1}^\alpha(\hat{\omega}) - i_{L2}^\alpha(\hat{\omega}))(v_{C1}^\beta(\hat{\omega}) - v_{C2}^\beta(\hat{\omega}))}{6} - \frac{(i_{L1}^\beta(\hat{\omega}) - i_{L2}^\beta(\hat{\omega}))(v_{C1}^\alpha(\hat{\omega}) - v_{C2}^\alpha(\hat{\omega}))}{6} \quad (3.79)$$

Table 8. Variable frequency active rectifier ratings

Parameter	Symbol	Value
Rated Power	S_{Rated}	20 kVA
Switching Frequency	f_{sw}	10 kHz
AC Bus Voltage	V_g	120V
Maximum Frequency	ω_{Max}	1884 rad/s
DC Bus Voltage	V_{DC}	500 V
DC link Capacitor	C_{DC}	50 μ F
Filter Inductor	L	0.25 mH
Filter Inductor Resistance	R	0.05 Ω
Filter Capacitor	C	60 μ F

The same modeling logic yields similar PQ state-space with direct control capability on the DM current as Chapter 2 derivations but considering variable frequency operation. Note that, the measurements are defined as (3.80) (see Figure 3.19(a)).

$$i_{PCC}^\alpha = \frac{i_{L1}^\alpha - i_{L2}^\alpha}{2}, i_{PCC}^\beta = \frac{i_{L1}^\beta - i_{L2}^\beta}{2}, v_{PCC}^\alpha = \frac{v_{C1}^\alpha - v_{C2}^\alpha}{2}, v_{PCC}^\beta = \frac{v_{C1}^\beta - v_{C2}^\beta}{2} \quad (3.80)$$

Furthermore, the variable frequency state-space model that includes $P(\omega)$ and $Q(\omega)$ as state variables is obtained as follows,

$$\frac{dP(\hat{\omega})}{dt} = -\frac{R}{L}P(\hat{\omega}) - \hat{\omega}Q(\hat{\omega}) + \frac{1}{2L} \left(m_\alpha(\hat{\omega})v_{DC}v_{PCC}^\alpha(\hat{\omega}) + m_\beta(\hat{\omega})v_{DC}v_{PCC}^\beta(\hat{\omega}) - \|v_{PCC}\|_2^2 \right) \quad (3.81)$$

$$\frac{dQ(\hat{\omega})}{dt} = -\frac{R}{L}Q(\hat{\omega}) + \hat{\omega}P(\hat{\omega}) + \frac{1}{2L} \left(m_\alpha(\hat{\omega})v_{DC}v_{PCC}^\beta(\hat{\omega}) - m_\beta(\hat{\omega})v_{DC}v_{PCC}^\alpha(\hat{\omega}) \right) \quad (3.82)$$

This state-space states can be controlled through the current controller depicted in Figure 3.19. The concept of the variable frequency active power decoupling capability is based on controlling the common mode voltage ($v_{C_{CM}}$) of the filter capacitors C_1 and C_2 in (3.83) and (3.84).

$$v_{C1}(t, \hat{\omega}) = \frac{1}{2}V_{DC} + \frac{1}{2}v_{PCC}(t, \hat{\omega}) + \frac{1}{2}v_{C_{CM}}(t, \hat{\omega}) \quad (3.83)$$

$$v_{C2}(t, \hat{\omega}) = \frac{1}{2}V_{DC} - \frac{1}{2}v_{PCC}(t, \hat{\omega}) + \frac{1}{2}v_{C_{CM}}(t, \hat{\omega}) \quad (3.84)$$

This common mode voltage is utilized as an additional degree of freedom to control the instantaneous power of the filter capacitors P_{C1} and P_{C2} as (3.85).

$$p_{C1}(t, \hat{\omega}) + p_{C2}(t, \hat{\omega}) = -\frac{1}{2} V_{PCC} I_{PCC} \cos(2\hat{\omega}t - \varphi) \quad (3.85)$$

where V_{PCC} is the peak of the point of common coupling voltage, I_{PCC} is the peak of the point of common coupling current, and φ is the power factor angle. The solution of (3.85) is obtained in (3.86) for $C_1 = C_2 = C$.

$$v_{C_{cm}}(t, \hat{\omega}) = -V_{DC} + \sqrt{-\frac{V_{PCC} I_{PCC} \sin(2\hat{\omega}t - \varphi)}{\hat{\omega}C} - \frac{V_{PCC}^2 \cos(2\hat{\omega}t)}{2} - \frac{V_{PCC}^2}{2} + A} \quad (3.86)$$

This voltage solution (3.86) can be induced indirectly by controlling the ripple of the rectifier load ($v_{DC_{Ripple}}$) as (3.87).

$$v_{DC_{Ripple}}(t, \hat{\omega}) = \frac{-V_{PCC} I_{PCC}}{4C_{DC} V_{DC} \hat{\omega}} \sin(2\hat{\omega}t - \varphi) \quad (3.87)$$

Equation (3.87) shows that the ripple of the variable frequency power exchanged at the point of common coupling is also reflected in the rectifier load voltage ripple. Therefore, regulating the rectifier load ripple to zero through a variable frequency proportional resonance controller at $2\hat{\omega}$ shown in Figure 3.19(b) would result in imposing the common mode voltage (3.86). Then using standard small-signal modeling methodology on Figure 3.18 active rectifier, it is straightforward to reach to the control transfer function (3.89) when $C_1 = C_2 = C$, $L_1 = L_2 = L$, and $R_1 = R_2 = R$.

$$\frac{\hat{v}_{DC_{Ripple}}}{\hat{m}_{APD}} = \left(\frac{sC_{DC} V_{DC} (2M_{APD} + 1)}{s^2 LC + sCR + 1} + I_{CM} \right) \left(\frac{HPF(s)}{sC_{DC}} \right) \quad (3.89)$$

Where \hat{m}_{APD} is the active power decoupling control modulation index, C_{DC} is the virtual DC decoupling capacitor, I_{CM} is the average inductor common mode current, M_{APD} is the average modulation index of the active power decoupling control, and $HPF(s)$ is the high pass filter that extracts the ripple. Regarding the stability of the variable frequency active power decoupling control, the open loop transfer function shows that the stability is guaranteed with a finite resistance existence in the filter elements. This finite resistance will

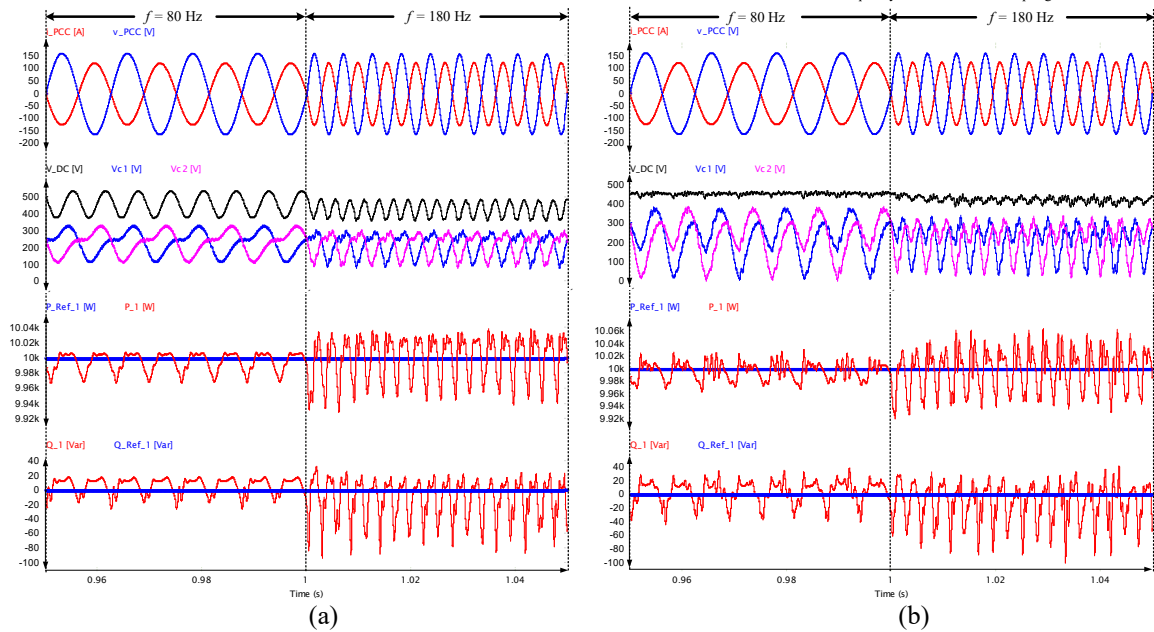


Figure 3.20. Scenario I: (a) without variable frequency active power decoupling control, and (b) with variable frequency active power decoupling control.

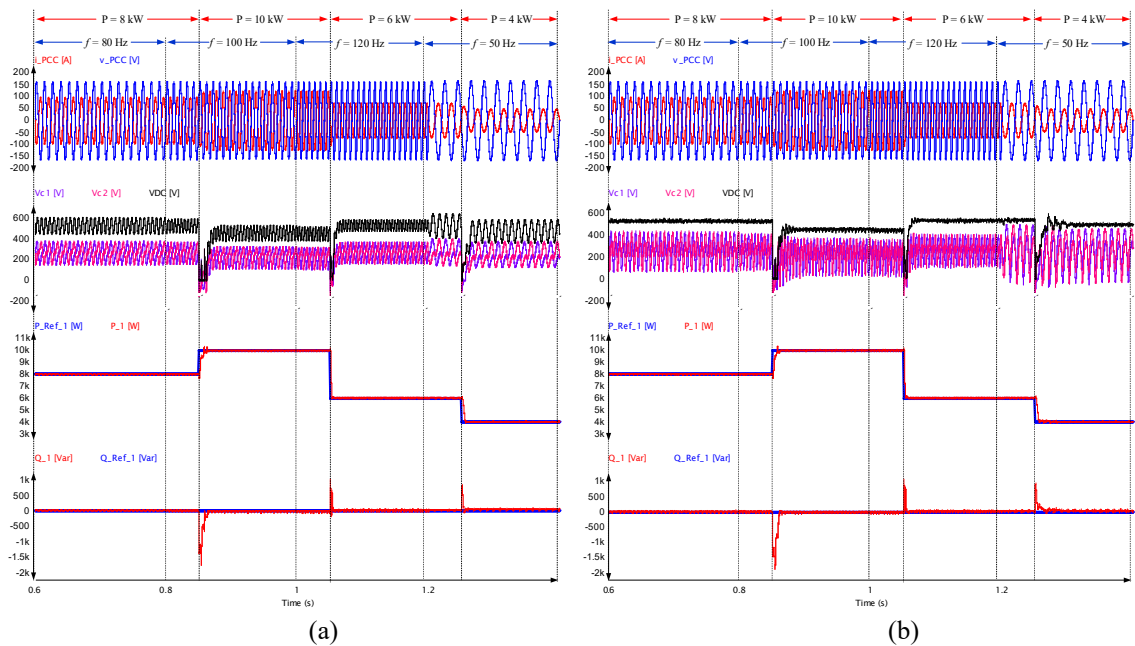


Figure 3.21. Scenario II: (a) without variable frequency active power decoupling control, and (b) with variable frequency active power decoupling control.

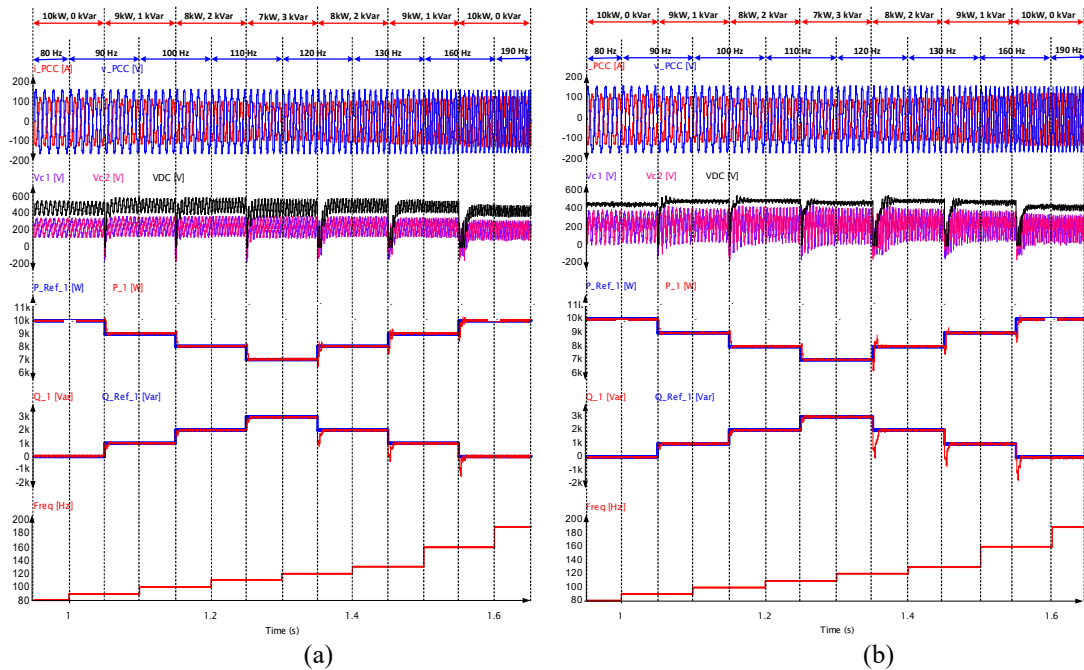


Figure 3.22. Scenario III: (a) without variable frequency active power decoupling control, and (b) with variable frequency active power decoupling control.

produce sufficient damping to the pair of the common mode resonance poles. Finally, the two mode modulation indices are merged as shown in Figure 3.19(c) to control the active rectifier switches.

The theoretical analysis is verified by simulation of a variable frequency single-phase active rectifier with the ratings depicted in Table 8. Three scenarios are simulated with a low DC link capacitor of 50 μ F. The first scenario is validating the performance of the variable frequency active power decoupling control during sudden changes in the AC supply frequency. The second scenario is validating the operation of the variable frequency rectifier with active power set-points and frequency variations under unity power factor operation. The third scenario is validating the performance of the variable frequency

decoupled active and reactive power control with frequency variations, and active and reactive set-points variations.

Scenario I is depicted in Figure 3.20. Particularly, in this scenario a comparison is shown with a dynamic variation in the frequency of the AC supply at time instant 1 s in Figure 3.20 (a) and (b). This comparison is depicting the importance of the variable frequency active power decoupling control in suppressing the rectifier load ripple. Initially, in both Figure 3.20(a) and (b) the AC supply operating frequency is 80 Hz with the active power exchange of 10 kW at unity power factor. It is noticeable that the voltage ripple of the rectifier load voltage (v_{DC}) is suppressed with activating the active power decoupling control in Figure 3.20(b). The 160 Hz voltage ripple is suppressed by the common mode voltage injected into the two filter capacitors v_{C1} and v_{C2} in Figure 3.20(b) before time instant 1 s. After time instant 1 s, the AC supply frequency is changed to 180 Hz in both Figure 3.20(a) and Figure 3.20(b). In this case, the rectifier load ripple frequency is 360 Hz. The active power decoupling control can suppress the rectifier load ripple even with AC supply frequency variations (see Figure 3.20(b) after time instant 1 sec).

Scenario II is validating the performance of the variable frequency rectifier operation with active power set-points dynamic changes at unity power factor operation (see Figure 3.21). Figure 3.21(a) and (b) are identical scenarios the only difference is the activation of the variable frequency active power decoupling capability in Figure 3.21(b). Moreover, initially the active rectifier is operating with 80 Hz, 8 kW at unity power factor (see Figure 3.21 before 0.8 s). Then, at 0.8 s in Figure 3.21(a) and (b) the AC supply frequency is increased to 100 Hz. After that, at 0.85 s the active power set-point is increased to 10 kW

in Figure 3.21(a) and (b). At time instant 1 s in Figure 3.21 the frequency is increase to 120 Hz and after 1.05 s the active power set-point is decreased to 6 kW. Then, at 1.2 s the frequency is decreased to 50 Hz. Finally, the active power set-point is moved to 4 kW. In this scenario that the variable frequency current control mode is capability of operating the rectifier in unity power factor with tracking the commanded active power set-point reference. As well as, comparing Figure 3.21(a) to Figure 3.21 (b) the rectifier load voltage ripple is suppressed with activating the variable frequency active power decoupling control.

The scenario III, which is depicted in Figure 3.22, is validation of operating the variable frequency active rectifier with active power decoupling capability under variations in the AC supply frequency, active power set-point reference, and reactive power set-point reference. Evidently, in scenario III in Figure 3.22, the variable frequency active rectifier is capability of operating the rectifier with tracking the active and reactive power set-point references accurately. As well as, comparing Figure 3.22(a) to Figure 3.22(b) the rectifier load voltage ripple is suppressed with activating the variable frequency active power decoupling control.

3.4. Conclusion

The first section of this chapter provided a detailed mathematical explanation of how the 2nd order power ripples are generated in single-phase nanogrids. Then, a solution based on conventional grid-following control was provided to mitigate the power ripples with detailed controller designs and stabilization scheme development. The second section of this chapter is introduction of utilizing the grid-following inverter control without PLL

requirement for different type of converters that can accommodate 2nd order power ripple mitigations. Therefore, generalizing the developed control in Chapter 2 to different converter. Lastly, the third section is including the adaptation to the frequency of the network to a converter that performs current control and 2nd order power ripple mitigation for a variable frequency operation. The linkage of this work to the future power electronics-dominated grid is that these solutions provide a mean to improve the stability regarding DC link failures that inject a 2nd order harmonics voltage that might trigger loss of generation assets. In addition, these solutions are adopted with no PLL requirement and adaptation to the frequency of the network. The adaptation to frequency variations is a futuristic notion in the power electronics-dominated grid paradigm. Explicitly, the frequency band limits might be relaxed compared to conventional power grid. As conventional synchronous machines will be absent in the 100% renewable based power grid.

Chapter 4

4. Stability Bound Identification

Part of this chapter, including figures and text are based on my following papers:

© 2018-2023 IEEE

- A. Khan, M. Hosseinzadehtaher, M. B. Shadmand and S. K. Mazumder, "Cybersecurity Analytics for Virtual Power Plants," *2021 IEEE 12th International Symposium on Power Electronics for Distributed Generation Systems (PEDG)*, pp. 1-5, 2021

- A. Khan and M. B. Shadmand, "Real-Time Stability Boundary Identification of Prosumers PCC in a Virtual Power Plant," *2021 IEEE 22nd Workshop on Control and Modelling of Power Electronics (COMPEL)*, pp. 1-6, 2021

- A. Khan, M. B. Shadmand and S. K. Mazumder, "On The Voltage Stability of the Power Electronics-Dominated Grid: Mathematical Derivation of The Stability Margin," *2023 IEEE Power & Energy Society General Meeting (PESGM)*, pp. 1-5, 2023

4.1. Voltage Stability in the Power Electronics-Dominated Grid

4.1.1. New Energy Paradigm Voltage Stability

The energy paradigm has brought both prospects and challenges to the power grid [130, 131]. Especially, the elevated penetration of renewables that is aligned with the energy paradigm realization necessitates sophisticated system level coordination and management [132]. This sophisticated system level coordination and management is essential to reinforce the flexibility, and reliability, and operational security of the power grid [133, 134]. Accordingly, latest investments are emphasizing on realizing the power electronics-dominated grid (PEDG) to facilitate superior observability and controllability over consumers owned grid-feeding inverters [135]. This futuristic PEDG is best described as a bundle of multiple small scale grid-feeding inverters situated at the grid-edge representing a coherent grid cluster that is capable of operating independently [136].

The futuristic PEDG characteristics are summarized in following bullet points: (1) low inertia, (2) stochastic generation, (3) generation at the point of load, (4) low X/R ratio, (5) short feeders, (6) generation and load proximity, and (7) low short circuit capacity [131]. These characteristics enforce the PEDG behavior in the context of voltage and frequency dynamics to be completely distinct compared to the conventional power system dynamics. Thus, this chapter tries to clear some misconception that has been witnessed in the literature due to employing conventional bulk power system theories on networks such as the futuristic PEDG. In particular, the authors noticed a variety of recent articles developing coordinated controls for improve voltage quality in grid-edge networks through reactive power set-point control. These authors assume that the network is inductive (i.e., the

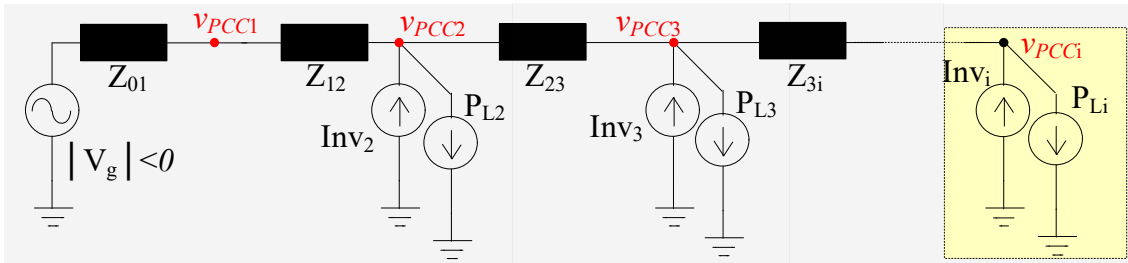


Figure 4.1. Futuristic PEDG illustrating the i^{th} PCC bus equivalent: original network.

network has high X/R ratio as in transmission level), and hence believe that the reactive power variation will provide a control degree of freedom over the bus voltage. In fact, reactive power flow in resistive networks of low X/R ratio is a challenge since it influences the frequency of the network. The authors took a random search about coordinate controls as a sample to show the misconception spread in the literature about reactive power control importance for the future power grid voltage quality. For instance, these publications are focused on voltage quality enhancement by coordinating reactive power as a function of the measured voltage [137-139]. In [137] reactive power injection is initiated when there is a short-term power variations is observed to mitigate voltage fluctuations. Similarly, reactive power control is proposed by [138] through port-Hamiltonian theory to assure optimal voltage profile in the network. Another paper is also focused on reactive power control by developing automatic voltage control based on Lyapunov based sliding mode controller [139]. These articles assume inductive network, which is not realistic for the futuristic PEDG that is located at the grid-edge. As the prosumers local point of common coupling (PCC) bus voltages will be strongly coupled to the active power set-point.

This chapter provides insights into voltage stability problem in the futuristic PEDG. The active power control will be significant for accomplishing voltage stability in the futuristic

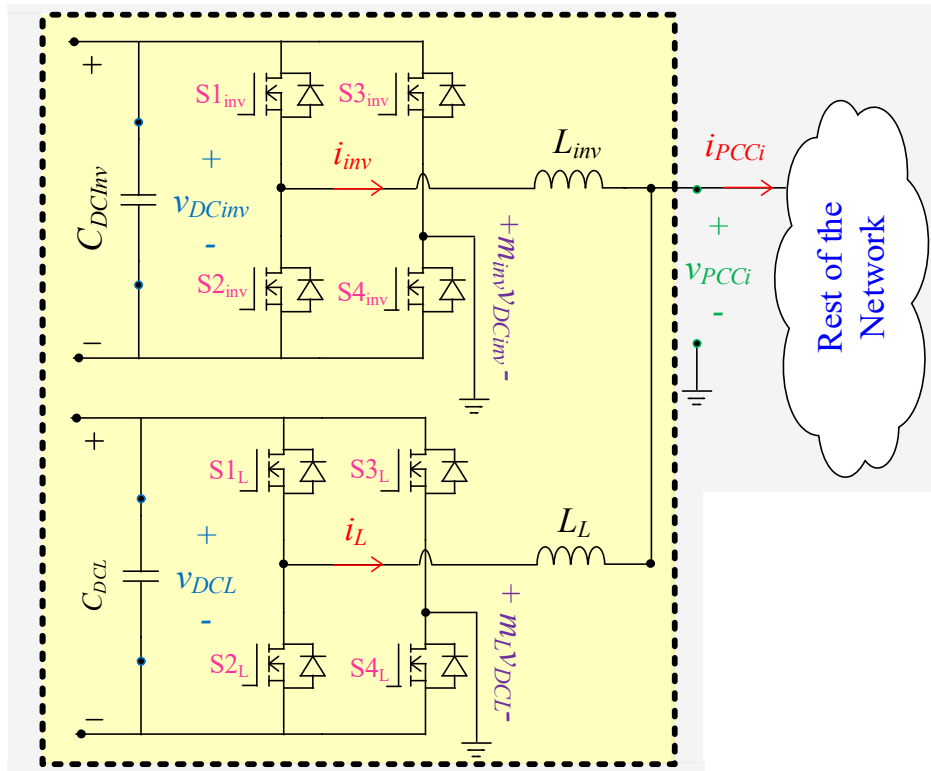


Figure 4.2. Futuristic PEDG illustrating the i^{th} PCC bus equivalent: switch level equivalent.

PEDG. This is due to its anticipated resistive nature as being a network situated at the grid-edge having a low X/R ratio. This resistive nature creates strong coupling between active power and voltage. Reactive power control will be irrelevant for resolving voltage stability problem in the futuristic PEDG. As the reactive power will be decoupled from the voltage. As well, this chapter revisits the mathematical derivation of how the voltage stability bound at PCC bus i is impacted by its self-set-point change. Then, it extends this derivation to how an adjacent PCC bus j set-point change impacts the voltage stability bound at PCC bus i . This chapter clear misconception witnessed in the literature about reactive power control importance in grid-edge networks such as the futuristic PEDG.

4.1.2. Impact of Prosumers Grid-Feeding Inverter's Active Power Set-Point Change on the Local PCC Voltage

The network in Figure 4.1 is reduced to two buses at the perception of the i^{th} PCC bus, where the i^{th} PCC bus perceives the rest of the network from its PCC bus terminals as a Thevenin impedance in-series with a Thevenin voltage source as Figure 4.2 and Figure 4.3. This Thevenin voltage source (\vec{v}_{Thi}) is a function of the rest of the network prosumers' set-points excluding the i^{th} PCC bus prosumer set-point. The relation between the Thevenin voltage (\vec{v}_{Thi}) and the PCC bus voltage for the i^{th} bus (\vec{v}_{PCCi}) (see Figure 4.2 and Figure 4.3) is given by,

$$\vec{v}_{PCCi} = R_{Thi} \vec{i}_{PCCi} + \vec{v}_{Thi} \quad (4.1)$$

where R_{Thi} is the Thevenin resistance, ω is the angular frequency of the network, and \vec{i}_{PCCi} is the current injected at the i^{th} PCC bus. The imaginary-part of the Thevenin impedance (Z_{Thi}) in Figure 4.3 is ignore because the network is resistive. Furthermore, in (4.1) the i^{th} PCC bus voltage is given by,

$$\vec{v}_{PCCi} = |V_{PCCi}| \angle \delta_{PCCi} = A_i + jB_i \quad (4.2)$$

Likewise, the rest of the network voltage is given by,

$$\vec{v}_{Thi} = |V_{Thi}| \angle \delta_{Thi} = |V_{Thi}| \cos(\delta_{Thi}) + j |V_{Thi}| \sin(\delta_{Thi}) \quad (4.3)$$

To relate the PCC bus voltage (\vec{v}_{PCCi}) to the set-points; the current (\vec{i}_{PCCi}) can be determined by,

$$\vec{i}_{PCCi} = (P_i^{Ref} - P_{Li}) \vec{v}_{PCCi}^*{}^{-1} = P_{PCCi} \vec{v}_{PCCi}^*{}^{-1} \quad (4.4)$$

Where \vec{v}_{PCCi}^* is the complex conjugate of \vec{v}_{PCCi} , P_i^{Ref} is the active power set-point of the i th inverter, P_{Li} is the active power load at the i th PCC bus, and P_{PCCi} is the net injected active power at the i th PCC bus. Merging (4.4) and (4.1) results in,

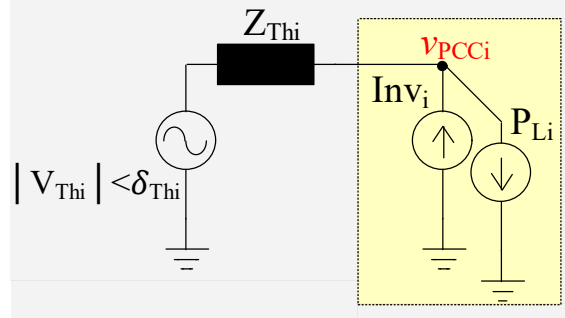


Figure 4.3. Futuristic PEDG illustrating the i^{th} PCC bus equivalent: reduced circuit representation.

$$\vec{v}_{PCCi} = R_{Thi} P_{PCCi} \vec{v}_{PCCi}^*{}^{-1} + \vec{v}_{Thi} \quad (4.5)$$

Then, multiplying (4.5) by the complex conjugate of \vec{v}_{PCCi} results in,

$$\frac{\vec{v}_{PCCi} \vec{v}_{PCCi}^*}{A_i^2 + B_i^2} = \frac{R_{Thi} P_{PCCi} + \vec{v}_{Thi} \vec{v}_{PCCi}^*}{R_{Thi} P_{PCCi} + |V_{Thi}| (A_i \cos(\delta_{Thi}) - B_i \sin(\delta_{Thi})) + j(|V_{Thi}| (A_i \sin(\delta_{Thi}) + B_i \cos(\delta_{Thi})))} \quad (4.6)$$

Then, from (4.6) the solution for A_i and B_i are given in (4.7) and (4.8),

$$A_i = \frac{|V_{Thi}| \left(1 + \sqrt{1 + 4 |V_{Thi}|^{-1} R_{Thi} P_{PCCi}} \right) \cos(\delta_{Thi})}{2} \quad (4.7)$$

$$B_i = \frac{|V_{Thi}| \left(1 + \sqrt{1 + 4 |V_{Thi}|^{-1} R_{Thi} P_{PCCi}} \right) \sin(\delta_{Thi})}{2} \quad (4.8)$$

now, $|\vec{v}_{PCCi}| = \sqrt{A_i^2 + B_i^2}$ describes the impact of the i^{th} of grid-feeding inverter set-point of the local i^{th} target PCC bus for a given Thevenin representation of the rest of network in (4.9).

$$|\vec{v}_{PCCi}| = \frac{|V_{Thi}|}{2} + \sqrt{\frac{|V_{Thi}|^2}{4} + R_{Thi} P_{PCCi}} \quad (4.9)$$

Active power set-points in (4.9) that satisfies the range $0.9V_g \leq |\vec{v}_{PCCi}| \leq 1.1V_g$ are defined as the allowable operation set-points. Note that, the assumption of narrow-band phasor withholds in this analysis as there is a timescale separation between the primary control in Figure 4.4 and the change in dispatched set-points [140]. The crucial deduction from (4.9) is that active power reversal at local PCC buses in grid-edge networks results in overvoltage and vice versa (see the graphical example in Figure 4.5). Therefore, an

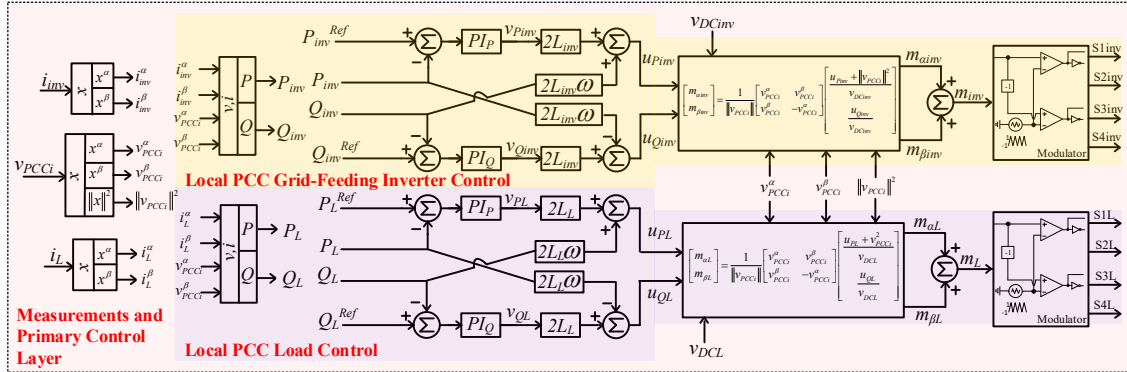


Figure 4.4. Futuristic PEDG illustrating the i^{th} PCC bus equivalent: controller representation for the i^{th} local PCC bus.

alternative active power cooperative control must be utilized to improve the network voltage quality and stability instead of a reactive power cooperative control. However, regarding the active power availability in the network, in the futuristic PEDG active power availability will not be a problem as in the future it is anticipated the battery technology will be mature enough enabling rich deployment of batteries by prosumers at the grid-edge [141].

4.1.3. Voltage Stability Bound Derivations

4.1.3.1. Voltage stability bound at PCC bus i with respect to change in self-set-point

The stability bound found from a $P(V)$ curve at PCC bus i by change in its self-set-point is described here for a given Thevenin representation. Consider (4.10),

$$|\bar{v}_{PCCi}| = \frac{|V_{Thi}|}{2} + \sqrt{\frac{|V_{Thi}|^2}{4} + R_{Thi} P_{PCCi}} \quad (4.10)$$

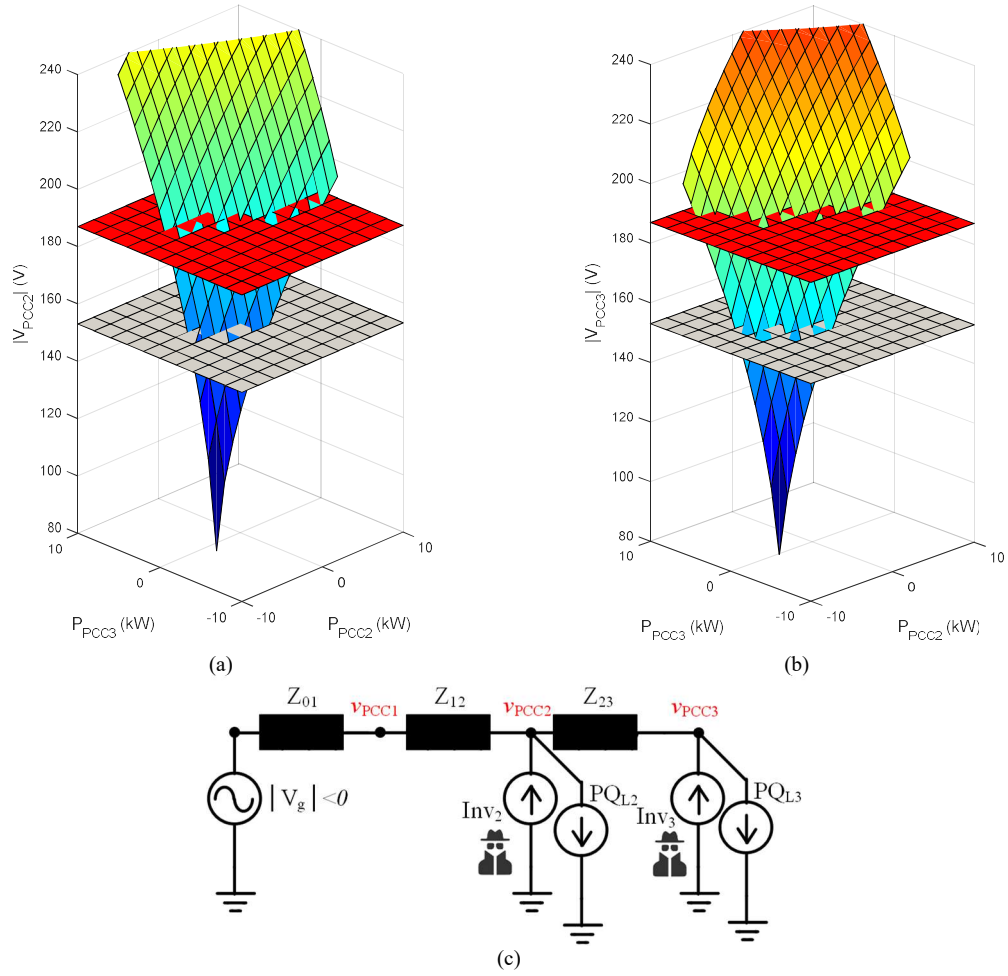


Figure 4.5. Impact of active power reversal on grid-edge network voltage: (a) internal PCC bus 2, internal PCC bus 3, PEDG network example.

the stability bound is found at a specific self-set-point (P_{PCCi}) when the condition (4.11) happens.

$$\left. \frac{\partial |\bar{v}_{PCCi}|}{\partial P_{PCCi}} \right| = \infty \quad (4.11)$$

Then, (4.11) is expanded to (4.12).

$$\left. \frac{\partial |\bar{v}_{PCCi}|}{\partial P_{PCCi}} \right| = \frac{R_{Thi}}{2\sqrt{\frac{|V_{Thi}|^2}{4} + R_{Thi}P_{PCCi}}} = \infty \quad (4.12)$$

This means that the stability bound at bus i due to change at its self-set-point (P_{PCCi}) is according to the following inequality shown in (4.13).

$$P_{PCCi} \geq -\frac{|V_{Thi}|^2}{4R_{Thi}}, \therefore P_{Stability\ Bound} = -\frac{|V_{Thi}|^2}{4R_{Thi}} \quad (4.13)$$

Now, the stability bound of PCC bus i with respect to variation of the active power set-point at an adjacent bus j (P_{PCCj}) can be deduced by the same reasoning in the next subsection.

4.1.3.2. Voltage stability bound at PCC bus i with respect to change in j^{th} PCC bus set-point

Following the analogy of the previous subsection, the stability bound of PCC bus i with respect to change of the active power set-point at adjacent bus j (P_{PCCj}) is direct resultant form (4.14).

$$\frac{\partial |\bar{v}_{PCCi}|}{\partial P_{PCCj}} = \infty \quad \text{or} \quad \frac{\partial P_{PCCj}}{\partial |\bar{v}_{PCCi}|} = 0 \quad (4.14)$$

Equation (4.14) is expanded into (4.15).

$$\frac{\partial |\bar{v}_{PCCi}|}{\partial P_{PCCj}} = \frac{1}{2} \frac{\partial |V_{Thi}|}{\partial P_{PCCj}} + \frac{|V_{Thi}| \frac{\partial |V_{Thi}|}{\partial P_{PCCj}}}{4\sqrt{\frac{|V_{Thi}|^2}{4} + R_{Thi}P_{PCCi}}} = \infty \quad (4.15)$$

Solving (4.15) is not trivial with methodologies that have been discussed previously in the literature so far. This is because there is no closed-form solution for Thevenin voltage and thereby there is no way to express the derivative of the i^{th} PCC bus voltage with respect to the j^{th} PCC bus active power set-point. Nevertheless, in this chapter for a given network that is shown in Figure 4.5 for instance, a derivation concept is provided for the Thevenin voltage expression as function of nearby buses excluding self-set point. This method of

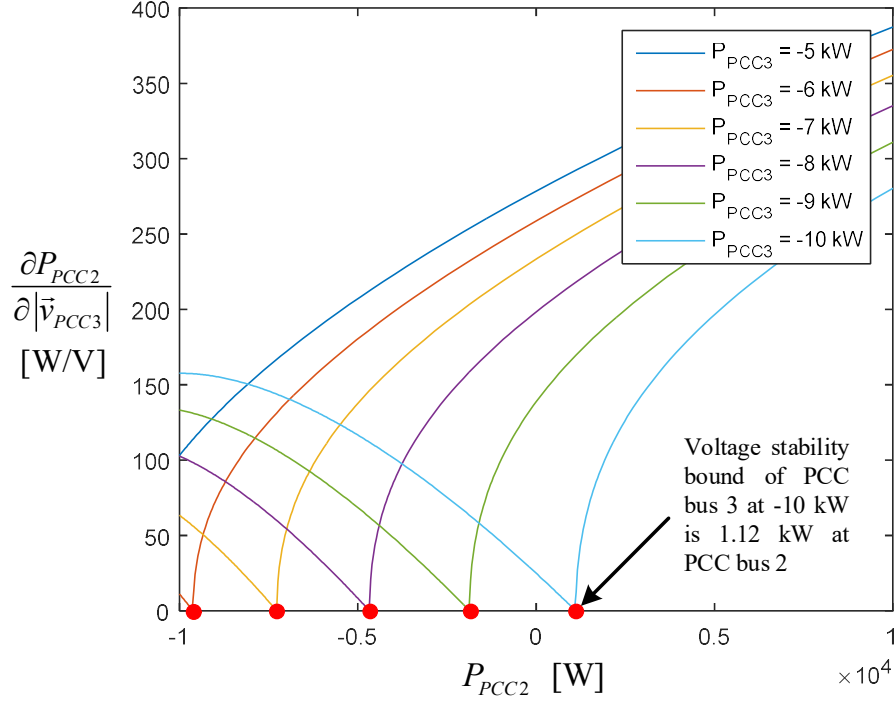


Figure 4.6. Stability bound prediction by observing the value of $\partial P_{PCC2}/\partial ||v_{PCC3}||$.

derivation is presented by the authors of this dissertation in the previous publication [142].

The internal PCC buses in Figure 4.5(c) are described by the manifolds (4.16) plotted in Figure 4.5(a) and (4.17) plotted in Figure 4.5(b).

$$|\bar{v}_{PCC2}| = \frac{|V_{Th2}|}{2} + \sqrt{\frac{|V_{Th2}|^2}{4} + R_{Th2} P_{PCC2}} \quad (4.16)$$

$$\text{where } |V_{Th2}| = \left(\sqrt{\frac{|V_g|^2}{4} + R_{Th3} P_{PCC3}} - \frac{|V_g|}{2} \right) R_{Th2} R_{Th3}^{-1} + |V_g|$$

$$|\bar{v}_{PCC3}| = \frac{|V_{Th3}|}{2} + \sqrt{\frac{|V_{Th3}|^2}{4} + R_{Th3} P_{PCC3}} \quad (4.17)$$

$$\text{where } |V_{Th3}| = \sqrt{\frac{|V_g|^2}{4} + R_{Th2} P_{PCC2}} + \frac{|V_g|}{2}$$

Hence, the voltage stability bound can be found in closed-form as in (4.18) for bus 3 with respect to bus 2 of Figure 4.5(c) network.

$$\frac{\partial |\vec{v}_{PCC3}|}{\partial P_{PCC2}} = \frac{1}{2} \frac{\partial |V_{Th3}|}{\partial P_{PCC2}} \left(1 + \frac{|V_{Th3}|}{2\sqrt{\frac{|V_{Th3}|^2}{4} + R_{Th3}P_{PCC3}}} \right) = \infty \quad (4.18)$$

$$\text{where } |V_{Th3}| = \sqrt{\frac{|V_g|^2}{4} + R_{Th2}P_{PCC2}} + \frac{|V_g|}{2}, \quad \frac{\partial |V_{Th3}|}{\partial P_{PCC2}} = \frac{R_{Th2}}{2\sqrt{\frac{|V_g|^2}{4} + R_{Th2}P_{PCC2}}}$$

The closed-form solution of (4.18) is expressed in simplified form as (4.19),

$$\frac{\partial |\vec{v}_{PCC3}|}{\partial P_{PCC2}} = \frac{\Gamma}{\Phi} \quad (4.19)$$

where

$$\Gamma = \frac{R_{Th2}}{4} \left(\frac{\left(\frac{|V_g|}{2} + \sqrt{R_{Th2}P_{PCC2} + \frac{|V_g|^2}{4}} \right)}{2} + \sqrt{P_{PCC3}R_{Th3} + \frac{\left(0.5|V_g| + \sqrt{R_{Th2}P_{PCC2} + \frac{|V_g|^2}{4}} \right)^2}{4}} \right)$$

$$\Phi = \frac{|V_g|^2 \sqrt{R_{Th2}P_{PCC2} + \frac{|V_g|^2}{4}}}{8} + \frac{|V_g|^3}{16} + \frac{R_{Th2}|V_g|P_{PCC2}}{4} + \frac{R_{Th2}P_{PCC2} \sqrt{R_{Th2}P_{PCC2} + \frac{|V_g|^2}{4}}}{4} + P_{PCC3}R_{Th3} \sqrt{R_{Th2}P_{PCC2} + \frac{|V_g|^2}{4}}$$

now, P_{PCC2} value that makes $\partial P_{PCC2} / \partial \vec{v}_{PCC3}$ equal to zero in (4.19) is the voltage stability bound for bus 3 with respect to active power change at bus 2 of Figure 4.5(c) network. Unfortunately, this involves polynomial with an order higher than 5, finding the deterministic roots of this polynomial is not feasible. This is proved by the fundamental theorem of Galois [143]. Galois theory provides a connection between field theory and group theory. This connection allows reducing certain problems (i.e., polynomial roots finding) in field theory to group theory such as permutation group of their roots. By Galois theory, it was proven that for a polynomial roots' to be solvable by radicals and the main

operations addition, subtraction, division, and multiplications; the order of the polynomial must be less than 5 because its group of symmetries is solvable. Alternatively, instead of seeking for P_{PCC2} that makes the $\partial P_{PCC2}/\partial \vec{v}_{PCC3}$ equal to zero, the imaginary part of this derivative can be plotted by spanning the active power set-point (P_{PCC2}). The voltage stability bound can be predicted by observing a non-zero imaginary part existence. The initial active power set-point where the imaginary value observed in $\partial P_{PCC2}/\partial \vec{v}_{PCC3}$ is the voltage stability bound. This can be seen in Figure 4.6 and Figure 4.7 for the network example Figure 4.5(c). In more details, when $P_{PCC3} = -7$ kW, the voltage stability bound of PCC bus 3 is -7.5 kW. Meaning that, PCC bus 2 can sink maximumly 7.5 kW before PCC bus 3 reaches to instability. Note that, observing the imaginary part in Figure 4.7 shows that after the voltage stability bound the function has a non-zero value but before hitting the voltage stability bound the imaginary part was always zero. This gives an advantage to check whether the set-point will produce an instable voltage situation just by looking at the imaginary part of this derivative.

The same concept is applied to study PCC bus 2 with respect to set-point change at PCC bus 3 as in (4.20).

$$\frac{\partial |\vec{v}_{PCC2}|}{\partial P_{PCC3}} = \frac{1}{2} \frac{\partial |V_{Th2}|}{\partial P_{PCC3}} \left(1 + \frac{|V_{Th2}|}{2\sqrt{\frac{|V_{Th2}|^2}{4} + R_{Th2} P_{PCC2}}} \right) = \infty \quad (4.20)$$

where $|V_{Th2}| = \left(\sqrt{\frac{|V_g|^2}{4} + R_{Th3} P_{PCC3}} - \frac{|V_g|}{2} \right) R_{Th2} R_{Th3}^{-1} + |V_g|$, $\frac{\partial |V_{Th2}|}{\partial P_{PCC3}} = \frac{R_{Th2}}{2\sqrt{\frac{|V_g|^2}{4} + R_{Th3} P_{PCC3}}}$

The closed-form solution of (4.20) is expressed in (4.21).

$$\frac{\partial |\vec{v}_{PCC2}|}{\partial P_{PCC3}} = \frac{\Pi}{\Lambda} \quad (4.21)$$

where

$$\Pi = \frac{R_{Th_2}}{4} \left(\frac{\left(R_{Th_2} \left(\frac{|V_g|^2}{2} + \sqrt{\frac{|V_g|^2}{4} + R_{Th_3} P_{PCC3}} \right) + |V_g| R_{Th_3} \right)}{2} + \frac{\left(R_{Th_2} \left(\frac{|V_g|^2}{2} + \sqrt{\frac{|V_g|^2}{4} + R_{Th_3} P_{PCC3}} \right) + |V_g| R_{Th_3} \right)^2}{4} \right) \sqrt{\frac{R_{Th_2} R_{Th_3}^2 P_{PCC2} + \left(R_{Th_2} \left(\frac{|V_g|^2}{2} + \sqrt{\frac{|V_g|^2}{4} + R_{Th_3} P_{PCC3}} \right) + |V_g| R_{Th_3} \right)^2}{4}}$$

$$\Lambda = -\frac{R_{Th_2}^2 |V_g|^4}{16} - \frac{R_{Th_2}^2 |V_g|^2 R_{Th_3} P_{PCC3}}{4} + \frac{R_{Th_2}^2 |V_g|^4 \sqrt{\frac{|V_g|^2}{4} + R_{Th_3} P_{PCC3}}}{16} + R_{Th_2} R_{Th_3}^2 P_{PCC2} \sqrt{\frac{|V_g|^2}{4} + R_{Th_3} P_{PCC3}}$$

$$- \frac{R_{Th_2} |V_g|^3 R_{Th_3} \sqrt{\frac{|V_g|^2}{4} + R_{Th_3} P_{PCC3}}}{4} + \frac{R_{Th_2} |V_g|^3 R_{Th_3}}{8} + \frac{R_{Th_2} |V_g| R_{Th_3}^2 P_{PCC3}}{2} +$$

$$\frac{|V_g|^2 R_{Th_3}^2 \sqrt{\frac{|V_g|^2}{4} + R_{Th_3} P_{PCC3}}}{4} + \frac{R_{Th_2}^2 |V_g|^2 \sqrt{\frac{|V_g|^2}{4} + R_{Th_3} P_{PCC3}}}{16} + \frac{R_{Th_2}^2 R_{Th_3} P_{PCC3} \sqrt{\frac{|V_g|^2}{4} + R_{Th_3} P_{PCC3}}}{4}$$

now, P_{PCC3} value that makes $\partial P_{PCC3} / \partial \vec{v}_{PCC2}$ equal to zero in (4.21) is the voltage stability bound for bus 2 with respect to active power change at bus 3 in Figure 4.5(c) network. Unfortunately, this involves polynomial with an order higher than 5. Therefore, no closed-form solution by radicals can be determined according to the fundamental theorem of Galois [143]. As a substitute of seeking for P_{PCC3} value that makes the $\partial P_{PCC3} / \partial \vec{v}_{PCC2}$ equal to zero, the imaginary part of this derivative can be plotted by spanning the active power set-point (P_{PCC3}). The stability bound can be predicted by

observing a non-zero imaginary part existence. The initial set-point where the imaginary value observed in $\partial P_{PCC3}/\partial \vec{v}_{PCC2}$ is the voltage stability bound.

Table 9. Individual grid-feeding inverter ratings

Parameter	Symbol	Value
Rated Power	S_{Rated}	20 kVA
Switching Frequency	f_{sw}	10 kHz
Nominal Grid Frequency	ω	376.8 rad/s
Voltage Peak	V_g	171 V
DC-Bus Voltage	V_{DCi}	420 V
DC-link Capacitor	C_{DCi}	2 mF
Filter Inductor	$L_{inv} = L_L$	0.5 mH
Filter Inductor Resistance	$R_{inv} = R_L$	0.05 Ω
Thevenin Resistance PCC bus 1	R_{Th1}	0.25 Ω
Thevenin Resistance PCC bus 2	R_{Th2}	0.5 Ω
Thevenin Resistance PCC bus 3	R_{Th3}	0.75 Ω
Line Impedances	Z_{ij}	0.25 Ω

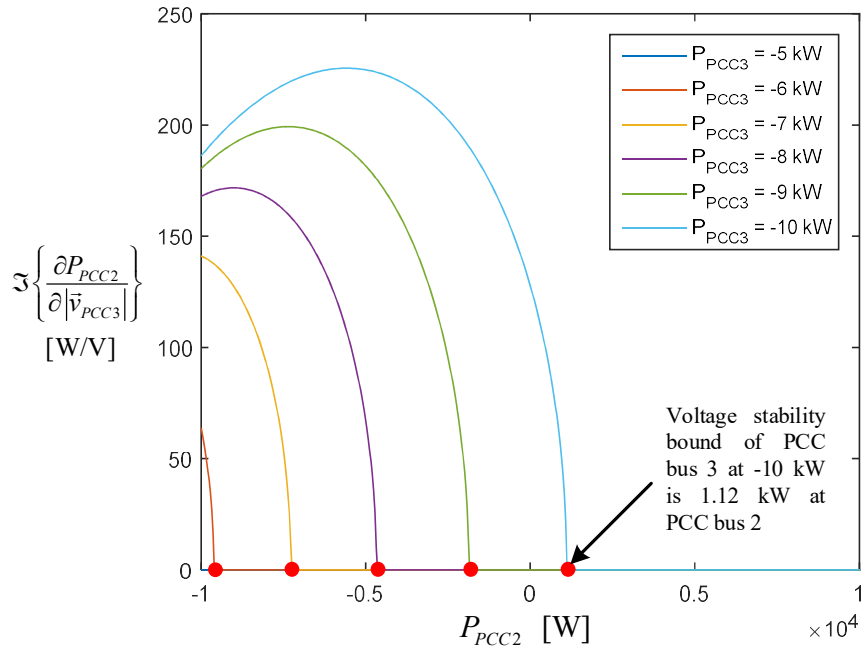


Figure 4.7. Stability bound prediction by observing the imaginary part of $\partial P_{PCC2}/\partial \vec{v}_{PCC3}$.

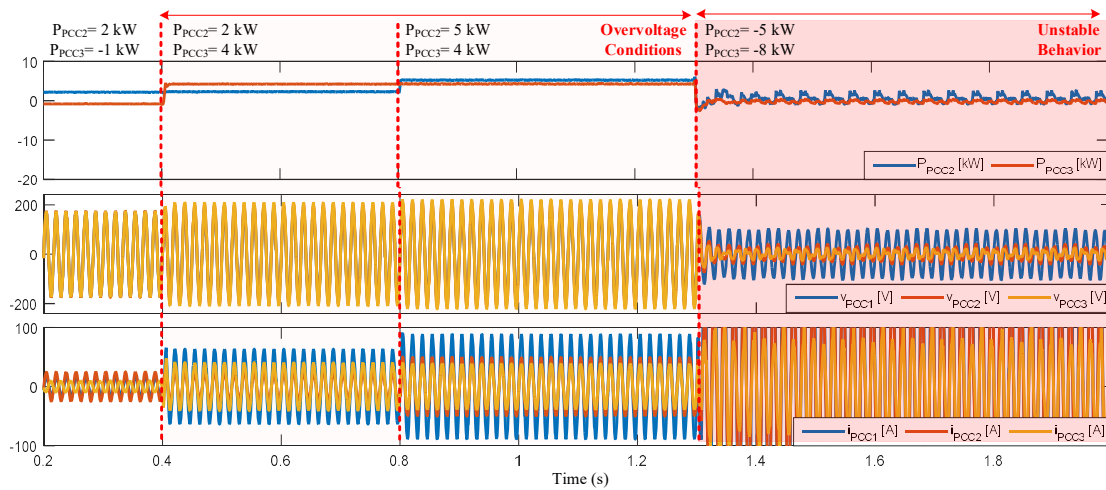


Figure 4.8. Validation of the derived mathematical voltage stability bounds

4.1.4. Voltage Stability Bound Validation

The mathematical derivations provided in this chapter are verified by the simulation scenario that is depicted in Figure 4.8. The grid-feeding inverters of this scenario are according to Table 9 ratings. Specifically, Figure 4.8 scenario is representing how active power set-point change impacts the local PCC bus voltages stability. In this scenario, initially P_{PCC2} is at 2 kW and P_{PCC3} is at -1 kW. These initial set-points are within the voltage limit specified by the standard (see Figure 4.8 before time instant 0.4 s). Then, after time instant 0.4 s the consumer at PCC₃ altered their set-points to 4 kW (see Figure 4.8 after time instant 0.4 s). This new set-point causes overvoltage in the network. After that, the consumer at PCC₂ cause further overvoltage in the network by increasing the set-point to 5 kW (see Figure 4.8 after time instant 0.8 s). Finally, the consumers cause more severe voltage violations by inducing voltage instability at PCC₂ and PCC₃ through requesting the set-point -5 kW at PCC₂ and -8 kW at PCC₃ (see Figure 4.8 after time instant 1.3 s). This

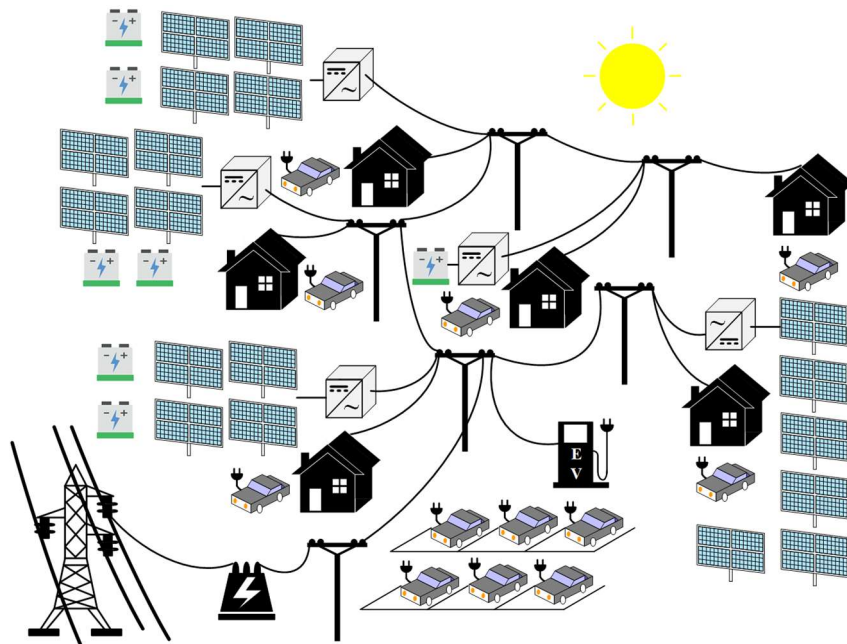


Figure 4.9. Virtual power plant concept as a power electronics-dominated grid.

verifies the voltage stability bound predicted theoretically in Figure 4.7. Particularly, evidence on the PCC bus 3 voltage stability bound at - 8 kW that is - 4.9 kW from PCC bus 2 (see in Figure 4.7 the purple curve initial crossing of the x-axis). Additionally, this scenario shows the strong coupling between voltage and active power in the futuristic PEDG and not with reactive power as assumed in most of the recent articles.

4.2. Online Voltage Stability Identification from Local PCC terminals

4.2.1. Online Voltage Stability Linkage to Cyber Security

To cope up with the energy transition paradigm, more power electronics driven renewable power generation are anticipated to be integrated at the low voltage side of the grid [131, 144]. The grid-following inverters are one of these power electronics driven

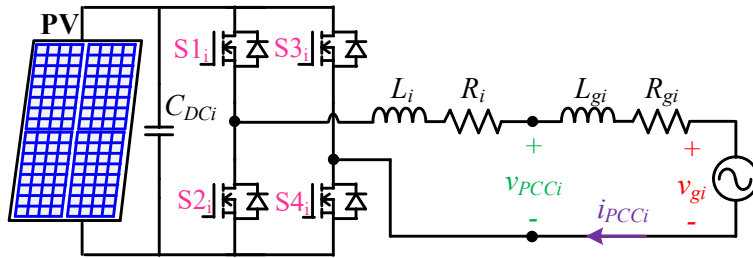


Figure 4.10. Virtual power plant cyber-layer from the perspective of i^{th} prosumer point of common coupling bus.

technologies that will be adopted extensively for interfacing photovoltaic, wind, and energy storage [15]. Furthermore, the grid-following inverter is perceived by the upstream network cyber-layer's slow time scale as a current source [145, 146]. Its capability is limited to supplying/absorbing current into/from their point of common coupling bus without considering upstream network constrains and requirements [147]. Hence, the upstream network operators are unobservable to grid-following inverter and vice-versa. To improve the observability for upstream network operators, the concept of the virtual power plant was introduced. The virtual power plant is a collection of different size and type distributed energy resources that are aggregated into a single entity. This is to facilitate more sophisticated interconnection and integration between transmission and distribution system operators [133]. The virtual power plant concept is exemplified graphically in Figure 4.9.

Nevertheless, this futuristic power grid layout is anticipated to be susceptible to cyber-attacks [148-151]. As more portion of the total generation will rely on power electronics driven entities that are functioning outside the realm of the conventional power plant authority. For example, cyber-attackers might take control over the virtual power plant cyber-layer. Meaning that, the operation set-points that are requested from the individual

prosumers in the virtual power plant network are compromised. Consequently, it is conceivable that the cyber-attacker intends to violate the stability boundary of the network with set-points manipulation. So, this chapter is proposing a technique to enable prosumer to perform real-time stability boundary identification from their point of common coupling bus. In other words, each prosumer is able observe the virtual power plant cyber-layer. This is crucial to improve the cybersecurity aspect of the virtual power plant. As this provides a secure alternative of the stability boundary that are communicated to the prosumers by the virtual power plant cyber-layer. This stability boundary is identified conventionally by performing power flow and time domain simulations at the virtual power plant cyber-layer. Which might be compromised in case of a cyber-attacker taking over the virtual power plant cyber-layer. In this chapter, a technique is presented that any specific prosumer can observe the grid voltage seen at its point of common coupling. Then, this observation is utilized in real-time in constructing the $P - V$ curve or $P - Q - V$ surface to determine the stability boundary and the impact of their active and reactive power injection/absorption. Moreover, the proposed observation method is based on correlating the variation in the active and reactive power measurements at the prosumer point of common coupling bus to the grid voltage seen at this bus. Specifically, through solving two simultaneous differential equations.

4.2.2. Nearby Prosumers' Set-Points Variation Impact on a Specific Targeted i^{th} Prosumer Point of Common Coupling Bus Voltage

From the perspective of an i^{th} specific targeted prosumer point of common coupling bus in the virtual power plant depicted in Figure 4.9, the remaining nearby prosumers

information are embedded in the voltage source (\vec{v}_{gi}). Similarly, the network topology and connection matrix information are embedded in the impedance $Z_{gi} = R_{gi} + j\omega L_{gi}$ (see Figure 4.10). Therefore, the targeted prosumer point of common coupling bus voltage (\vec{v}_{PCCi}) is denoted by (4.22).

$$\begin{aligned}\vec{v}_{PCCi} &= (R_{gi} + j\omega L_{gi})\vec{i}_{PCCi} + \vec{v}_{gi} = \|V_{PCCi}\|_2 \angle \delta_{PCCi} = \mu_i + j\eta_i \\ \vec{v}_{gi} &= f(P_{PCC(i+1)}, Q_{PCC(i+1)}, \dots, P_{PCCn}, Q_{PCCn}) \\ \vec{v}_{gi} &= \|V_{gi}\|_2 \angle \delta_{gi} = \|V_{gi}\|_2 \cos(\delta_{gi}) + j\|V_{gi}\|_2 \sin(\delta_{gi})\end{aligned}\quad (4.22)$$

where \vec{i}_{PCCi} is the net current at the i^{th} prosumer point of common coupling bus. \vec{v}_{PCCi} is correlated to the targeted prosumer operation set-points through the point of common coupling current (\vec{i}_{PCCi}) as in (4.23)

$$\vec{i}_{PCCi} = (P_{PCCi} - jQ_{PCCi})\vec{v}_{PCCi}^*{}^{-1} \quad (4.23)$$

where P_{PCCi} is the net active power at the i^{th} prosumer point of common coupling bus, and Q_{PCCi} is the net reactive power at the i^{th} prosumer point of common coupling bus. Merging (4.22) and (4.23) consequences in (4.24).

$$\vec{v}_{PCCi} = (R_{gi} + j\omega L_{gi})(P_{PCCi} - jQ_{PCCi})\vec{v}_{PCCi}^*{}^{-1} + \vec{v}_{gi} \quad (4.24)$$

Equation (3) is rearranged to (4) considering (1).

$$\begin{aligned}\mu_i^2 + \eta_i^2 &= R_{gi}P_{PCCi} + \omega L_{gi}Q_{PCCi} + \|V_{gi}\|_2 (\mu_i \cos(\delta_{gi}) + \eta_i \sin(\delta_{gi})) \\ &+ j(\omega L_{gi}P_{PCCi} - R_{gi}Q_{PCCi} + \|V_{gi}\|_2 (\mu_i \sin(\delta_{gi}) - \eta_i \cos(\delta_{gi})))\end{aligned}\quad (4.25)$$

It is straightforward to obtain a closed form solution for the parameters μ_i and η_i from (4.25) in (4.26) and (4.27).

$$\begin{aligned}\mu_i &= 0.5\|V_{gi}\|_2 \cos(\delta_{gi}) + (R_{gi}Q_{PCCi} - \omega L_{gi}P_{PCCi})\|V_{Thi}\|_2^{-1} \sin(\delta_{gi}) \\ &+ \sqrt{0.25\|V_{gi}\|_2^2 \cos^2(\delta_{gi}) + ((\omega L_{gi}P_{PCCi} - R_{gi}Q_{PCCi})\|V_{gi}\|_2^{-1})^2 \sin^2(\delta_{gi}) + (\omega L_{gi}P_{PCCi} - R_{gi}Q_{PCCi})\cos(\delta_{gi})\sin(\delta_{gi})} \\ &+ \sqrt{-((\omega L_{gi}P_{PCCi} - R_{gi}Q_{PCCi})\|V_{gi}\|_2^{-1})^2 + (R_{gi}P_{PCCi} + \omega L_{gi}Q_{PCCi})\cos^2(\delta_{gi})}\end{aligned}\quad (4.26)$$

$$\begin{aligned}
\eta_i &= (\omega L_{gi} P_{PCCi} - R_{gi} Q_{PCCi}) \|V_{gi}\|_2^{-1} \sec(\delta_{gi}) + 0.5 \|V_{gi}\|_2 \sin(\delta_{gi}) \\
&+ (R_{gi} Q_{PCCi} - \omega L_{gi} P_{PCCi}) \|V_{gi}\|_2^{-1} \sin(\delta_{gi}) \tan(\delta_{gi}) + \\
&\tan(\delta_{gi}) \sqrt{0.25 \|V_{gi}\|_2^2 \cos^2(\delta_{gi}) + \left((\omega L_{gi} P_{PCCi} - R_{gi} Q_{PCCi}) \|V_{gi}\|_2^{-1} \right)^2 \sin^2(\delta_{gi})} \\
&\quad + (\omega L_{gi} P_{PCCi} - R_{gi} Q_{PCCi}) \cos(\delta_{gi}) \sin(\delta_{gi}) - \left((\omega L_{gi} P_{PCCi} - R_{gi} Q_{PCCi}) \|V_{gi}\|_2^{-1} \right)^2 \\
&\quad + (R_{gi} P_{PCCi} + \omega L_{gi} Q_{PCCi}) \cos^2(\delta_{gi})}
\end{aligned} \tag{4.27}$$

This derivation concludes that the i^{th} prosumer point of common coupling bus voltage is not only impacted by the set-point of the i^{th} prosumer set-points, but the nearby prosumers also impact the i^{th} prosumer point of common coupling bus voltage. The information of the nearby prosumers is embedded in the grid voltage (\vec{v}_{gi}) that is seen from this specific targeted prosumer point of common coupling bus. Furthermore, for a given constant value of the grid voltage (\vec{v}_{gi}) the stability boundary is identified by either through $P - V$ curve or a $P - Q - V$ surface (i.e., $\|\vec{v}_{PCCi}\|_2$ which is the modulus constructed from (4.26) and (4.27) when $\partial \|\vec{v}_{PCCi}\|_2 / \partial P_{PCCi} = \infty$). In the virtual power plant, the information of this grid voltage seen from each prosumer point of common coupling bus is communicated after performing power flow and time domain simulations for equivalent circuit estimation at the cyber-layer. Which might be compromised in case of a cyber-attacker taking over the virtual power plant cyber-layer. In other words, the stability boundary that is verified and communicated by the virtual power plant cyber-layer is compromised. Therefore, the next section describes a method to estimate this grid voltage \vec{v}_{gi} that is seen by a targeted prosumer point of common coupling bus in real-time for the identification of the stability boundary in real-time.

4.2.3. Real-Time Observation of Nearby Prosumers' Set-Points Variation at a Targeted i^{th} Prosumer Point of Common Coupling Bus

The active and reactive power measured at the point of common coupling by a specific targeted i^{th} prosumer in a network is given in (4.28) and (4.29) [140].

$$P_{PCCi} = \frac{1}{2} i_{PCCi}^{\alpha} v_{PCCi}^{\alpha} + \frac{1}{2} i_{PCCi}^{\beta} v_{PCCi}^{\beta} \quad (4.28)$$

$$Q_{PCCi} = \frac{1}{2} i_{PCCi}^{\alpha} v_{PCCi}^{\beta} - \frac{1}{2} i_{PCCi}^{\beta} v_{PCCi}^{\alpha} \quad (4.29)$$

The gradients of the active and reactive power with respect to time vector is expressed in (4.30) and (4.31).

$$\frac{dP_{PCCi}}{dt} = \frac{1}{2} v_{PCCi}^{\alpha} \frac{di_{PCCi}^{\alpha}}{dt} + \frac{1}{2} i_{PCCi}^{\alpha} \frac{dv_{PCCi}^{\alpha}}{dt} + \frac{1}{2} v_{PCCi}^{\beta} \frac{di_{PCCi}^{\beta}}{dt} + \frac{1}{2} i_{PCCi}^{\beta} \frac{dv_{PCCi}^{\beta}}{dt} \quad (4.30)$$

$$\frac{dQ_{PCCi}}{dt} = \frac{1}{2} v_{PCCi}^{\beta} \frac{di_{PCCi}^{\alpha}}{dt} + \frac{1}{2} i_{PCCi}^{\alpha} \frac{dv_{PCCi}^{\beta}}{dt} - \frac{1}{2} v_{PCCi}^{\alpha} \frac{di_{PCCi}^{\beta}}{dt} - \frac{1}{2} i_{PCCi}^{\beta} \frac{dv_{PCCi}^{\alpha}}{dt} \quad (4.31)$$

Then, the chain rule is used to further simplify the gradients of the active and reactive power using the expression of the point of common coupling currents and voltages gradients with respect to time vector (i.e., the derivatives of i_{PCCi}^{α} , i_{PCCi}^{β} , v_{PCCi}^{α} , and v_{PCCi}^{β} that are given in (4.32)-(4.35))

$$\frac{di_{PCCi}^{\alpha}}{dt} = \frac{v_{PCCi}^{\alpha}}{L_{gi}} - \frac{v_{gi}^{\alpha}}{L_{gi}} - \frac{R_{gi} i_{PCCi}^{\alpha}}{L_{gi}} \quad (4.32)$$

$$\frac{di_{PCCi}^{\beta}}{dt} = \frac{v_{PCCi}^{\beta}}{L_{gi}} - \frac{v_{gi}^{\beta}}{L_{gi}} - \frac{R_{gi} i_{PCCi}^{\beta}}{L_{gi}} \quad (4.33)$$

$$\frac{dv_{PCCi}^{\alpha}}{dt} = -\omega v_{PCCi}^{\beta} \quad (4.34)$$

$$\frac{dv_{PCCi}^{\beta}}{dt} = \omega v_{PCCi}^{\alpha} \quad (4.35)$$

where L_{gi} is the inductance seen by the i^{th} prosumer from its point of common coupling, and R_{gi} is the resistance seen by the i^{th} prosumer from its point of common coupling, ω is the angular frequency of the network, and v_{gi}^{α} , and v_{gi}^{β} are the voltages that embed the

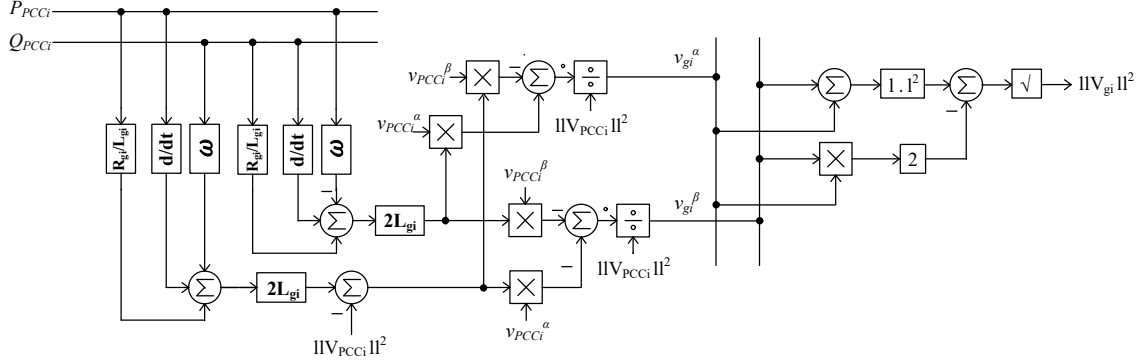


Figure 4.11. Online observation of the grid voltage (v_{gi}) seen at i^{th} prosumers point of common coupling bus for online real-time stability boundary identification.

information related to prosumers set-points. Furthermore, with combining (4.32)-(4.35) with (4.28) and (4.32)-(4.35) with (4.29), these two simultaneous ordinary differential equations are obtained (4.36) and (4.37).

$$\frac{dP_{PCCi}}{dt} = -\frac{R_{gi}P_{PCCi}}{L_{gi}} - \omega Q_{PCCi} + \frac{|v_{PCCi}^\alpha + v_{PCCi}^\beta|^2 - 2v_{PCCi}^\alpha v_{PCCi}^\beta - v_{PCCi}^\alpha v_{gi}^\alpha - v_{PCCi}^\beta v_{gi}^\beta}{2L_{gi}} \quad (4.36)$$

$$\frac{dQ_{PCCi}}{dt} = \omega P_{PCCi} - \frac{R_{gi}Q_{PCCi}}{L_{gi}} + \frac{v_{PCCi}^\alpha v_{gi}^\beta - v_{PCCi}^\beta v_{gi}^\alpha}{2L_{gi}} \quad (4.37)$$

These pair of differential equations are solvable by each prosumer in the virtual power plant to obtain a real-time solution for v_{gi}^α and v_{gi}^β , which embeds information related to real-time variation in other nearby prosumers set-points requested from the virtual power plant cyber-layer. Explicitly, the solution for v_{gi}^α and v_{gi}^β is in (4.38). This is shown graphically in Figure 4.11.

$$\begin{bmatrix} v_{gi}^\alpha \\ v_{gi}^\beta \end{bmatrix} = \frac{1}{\|v_{PCCi}\|_2^2} \begin{bmatrix} -v_{PCCi}^\alpha & -v_{PCCi}^\beta \\ -v_{PCCi}^\beta & v_{PCCi}^\alpha \end{bmatrix} \begin{bmatrix} 2L_{gi} \frac{dP_{PCCi}}{dt} + 2R_{gi}P_{PCCi} + 2L_{gi}\omega Q_{PCCi} - \|v_{PCCi}\|_2^2 \\ 2L_{gi} \frac{dQ_{PCCi}}{dt} - 2L_{gi}\omega P_{PCCi} + 2R_{gi}Q_{PCCi} \end{bmatrix} \quad (4.38)$$

$$\|v_{PCCi}\|_2^2 = |v_{PCCi}^\alpha + v_{PCCi}^\beta|^2 - 2v_{PCCi}^\alpha v_{PCCi}^\beta$$

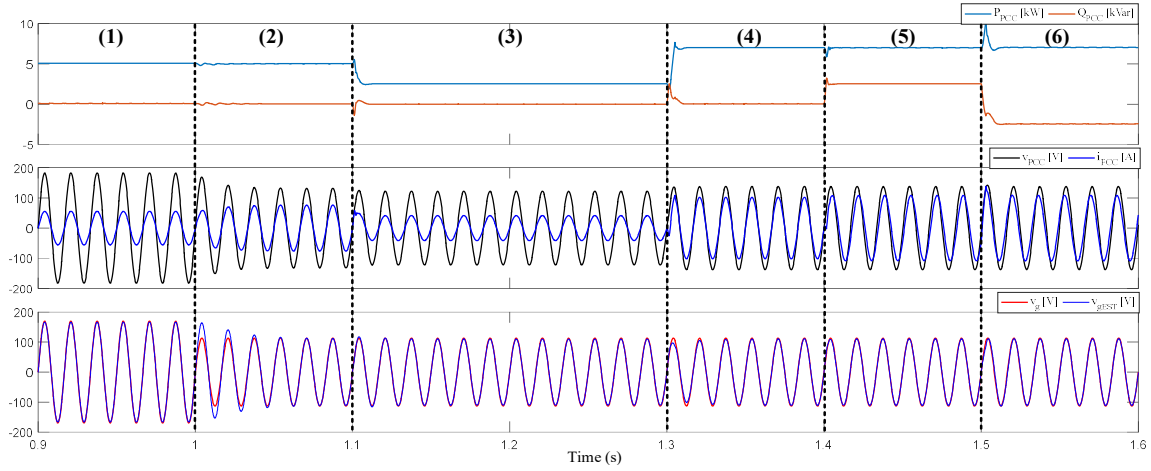


Figure 4.12. Scenario I: duration (1) 5 kW with 0 kVar, duration (2) grid voltage sag, duration (3) 2.5 kW with 0 kVar, duration (4) 8 kW with 0 kVar, duration (5) 8 kW with 2.5 kVar, and (6) 8 kW with -2.5 kVar.

Then, to construct the $P - V$ curve or the $P - Q - V$ surface with (4.26) and (4.27) for the targeted i^{th} prosumer point of common coupling bus the instantaneous voltage (v_{gi}) and the angle (δ_{gi}) are given in (4.39).

$$\|v_{gi}\|_2 = \sqrt{|v_{gi}^\alpha + v_{gi}^\beta|^2 - 2v_{gi}^\alpha v_{gi}^\beta}, \delta_{gi} = \tan^{-1}(v_{gi}^\beta / v_{gi}^\alpha) \quad (4.39)$$

4.2.4. On-Line Voltage Stability Bound Identification Validations

The theoretical analyses are verified by three scenarios. The first scenario is validating the proposed observation of the grid voltage (\vec{v}_{gi}) for a single prosumer grid-following inverter that is connected to a weak grid. This scenario includes grid voltage sag and the targeted prosumer point of common coupling bus set-points variations. In this scenario the stability boundary is identified in real-time with every variation estimated in the grid voltage (\vec{v}_{gi}).

The main purpose of the scenario I is to verify the accuracy of the observation. Scenario II is addressing the online real-time stability boundary identification with nearby prosumer point of common coupling bus set-points variations. Then, scenario III is a thirteen

prosumers point of common coupling bus virtual power plant. In this scenario, the targeted prosumer bus grid voltage is estimated for various random variation in the network operation set-points.

4.2.4.1. Scenario I: Targeted Prosumer Point of Common Coupling Bus Set-Point Variation and Grid Voltage Sag

The scenario I shown in Figure 4.12 validates the performance of the proposed real-time observation of the voltage v_g seen by a specific prosumer grid-following inverter with voltage sag and set-points variations. In this scenario, a single grid-following inverter is connected to a weak grid. Initially, the grid-following inverter before time instant 1 sec is

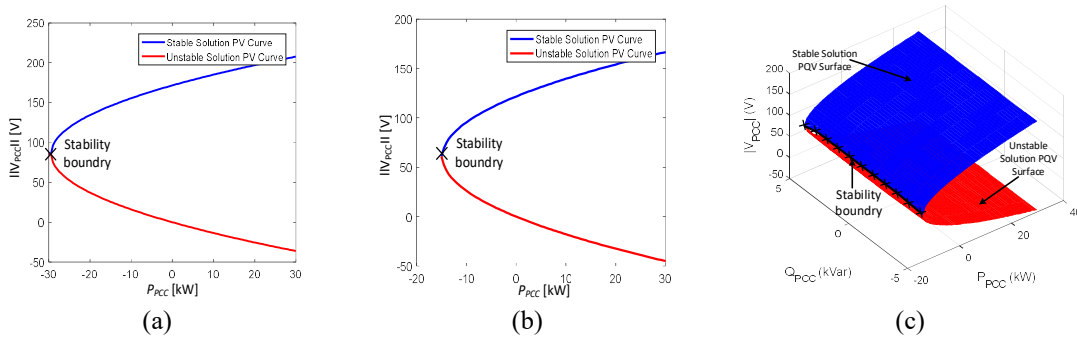


Figure 4.13. Scenario I online stability boundary identification: (a) stability boundary for duration (1), (b) stability boundary for durations (2), (3), (4), and (c) stability boundary for durations (5) and (6).

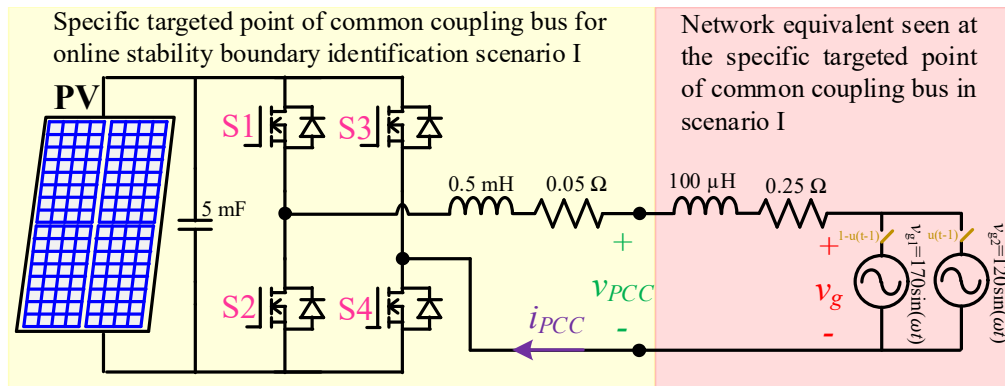


Figure 4.14. Scenario I real-time stability boundary identification, the simulation set-up showing the targeted prosumer point of common coupling bus.

operating with 5 kW at unity power factor (see Figure 4.12). At this duration, the proposed voltage observation is matching the measured voltage (see v_g vs. v_{gEST} in Figure 4.12). In addition, the real-time stability boundary is identified in Figure 4.13(a) using the proposed observation and spanning the range of active power set-points. Then after time instant 1 sec, a voltage sag occurs in v_g , The proposed real-time observation is able to predict this in less than one cycle of the grid voltage (see Figure 4.12 after time instant 1 sec). The consecutive durations (3), (4), (5), and (6) highlighted at Figure 4.12 are for testing the performance of the proposed real-time observation with active and reactive power set-point

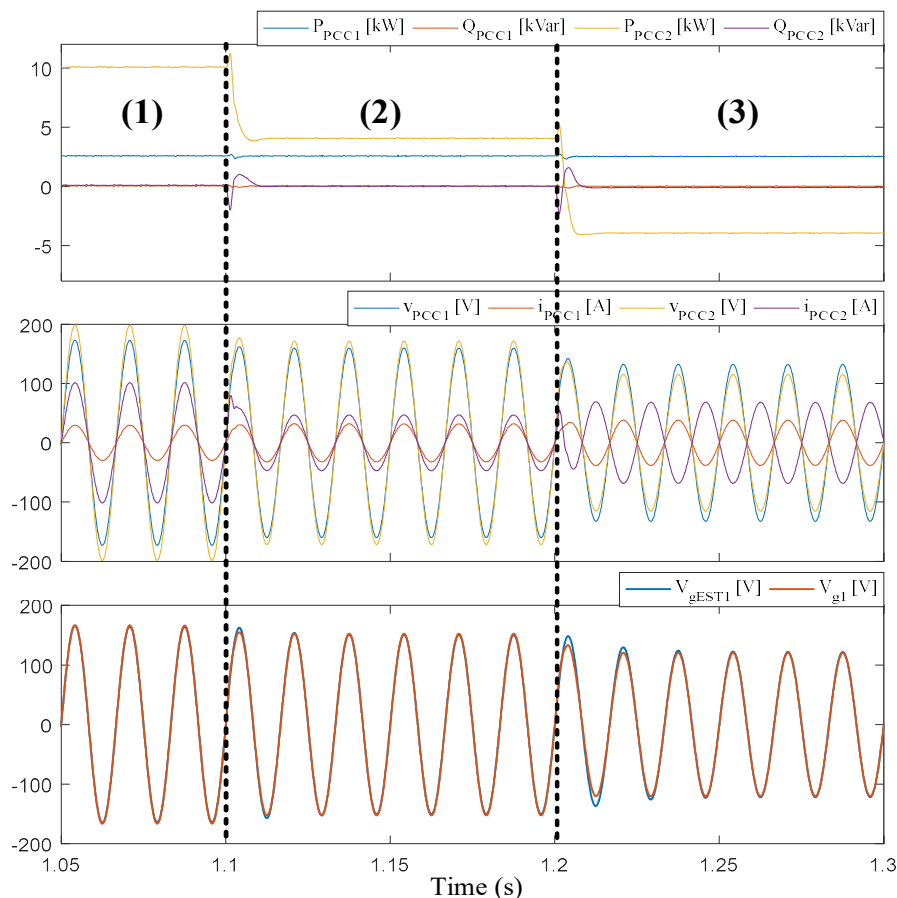


Figure 4.15. Scenario II targeted prosumer point of common coupling bus at 2.5 kW with 0 kVar: duration (1) nearby inverter 10 kW with 0 kVAR, duration (2) nearby inverter 5 kW with 0 kVAR, and duration (3) nearby inverter -5 kW with 0 kVar

dynamic change. As predicted theoretically that the voltage v_g is independent from the variation that occurs at the specific targeted prosumer point of common coupling bus itself. In fact, this observed voltage is function of other nearby prosumers' set-points. The real-time stability boundary identified after the voltage sag is depicted in Figure 4.13(b) and Figure 4.13(c). However, Figure 4.13(c) is considering the variation in the reactive power impact on the stability boundary. As seen in Figure 4.13(c) with reactive power inclusion the stability boundary identified is no longer a single point, it is a line in the three-

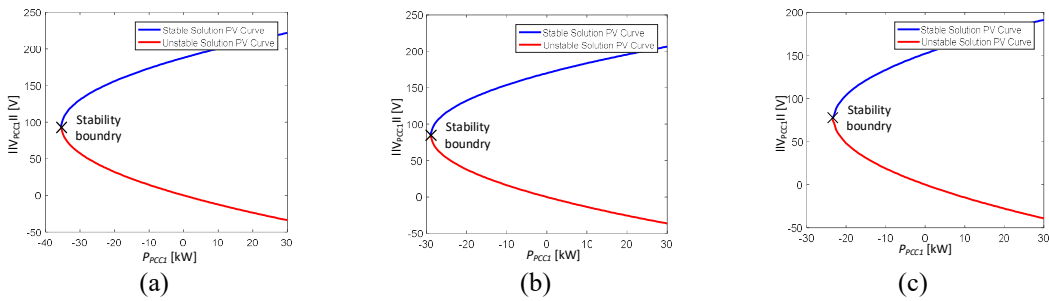


Figure 4.16. Scenario II real-time stability boundary identification: (a) stability boundary for duration (1), (b) stability boundary for duration (2), and (c) stability boundary for duration (3).

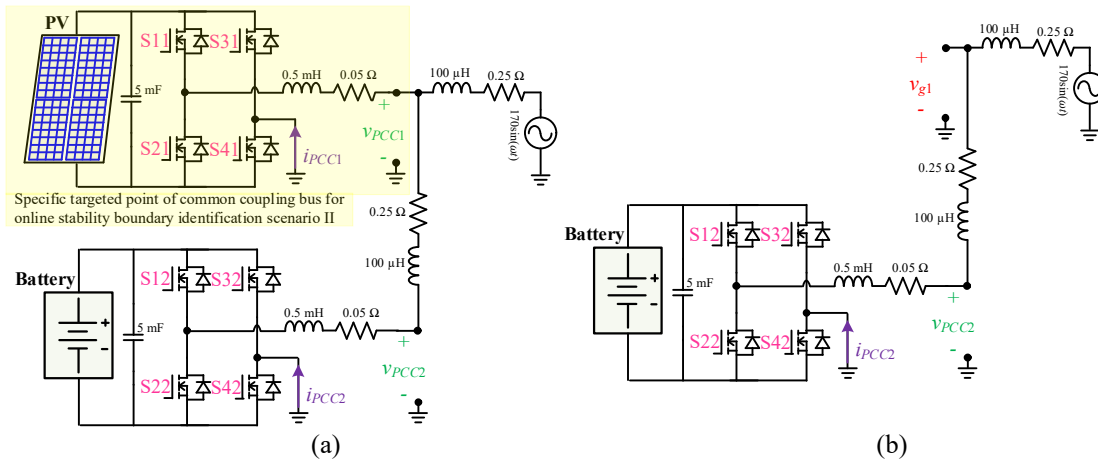


Figure 4.17. Scenario II real-time stability boundary identification: (a) simulation set-up showing the targeted prosumer point of common coupling bus, and (b) alternative simulation to validate the estimated value of v_{gl} .

dimensional space of the $P - Q - V$ surface. The simulation set-up and scenario are shown in Figure 4.14.

4.2.4.2. Scenario II: Nearby Prosumers Set-Point Variations Impact on a Targeted Prosumer Point of Common Coupling Bus.

Scenario II depicted in Figure 4.15 validates the proposed real-time observation of the voltage v_{g1} by dynamic variation due to a nearby prosumer grid-following inverter at point

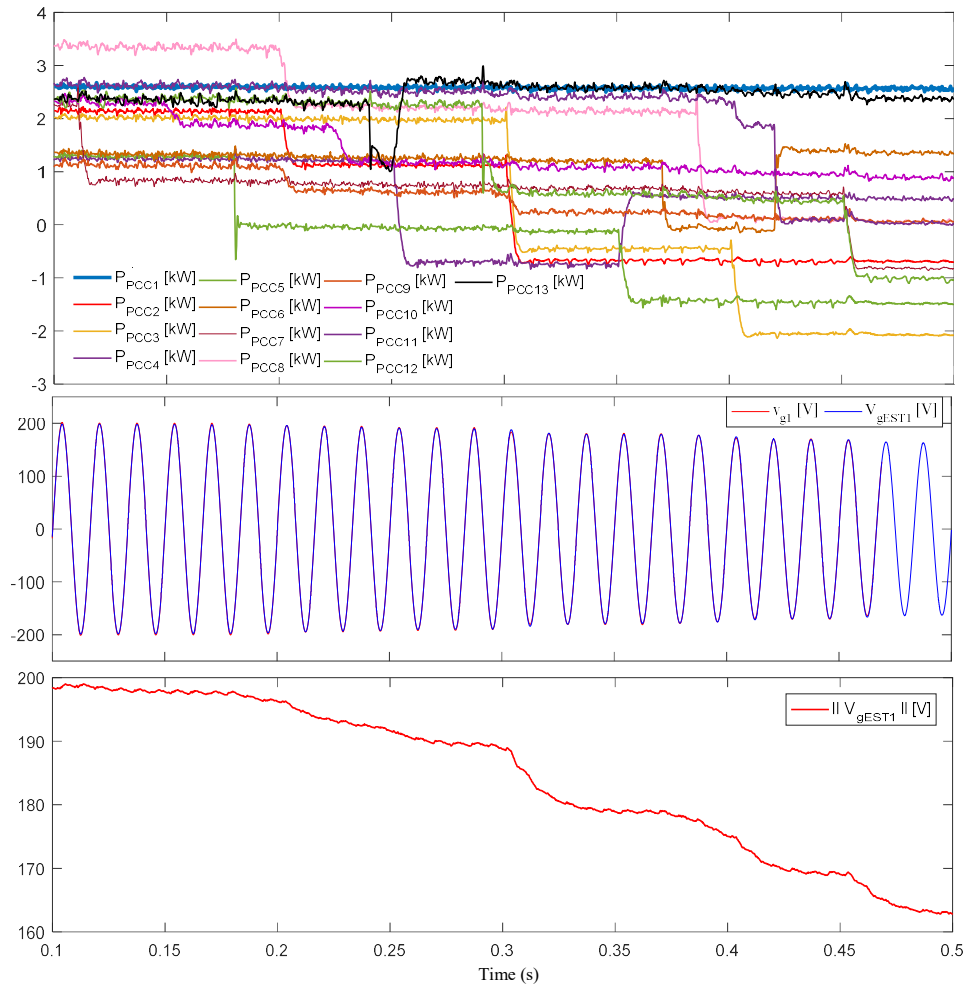


Figure 4.18. Scenario III real-time stability boundary identification 13 prosumers point of common coupling bus virtual power plant.

of common coupling bus v_{PCC2} . The targeted bus is operating with constant 2.5 kW at unity power factor for the whole scenario duration shown in Figure 4.15. At duration (1) in Figure 4.15, the nearby grid-following inverter is operating at 10 kW. Then, at duration (2) in Figure 4.15, the active power set-point changed to 4 kW. Notice that, the proposed observation is consistent with the actual measurement (i.e., see v_{g1} vs. v_{gEST1} in Figure 4.15). Furthermore, at duration (3) in Figure 4.15, the nearby grid-following inverter operation set-point is changed to sinking 4 kW. Similarly, the observation of v_{g1} is consistent with the actual measurement v_{gE} . The stability boundary is shown in Figure 4.16(a) –(c) for the highlighted durations (1), (2), and (3) in Figure 4.15. The simulation set-up is shown in Figure 4.17(a). Note that, in these scenarios the actual measurement is not possible in a real system. It was provided in this chapter by an alternative simulation where the targeted prosumer point of common coupling bus is omitted (see Figure 4.17(b)). This shows the importance of the proposed real-time observation.

4.2.4.3. Scenario III: Targeted Prosumer Point of Common Coupling Bus Real-Time Stability Boundary in Thirteen Bus Virtual Power Point

In scenario III that is shown in Figure 4.18, the virtual power plant network consists of thirteen prosumers point of common coupling busses in radial network. The network layout is extension of the layout of Figure 4.17(a). Specifically, each two consecutive prosumers point of common coupling bus's impedance composed of a 0.25 Ω resistance with 100 μ H inductance (see Figure 4.19 for the network detailed layout). Furthermore, in scenario III the targeted point of common coupling bus (v_{PCC_1}) is examined with the proposed method

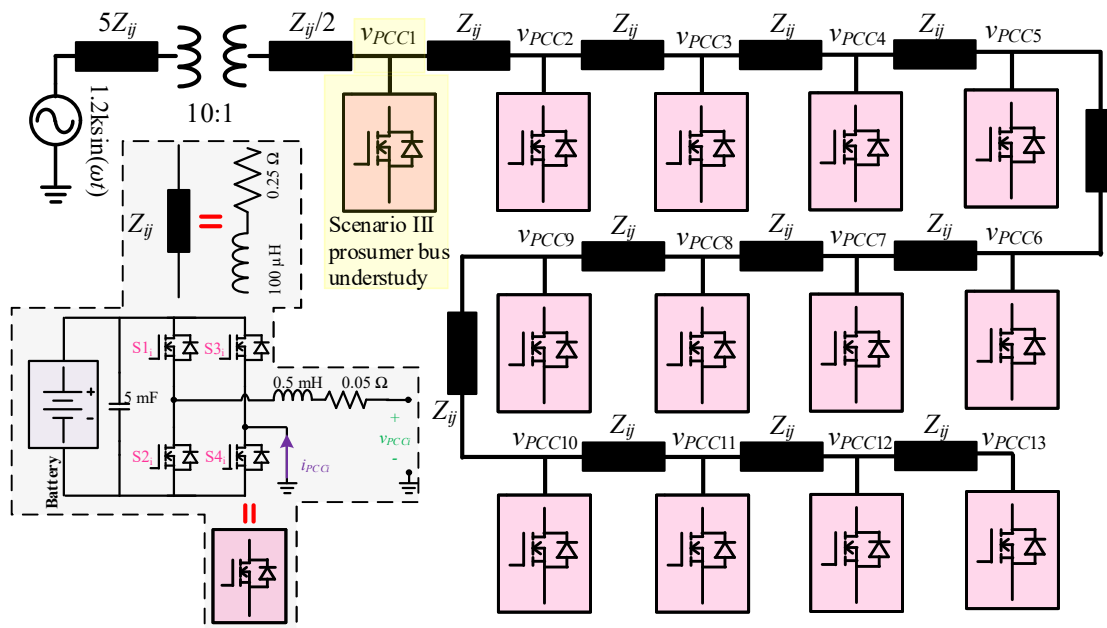


Figure 4.19. Scenario III real-time stability boundary identification, simulation set-up showing the targeted prosumer point of common coupling bus.

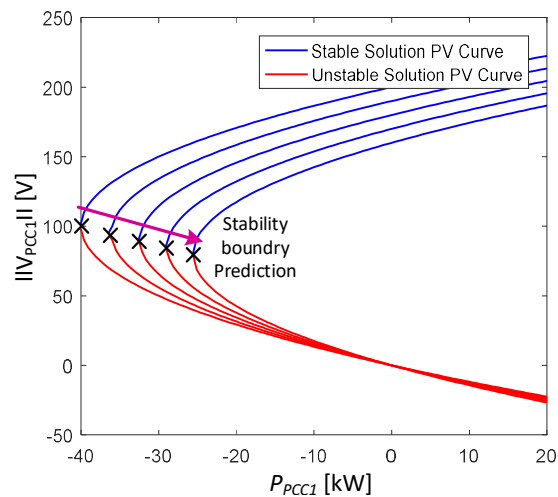


Figure 4.20. Scenario III online stability boundary identification 13 prosumers point of common coupling bus virtual power plant: real-time movement of the stability bound on the $P - V$ curves at v_{PCC1} (The arrow indicates time progression in scenario III from 0.1 sec to 0.5 sec in Figure 4.60).

to estimate the stability bound in real-time. Also, in this scenario the remaining prosumers point of common coupling bus set-points are changing randomly (see Figure 4.18).

However, the proposed method will construct a $P - V$ curve for stability prediction online in real-time (see Figure 4.20).

4.3. Cybersecurity Linkage to Stability Bounds

4.3.1. Cybersecurity in the New Energy Paradigm

The envisioned energy paradigm will implicate high deployment of renewable based generation through the utilization of distributed energy generators (DEGs) [144, 152]. At the low voltage side of the grid, grid-connected inverters are the dominant type of DEGs. Grid-connected inverters are following the inertial response of the network through their internal point of common coupling (PCC). In addition, these DEGs' capabilities are narrowed down to supplying current into the internal PCC terminals without considering upstream network prerequisites [147]. In other words, DEGs at the low voltage side are

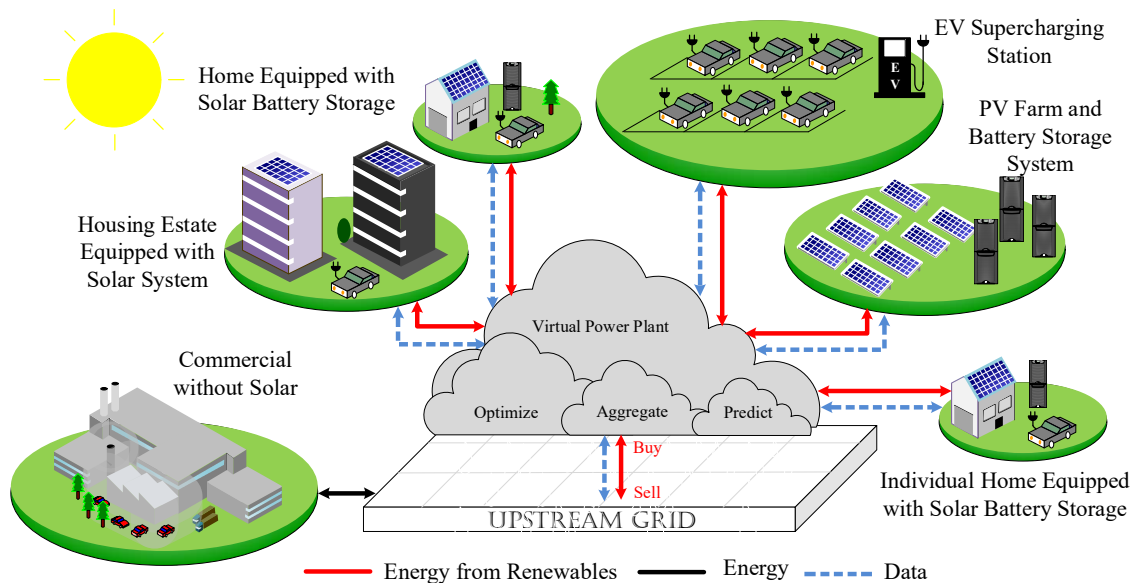


Figure 4.21. VPP concept illustration as a power electronics-dominated grid

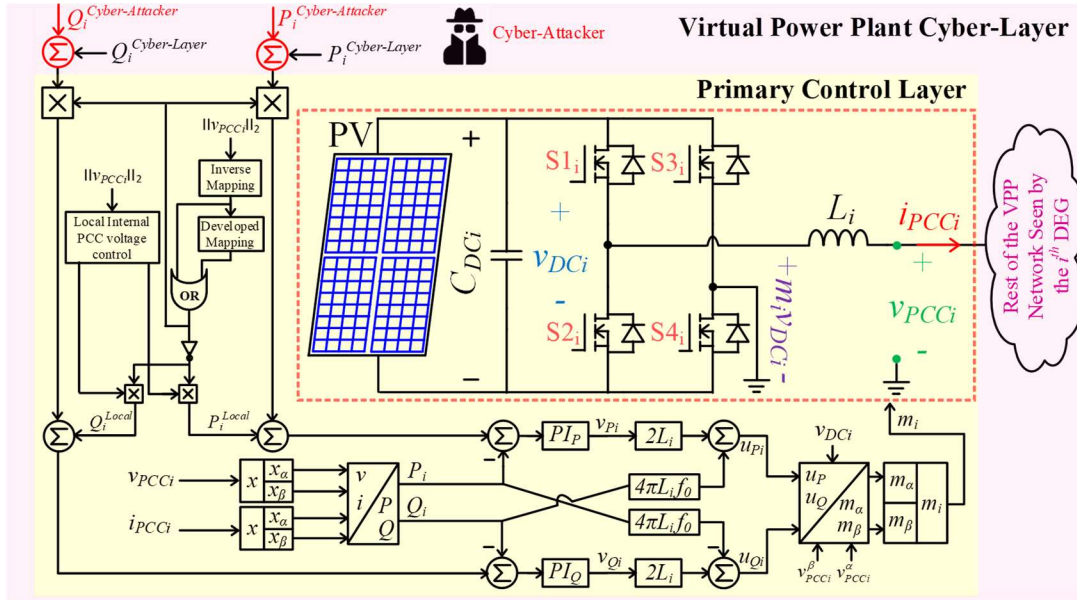


Figure 4.22. Primary control layout considered for DEGs detailing the cybersecurity analytics and switch level depiction.

unobservable to utility operators and vice versa. Thereby, it is essential to execute real-time system level coordination and management to enable optimal utilization of these unobservable DEGs that are deployed at the low voltage side [133].

The virtual power plant (VPP) concept is exemplifying to be an inspiring exemplar that will expedite DEGs efficient integration with the utility grid. According to [153], VPP is a collection of numerous size of DEGs that are aggregated into a single consortium. Thereby, the VPP is an intermediate operator that facilitate the effective interconnection between transmission and distribution system operators. In fact, VPP perception introduction runs higher observability and controllability on DEGs and enables the optimal utilization of inverter based generation features. Several practical VPPs are reported around the world such as the European VPPs detailed implementations in [154] and [155].

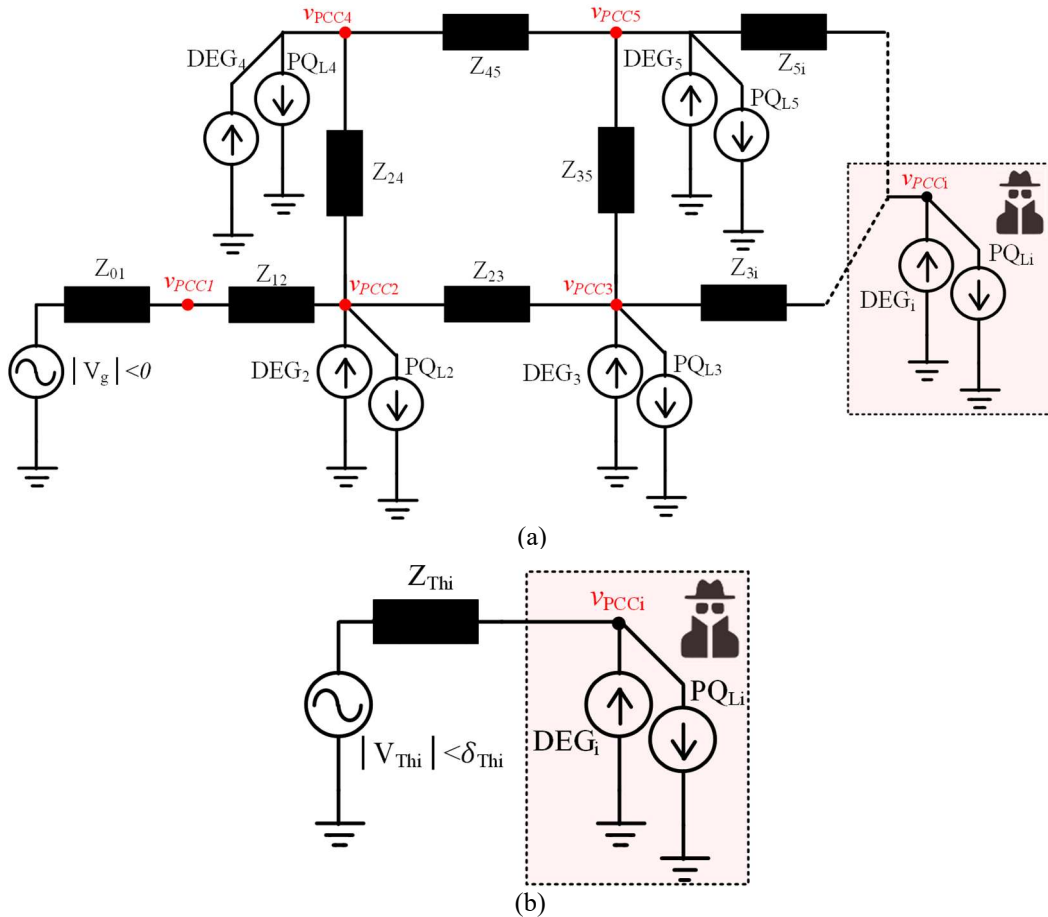


Figure 4.23. (a) VPP general network, (b) illustrating the i^{th} local PCC bus equivalent circuit at the secondary control layer time scale.

Nevertheless, this futuristic grid layout is anticipated to be vulnerable to malicious cyber-attacks [148, 149, 151, 156]. As more generation portion and intelligent devices will function outside the conventional power plant administrative layout [150, 157]. For instance, cyber-attackers might take advantage of the VPP infrastructure to initiate catastrophic events disrupting the utility grid operation and create serious damages [158,

159]. The detection of such type of cyber-attack is extremely difficult at early stages. Thereby, this chapter improves the cybersecurity aspects of a VPP (see Figure 4.21). Explicitly, by detection of a cyber-attacker manipulating the VPP cyber layer operation set-points gradually to violate network stability bound. Furthermore, the cybersecurity analytics proposed is based on a developed normal operation region identification framework. This normal operation region provides a one-to-one mapping between the network internal PCC bus voltage and the VPP cyber-layer generated set-points. This derived mapping is compared with an inverse mapping through internal PCC bus voltage monitoring for anomalies. Once, an inconsistency is witnessed by the cybersecurity analytics between the one-to-one mapping and the inverse mapping, the voltage anomaly is due to a cyber-attack. Then, after cyber-attack detection, the VPP control system is alerted. Network stability bounds identification is an offline process. For instance, conventional generator stability bounds are assessed with capability curve concept [160].

This curve provides the range of the dispatchable active and reactive power set-point that guaranties the generator stable operation. The idea of the capability curve is extended to VPP perception with exploiting upstream network constrains in [161]. Universally, the capability curve is acquired by repetitive power flow solutions for several operational

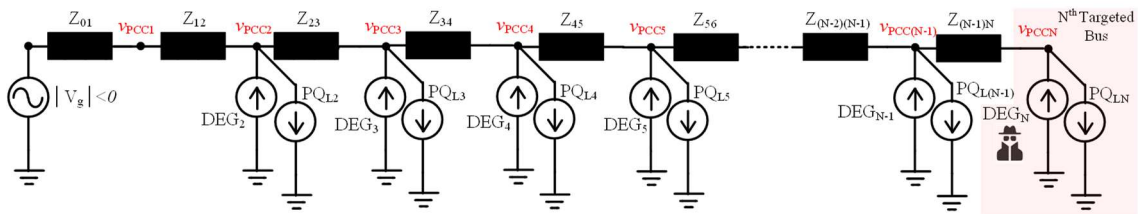


Figure 4.24. Example of N DEGs VPP for Thévenin voltage closed form derivation

scenarios that are chosen arbitrarily. Then, the realistic solution scenarios are mapped to points in the capability curve. Thereby, up to the authors' knowledge, exploiting the existing body of knowledge of the capability curves for rapid cyber-attack detection against operational set-points manipulation and breaches is not feasible.

4.3.2. Cyber-Attack Hypothesis, Normal Operation Region Derivation, and Cybersecurity Analytics

4.3.2.1. Cyber-Attack Hypothesis and Malicious Set-Points Impact

Based on the time scale separation principle in Figure 4.22 DEG layout, the VPP in Figure 4.21 from the perspective of the slow time scale cyber-layer is represented as Figure 4.23(a). Now, consider that a cyber-attacker is manipulating the operation set-points of the i^{th} concerned internal PCC bus that are assigned by the cyber-layer to the primary control of the DEG. From this cyber-attacker perspective, the impact of his manipulation can only be comprehended from the measurements. This is because the cyber-attacker lacks

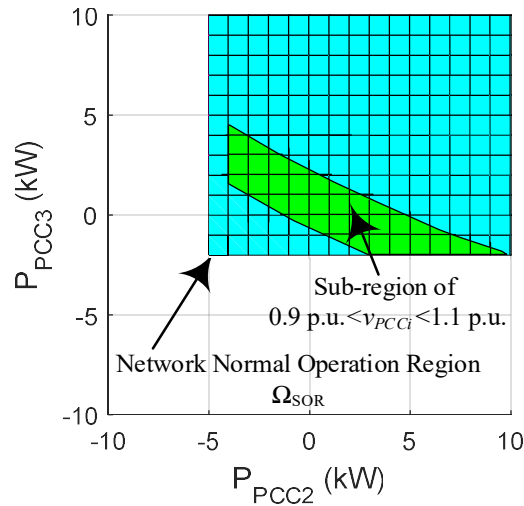


Figure 4.25. Normal operation region of the whole network

Algorithm 1: Cybersecurity Analytics System

Function [*Intrusion*] = IDS [$\vec{v}_{PCCi}, P_{PCC1}, Q_{PCC1}, \dots, P_{PCCN}, Q_{PCCN}$]

1: Continuously monitor the internal PCC bus voltages

$$\|\vec{v}_{PCCi}\|_2 \rightarrow \langle P_{PCC1}, Q_{PCC1}, \dots, P_{PCCN}, Q_{PCCN} \rangle$$

If ($\|\vec{v}_{PCCi}\|_2 \rightarrow \langle P_{PCC1}, Q_{PCC1}, \dots, P_{PCCN}, Q_{PCCN} \rangle \neq \mathbb{R} \rightarrow \mathbb{R}^{2N}$)

Internal PCC bus voltage is anomalous

2: Utilize the normal operation region one-to-one mapping

$$\langle P_{PCC1}, Q_{PCC1}, \dots, P_{PCCN}, Q_{PCCN} \rangle \rightarrow \|\vec{v}_{PCCi}\|_2$$

If ($\langle P_{PCC1}, Q_{PCC1}, \dots, P_{PCCN}, Q_{PCCN} \rangle \rightarrow \|\vec{v}_{PCCi}\|_2 \neq \mathbb{R}^{2N} \rightarrow \mathbb{R}$)

The anomaly detect is due to an intruder. Then, *Intrusion* = 1

Else

Intrusion = 0

Else

Intrusion = 0

knowledge associated with the network topology or nearby DEGs. Given this absence of this knowledge by the cyber--attacker could induce catastrophic effect by pushing the i^{th} concerned internal PCC bus to operate outside its stability bound by slowly and randomly changing the operation set-points.

4.3.2.2. Developed One-To-One Mapping Between Internal PCC Bus Voltages and the Cyber-Layer Operation Set-Points

From the perspective of an i^{th} specific DEG in the network, the remaining VPP network elements are seen as a Thèvenin voltage source (\vec{v}_{Thi}) with a series Thèvenin impedance ($Z_{Thi} = R_{Thi} + jX_{Thi}$) after the i^{th} internal PCC bus terminal (see Figure 4.23(b)).

Therefore, mathematically the internal PCC voltage (\vec{v}_{PCCi}) is represented by (4.40).

$$\begin{aligned} \vec{v}_{PCCi} &= (R_{Thi} + jX_{Thi})\vec{i}_{PCCi} + \vec{v}_{Thi} = \|V_{PCCi}\|_2 \angle \delta_{PCCi} = \xi_i + j\psi_i \\ \vec{v}_{Thi} &= \|V_{Thi}\|_2 \angle \delta_{Thi} = \|V_{Thi}\|_2 \cos(\delta_{Thi}) + j\|V_{Thi}\|_2 \sin(\delta_{Thi}) \end{aligned} \quad (4.40)$$

where \vec{i}_{PCCi} is the net current supplied at the i^{th} internal PCC bus. \vec{v}_{PCCi} is correlated to the set-points of the cyber-layer through the internal PCC current (\vec{i}_{PCCi}) as in (4.41)

$$\vec{i}_{PCCi} = (P_{PCCi} - jQ_{PCCi})\vec{v}_{PCCi}^*{}^{-1} \quad (4.41)$$

where \vec{v}_{PCCi}^* is the complex conjugate of \vec{v}_{PCCi} , P_{PCCi} is the total supplied active power at the i^{th} concerned internal PCC bus, and Q_{PCCi} is the total supplied reactive power at the i^{th} concerned internal PCC bus. Unifying (4.41) and (4.40) results in (4.42).

$$\vec{v}_{PCCi} = (R_{Thi} + jX_{Thi})(P_{PCCi} - jQ_{PCCi})\vec{v}_{PCCi}^{-1} + \vec{v}_{Thi} \quad (4.42)$$

Equation (4.42) is rearranged to (4.43) considering (4.40).

$$\begin{aligned} \xi_i^2 + \psi_i^2 &= R_{Thi}P_{PCCi} + X_{Thi}Q_{PCCi} + \|V_{Thi}\|_2 (A_i \cos(\delta_{Thi}) + B_i \sin(\delta_{Thi})) \\ &+ j(X_{Thi}P_{PCCi} - R_{Thi}Q_{PCCi} + \|V_{Thi}\|_2 (A_i \sin(\delta_{Thi}) - B_i \cos(\delta_{Thi}))) \end{aligned} \quad (4.43)$$

It is fairly straightforward to obtain a closed form solution for the parameters ξ_i and ψ_i from (4.43) for a particular Thèvenin depiction of the other elements in the network.

$$\begin{aligned} \xi_i &= 0.5\|V_{Thi}\|_2 \cos(\delta_{Thi}) + (R_{Thi}Q_{PCCi} - X_{Thi}P_{PCCi})\|V_{Thi}\|_2^{-1} \sin(\delta_{Thi}) \\ &+ \sqrt{0.25\|V_{Thi}\|_2^2 \cos^2(\delta_{Thi}) + ((X_{Thi}P_{PCCi} - R_{Thi}Q_{PCCi})\|V_{Thi}\|_2^{-1})^2 \sin^2(\delta_{Thi})} \\ &+ \sqrt{(X_{Thi}P_{PCCi} - R_{Thi}Q_{PCCi})\cos(\delta_{Thi})\sin(\delta_{Thi}) - ((X_{Thi}P_{PCCi} - R_{Thi}Q_{PCCi})\|V_{Thi}\|_2^{-1})^2} \\ &+ (R_{Thi}P_{PCCi} + X_{Thi}Q_{PCCi})\cos^2(\delta_{Thi}) \end{aligned} \quad (4.44)$$

$$\begin{aligned} \psi_i &= (X_{Thi}P_{PCCi} - R_{Thi}Q_{PCCi})\|V_{Thi}\|_2^{-1} \sec(\delta_{Thi}) + 0.5\|V_{Thi}\|_2 \sin(\delta_{Thi}) \\ &+ (R_{Thi}Q_{PCCi} - X_{Thi}P_{PCCi})\|V_{Thi}\|_2^{-1} \sin(\delta_{Thi}) \tan(\delta_{Thi}) + \\ &\tan(\delta_{Thi}) \sqrt{0.25\|V_{Thi}\|_2^2 \cos^2(\delta_{Thi}) + ((X_{Thi}P_{PCCi} - R_{Thi}Q_{PCCi})\|V_{Thi}\|_2^{-1})^2 \sin^2(\delta_{Thi})} \\ &+ (X_{Thi}P_{PCCi} - R_{Thi}Q_{PCCi})\cos(\delta_{Thi})\sin(\delta_{Thi}) - ((X_{Thi}P_{PCCi} - R_{Thi}Q_{PCCi})\|V_{Thi}\|_2^{-1})^2} \\ &+ (R_{Thi}P_{PCCi} + X_{Thi}Q_{PCCi})\cos^2(\delta_{Thi}) \end{aligned} \quad (4.45)$$

$\|\vec{v}_{PCCi}\|_2 = \sqrt{\xi_i^2 + \psi_i^2}$ describes the stability bound of the i^{th} concerned internal PCC bus

for a particular Thèvenin depiction of the rest of network. The normal operation region of the concerned i^{th} PCC bus is the projection of $\|\vec{v}_{PCCi}\|_2$ on the P_{PCCi} and Q_{PCCi} plane (i.e., the domain when $\|\vec{v}_{PCCi}\|_2 \in \mathbb{R}$). Yet, this normal operation region cannot be exploited for rapid analysis. This is because the Thèvenin source representing the remaining elements in the network is obtained numerically with power flow. To extend

this analysis, the insertion of adjacent PCC buses set-points on the i^{th} concerned PCC bus is described by obtaining the expression of the Thèvenin source in (4.40) as a function of all the other grid-connected DEGs set-points. This results in generalizing the concerned internal PCC bus voltage to a manifold. This process is repetitive for every individual internal PCC bus in the network and then the intersection of all PCC buses normal operation regions is considered as the whole network normal operation region. The whole network normal operation region is the developed one-to-one mapping between the network internal point of common coupling PCC bus voltages and the cyber-layer generated set-points. Furthermore, to understand the Thèvenin closed form, the network with N DEGs shown in Figure 4.24 is taken as an example. The aim is to find the manifold of the DEG at the N^{th} internal PCC bus in Figure 4.24. The N^{th} internal PCC bus manifold is given in (4.46).

$$\begin{aligned}
\|\vec{v}_{PCC_N}\|_2 &= \sqrt{\xi_N^2 + \psi_N^2}, \quad \vec{v}_{Th_N} = (3-N)\vec{v}_g + \sum_{i=2}^{N-1} \vec{v}_{Bus_i}, \quad \vec{v}_g = |V_g| \angle 0 \\
\vec{v}_{Bus_i} &= 0.5|V_g| + j(R_{Th_i} Q_{PCCi} - X_{Th_i} P_{PCCi})|V_g|^{-1} + \\
&\sqrt{0.25|V_g|^2 - \left((R_{Th_i} Q_{PCCi} - X_{Th_i} P_{PCCi})|V_g|^{-1}\right)^2 + (R_{Th_i} P_{PCCi} + X_{Th_i} Q_{PCCi})} \\
Z_{Th_i} &= \sum_{j=0, k=1}^{j=N-1, k=N} Z_{jk}, \quad R_{Th_i} = \text{Re}\{Z_{Th_i}\}, \quad X_{Th_i} = \text{Im}\{Z_{Th_i}\}
\end{aligned} \tag{4.46}$$

The, normal operation region (Ω_{NOR_N}) of this DEGs at N^{th} internal PCC bus is defined as (4.47).

$$\begin{aligned}
\Omega_{NOR_N} &= \text{Proj}_{P_2, Q_2, P_3, Q_3, \dots, P_N, Q_N} \left(\|\vec{v}_{PCC_N}\|_2 \right) \mid \|\vec{v}_{PCC_N}\|_2 \in \mathbb{R} \\
\text{For } \forall P_2, Q_2, P_3, Q_3, \dots, P_N, Q_N &\in \mathbb{R}
\end{aligned} \tag{4.47}$$

Similar conclusions for the normal operation region are deducible to all other internal PCC buses in the network. Thereby, the whole network normal operation region (Ω_{NOR}) is described by (4.48).

$$\Omega_{\text{NOR}} = \Omega_{\text{NOR}_1} \cap \Omega_{\text{NOR}_2} \cap \Omega_{\text{NOR}_3} \cap \dots \cap \Omega_{\text{NOR}_{N-1}} \cap \Omega_{\text{NOR}_N} \quad (4.48)$$

A four bus VPP example is considered, the network normal operation region depicted in Figure 4.25.

4.3.2.3. Cybersecurity Analytics Framework

The cybersecurity analytics system is depicted in Algorithm 1. As aforementioned earlier that this cybersecurity analytics system is mainly founded on the normal operation region deduced in the previous subsection in (4.40)-(4.48). Particularly, the normal operation region is the derived one-to-one mapping between the network internal PCC bus voltages and the cyber-layer generated set-points. This derived mapping is compared with an inverse mapping through internal PCC bus voltage monitoring for anomalies. Once, an inconsistency is witnessed by the cybersecurity analytics system between the one-to-one mapping and the inverse mapping, the voltage anomaly is due to an intrusion. Then, the VPP is alerted.

4.3.3. Validation of the Derived Operation Regions

The cybersecurity analytics system performance is validated through simulation of two cyber intrusion scenarios. The grid-connected inverter DEGs in the VPP are rated to 20 kVA apparent power, 10 kHz switching frequency, 420 V DC bus voltage, 0.5 mH filter inductor with equivalent series resistance of 50 mΩ , and 2 mF decoupling capacitor. The utility grid is 120 V_{RMS} at 60 Hz. Moreover, the two scenarios of Figure 4.26 and Figure 4.27 are identical regarding set-points gradual manipulation by the cyber-attacker seeking for network stability boundary violation. However, in scenario II the DEGs are equipped with the developed cybersecurity analytics system.

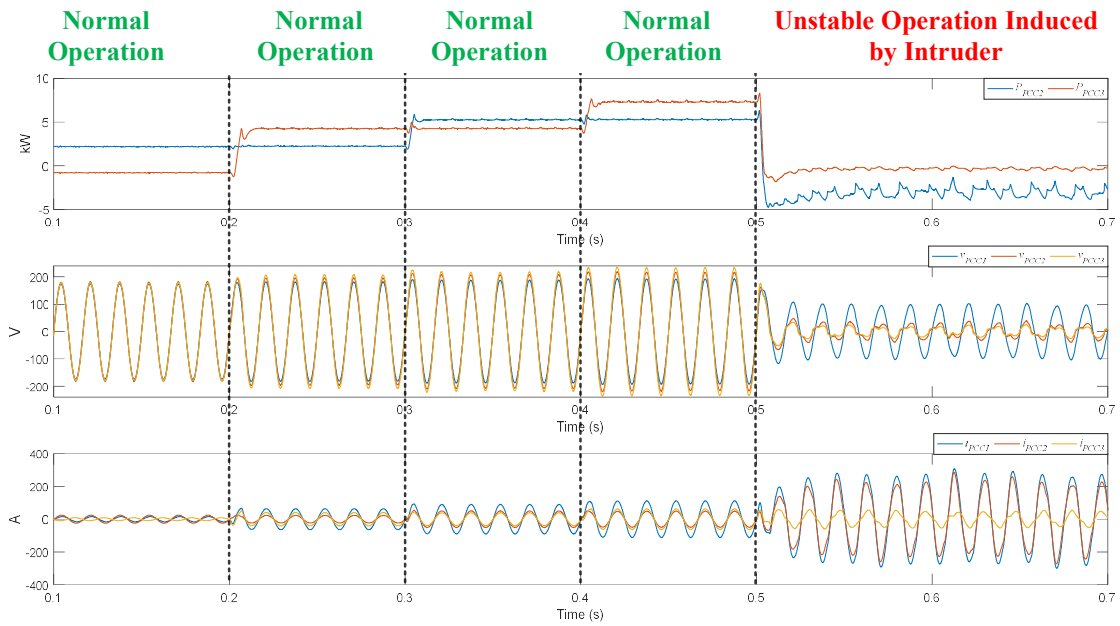


Figure 4.26. Cyber-attack scenario I without activating the proposed cybersecurity analytics system

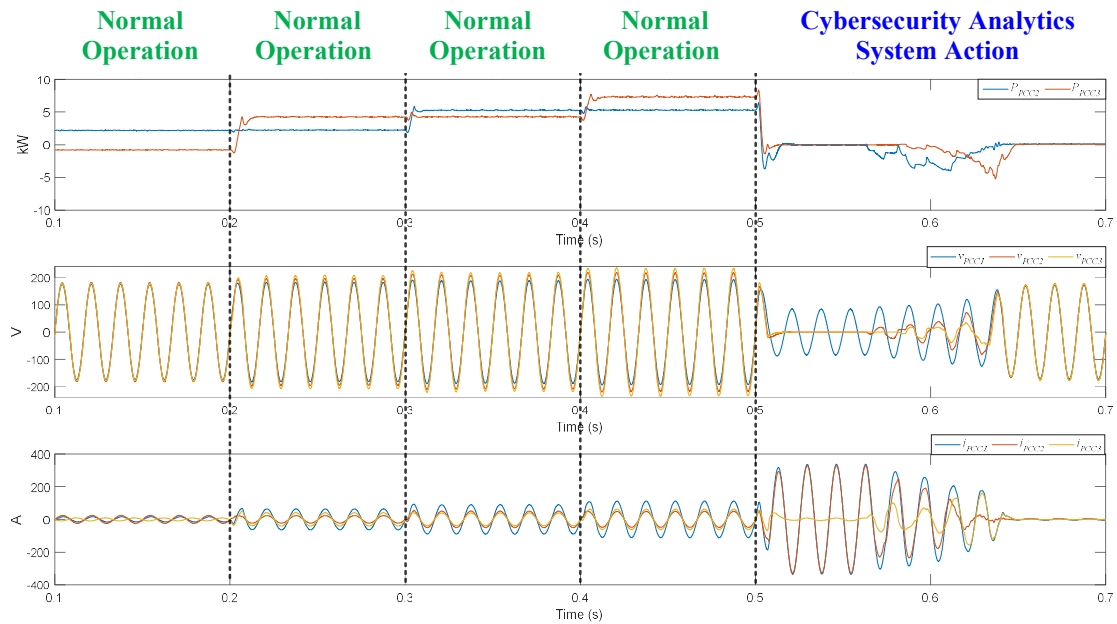


Figure 4.27. Cyber-attack scenario II with activating the proposed cybersecurity analytics system

4.3.3.1. Scenario I

In the scenario I that is depicted in Figure 4.26, the cyber-attacker is seeking for violating the network stability boundary. Initially, v_{PCC2} is operating at 2 kW and v_{PCC3} is sinking 1 kW. These initial operating points belong to the normal operation region. Then, after time instant 0.2 sec in Figure 4.26, the cyber-attacker increases the operation set-point passing to the primary control layer from the VPP cyber-layer to 4 kW at v_{PCC3} . This new manipulated set-point assignment by the cyber-attacker fails to violate the stability boundary of network. After that, the cyber-attacker further pushes the operation set-point at v_{PCC2} to 5 kW after time instant 0.3 sec in Figure 4.26. Again, the cyber-attacker fails to jeopardize the operation of the network as this set-point falls within the normal operation region boundary. Therefore, the cyber-attacker once again changes the set-point of v_{PCC3} to 7 kW after time instant 0.4 sec in Figure 4.26. However, still he is incapable of jeopardizing the network stability. Hence, the cyber-attacker decides to moves v_{PCC2} and v_{PCC3} to sinking 5 kW after time instant 0.5 sec. In this situation, the cyber-attacker successfully jeopardizes the network operation as this set-point is outside the normal operation region boundary (see Figure 4.25)). In fact, it is obvious that the network enters voltage collapse situation after time instant 0.5 sec in Figure 4.26.

4.3.3.2. Scenario II

In scenario II, the exact same operation set-point variation with respect to time evolution of scenario I is occurring (see Figure 4.27). However, in scenario II the DEGs are equipped with the proposed cybersecurity analytics. Therefore, once the cyber-attacker breaches the network stability boulder after 0.5 sec in Figure 4.27, the DEGs are moved to internal PCC

voltage control mode to regain internal PCC bus voltage normal operation (see Figure 4.27 after 0.5 sec). In other words, the cyber-layer set-points are ignored. Note that, the network is no longer operating in optimal operation, but the cybersecurity analytics system avoids catastrophic impacts on the network due to early intrusion detection and alerting the VPP owner for further diagnoses.

4.4. Conclusion

In conclusion, the first section in this chapter provided insights into voltage stability bound identification in the power electronics-dominated grid (PEDG). Specifically, revisiting the mathematical derivation of how the voltage stability bound at PCC bus i is affected by its self-set-point change. Then, extending this derivation to how an adjacent PCC bus j set-point change influences the voltage stability bound at PCC bus i . These derivations give a hint using the structure of the $P - V$ curves to identify the voltage stability bounds instead of the function values. Then, in the second section of this chapter, an online voltage stability bound identification method is derived from the perspective of consumer local point of common coupling point (PCC) bus. This online stability bounds identification is inspired by the feedback linearization theories used in Chapter 2. These bounds are utilized to improve the cybersecurity to grid edge consumers. Lastly, the third section of this chapter, provided a method to derive the operation regions for multiple $P - V$ curves at different local PCC buses to improve the cybersecurity of the PEDG against malicious set-points induced on the upper secondary control layer. This chapter facilitates an introduction of the mathematical background and theory that will be utilized in the next chapter to design an intrusion detection system.

Chapter 5

5. Intrusion Detection System

Part of this chapter, including figures and text are based on my following papers:

© 2018-2022 IEEE

- A. Khan, M. B. Shadmand and S. K. Mazumder, "Intrusion Detection System for Multilayer-Controlled Power Electronics-Dominated Grid," *IEEE Access*, vol. 10, pp. 98329-98347, 2022

- A. Khan, M. Hosseinzadehtaher, M. B. Shadmand, D. Saleem and H. Abu-Rub, "Intrusion Detection for Cybersecurity of Power Electronics Dominated Grids: Inverters PQ Set-Points Manipulation," *2020 IEEE CyberPELS (CyberPELS)*, pp. 1-8, 2020

5.1. Future Power Grid and Cyber Threats

The futuristic energy paradigm implicates high penetration of nonsynchronous generation at the grid edge through embracing dispersed energy generators (DEGs) [162]. At the grid edge, grid-feeding inverters are projected to be the prevailing type of DEGs. In this mode of operation, the DEGs are following the inertial response of the network and their capabilities are confined in injecting/absorbing current into/from their local point of common coupling (PCC) without considering upstream network constraints and requirements [147]. Accordingly, these DEGs are typically unobservable to the upstream network and vice versa. Henceforth, real-time system level coordination and management is crucial to ensure the optimal utilization of unobservable DEGs that are installed behind the meters and offer an additive situational awareness to the system [133, 163].

The multi-layer-controlled power electronics-dominated grid (PEDG) is demonstrating to be an effective example that is enabling DEGs to achieve the U.S. Department of Energy's 100% nonsynchronous generation based U.S. power grid [164]. The PEDG is a cluster of distinct scale DEGs that can be aggregated into a single coherent entity. The multi-layer-controlled PEDG is able to function as an intermediate interface between transmission and distribution system operators [153]. Consequently, offering superior observability and controllability on DEGs and permits optimal utilization of inverter-based resources features. Various multi-layer controlled PEDG deployments exist around the world such as the ones reported in documents in [154] and [155].

The futuristic 100% nonsynchronous generation-based power grid targeted in 2050 by the U.S. Department of Energy is anticipated to be vulnerable to malicious cyber-attacks.

This is because of the more dispersed generation that will operate outside the realm of old-fashioned power-plant administrative domain through employing more DEGs at the grid edge [150, 165-167]. The attack might be introduced into the PEDG infrastructure through the communication medium that enables its harmonious operation. Security breach in the cyber-layer of a PEDG has a direct influence on its physical layer, which disrupts its nominal operation. A severe stealthy cyber-attack typically spreads throughout the grid steadily compromising the cyber layer. This makes the detection of such a stealthy attack extremely challenging at early stages using conventional protection and intrusion detection schemes [134, 158, 168].

This chapter is enhancing the situational awareness against malicious PQ set-points requests from a compromised secondary and cyber layer. These malicious set-points are assigned by a stealthy intruder breaching undetectably into the secondary control and cyber layer of the PEDG depicted in Figure 5.1. Furthermore, this situational awareness improvement impacts positively the cybersecurity of the PEDG. In fact, according [169], situational awareness feature offers a direct improvement of the system cyber-security aspects. As situational awareness does not only provide accurate observation, but also ensures availability of necessary functions that support predicting operation projections and identifying potential risks [170]. Moreover, a mathematical theory is developed for deriving a safe operation region (SOR). This mathematical theory extends the stability margins inferred from $P - V$ curves to the abstract concept of morphisms (see 5.6.3 for Morphism theoretical background). Particularly, there are two morphisms for each PCC bus when operating in the SOR: (*Morphism 1*) PCC bus voltage mapped to network set-

points that is structured as \mathbb{R} to \mathbb{R}^{2N} mapping, and (*Morphism 2*) network set-points mapped to the PCC bus voltage that is structured as \mathbb{R}^{2N} to \mathbb{R} mapping. Where N is the number of PCC buses. *Morphism 1* is used for anomaly detection originating from the secondary layer dispatched set-points manipulation. Explicitly, observation of a non-zero imaginary-part in the PCC voltage L_2 norm is evidence of an anomaly. Note that, L_2 norm properties are: nonnegativity, definiteness, triangle inequality, and homogeneity must be satisfied in SOR for PCC voltage as this preserves the \mathbb{R} to \mathbb{R}^{2N} mapping structure. Inspecting an imaginary-part invalidates nonnegativity property of the PCC voltage L_2 norm (i.e., \mathbb{R} to \mathbb{R}^{2N} is not preserved see 5.6.4 for theoretical proof). *Morphism 2* is utilized for independent decision making at the primary layer of the DEG during cyber intrusion scenarios. In other words, *Morphism 2* is an alternative for the secondary layer when the dispatched set-points are not trusted.

In the literature, the capability of synchronous generator is estimated through the concept of capability chart. This chart provides the range of dispatchable PQ set-points without jeopardizing the stability of the synchronous generator [160]. The notion of capability chart was first time utilized for multi-layer-controlled renewable based grid in [161]. This capability chart was used as conventional generators capability charts that are employed in scheduling and dispatching optimization. In other words, set-points that belong to the capability chart are guaranteed to be executable when requested by the upstream network. Though, the capability charts for renewable based grids are more complex compared to conventional generators. This is because renewable based grid capability charts are representing aggregation of various DEGs. An example of such

capability charts is used to estimate the reactive power injection capability at different active power levels in [171]. Another work is suggesting a methodology for approximating capability chart numerically using repeated time domain simulations in [172]. In general, the capability chart is obtained by repeated load flow solutions for various scenarios that often are selected randomly. After that, the realistic load flow solutions consequence to points that are constructing the capability chart. Another approaches that are reported in the literature for approximating the capability charts are employing geometrical hypothesis such as polyhedron, ellipse, and so on [173]. Furthermore, capability charts estimation with incorporation of randomness is reported in [135]. Yet, these methods extensively rely on repetitive load flow solutions that needs to be executed in secondary or tertiary layers, which even turns out to be challenging to utilize fast load flow algorithms due to the dominate resistive nature for the distribution network [174]. Furthermore, the considered potential attack model, in which the intruder is compromising the secondary layer controller and existing load flow algorithms, mandates another sanity checkpoint at the primary layer for realizing an effective intrusion detection. Hence, to our knowledge, utilizing the existing capability charts for intrusion detection against operational PQ set-points manipulation is not viable from the perspective of the primary layer. The contributions of chapter are summarized in the following bullet points:

- A mathematical theory extends the stability margins inferred from $P - V$ curves to the abstract concept of morphism. This morphism simplifies understanding the operation limits of the unobservable DEGs without relying on repeated load flow solution at

secondary/tertiary control layers, thus creating an independent framework for decisions making at the primary layer.

- Intrusion detection by utilizing the SOR as a sanity checkpoint for PQ set-points assignments by potentially compromised secondary layer; thus, detecting and preventing a cyber intruder that is requesting malicious set-points from the DEGs.

5.2. Multi-Layer Controlled PEDG Network Understudy

5.2.1. List of Symbols Used in this Chapter

t	Time
τ	Dummy intermediate variable for integrals
C_{DCi}	DC-link capacitor of the i^{th} grid-feeding inverter
L_i	Filter inductor of the i^{th} grid-feeding inverter
R_i	Filter inductor resistance of the i^{th} grid-feeding inverter
ω	Nominal angular frequency of the network
P_i	Active power of the i^{th} grid-feeding inverter
P_{Li}	Active power of the i^{th} grid-feeding inverter load
P_{PCCI}	Active power of the i^{th} local PCC bus
Q_i	Reactive power of the i^{th} grid-feeding inverter
Q_{Li}	Reactive power of the i^{th} grid-feeding inverter load
Q_{PCCI}	Reactive power of the i^{th} local PCC bus
S_{Rated}	Rated appeared power of the i^{th} grid-feeding inverter
f_{SW}	Switching frequency of the i^{th} grid-feeding inverter
P_{Refi}	Active power reference of the i^{th} grid-feeding inverter
Q_{Refi}	Reactive power reference of the i^{th} grid-feeding inverter
Z_{ij}	Line impedance between PCC bus i and j
R_{ij}	Line resistance between PCC bus i and j

L_{ij}	Line inductance between PCC bus i and j
j	Square root of -1
\mathbb{R}	Real number set symbol
\mathbb{C}	Complex number set symbol
N	Number of DEGs
$\ X\ _2$	L_2 norm of X
X^*	Complex conjugate of X
X^T	Transposition of X
\vec{X}	Phasor quantity of X
$Re\{X\}$	Real part of X
$Im\{X\}$	Imaginary part of X
u_{pi}	LTI MIMO open loop state space active power dynamics input
u_{qi}	LTI MIMO open loop state space reactive power dynamics input
v_{DCi}	DC link voltage of the i^{th} grid-feeding inverter
v_{PCCi}	i^{th} local PCC voltage
v_{PCCi}^α	Alpha component of the i^{th} local PCC voltage
v_{PCCi}^β	Beta component of the i^{th} local PCC voltage
i_{PCCi}	i^{th} local PCC current
i_{PCCi}^α	Alpha component of the i^{th} local PCC current
i_{PCCi}^β	Beta component of the i^{th} local PCC current
m_i	i^{th} grid-feeding inverter modulation index
m_i^α	Alpha component of the i^{th} grid-feeding inverter modulation index
m_i^β	Beta component of the i^{th} grid-feeding inverter modulation index
Ω_{SOR_i}	Projection function for safe operation region of the i^{th} local PCC bus
Ω_{SNOR_i}	Projection function for stable/normal operation region of the i^{th} local PCC bus
e_{pi}	Error on active power of the i^{th} grid-feeding inverter
e_{qi}	Error on reactive power of the i^{th} grid-feeding inverter
v_{pi}	Active power control output of the i^{th} grid-feeding inverter

v_{Qi}	Reactive power control output of the i^{th} grid-feeding inverter
K_{Ppi}	Active power control proportional gain of the i^{th} grid-feeding inverter
K_{Qpi}	Reactive power control proportional gain of the i^{th} grid-feeding inverter
K_{Pii}	Active power control integral gain of the i^{th} grid-feeding inverter
K_{Qii}	Reactive power control integral gain of the i^{th} grid-feeding inverter
\vec{v}_{Thi}	Thevenin voltage phasor seen at the i^{th} local PCC bus
δ_{Thi}	Thevenin voltage angle seen at the i^{th} local PCC bus
δ_{PCCi}	i^{th} local PCC bus voltage phasor angle
V_g	Grid voltage peak
A_i	Real part of the i^{th} local PCC bus phasor voltage
B_i	Imaginary part of the i^{th} local PCC bus phasor voltage
R_{Thi}	Thevenin resistance seen at the i^{th} local PCC bus
L_{Thi}	Thevenin inductance seen at the i^{th} local PCC bus
f	Developed <i>Morphism 1</i> : Generalization of the inverse of the $\mathbf{P} - \mathbf{V}$ curve
g	Developed <i>Morphism 2</i> : Generalization of the $\mathbf{P} - \mathbf{V}$ curve
h	Ohm's law across linear resistor (R) as a morphism mapping current (i_R) into voltage (v_R)
w	Ohm's law across linear resistor (R) as a morphism mapping voltage (v_R) into current (i_R)
A_{CLi}	Closed loop control of the i^{th} grid-feeding inverter state matrix
x_{CLi}	Closed loop control of the i^{th} grid-feeding inverter states vector
P_{CLi}	Closed loop control of the i^{th} grid-feeding inverter linear quadratic Lyapunov stability theorem P matrix
Q_{CLi}	Closed loop control of the i^{th} grid-feeding inverter linear quadratic Lyapunov stability theorem Q matrix
$V_{CLi}(x_{CLi})$	Lyapunov function of the i^{th} grid-feeding inverter closed loop control

5.2.2. Preliminary Considerations

The multi-layer controlled PEDG network understudy is portrayed in Figure 5.1. In this PEDG, the main PCC bus voltage is the potential difference between the low side positive terminal of the distribution pole transformer and the ground conductor (see v_{PCC1} in

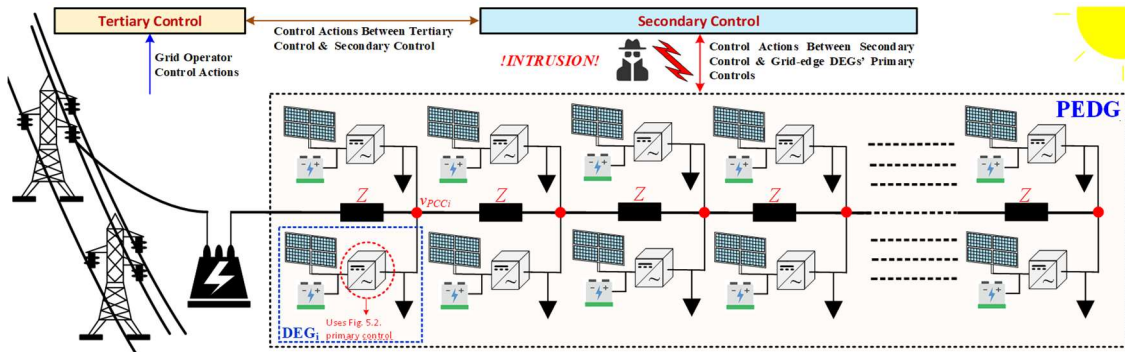


Figure 5.1. Multi-layered controlled PEDG concept extended to the grid edge with unobservable single-phase DEGs in grid-feeding mode of operation.

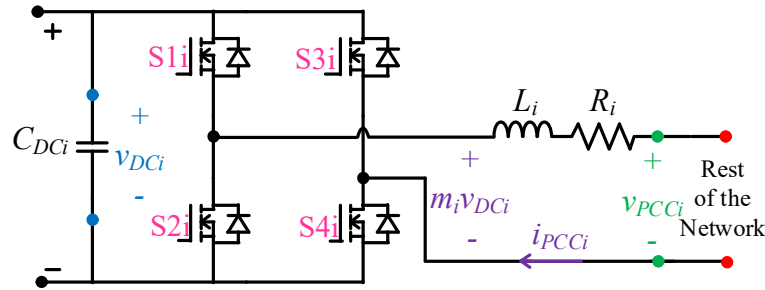


Figure 5.2. Grid-feeding primary control layer considered for DEGs in the PEDG: inverter structure.

Figure 5.1). Similarly, the internal local PCC buses are considered as each node that consumers at the grid edge are feeding their local loads (see v_{PCC2} v_{PCC3} , ..., v_{PCCN} in Figure 5.1). In addition, DEGs are installed at internal local PCC buses. The grid-feeding inverter's in Figure 5.2 primary control layer considered in this work for DEGs is depicted in Figure 5.3. The open loop system is represented by the multiple input multiple output (MIMO) linear time invariant (LTI) state space in (5.1).

$$\begin{aligned}
 \begin{bmatrix} \frac{dP_i}{dt} \\ \frac{dQ_i}{dt} \end{bmatrix} &= \begin{bmatrix} -R_i L_i^{-1} & -\omega \\ \omega & -R_i L_i^{-1} \end{bmatrix} \begin{bmatrix} P_i \\ Q_i \end{bmatrix} + \begin{bmatrix} 0.5L_i^{-1} & 0 \\ 0 & 0.5L_i^{-1} \end{bmatrix} \begin{bmatrix} u_{P_i} \\ u_{Q_i} \end{bmatrix} \\
 u_{P_i} &= m_{\alpha i} v_{DCi} v_{PCCi}^{\alpha} + m_{\beta i} v_{DCi} v_{PCCi}^{\beta} - \|v_{PCCi}\|_2^2 \\
 u_{Q_i} &= m_{\alpha i} v_{DCi} v_{PCCi}^{\beta} - m_{\beta i} v_{DCi} v_{PCCi}^{\alpha} \\
 \|v_{PCCi}\|_2 &= \sqrt{v_{PCCi}^{\alpha 2} + v_{PCCi}^{\beta 2}}
 \end{aligned} \tag{5.1}$$

$$\begin{aligned}
e_{P_i} &= P_{Ref_i} - P_i \\
v_{P_i} &= e_{P_i} K_{P_{pi}} + K_{P_{ii}} \int e_{P_i}(\tau) d\tau \\
e_{Q_i} &= Q_{Ref_i} - Q_i \\
v_{Q_i} &= e_{Q_i} K_{Q_{pi}} + K_{Q_{ii}} \int e_{Q_i}(\tau) d\tau \\
\frac{d^2 e_{P_i}}{dt^2} &= -(K_{P_{pi}} + R_i L_i^{-1}) \frac{de_{P_i}}{dt} - K_{P_{ii}} e_{P_i} \\
\frac{d^2 e_{Q_i}}{dt^2} &= -(K_{Q_{pi}} + R_i L_i^{-1}) \frac{de_{Q_i}}{dt} - K_{Q_{ii}} e_{Q_i}
\end{aligned}$$

This control is guaranteeing that primary control layer stability. The proof for the stability of the primary control layer equilibrium is detailed in 5.6.1 with linear quadratic Lyapunov stability theorem. Similarly, 5.6.2 details potential instabilities that might originate from a cyber-attacker at the secondary control layer manipulating the dispatched PQ set-points.

5.3. Safe Operation Region Derivations and Intrusion Scenario

5.3.1. Intrusion and Malicious PQ Set-Points Impact

Consider the exemplification in Figure 5.4 of the multi-layer controlled PEDG understudy shown in Figure 5.1, if a stealthy cyber intruder took control over the cyber layer and he is targeting the i^{th} local PCC bus in Figure 5.4 by manipulating the operation PQ set-points that are passing from the secondary layer to the primary layer of the DEG. From the stealthy intruder perspective, he is altering the operation set-points and observing the local measurement to understand the impact of his set-points manipulation. The intruder could initiate catastrophic effect by pushing the targeted PCC bus to operate outside its stable set-points domain by slowly and randomly changing the PQ set-points. Therefore, the hypothesis in this chapter is that the primary layer will be equipped with the SOR, as a sub-layer in primary. Then, if the DEG is pushed to operate outside SOR by the secondary

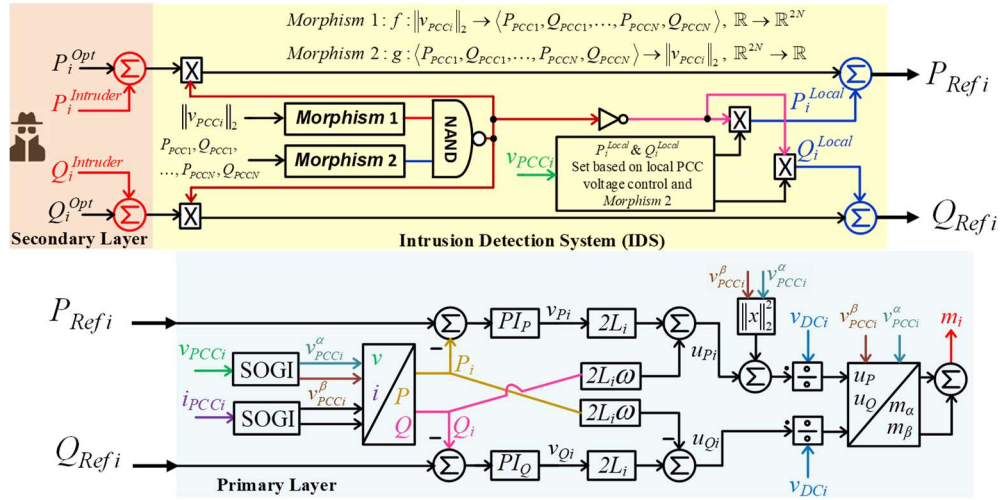


Figure 5.3. Grid-feeding primary control layer considered for DEGs in the PEDG: controller structure with measurements, nonlinear coordinate transformation illustration, and the intrusion detection system.

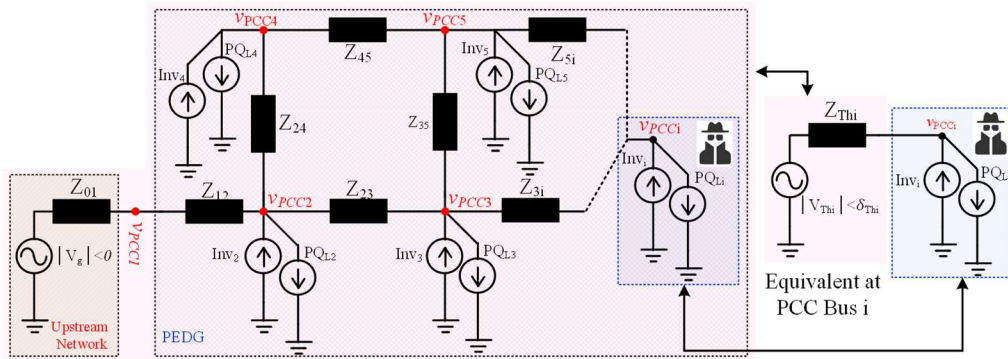


Figure 5.4. General PEDG network, illustrating the \$i\$th local PCC terminals equivalent circuit.

layer manipulated PQ set-points, the primary layer considers that the set-points passing from the secondary layer are compromised. Moreover, the methodology that is optimal to understand an intrusion occurred or not is by witnessing if the PQ dispatched set-points passing to primary control layer from the upper control layer are intended to induce an instability. Since rationally, the upper control must solve optimization on network level and thus the stability of the network is one of the crucial constrains in that optimization. Hence, to catch that there is stealthy intruder from the limited primary layer perspective, witnessing requests of PQ set-points that belongs to unstable operation region (UOR) is

helpful in detection. The method applied does not depend on measurements for deciding intrusion occurred or not. The process of intrusion detection is initiated by checking the structural preservation of the *Morphism 1* which is a sort of abstraction of the inverse of the generalized $P - V$ curve (5.2).

$$f : \|\vec{v}_{PCCi}\|_2 \rightarrow \langle P_{PCC1}, Q_{PCC1}, \dots, P_{PCCN}, Q_{PCCN} \rangle, \mathbb{R} \rightarrow \mathbb{R}^{2N} \quad (5.2)$$

The structure preservation is not sustained when *Morphism 1* is producing a non-zero imaginary valued L_2 norm. Then, the decision that this anomaly is due to an intrusion or not is based on authenticating the set-point passing for upper layer into *Morphism 2* (i.e., the generalized $P - V$ curve expressed in (5.3)).

$$g : \langle P_{PCC1}, Q_{PCC1}, \dots, P_{PCCN}, Q_{PCCN} \rangle \rightarrow \|\vec{v}_{PCCi}\|_2, \mathbb{R}^{2N} \rightarrow \mathbb{R} \quad (5.3)$$

If the structure of *Morphism 2* is not preserved i.e., non-zero imaginary valued L_2 in

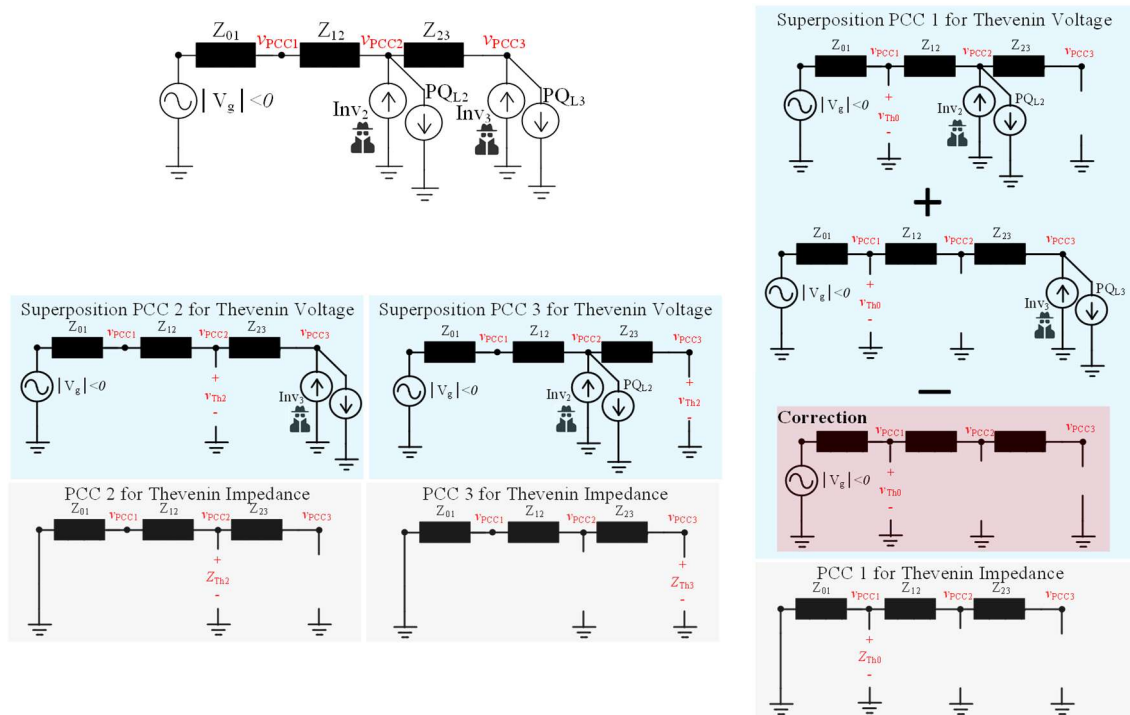


Figure 5.5. Four bus single-phase PEDG considered for illustrating the operation regions graphically in scenario I.

Morphism 2, then definitely the upper network set-point are compromised. Furthermore, Figure 5.3 shows the details of the intrusion detection system. Specifically, the *Morphism 1* and *Morphism 2* in Figure 5.3 produce a binary output 1 when their structure preservation are not sustained (i.e., both L_2 norms produce a non-zero imaginary part). Otherwise, the *Morphism 1* and *Morphism 2* produce binary output 0. Then, these two signals pass through a NAND gate to ignore or consider the upper layer set-point request. If intrusion happened the DEGs operate in alternative control scheme that corrects the local PCC voltage terminal using *Morphism 2*. Additionally, see 5.6.3 for Morphism background. 5.6.4 proves having a none-zero imaginary part in the L_2 norm means that the set-points belong to UOR and structural preservation of *Morphism 2* is no sustained.

5.3.2. Safe Operation Region “i.e., Morphism 2”

To understand how the PEDG stability is impacted by grid-feeding inverters’ set-points variations; in this subsection, an illustration of how a single grid-feeding inverter (i.e., representing an unobservable DEG at the grid edge) impacts its local PCC voltage in a general single-phase network is carried out. In this situation, the network is reduced to two buses where the i^{th} targeted grid-feeding inverter sees the rest of the network from its local PCC terminals as a large synchronous impedance in series connection with a Thevenin voltage source (see Figure 5.4). This Thevenin voltage source (\vec{v}_{Thi}) is embedding the rest of the network PQ set-points. Then, the relation between the Thevenin voltage (\vec{v}_{Thi}) and the local PCC voltage for the i^{th} grid-feeding inverter (\vec{v}_{PCCi}) is given by,

$$\vec{v}_{PCCi} = (R_{Thi} + j\omega L_{Thi})\vec{i}_{PCCi} + \vec{v}_{Thi} \quad (5.4)$$

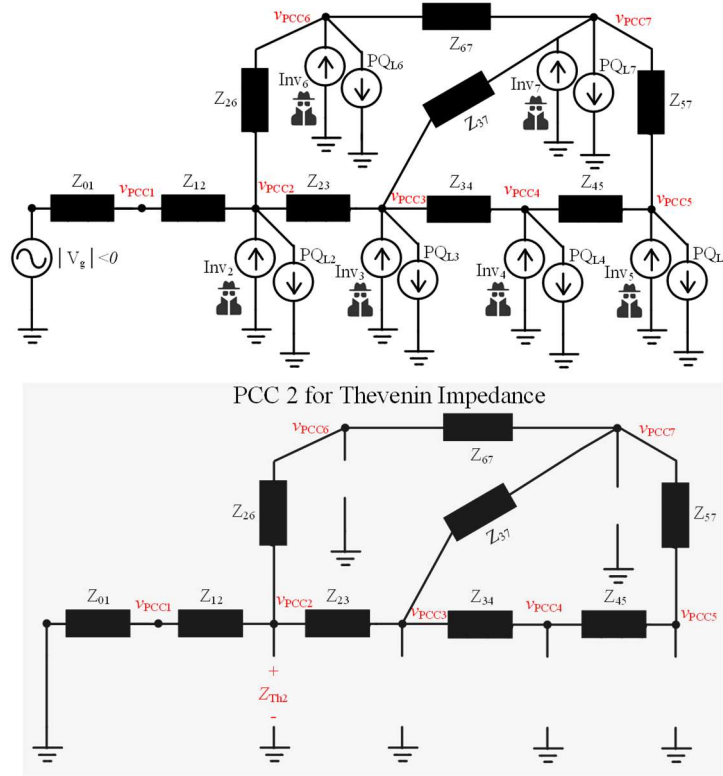


Figure 5.6. Eight bus single-phase PEDG example and the Thevenin impedance of PCC2.

where R_{Thi} is the Thevenin resistance seen by the i^{th} grid-feeding inverter from its local PCC terminals to the main PCC bus terminal, L_{Thi} is the Thevenin inductance seen by the i^{th} grid-feeding inverter from its local PCC terminals to the main PCC bus terminals, ω is the nominal angular frequency of the network, and \vec{i}_{PCCi} is the current injected by the i^{th} grid-feeding inverter into its local PCC terminals. Furthermore, in equation (5.2) the local PCC voltage is as (5.5).

$$\vec{v}_{PCCi} = \|V_{PCCi}\|_2 \angle \delta_{PCCi} = A_i + jB_i \quad (5.5)$$

Similarly, the Thevenin voltage is given by,

$$\vec{v}_{Thi} = \|V_{Thi}\|_2 \angle \delta_{Thi} = \|V_{Thi}\|_2 \cos(\delta_{Thi}) + j \|V_{Thi}\|_2 \sin(\delta_{Thi}) \quad (5.6)$$

To relate the local PCC voltage (\vec{v}_{PCCi}) to the dispatched PQ set-points of the i^{th} targeted grid-feeding inverter; the local PCC current (\vec{i}_{PCCi}) can be written as (5.7).

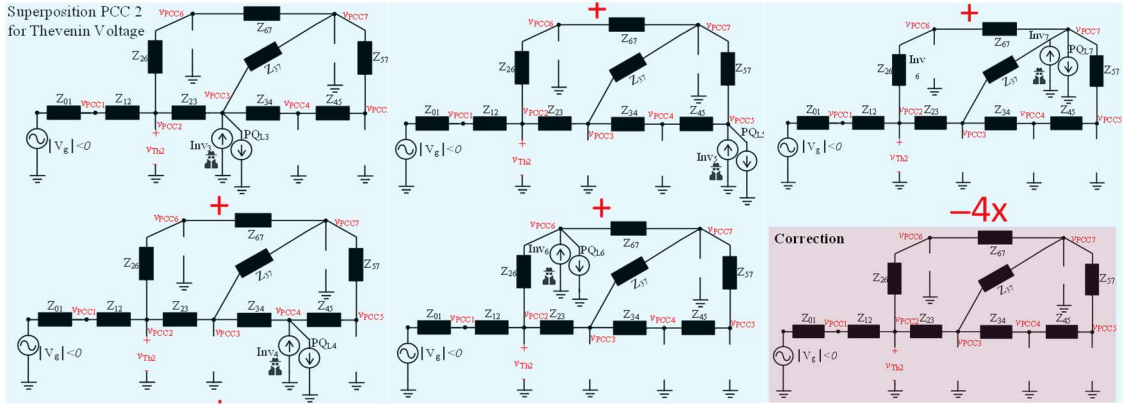


Figure 5.7. Eight bus single-phase PEDG example with the correction for Thevenin voltage on superposition theory to obtain PCC2.

$$\bar{i}_{PCCi} = \left((P_i^{Ref} - P_{Li}) - j(Q_i^{Ref} - Q_{Li}) \right) \bar{v}_{PCCi}^*{}^{-1} = (P_{PCCi} - jQ_{PCCi}) \bar{v}_{PCCi}^*{}^{-1} \quad (5.7)$$

Where \bar{v}_{PCCi}^* is the complex conjugate of \bar{v}_{PCCi} , P_i^{Ref} is the dispatched active power reference by the i^{th} targeted grid-feeding inverter, Q_i^{Ref} is the dispatched reactive power reference i^{th} targeted grid-feeding inverter, P_{Li} is the active power load at the i^{th} targeted local PCC bus, Q_{Li} is the reactive power load at the i^{th} targeted local PCC bus, P_{PCCi} is the net injected active power at the i^{th} targeted local PCC bus, and Q_{PCCi} is the net injected reactive power at the i^{th} targeted local PCC. Combining (5.7) and (5.4) results in (5.8).

$$\bar{v}_{PCCi} = (R_{Thi} + j\omega L_{Thi})(P_{PCCi} - jQ_{PCCi}) \bar{v}_{PCCi}^*{}^{-1} + \bar{v}_{Thi} \quad (5.8)$$

Then, multiplying (6) by the complex conjugate of \bar{v}_{PCCi} results in (5.9).

$$\bar{v}_{PCCi} \bar{v}_{PCCi}^* = (R_{Thi} + j\omega L_{Thi})(P_{PCCi} - jQ_{PCCi}) + \bar{v}_{Thi} \bar{v}_{PCCi}^* \quad (5.9)$$

The key point from reaching to (5.9) is that the left-hand side (LHS) is all real valued terms. In other words, the imaginary part is zero. This is an obvious resultant form multiplication of the local PCC phasor voltage by its complex conjugate. Thereby, (5.9) can be rewritten as (5.10).

$$A_i^2 + B_i^2 = R_{Thi}P_{PCCi} + \omega L_{Thi}Q_{PCCi} + \|V_{Thi}\|_2 (A_i \cos(\delta_{Thi}) + B_i \sin(\delta_{Thi})) + j(\omega L_{Thi}P_{PCCi} - R_{Thi}Q_{PCCi} + \|V_{Thi}\|_2 (A_i \sin(\delta_{Thi}) - B_i \cos(\delta_{Thi}))) \quad (5.10)$$

Then, by equating the real parts of the LHS and right-hand side (RHS) of (5.10); (5.11) is deduced.

$$A_i^2 + B_i^2 = R_{Thi}P_{PCCi} + \omega L_{Thi}Q_{PCCi} + A_i \|V_{Thi}\|_2 \cos(\delta_{Thi}) + B_i \|V_{Thi}\|_2 \sin(\delta_{Thi}) \quad (5.11)$$

Similarly, by equating the imaginary parts of the LHS and RHS of (5.10); (5.12) is obtained.

$$0 = \omega L_{Thi}P_{PCCi} - R_{Thi}Q_{PCCi} + A_i \|V_{Thi}\|_2 \sin(\delta_{Thi}) - B_i \|V_{Thi}\|_2 \cos(\delta_{Thi}) \quad (5.12)$$

Now, from (5.11) and (5.12) a solution of A_i and B_i parameters can be determined. Recall that these parameters construct the real and the imaginary component of the i^{th} targeted local PCC voltage given previously by (5.5). B_i is written in term of A_i from (5.12) as expressed in (5.13).

$$B_i = (\omega L_{Thi}P_{PCCi} - R_{Thi}Q_{PCCi}) \|V_{Thi}\|_2^{-1} \sec(\delta_{Thi}) + A_i \tan(\delta_{Thi}) \quad (5.13)$$

For finding a solution for A_i ; from combining (5.13) and (5.11) this parametric quadratic equation expressed in (5.14) can be solved.

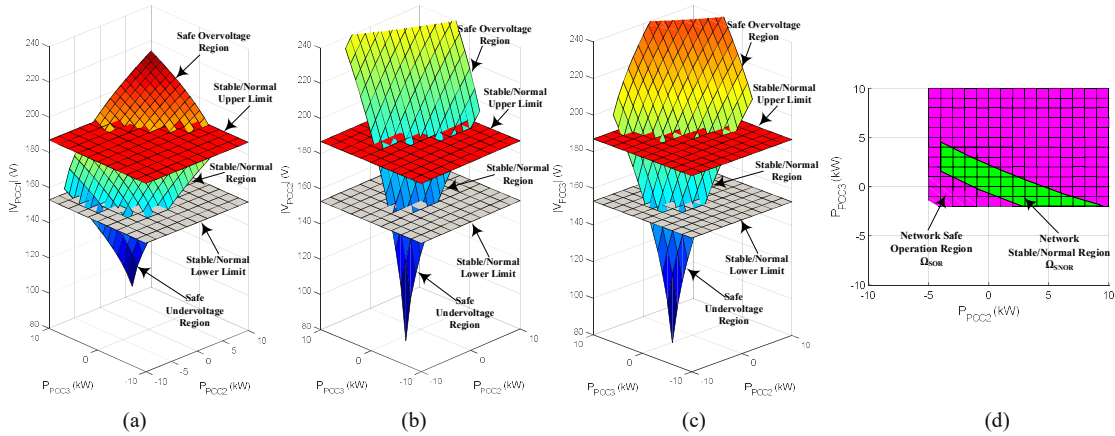


Figure 5.8. Operation regions of (a) PCC 1, (b) PCC 2, (c) PCC 3, and (d) SOR and SNOR of the four PCC bus single-phase PEDG for scenario I.

$$A_i^2 - A_i \left(2(R_{Thi}Q_{PCCi} - \omega L_{Thi}P_{PCCi})\|V_{Thi}\|_2^{-1} \sin(\delta_{Thi}) \right) + \left((\omega L_{Thi}P_{PCCi} - R_{Thi}Q_{PCCi})\|V_{Thi}\|_2^{-1} \right)^2 \quad (5.14)$$

$$-(R_{Thi}P_{PCCi} + \omega L_{Thi}Q_{PCCi})\cos^2(\delta_{Thi}) - (\omega L_{Thi}P_{PCCi} - R_{Thi}Q_{PCCi})\cos(\delta_{Thi})\sin(\delta_{Thi}) = 0$$

where

$$a = 1$$

$$, b = -\left(2(R_{Thi}Q_{PCCi} - \omega L_{Thi}P_{PCCi})\|V_{Thi}\|_2^{-1} \sin(\delta_{Thi}) + \|V_{Thi}\|_2 \cos(\delta_{Thi}) \right)$$

$$, c = \left((\omega L_{Thi}P_{PCCi} - R_{Thi}Q_{PCCi})\|V_{Thi}\|_2^{-1} \right)^2 - (R_{Thi}P_{PCCi} + \omega L_{Thi}Q_{PCCi})\cos^2(\delta_{Thi}) - (\omega L_{Thi}P_{PCCi} - R_{Thi}Q_{PCCi})\cos(\delta_{Thi})\sin(\delta_{Thi})$$

Theoretically, equation (5.14) has two bifurcation solutions. However, only the solution with a positive sign root is practical. This is because if the grid-feeding inverter is not injecting any current at its local PCC terminals, the local PCC voltage must be equal to the Thevenin voltage. While the impractical solution is giving a contradictory result of $\vec{v}_{PCCi} = 0$. The solution for A_i is given in (5.15).

$$A_i = \frac{0.5\|V_{Thi}\|_2 \cos(\delta_{Thi}) + (R_{Thi}Q_{PCCi} - \omega L_{Thi}P_{PCCi})\|V_{Thi}\|_2^{-1} \sin(\delta_{Thi})}{\sqrt{0.25\|V_{Thi}\|_2^2 \cos^2(\delta_{Thi}) + \left((\omega L_{Thi}P_{PCCi} - R_{Thi}Q_{PCCi})\|V_{Thi}\|_2^{-1} \right)^2 \sin^2(\delta_{Thi}) + (\omega L_{Thi}P_{PCCi} - R_{Thi}Q_{PCCi})\cos(\delta_{Thi})\sin(\delta_{Thi}) - \left((\omega L_{Thi}P_{PCCi} - R_{Thi}Q_{PCCi})\|V_{Thi}\|_2^{-1} \right)^2 + (R_{Thi}P_{PCCi} + \omega L_{Thi}Q_{PCCi})\cos^2(\delta_{Thi})}} \quad (5.15)$$

Furthermore, the solution for B_i is given in (16).

$$B_i = (\omega L_{Thi}P_{PCCi} - R_{Thi}Q_{PCCi})\|V_{Thi}\|_2^{-1} \sec(\delta_{Thi}) + 0.5\|V_{Thi}\|_2 \sin(\delta_{Thi}) + (R_{Thi}Q_{PCCi} - \omega L_{Thi}P_{PCCi})\|V_{Thi}\|_2^{-1} \sin(\delta_{Thi}) \tan(\delta_{Thi}) + \tan(\delta_{Thi}) \sqrt{\frac{0.25\|V_{Thi}\|_2^2 \cos^2(\delta_{Thi}) + \left((\omega L_{Thi}P_{PCCi} - R_{Thi}Q_{PCCi})\|V_{Thi}\|_2^{-1} \right)^2 \sin^2(\delta_{Thi}) + (\omega L_{Thi}P_{PCCi} - R_{Thi}Q_{PCCi})\cos(\delta_{Thi})\sin(\delta_{Thi})}{-\left((\omega L_{Thi}P_{PCCi} - R_{Thi}Q_{PCCi})\|V_{Thi}\|_2^{-1} \right)^2 + (R_{Thi}P_{PCCi} + \omega L_{Thi}Q_{PCCi})\cos^2(\delta_{Thi})}} \quad (5.16)$$

now, $\|\vec{v}_{PCCi}\|_2 = \sqrt{A_i^2 + B_i^2}$ describes the SOR of the i^{th} targeted local PCC bus in a three-dimensional surface for a given Thevenin representation of the rest of network. In this case, the SOR of the targeted i^{th} PCC bus is the projection of the surface on the P_{PCCi} and Q_{PCCi} plane where $\|\vec{v}_{PCCi}\|_2 \in \mathbb{R}$. Also, subspace of the stable/normal operation region

(SNOR) is described by projection of the surface with co-domain of $\|\vec{v}_{PCCi}\|_2 \|\vec{v}_g\|_2^{-1} \in [0.8, 1.2]$ on the P_{PCCi} and Q_{PCCi} plane. On the other hand, any operation set-points that satisfies $\|\vec{v}_{PCCi}\|_2 \notin \mathbb{R}$ is in the UOR (see the proof in 5.6.4). Yet, these operation regions cannot be utilized. As finding the Thevenin voltage of the rest of the network requires repeated load flow solutions.

To extend this analysis to closed-form, the inclusion of nearby PCC buses PQ set-points on the i^{th} targeted PCC bus is deliberated by finding the expression of the Thevenin voltage in (5.6) as a function of all the other grid-feeding inverters PQ set-points except the targeted i^{th} grid-feeding inverter. In fact, with such consideration the targeted PCC voltage is expressed with a multi-dimensional manifold. This process is repeated for every local PCC bus in the network and then the intersection of all PCC buses SOR is considered as the whole PEDG SOR (i.e., *Morphism 2* expressed in (5.3)) Note that, *Morphism 2* closed-form is developed mathematically in the next subsection. Whereas, *Morphism 1* that is expressed in (5.2)) cannot be derived in closed-form its $\mathbb{R} \rightarrow \mathbb{R}^{2N}$ mapping structure preservation is measured through observing the imaginary-part of the PCC voltage L_2 norm.

5.3.3. Graphical Example of Morphism 2 Derivation

The inclusion of nearby grid-feeding inverters (i.e., DEGs) influence is determined by finding the closed form solution of the Thevenin voltage depicted (5.4)-(5.16). To understand this, an example is taken here of the PEDG network shown in Figure 5.5. This example can be extended to any network with an arbitrary number of grid-feeding inverters. In this case, the Thevenin voltage of the grid-feeding inverter at local PCC bus 2

is as (5.17). Then, this Thevenin voltage is combined with (5.15) and (5.16) considering the index i equal to 2.

$$\begin{aligned}
\|\vec{v}_{PCC2}\|_2 &= \sqrt{A_2^2 + B_2^2}, \vec{v}_{Th_2} = (\vec{v}_{Bus3} - \vec{v}_g)(Z_{Th_2})(Z_{Th_3})^{-1} + \vec{v}_g, \vec{v}_g = \|V_g\|_2 \angle 0 \\
\vec{v}_{Bus3} &= 0.5\|V_g\|_2 + j(R_{Th_3}Q_{PCC3} - \omega L_{Th_3}P_{PCC3})\|V_g\|_2^{-1} \\
&+ \sqrt{0.25\|V_g\|_2^2 - \left((R_{Th_3}Q_{PCC3} - \omega L_{Th_3}P_{PCC3})\|V_g\|_2^{-1}\right)^2 + (R_{Th_3}P_{PCC3} + \omega L_{Th_3}Q_{PCC3})} \\
Z_{Th_2} &= Z_{01} + Z_{12}, R_{Th_2} = \text{Re}\{Z_{Th_2}\}, L_{Th_2} = \text{Im}\{Z_{Th_2}\}\omega^{-1} \\
Z_{Th_3} &= Z_{01} + Z_{12} + Z_{23}, R_{Th_3} = \text{Re}\{Z_{Th_3}\}, L_{Th_3} = \text{Im}\{Z_{Th_3}\}\omega^{-1}
\end{aligned} \tag{5.17}$$

Similarly, the voltage at the local PCC bus 3 is a function of all PQ set-points in the network and can be described by (5.15) and (5.16) with index i equal to 3 and (5.18).

$$\begin{aligned}
\|\vec{v}_{PCC3}\|_2 &= \sqrt{A_3^2 + B_3^2}, \vec{v}_{Th_3} = \vec{v}_{Bus2} \\
\vec{v}_{Bus2} &= 0.5\|V_g\|_2 + j(R_{Th_2}Q_{PCC2} - \omega L_{Th_2}P_{PCC2})\|V_g\|_2^{-1} + \\
&\sqrt{0.25\|V_g\|_2^2 - \left((R_{Th_2}Q_{PCC2} - \omega L_{Th_2}P_{PCC2})\|V_g\|_2^{-1}\right)^2 + (R_{Th_2}P_{PCC2} + \omega L_{Th_2}Q_{PCC2})}
\end{aligned} \tag{5.18}$$

Also, the voltage at main PEDG bus is a function of all PQ set-points in the network and described by (5.19).

$$\begin{aligned}
\|\vec{v}_{PCC1}\|_2 &= \left\| (\vec{v}_{Bus2} - \vec{v}_g)(Z_{Th_0})(Z_{Th_2})^{-1} + (\vec{v}_{Bus3} - \vec{v}_g)(Z_{Th_0})(Z_{Th_3})^{-1} + \vec{v}_g \right\|_2 \\
Z_{Th_0} &= Z_{01}, R_{Th_0} = \text{Re}\{Z_{Th_0}\}, L_{Th_0} = \text{Im}\{Z_{Th_0}\}\omega^{-1}
\end{aligned} \tag{5.19}$$

In this example, each PCC bus is five dimensional manifold. A correction is needed in finding the main PEDG multi-dimensional manifold. This correction is related to the usage of the source \vec{v}_g twice in the superposition analysis. Furthermore, this correction is depicted graphically in Figure 5.5. This correction can be applied to any general network architecture radial or mesh. In fact, a more complex PEDG network is taken as an example to illustrate this correction on superposition theory application for obtaining local PCC bus 2 Thevenin voltage in Figure 5.6. Furthermore, the Thevenin voltage for local PCC bus 2 is summation of \vec{v}_{Th2} in all the five equivalent circuits shown in Figure 5.7. However, the

correction in this example is to subtract four times the impact of \vec{v}_g on the local PCC bus 2. This approach allows obtaining local PCC bus 2 as a function of all PEDG PQ set-points. Note that, this analysis focused on superposition is because the basis of this analysis is on repetitive utilization of subsection 5.3.2.

Without loss of generality, let us consider Q_{PCC2} and Q_{PCC3} are zero. Then, the realization of the different operation regions for each local PCC bus in Figure 5.5 is reduced from a five-dimensional manifold to a three-dimensional surface depicted in Figure 5.8(a), (b) and (c) for each PCC bus. Let Ω_{SOR_1} be the projection of the surface \vec{v}_{PCC_1} on the P_{PCC2} and P_{PCC3} plane. Then, SOR for PCC₁ bus described by (5.20).

$$\Omega_{\text{SOR}_1} \triangleq \text{Proj}_{P_2, Q_2, P_3, Q_3,} \left(\|\vec{v}_{PCC_1}\|_2 \right) \mid \|\vec{v}_{PCC_1}\|_2 \in \mathbb{R}; \forall P_2, Q_2, P_3, Q_3 \in \mathbb{R} \quad (5.20)$$

Similarly, SORs (Ω_{SOR_2}) and (Ω_{SOR_3}) for PCC2 and PCC3 are described in (5.21) and (5.22), respectively.

$$\Omega_{\text{SOR}_2} \triangleq \text{Proj}_{P_2, Q_2, P_3, Q_3,} \left(\|\vec{v}_{PCC_2}\|_2 \right) \mid \|\vec{v}_{PCC_2}\|_2 \in \mathbb{R}; \forall P_2, Q_2, P_3, Q_3 \in \mathbb{R} \quad (5.21)$$

$$\Omega_{\text{SOR}_3} \triangleq \text{Proj}_{P_2, Q_2, P_3, Q_3,} \left(\|\vec{v}_{PCC_3}\|_2 \right) \mid \|\vec{v}_{PCC_3}\|_2 \in \mathbb{R}; \forall P_2, Q_2, P_3, Q_3 \in \mathbb{R} \quad (5.22)$$

The SNORs of each PCC bus (i.e., Ω_{SNOR_1} , Ω_{SNOR_2} , and Ω_{SNOR_3}) is a subspace of the SOR described by (5.23)-(5.25).

$$\Omega_{\text{SNOR}_1} \triangleq \text{Proj}_{P_2, Q_2, P_3, Q_3,} \left(\|\vec{v}_{PCC_1}\|_2 \right) \mid \|\vec{v}_{PCC_1}\|_2 \|\vec{v}_g\|_2^{-1} \in [0.8, 1.2] \quad (5.23)$$

$$\forall P_2, Q_2, P_3, Q_3 \in \mathbb{R}$$

$$\Omega_{\text{SNOR}_2} \triangleq \text{Proj}_{P_2, Q_2, P_3, Q_3,} \left(\|\vec{v}_{PCC_2}\|_2 \right) \mid \|\vec{v}_{PCC_2}\|_2 \|\vec{v}_g\|_2^{-1} \in [0.8, 1.2] \quad (5.24)$$

$$\forall P_2, Q_2, P_3, Q_3 \in \mathbb{R}$$

$$\Omega_{\text{SNOR}_3} \triangleq \text{Proj}_{P_2, Q_2, P_3, Q_3,} \left(\|\vec{v}_{PCC_3}\|_2 \right) \mid \|\vec{v}_{PCC_3}\|_2 \|\vec{v}_g\|_2^{-1} \in [0.8, 1.2] \quad (5.25)$$

$$\forall P_2, Q_2, P_3, Q_3 \in \mathbb{R}$$

Therefore, the network SOR (Ω_{SOR}) is given by (5.26).

$$\Omega_{\text{SOR}} \triangleq \Omega_{\text{SOR}_1} \cap \Omega_{\text{SOR}_2} \cap \Omega_{\text{SOR}_3} \quad (5.26)$$

Then, the subspace of the network SNOR (Ω_{SNOR}) is as (5.27).

$$\Omega_{\text{SNOR}} \triangleq \Omega_{\text{SNOR}_1} \cap \Omega_{\text{SNOR}_2} \cap \Omega_{\text{SNOR}_3} \quad (5.27)$$

The network SOR (Ω_{SOR}) is depicted in Figure 5.8(d) and the network SNOR (Ω_{SNOR}) is depicted by the green area in Figure 5.8(d).

5.4. Cyber Intrusion Detection System and Situational Awareness Improvement Based on Morphism 1 And Morphism 2

Summary of the designed IDS at the primary layer is illustrated in Figure 5.3. This IDS is leveraging the developed SOR. Initially, an anomalous i^{th} local PCC voltage is considered by the voltage monitoring system once the *Morphism 1* is violated. Meaning that, a non-zero imaginary-part in the PCC voltage L_2 norm is observed. Hence, the morphism 2 is not producing $\mathbb{R} \rightarrow \mathbb{R}^{2N}$ mapping. Remember that it is not possible to derive a closed-form compact solution for *Morphism 1*. Recall that, L_2 norm properties nonnegativity, definiteness, triangle inequality, and homogeneity must be satisfied in SOR for PCC voltage (see subsection 5.6.4 for the proof). In fact, inspecting the non-zero imaginary-part test validates holding nonnegativity property of the PCC voltage L_2 norm and the mapping structure preservation. *Morphism 2* is utilized for independent decision making at the primary layer of the DEG during cyber intrusion scenarios. *Morphism 2* is an alternative for the secondary layer when the dispatched set-points are not trusted. In fact, directly after detection of an anomaly by *Morphism 1*, *Morphism 2*: is used to validate if the mapping is satisfying $\mathbb{R}^{2N} \rightarrow \mathbb{R}$ in the primary layer with the closed-form solution provided in subsection 5.3.2. If also *Morphism 2* is not providing $\mathbb{R}^{2N} \rightarrow \mathbb{R}$ mapping; the

set-points passing from the secondary layer are disregarded and the grid-feeding inverters are changing the set-points and monitor if the local PCC voltage of the bus is regaining safe operation (i.e., move the network to SOR).

The steps to generate the analytic expression of each PCC bus in the single-phase PEDG as a function of all the network DEGs' PQ operation set-points are as follows:

1 - Each local PCC bus can be described by (5.15) and (5.16). These equations include the remaining non-targeted PCC buses operation set-points in the Thevenin voltage expression.

2 - Then, finding the Thevenin voltage expression analytically requires application of superposition multiple times. However, a correction must be done at the end to eliminate the effect of using some sources multiple times. The repetition of these sources is used for sake of solvability. In other words, this approach is followed to utilize repetitively the analogy introduced in subsection 5.3.2.

3 - After that, for each local PCC bus a multi-dimensional manifold is acquired. These manifolds are used to define the SOR of each local PCC bus when $\|\vec{v}_{PCCi}\|_2 \in \mathbb{R}$ is satisfied (This is the developed *Morphism 2* when $\mathbb{R}^{2N} \rightarrow \mathbb{R}$). This is graphically representing the projection of the manifold on the independent variables domain. Also, the subspace that defined SNOR is the projection portion of SOR where the co-domain is $\|\vec{v}_{PCCi}\|_2 \|\vec{v}_g\|_2^{-1} \in [0.8,1.2]$. In addition, any operation point outside SOR is in UOR of the local PCC bus, i.e., $\|\vec{v}_{PCCi}\|_2 \notin \mathbb{R}$.

4 - The intersection of all local PCC SORs obtains the SOR of the whole single-phase PEDG. This SOR region is used to enable understanding compromised secondary control

layer dispatched PQ set-points that are passing to the primary control layer of the unobservable DEGs.

The challenge that might arise is finding the Thevenin impedance or reduction of the impedance network during each stage of superposition, if it is non-solvable due to network connection complexity. This can be elucidated with using the general two point impedance theory introduced in [175], [176] by using the network Laplacian matrix (see 5.6.5).

5.5. Validation on Intrusion Detection System Performance

The theoretical analyses established are validated by simulation of two scenarios. In these two scenarios, the DEGs in the multi-layer controlled PEDG network are rated

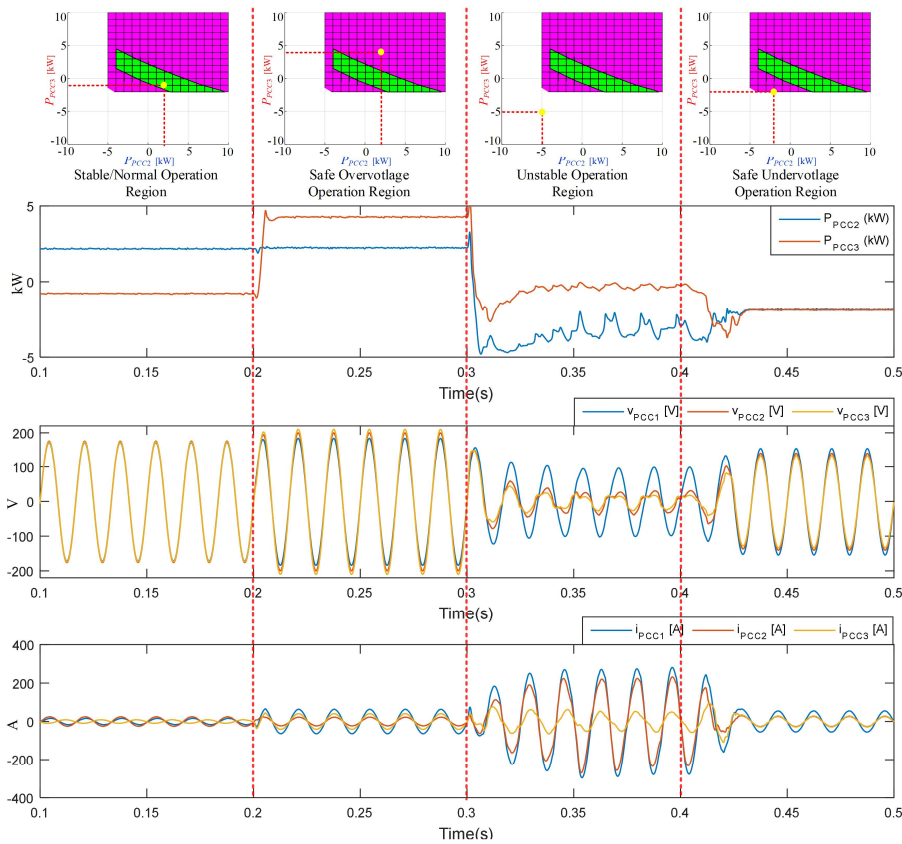


Figure 5.9. Scenario I effectiveness using the identified real-time operation regions for intrusion detection in PEDG of Figure 5.5.

Table 10. Individual Grid-Feeding Inverter DEGs Ratings

Parameter	Symbol	Value
Rated Power	S_{Rated}	20 kVA
Switching Frequency	f_{sw}	10 kHz
Nominal Grid Frequency	ω	376.8 rad/s
Voltage Peak	V_g	171 V
DC-Bus Voltage	V_{DCi}	420 V
DC-link Capacitor	C_{DCi}	2 mF
Filter Inductor	L_i	0.5 mH
Filter Inductor Resistance	R_i	0.05 Ω

according to Table 10. Particularly, the inverters representing DEGs in the PEDG are rated to 10 kVA, 60 Hz nominal frequency operation, 10 kHz switching frequency, 420 V DC link voltage, and 0.5 mH filter inductor. These DEGs are controlled in grid-feeding mode of operation through the primary current control scheme illustrated above in Figure 5.3.

5.5.1. Malicious Cyber-Attack Scenario I

The malicious cyber-attack scenario depicted in Figure 5.9 validates the operation regions derived and shows the effectiveness of using these operation regions for intrusion detection. Initially, the single-phase PEDG of Figure 5.5 is operating in the network SNOR with $P_{PCC2} = 2$ kW, $P_{PCC3} = -1$ kW (see Figure 5.9 from 0.1 s to 0.2 s). Then, the intruder manipulates the DEGs operation set-points passing from the secondary control layer by utilizing the reserved generation (i.e., PV power reserve, or energy storage) at PCC2. The new operation set-points results in surplus of 4 kW at PCC2 bus (see Figure 5.9 from 0.2 s to 0.3 s). At this duration, the PEDG is moved to the overvoltage SOR and the attacker

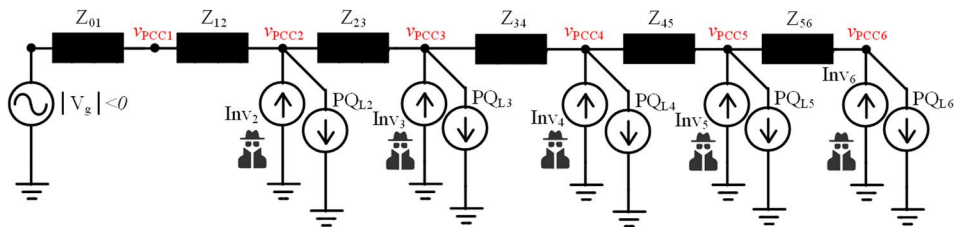


Figure 5.10. Seven bus single phase PEDG for scenario II

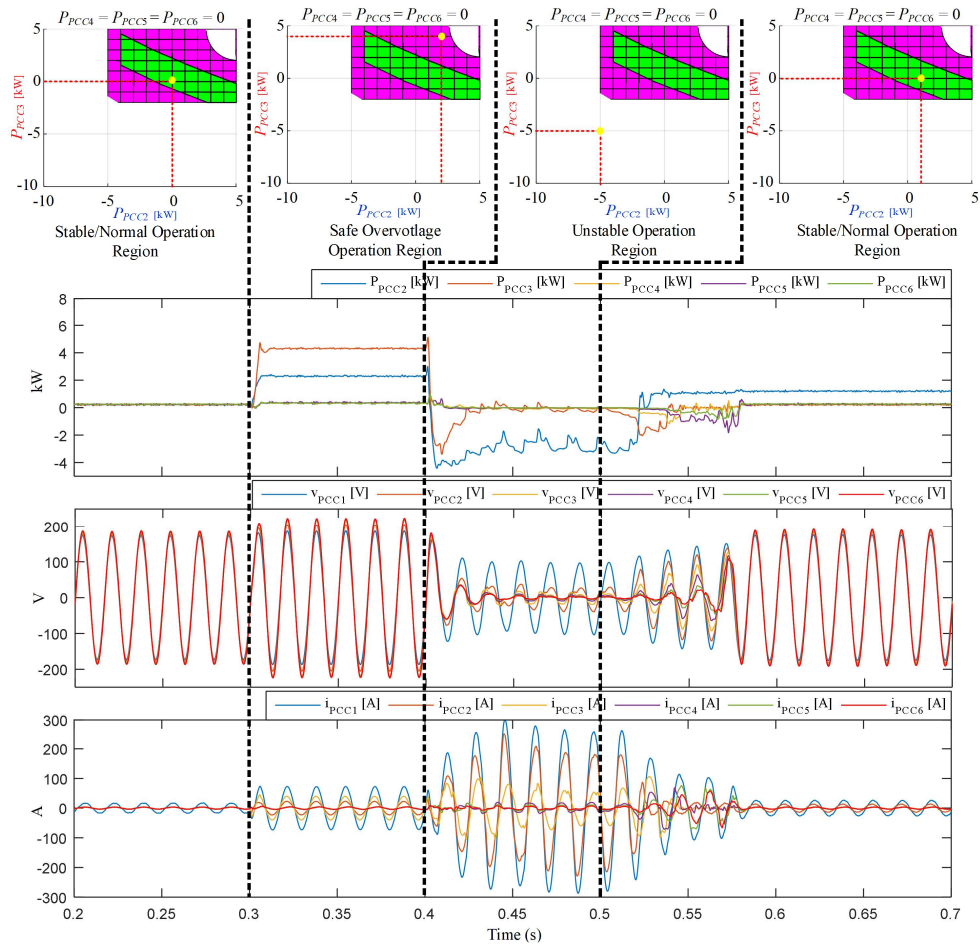


Figure 5.11. Scenario II for the seven bus single-phase PEDG shown in Figure 5.10 the PEDG operator is utilizing the operation regions after detecting anomalous voltage at PCC2 and PCC3.

fails to jeopardize the operation of the network also the IDS is not performing any action as no anomalous voltage is observed. After that, at time instant 0.3 s in Figure 5.9 the attacker manipulates the generation at PCC2 and PCC3 by reducing the generation so the net power appearing at PCC2 and PCC3 is -5 kW. Now, the PEDG is witnessing unstable operation seen in the voltage waveforms, power oscillations, and overcurrent after 0.3 s in Figure 5.9. In this situation, the IDS catches through *Morphism 2* and *Morphism 1* mapping nature that the last operation set-points belong to the UOR. After that, PCC2 and PCC3 grid-feeding inverter are controlling their local PCC voltage through the set-points and

disregard the PEDG secondary layer dispatched set-points after 0.4 s in Figure 5.9. The new operation PQ set-points are obtained by using the generation reserved at PCC2 and PCC3 to 2 kW and 4 kW. As consequence, the PEDG regains operation in the undervoltage SOR after 0.4 s in Figure 5.9.

5.5.2. Malicious Cyber-Attack Scenario II

Now, for the scenario of the PEDG with seven buses that is shown in Figure 5.10, each local PCC bus is described with eleven dimensional manifolds. Furthermore, in this scenario initially the PEDG is operating in the SNOR of the network (see Figure 5.11

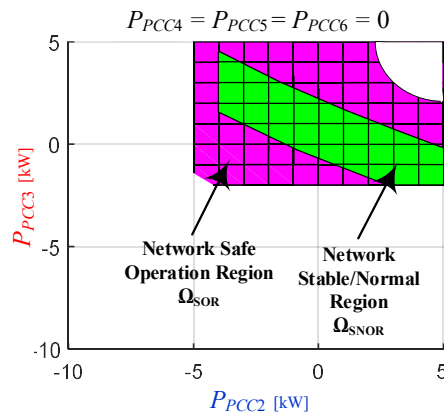


Figure 5.12. Seven bus single phase PEDG for scenario II operation regions.

before time instant 0.3 s). All consumers DEGs are meeting their local loads and not injecting any power into their local PCC terminals. After that, power reversal occurs at PCC2 and PCC3 after time instant 0.3 s in Figure 5.11 due to a manipulation by a cyber intruder at the secondary layer. At this duration, the set-points 2 kW for PCC2 4 kW for PCC3 belong to the SOR and the intruder fails to jeopardize the network operation. Then, after 0.4 s in Figure 5.11, PCC2 and PCC3 are pushed to unstable operation by the intruder. This new operation set-point -5 kW for PCC2 and PCC3 are in the UOR and the intruder

is successful to induce an unstable operation. The IDS will alert the DEG that an anomalous voltage is detected, then the DEGs are moved to local primary control mode based on PCC voltage condition to push the PEDG to the SNOR (see Figure 5.11 after time instant 0.5 s). For this example, the local PCC buses and the main PEDG bus eleven dimensional manifolds are described by (5.28) – (5.33).

$$\|\bar{v}_{PCC1}\|_2 = \left\| \bar{v}_g + \sum_{i=2}^6 (\bar{v}_{Busi} - \bar{v}_g)(Z_{Th0})(Z_{Thi})^{-1} \right\|_2, \bar{v}_g = |V_g| \angle 0 \quad (5.28)$$

$$\begin{aligned} \bar{v}_{Busi} = & 0.5 \|V_g\|_2 + j(R_{Thi} Q_{PCCi} - \omega L_{Thi} P_{PCCi}) \|V_g\|_2^{-1} + \\ & \sqrt{0.25 \|V_g\|_2^2 - \left((R_{Thi} Q_{PCCi} - \omega L_{Thi} P_{PCCi}) \|V_g\|_2^{-1} \right)^2 + (R_{Thi} P_{PCCi} + \omega L_{Thi} Q_{PCCi})} \\ Z_{Thi} = & \sum_{x=0, y=1}^{x=N-1, y=N} Z_{xy}, R_{Thi} = \text{Re}\{Z_{Thi}\}, L_{Thi} = \text{Im}\{Z_{Thi}\} \omega^{-1}, N = 6 \end{aligned}$$

$$\|\bar{v}_{PCC2}\|_2 = \sqrt{A_2^2 + B_2^2}, \bar{v}_{Th2} = \bar{v}_g + \sum_{i=3}^6 (\bar{v}_{Busi} - \bar{v}_g)(Z_{Th2})(Z_{Thi})^{-1} \quad (5.29)$$

$$\|\bar{v}_{PCC3}\|_2 = \sqrt{A_3^2 + B_3^2}, \bar{v}_{Th3} = \bar{v}_{Bus2} + \sum_{i=4}^6 (\bar{v}_{Busi} - \bar{v}_g)(Z_{Th3})(Z_{Thi})^{-1} \quad (5.30)$$

$$\|\bar{v}_{PCC4}\|_2 = \sqrt{A_4^2 + B_4^2}, \bar{v}_{Th4} = \bar{v}_{Bus2} + \bar{v}_{Bus3} - \bar{v}_g + \sum_{i=5}^6 (\bar{v}_{Busi} - \bar{v}_g)(Z_{Th4})(Z_{Thi})^{-1} \quad (5.31)$$

$$\|\bar{v}_{PCC5}\|_2 = \sqrt{A_5^2 + B_5^2}, \bar{v}_{Th5} = (\bar{v}_{Bus6} - \bar{v}_g)(Z_{Th5})(Z_{Th6})^{-1} - 2\bar{v}_g + \sum_{i=2}^4 \bar{v}_{Busi} \quad (5.32)$$

$$\|\bar{v}_{PCC6}\|_2 = \sqrt{A_6^2 + B_6^2}, \bar{v}_{Th6} = -3\bar{v}_g + \sum_{i=2}^5 \bar{v}_{Busi} \quad (5.33)$$

The SOR and SNOR of each PCC bus is described in (5.34) and (5.35), respectively.

$$\begin{aligned} \Omega_{SOR_i} \triangleq & \text{Proj}_{P_2, Q_2, \dots, P_6, Q_6, \left(\|\bar{v}_{PCC_i}\|_2 \right)} \left| \|\bar{v}_{PCC_i}\|_2 \in \mathbb{R} \right. \\ & \forall P_2, Q_2, \dots, P_6, Q_6 \in \mathbb{R} \end{aligned} \quad (5.34)$$

$$\begin{aligned} \Omega_{SNOR_i} \triangleq & \text{Proj}_{P_2, Q_2, \dots, P_6, Q_6, \left(\|\bar{v}_{PCC_i}\|_2 \right)} \left| \|\bar{v}_{PCC_i}\|_2 \|\bar{v}_g\|_2^{-1} \in [0.8, 1.2] \right. \\ & \forall P_2, Q_2, \dots, P_6, Q_6 \in \mathbb{R} \end{aligned} \quad (5.35)$$

Consequently, the network SOR (Ω_{SOR}) is given by (5.36).

$$\Omega_{SOR} \triangleq \Omega_{SOR_1} \cap \Omega_{SOR_2} \cap \Omega_{SOR_3} \cap \Omega_{SOR_4} \cap \Omega_{SOR_5} \cap \Omega_{SOR_6} \quad (5.36)$$

Then, the subspace of the network SNOR (Ω_{SNOR}) is as (5.37).

$$\Omega_{\text{SNOR}} \triangleq \Omega_{\text{SNOR}_1} \cap \Omega_{\text{SNOR}_2} \cap \Omega_{\text{SNOR}_3} \cap \Omega_{\text{SNOR}_4} \cap \Omega_{\text{SNOR}_5} \cap \Omega_{\text{SNOR}_6} \quad (5.37)$$

Based on (5.28)-(5.37) the operation regions are depicted in Figure 5.12 for scenario II.

It worth mentioning that once the IDS identified malicious PQ set-point and the DEG disregard the secondary layer controller set-point assignment, the DEG network may not operate in optimal operation set-point anymore which was the task of secondary layer controller, but it prevents the collapse of the network which may have catastrophic impact on the PEDG. Thus, the objective of the proposed approach is prevention of the catastrophic grid failure and large blackouts by intrusion detection at early stage while the grid operates are being alerted for further diagnosis, devices and controllers reset, etc.

5.6. Mathematical Background and Proofs

5.6.1. Stability of the i^{th} Grid-Feeding Inverter Primary Layer Used for DEGs In The Single-Phase PEDG (Time Separation Proof)

Consider the i^{th} single-phase grid-feeding inverter that is connected to its local PCC terminals in Figure 5.1. The active power (P_i) and reactive power (Q_i) injected into the network by this inverter can be measured by using the second order generalized integrator (SOGI) presented as (5.38) and (5.39), respectively.

$$P_i = \frac{i_{PCCi}^{\alpha} v_{PCCi}^{\alpha}}{2} + \frac{i_{PCCi}^{\beta} v_{PCCi}^{\beta}}{2} \quad (5.38)$$

$$Q_i = \frac{i_{PCCi}^{\alpha} v_{PCCi}^{\beta}}{2} - \frac{i_{PCCi}^{\beta} v_{PCCi}^{\alpha}}{2} \quad (5.39)$$

By differentiating equations (5.38) and (5.39), the state-space model that includes active and reactive power as state variables can be determined,

$$\frac{dP_i}{dt} = \frac{v_{PCCi}^{\alpha}}{2} \frac{di_{PCCi}^{\alpha}}{dt} + \frac{i_{PCCi}^{\alpha}}{2} \frac{dv_{PCCi}^{\alpha}}{dt} + \frac{v_{PCCi}^{\beta}}{2} \frac{di_{PCCi}^{\beta}}{dt} + \frac{i_{PCCi}^{\beta}}{2} \frac{dv_{PCCi}^{\beta}}{dt} \quad (5.40)$$

$$\frac{dQ_i}{dt} = \frac{v_{PCCi}^\beta}{2} \frac{di_{PCCi}^\alpha}{dt} + \frac{i_{PCCi}^\alpha}{2} \frac{dv_{PCCi}^\beta}{dt} - \frac{v_{PCCi}^\alpha}{2} \frac{di_{PCCi}^\beta}{dt} - \frac{i_{PCCi}^\beta}{2} \frac{dv_{PCCi}^\alpha}{dt} \quad (5.41)$$

Furthermore, the expression for the derivatives of the stationary reference frame PCC currents i_{PCCi}^α and i_{PCCi}^β in (5.40) and (5.41) are deduced by applying Kirchhoff voltage law at the loop of common coupling depicted in Figure 5.2. Hence, the PCC currents derivatives are as (5.42) and (5.43).

$$\frac{di_{PCCi}^\alpha}{dt} = L_i^{-1} m_{\alpha i} v_{DCi} - L_i^{-1} v_{PCCi}^\alpha - L_i^{-1} R_i i_{PCCi}^\alpha \quad (5.42)$$

$$\frac{di_{PCCi}^\beta}{dt} = L_i^{-1} m_{\beta i} v_{DCi} - L_i^{-1} v_{PCCi}^\beta - L_i^{-1} R_i i_{PCCi}^\beta \quad (5.43)$$

where m_i^α and m_i^β are stationary reference frame modulation indices of the i^{th} inverter, L_i is the filter inductance of the i^{th} inverter, and R_i is the filter resistance of the i^{th} inverter. Similarly, expression of the derivatives of the stationary reference PCC voltages v_{PCCi}^α and v_{PCCi}^β in equations (5.40) and (5.41) are given as (5.44) and (5.45).

$$\frac{dv_{PCCi}^\alpha}{dt} = -\omega v_{PCCi}^\beta \quad (5.44)$$

$$\frac{dv_{PCCi}^\beta}{dt} = \omega v_{PCCi}^\alpha \quad (5.45)$$

where ω is the angular frequency of the network. Therefore, substituting (5.42), (5.43), (5.44) and (5.45) into (5.40) and (5.41) results in the time varying MIMO state-space system given by (5.46). The system is time varying because the stationary reference modulation indices m_i^α and m_i^β are multiplied by the PCC voltages. In addition, this MIMO state space control inputs are coupled in both states.

$$\begin{bmatrix} \frac{dP_i}{dt} \\ \frac{dQ_i}{dt} \end{bmatrix} = \begin{bmatrix} -R_i L_i^{-1} & -\omega \\ \omega & -R_i L_i^{-1} \end{bmatrix} \begin{bmatrix} P_i \\ Q_i \end{bmatrix} + 0.5 L_i^{-1} \begin{bmatrix} m_i^\alpha v_{DCi} v_{PCCi}^\alpha + m_i^\beta v_{DCi} v_{PCCi}^\beta - \|\vec{v}_{PCCi}\|_2^2 \\ m_i^\alpha v_{DCi} v_{PCCi}^\beta - m_i^\beta v_{DCi} v_{PCCi}^\alpha \end{bmatrix} \quad (5.46)$$

where $\|\vec{v}_{PCCi}\|_2^2$ is the L_2 norm of \vec{v}_{PCCi} . However, if the two inputs are defined as (5.47) and (5.48), then, the state-space in (5.46) transform into a simple linear time invariant (LTI) MIMO state-space as (5.47).

$$u_{P_i} = m_i^\alpha v_{DCi} v_{PCCi}^\alpha + m_i^\beta v_{DCi} v_{PCCi}^\beta - \|\vec{v}_{PCCi}\|_2^2 \quad (5.47)$$

$$u_{Q_i} = m_i^\alpha v_{DCi} v_{PCCi}^\beta - m_i^\beta v_{DCi} v_{PCCi}^\alpha \quad (5.48)$$

$$\begin{bmatrix} \frac{dP_i}{dt} \\ \frac{dQ_i}{dt} \end{bmatrix} = \begin{bmatrix} -R_i L_i^{-1} & -\omega \\ \omega & -R_i L_i^{-1} \end{bmatrix} \begin{bmatrix} P_i \\ Q_i \end{bmatrix} + 0.5 L_i^{-1} \begin{bmatrix} u_{P_i} \\ u_{Q_i} \end{bmatrix} \quad (5.49)$$

now, consider the error on the instantaneous active and reactive power for the i^{th} inverter as (5.50) and (5.51),

$$e_{P_i} = P_{Refi} - P_i \quad (5.50)$$

$$e_{Q_i} = Q_{Refi} - Q_i \quad (5.51)$$

where P_{Refi} is the reference commanded active power and Q_{Refi} is the reference commanded reactive power. Moreover, the cancellation of the coupling terms in (5.49) is achieved by taking the following control law that includes feedback and feedforward as (5.52) and (5.53).

$$u_{P_i} = \underbrace{2L_i \omega Q_i}_{\text{Feedforward}} + \underbrace{2L_i v_{P_i}}_{\text{Feedback}} \quad (5.52)$$

$$u_{Q_i} = \underbrace{-2L_i \omega P_i}_{\text{Feedforward}} + \underbrace{2L_i v_{Q_i}}_{\text{Feedback}} \quad (5.53)$$

The feedback term v_P in (5.52) is obtained with a Proportional Integral (PI) controller as (5.54) that tracks the desired active power reference.

$$v_{P_i} = K_{P_i} e_{P_i} + K_{I_i} \int_0^t e_{P_i}(\tau) d\tau \quad (5.54)$$

Similarly, the feedback term v_Q in (5.53) is deduced with a PI controller as (5.55), this PI controller assures tracking the desired reactive power reference.

$$v_{Q_i} = K_{Q_i} e_{Q_i} + K_{I_i} \int_0^t e_{Q_i}(\tau) d\tau \quad (5.55)$$

Moreover, substituting (5.54) into (5.52) and then placing the resulting expression into (5.49) yields the error dynamics of the active power that is given by (5.56).

$$\frac{de_{p_i}}{dt} = -(K_{P_{pi}} + R_i L_i^{-1})e_{p_i} - K_{P_{pi}} \int_0^t e_{p_i}(\tau) d\tau \quad (5.56)$$

Likewise, inserting (5.55) into (5.53) and then substituting the resulting expression into (5.49) yields the error dynamics of the reactive power as (5.57).

$$\frac{de_{q_i}}{dt} = -(K_{Q_{pi}} + R_i L_i^{-1})e_{q_i} - K_{Q_{pi}} \int_0^t e_{q_i}(\tau) d\tau \quad (5.57)$$

The active and reactive power error dynamics in (5.58) and (5.59) indicate that if the controller gains $K_{P_{pi}}$, $K_{P_{ii}}$, $K_{Q_{pi}}$ and $K_{Q_{ii}}$ are positive, the primary control layer is exponentially globally asymptotically stable. This is proved by linear quadratic Lyapunov stability theorem as follows, (5.56) and (5.57) are expressed by the state-space (5.58).

$$\begin{aligned} \frac{dx_{CL_i}}{dt} &= A_{CL_i} x_{CL_i} \\ x_{CL_i} &\in \mathbb{R}^4, A_{CL_i} \in \mathbb{R}^{4 \times 4} \\ x_{CL_i} &= \begin{bmatrix} e_{p_i} & \frac{de_{p_i}}{dt} & e_{q_i} & \frac{de_{q_i}}{dt} \end{bmatrix}^T \\ A_{CL_i} &= \begin{bmatrix} 0 & 1 & 0 & 0 \\ -K_{P_{ii}} & -(K_{P_{pi}} + R_i L_i^{-1}) & 0 & 0 \\ 0 & 0 & 0 & 1 \\ 0 & 0 & -K_{Q_{ii}} & -(K_{Q_{pi}} + R_i L_i^{-1}) \end{bmatrix} \end{aligned} \quad (5.58)$$

Then, to prove the stability of the closed loop control, the selection of a positive definite symmetrical matrix ($Q_{CL_i} \in \mathbb{R}^{4 \times 4}$), results in a positive definite symmetrical matrix ($P_{CL_i} \in \mathbb{R}^{4 \times 4}$) for satisfying the (5.59).

$$P_{CL_i} A_{CL_i} + A_{CL_i}^T P_{CL_i} + Q_{CL_i} = 0 \quad (5.59)$$

To show this, the selection of $Q_{CL_i} = I^{4 \times 4}$ ($I^{4 \times 4}$ is the identity matrix with dimension of 4x4) which is a positive definite symmetrical matrix. The solution of (5.59) will be as given in (5.60).

$$P_{CL_i} = \begin{bmatrix} \Theta_{11} & 0.5\Theta_{12} & 0 & 0 \\ -0.5\Theta_{12} & \Theta_{22} & 0 & 0 \\ 0 & 0 & \Lambda_{11} & 0.5\Lambda_{12} \\ 0 & 0 & -0.5\Lambda_{12} & \Lambda_{22} \end{bmatrix} \quad (5.60)$$

$$\Theta_{11} = K_{Pii}^2 + (K_{Ppi} + R_i L_i^{-1})^2 + K_{Pii}, \Theta_{12} = K_{Pii}^{-1}, \Theta_{22} = K_{Pii}^{-1} (K_{Ppi} + R_i L_i^{-1})^{-1} - 1,$$

$$\Lambda_{11} = K_{Qii}^2 + (K_{Qpi} + R_i L_i^{-1})^2 + K_{Qii}, \Lambda_{12} = K_{Qii}^{-1}, \Lambda_{22} = K_{Qii}^{-1} (K_{Qpi} + R_i L_i^{-1})^{-1} - 1$$

If the parameters K_{Ppi} , K_{Pii} , K_{Qpi} and K_{Qii} are designed respecting the conditions shown in (5.60),

$$K_{Ppi} + R_i L_i^{-1} > 0, K_{Pii} > 0, K_{Qpi} + R_i L_i^{-1} > 0, K_{Qii} > 0 \quad (5.61)$$

Then, $P_{CL_i} > 0$ (i.e., positive definite symmetrical matrix since all leading minors and the determinant are positive). Therefore, the equilibrium point $(0, 0, 0, 0)$ is globally exponentially asymptotically stable. Hence, convergence of the error dynamics to the equilibrium point $(0, 0, 0, 0)$ means the original system is converging to $(P_{Refi}, 0, Q_{Refi}, 0)$ as $t \rightarrow \infty$. The Lyapunov candidate energy function is mathematically described in (5.62).

$$V_{CL_i}(x_{CL_i}) = x_{CL_i}^T P_{CL_i} x_{CL_i},$$

$$\frac{dV_{CL_i}(x_{CL_i})}{dx_{CL_i}} = x_{CL_i}^T (P_{CL_i} A_{CL_i} + A_{CL_i}^T P_{CL_i}) x_{CL_i}$$

$$\because A_{CL_i} < 0, P_{CL_i} > 0$$

$$\therefore V_{CL_i}(x_{CL_i}) > 0, \frac{dV_{CL_i}(x_{CL_i})}{dx_{CL_i}} < 0 \quad (5.62)$$

To retrieve the original system inputs which are the inverter stationary reference modulation indices m_i^α and m_i^β ,

$$\begin{bmatrix} m_i^\alpha \\ m_i^\beta \end{bmatrix} = \frac{1}{\|\vec{v}_{PCCi}\|_2} \begin{bmatrix} v_{PCCi}^\alpha & v_{PCCi}^\beta \\ v_{PCCi}^\beta & -v_{PCCi}^\alpha \end{bmatrix} \begin{bmatrix} \left(u_{Pi} + \|\vec{v}_{PCCi}\|_2 \right) v_{DCi}^{-1} \\ u_{Qi} v_{DCi}^{-1} \end{bmatrix} \quad (5.63)$$

L_2 norm $\|\vec{v}_{PCCi}\|_2$ in (5.63) is $\|\vec{v}_{PCCi}\|_2 \in \mathbb{R}$ in network stable conditions, since \vec{v}_{PCCi} is well-posed and the signals v_{PCCi}^α and v_{PCCi}^β are always orthogonal. Finally, the modulation index that controls the single-phase grid-feeding inverter is given as (5.64).

$$m_i = [1 \quad 1] \begin{bmatrix} m_i^\alpha \\ m_i^\beta \end{bmatrix} \quad (5.64)$$

The controller structure is illustrated in Figure 5.3.

5.6.2. Implication of L_2 Norm $\|\vec{v}_{PCCi}\|_2$ in Unstable PEDG Conditions Induced By Cyber Intruder Set-Points

The impact of unstable network conditions can be understood from the conditions where the L_2 norm $\|\vec{v}_{PCCi}\|_2$ of (5.63) is non-real or the existence of the active and reactive power measurement for the primary controller feedback in (5.38) and (5.39). Specifically, when there is an ill-posed local PCC voltage imposed on the terminals of the grid-feeding inverter due to a cyber-attacker requesting malicious set-points at the secondary control layer, the L_2 norm expressed in (5.65) belong to the complex subspace.

$$\begin{aligned} \|\vec{v}_{PCCi}\|_2 &= \sqrt{v_{PCCi}^\alpha{}^2 + v_{PCCi}^\beta{}^2} \in \mathbb{C} \\ \therefore \text{Im} \left\{ \|\vec{v}_{PCCi}\|_2 \right\} &\neq 0 \end{aligned} \quad (5.65)$$

L_2 norm $\in \mathbb{C}$ means singularity, which results in non-existing stationary reference modulation indices (i.e., no solution for (5.63)). Also, with no PCC voltage, measuring the active and reactive power by (5.38) and (5.39) for the primary controller feedback will not be possible. Hence, these unstable conditions will cause PEDG DEGs operation failure. Hence, this proves that any instability witnessed in this PEDG is originated from unstable network conditions and not from the primary control layer.

5.6.3. Morphism Terminology Linked to Safe Operation Region

A morphism is a structure-preserving map from one mathematical structure to another mathematical structure. In contemporary mathematics, the terminology morphism is an abstraction for any sort of mapping concept. For example, in linear algebra, the linear

transformation is a special type of morphism that provides a linkage between two different linear systems, in topology, a continuous function is a morphism that provides an image of a specific quantity to another quantity. For example, the voltage (v_R) and current (i_R) relation across a resistor (R) are described by the two morphisms h in (5.66) and w in (5.67) that are $\mathbb{C} \rightarrow \mathbb{C}$ mappings.

$$h: v_R \rightarrow i_R, \mathbb{C} \rightarrow \mathbb{C} \quad (5.66)$$

$$w: i_R \rightarrow v_R, \mathbb{C} \rightarrow \mathbb{C} \quad (5.67)$$

Trivially, the morphisms h and w are described deterministically in closed-form functions by Ohm's Law in (5.68) and (5.69) for a specific special case of a linear Ohmic resistor. However, the morphisms that are presented in (5.66) and (5.67) are abstraction of these structure-preserving maps from one mathematical structure (v_R) to another mathematical structure (i_R), or vice-versa.

$$h(i_R) = v_R = i_R R \quad (5.68)$$

$$w(v_R) = i_R = v_R R^{-1} \quad (5.69)$$

In other words, morphism is a generalization of all mapping used in different mathematical fields in the sense that the mathematical objects involved are not necessarily sets. In fact, the connections between them may be somewhat other than maps. Even though, intuitively the morphisms between the objects of a given category must behave equally to maps. In this chapter these concepts are borrowed for cyber intrusion detection and two morphisms are described that are extension of the $P - V$ curve and its inverse in the following subsections.

5.6.3.1. Morphism 1 "Generlization of the $P-V$ Curve Inverse"

For each PCC bus when operating in the SOR this property holds.

$$f: \|\vec{v}_{PCCi}\|_2 \rightarrow \langle P_{PCC1}, Q_{PCC1}, \dots, P_{PCCN}, Q_{PCCN} \rangle, \mathbb{R} \rightarrow \mathbb{R}^{2N} \quad (5.70)$$

(5.70) means there is some sort of mathematical mapping (i.e., morphism) that transforms the real-valued L_2 norm $\|v_{PCCi}\|_2$ to real-valued set-points $\langle P_{PCC1}, Q_{PCC1}, \dots, P_{PCCN}, Q_{PCCN} \rangle$. Morphism 1 cannot be derived in closed-form. In this chapter, its structure by being an \mathbb{R} to \mathbb{R}^{2N} mapping is observed from measuring the imaginary-part of the L_2 norm $\|\vec{v}_{PCCi}\|_2$.

5.6.3.2. Morphism 2 “Generalization of the P - V Curve”

For each PCC bus when operating in the SOR this property holds.

$$g: \langle P_{PCC1}, Q_{PCC1}, \dots, P_{PCCN}, Q_{PCCN} \rangle \rightarrow \|\vec{v}_{PCCi}\|_2, \mathbb{R}^{2N} \rightarrow \mathbb{R} \quad (5.71)$$

(5.71) is a generalization of the $P - V$ curve used for stability analysis to morphism. This morphism is describing that the set-points $\langle P_{PCC1}, Q_{PCC1}, \dots, P_{PCCN}, Q_{PCCN} \rangle$ that are real-valued are transformed to real-valued L_2 norm $\|\vec{v}_{PCCi}\|_2$. *Morphism 2* is an alternative for the secondary layer when the dispatched set-points are not trusted.

5.6.4. Proof On L_2 Norm Non-Zero Imaginary Value Indicates That the Set-Point Requested From The Upper Layer Belongs To Unstable Operation Region (UOR)

The theoretical proof behind having a non-zero imaginary part in the L_2 norm of the local PCC voltage results in concluding that the set-points belong to unstable operation region (UOR) can be understood from the following example of Figure 5.5 network. The stability margin found from a $P - V$ curve at PCC bus i by change in its self-set-point is described here for a given Thevenin representation. Consider (5.72),

$$\|\vec{v}_{PCCi}\|_2 = \frac{\|V_{Thi}\|_2}{2} + \sqrt{\frac{\|V_{Thi}\|_2^2}{4} + R_{Thi} P_{PCCi}} \quad (5.72)$$

(5.72) is an example of Morphism 2, the stability margin is found at a specific self-set-point (P_{PCCi}) when the condition (5.73) happens.

$$\left. \frac{\partial \|\bar{v}_{PCCi}\|_2}{\partial P_{PCCi}} \right| = \infty \quad (5.73)$$

Then, (5.73) is expanded to (5.74).

$$\left. \frac{\partial \|\bar{v}_{PCCi}\|_2}{\partial P_{PCCi}} \right| = \frac{R_{Thi}}{2\sqrt{\frac{\|V_{Thi}\|_2^2}{4} + R_{Thi} P_{PCCi}}} = \infty \quad (5.74)$$

This means that the stability margin at bus i due to change at it self-set-point (P_{PCCi}) is according to the following inequality shown in (5.75).

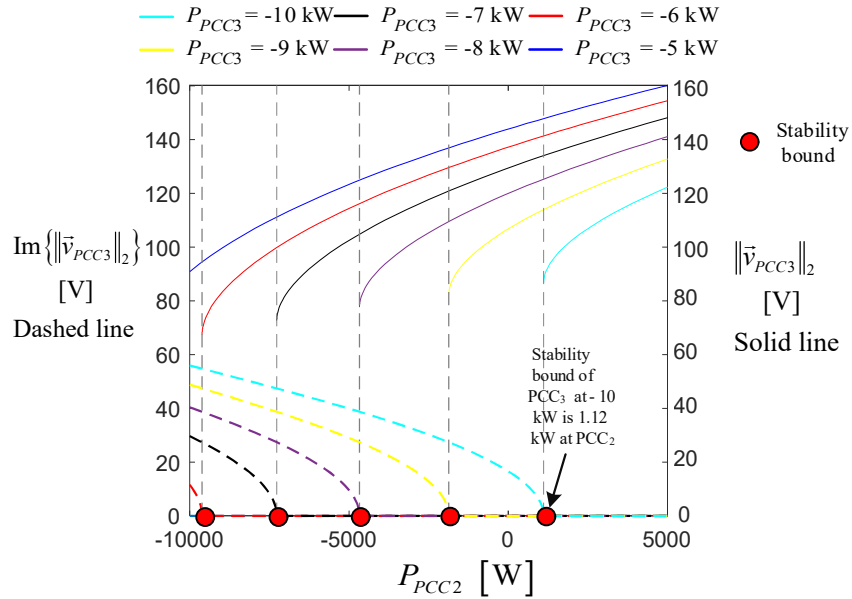


Figure 5.13. Stability margin observation from the developed generalized $P - V$ curves at local PCC bus 3 ($\|\bar{v}_{PCC3}\|_2$) (i.e., Morphism 2) showing that the after the stability margin the structure of Morphism 2 is not sustained from \mathbb{R}^{2N} to \mathbb{R} .

$$P_{PCCi} \geq -\frac{\|V_{Thi}\|_2^2}{4R_{Thi}}, \therefore P_{Stability\ Bound} = -\frac{\|V_{Thi}\|_2^2}{4R_{Thi}} \quad (5.75)$$

now, the stability margin of PCC bus i with respect to variation of the active power set-point at an adjacent bus j (P_{PCCj}) can be deduced by the same reasoning. Following the

analogy, the stability margin of PCC bus i with respect to change of the active power set-point at adjacent PCC bus j (P_{PCCj}) is direct resultant from (5.76).

$$\frac{\partial \|\bar{v}_{PCCi}\|_2}{\partial P_{PCCj}} = \infty \text{ or } \frac{\partial P_{PCCj}}{\partial \|\bar{v}_{PCCi}\|_2} = 0 \quad (5.76)$$

Equation (5.76) is expanded into (5.77).

$$\frac{\partial \|\bar{v}_{PCCi}\|_2}{\partial P_{PCCj}} = \frac{1}{2} \frac{\partial \|V_{Thi}\|_2}{\partial P_{PCCj}} + \frac{|V_{Thi}| \frac{\partial \|V_{Thi}\|_2}{\partial P_{PCCj}}}{4\sqrt{\frac{\|V_{Thi}\|_2^2}{4} + R_{Thi} P_{PCCi}}} = \infty \quad (5.77)$$

Solving (5.77) is not trivial. This is because there is no closed-form solution for Thevenin voltage and thereby there is no way to express the derivative of the i^{th} PCC bus voltage with respect to the j^{th} PCC bus active power set-point. Nevertheless, for a given network that is shown in Figure 5.5 for instance, a derivation concept is provided for the Thevenin voltage expression as function of nearby buses excluding self-set point is provided in the developed morphism 2. The internal PCC buses in Figure 5.5 are described by the manifolds (5.78) and (5.79).

$$\|\bar{v}_{PCC2}\|_2 = \frac{\|V_{Th2}\|_2}{2} + \sqrt{\frac{\|V_{Th2}\|_2^2}{4} + R_{Th2} P_{PCC2}} \quad (5.78)$$

where $\|V_{Th2}\|_2 = \left(\sqrt{\frac{\|V_g\|_2^2}{4} + R_{Th3} P_{PCC3}} - \frac{\|V_g\|_2}{2} \right) R_{Th2} R_{Th3}^{-1} + \|V_g\|_2$

$$\|\bar{v}_{PCC3}\|_2 = \frac{\|V_{Th3}\|_2}{2} + \sqrt{\frac{\|V_{Th3}\|_2^2}{4} + R_{Th3} P_{PCC3}} \quad (5.79)$$

where $\|V_{Th3}\|_2 = \sqrt{\frac{\|V_g\|_2^2}{4} + R_{Th2} P_{PCC2}} + \frac{\|V_g\|_2}{2}$

(5.79) is an example on the proposed generalized $P - V$ curve (i.e., *Morphism 2*) for the internal PCC bus 3 in the network in Figure 5.5. Furthermore, this Morphism 2 is plotted in Figure 5.13. Specifically, the Morphism 2 structure preservation is not sustained as seen

in Figure 5.13 after passing the set-point that belongs to the UOR. Moreover, the stability margin can be found in closed-form as in (5.80) for bus 3 with respect to bus 2 of Figure 5.5 network.

$$\frac{\partial \|\vec{v}_{PCC3}\|_2}{\partial P_{PCC2}} = \frac{1}{2} \frac{\partial \|V_{Th3}\|_2}{\partial P_{PCC2}} \left(1 + \frac{\|V_{Th3}\|_2}{2\sqrt{\frac{\|V_{Th3}\|_2^2}{4} + R_{Th3}P_{PCC3}}} \right) = \infty$$

$$\text{where } \|V_{Th3}\|_2 = \sqrt{\frac{\|V_g\|_2^2}{4} + R_{Th2}P_{PCC2}} + \frac{\|V_g\|_2}{2},$$

$$\frac{\partial \|V_{Th3}\|_2}{\partial P_{PCC2}} = \frac{R_{Th2}}{2\sqrt{\frac{\|V_g\|_2^2}{4} + R_{Th2}P_{PCC2}}}$$
(5.80)

The closed-form solution of (5.80) is expressed in simplified form as (5.81),

$$\frac{\partial \|\vec{v}_{PCC3}\|_2}{\partial P_{PCC2}} = \frac{\Gamma}{\Phi}$$

where

$$\Gamma = \frac{R_{Th2}}{4} \left(\frac{\left(\frac{\|V_g\|_2}{2} + \sqrt{R_{Th2}P_{PCC2} + \frac{\|V_g\|_2^2}{4}} \right)}{2} + \sqrt{P_{PCC3}R_{Th3} + \frac{\left(\frac{\|V_g\|_2}{2} + \sqrt{R_{Th2}P_{PCC2} + \frac{\|V_g\|_2^2}{4}} \right)^2}{4}} \right)$$

$$\Phi = \frac{\|V_g\|_2^2 \sqrt{R_{Th2}P_{PCC2} + \frac{\|V_g\|_2^2}{4}}}{8} + \frac{\|V_g\|_2^3}{16} + \frac{R_{Th2}\|V_g\|_2 P_{PCC2}}{4} + \frac{R_{Th2}P_{PCC2} \sqrt{R_{Th2}P_{PCC2} + \frac{\|V_g\|_2^2}{4}}}{4}$$

$$+ P_{PCC3}R_{Th3} \sqrt{R_{Th2}P_{PCC2} + \frac{\|V_g\|_2^2}{4}}$$

now, P_{PCC2} value that makes $\partial P_{PCC2} / \partial \|\vec{v}_{PCC3}\|_2$ equal to zero in (5.81) is the stability margin for bus 3 with respect to active power change at bus 2 of Figure 5.5 network. Unfortunately, this involves polynomial with an order higher than 5, finding the

deterministic roots of this polynomial is not feasible. This is proved by the fundamental theorem of Galois [143]. Galois theory provides a connection between field theory and group theory. This connection allows reducing certain problems (i.e., polynomial roots finding for our case) in field theory to group theory such as permutation group of their roots. By Galois theory, it was proven that for a polynomial roots' to be solvable by radicals and the main operations addition, subtraction, division, and multiplications; the order of the polynomial must be less than 5. Alternatively, instead of seeking for P_{PCC2} that makes the $\partial P_{PCC2} / \partial \|\vec{v}_{PCC3}\|_2$ equal to zero, the imaginary part of this derivative can be plotted by spanning the active power set-point (P_{PCC2}). The stability margin can be predicted by

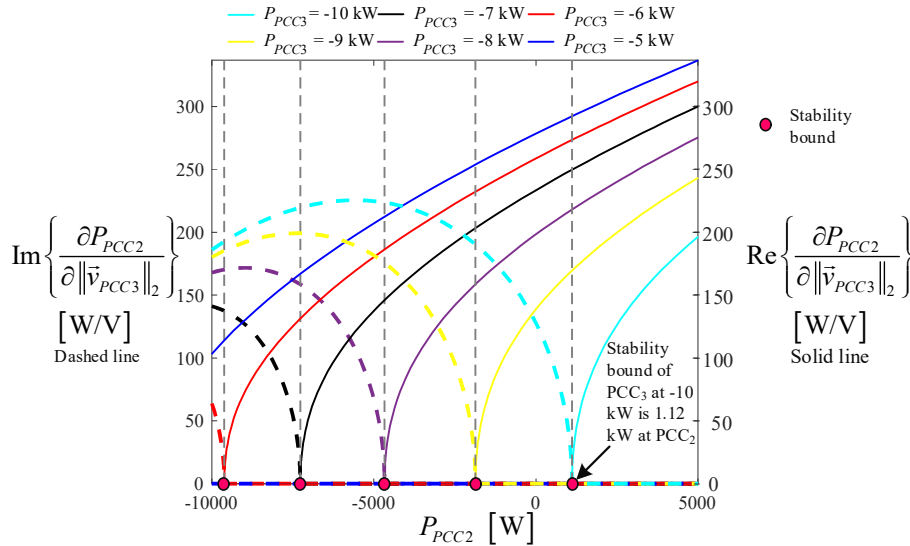


Figure 5.14. Stability margin prediction by observing the real and imaginary parts of $\partial P_{PCC2} / \partial \|\vec{v}_{PCC3}\|_2$

observing a non-zero imaginary part existence. The initial active power set-point where the imaginary value observed in $\partial P_{PCC2} / \partial \|\vec{v}_{PCC3}\|_2$ is the stability margin. This can be seen in Figure 5.14 for the network example Figure 5.5. In more details, when $P_{PCC3} = -7$ kW, the stability margin of PCC bus 3 is -7.5 kW. Meaning that, PCC bus 2 can sink maximumly

7.5 kW before PCC bus 3 reaches to instability. Note that, observing the imaginary part in Figure 5.14 shows that after the stability margin the function has a non-zero value but before hitting the stability margin the imaginary part was always zero. This gives an advantage to check whether the set-point will produce an instable voltage situation just by looking at the imaginary part of this derivative. Note that, real-valued functions cannot produce a derivative that has a non-zero imaginary part. In other words, even though these stability margins are deduced from the derivatives of *Morphism 2*, the structural preservation of the *Morphism 2* is not preserved when a non-zero imaginary part is observed at the derivative of these morphisms. Meaning that, the results are valid to provide a conclusion about the structure of *Morphism 2*.

5.6.5. The Two Point Impedance Theory Used in *Morphism 2* Analysis

This two-point impedance theory was developed to anticipate possible *LC* resonance excitation modes in a general impedance network by finding the vanishing eigenvalues in [175], [176]. The theory is leveraged to evaluate the equivalent impedance for simplifying the reduction of the network for developing *Morphism 2*.

At any reduction stage in developing *Morphism 2* for any targeted bus the network, denoted by \mathcal{L} , which consists of N nodes numbered as $\alpha = 1, 2, \dots, N$. For a given current configuration, \vec{i} , the effective impedance between two general points, p and q (Z_{pq}) can be obtained after solving the Kirchhoff equation of the network expressed in equation (5.82).

$$Y \vec{v} = \vec{i} \quad (5.82)$$

where Y is the admittance matrix (i.e., the Laplacian matrix from a graph theoretic point of view), and \vec{v} equals the network of node voltages. Specifically, the effective impedance between p and q points is given by

$$Z_{pq} = \frac{V_p - V_q}{I_\alpha / (\delta_{\alpha p} - \delta_{\alpha q})} \quad (5.83)$$

(5.83) depends on the fact that the admittance matrix, (Y) is invertible. Nevertheless, because the admittance matrix is a symmetrical matrix, Y matrix is always singular (i.e., determinant Y matrix is equal to zero).

The singularity issue of admittance matrix Y is resolved by modifying equation (5.82) into equation (5.84).

$$Y(\varepsilon)\vec{v}(\varepsilon) = \vec{i} \quad (5.84)$$

where the modified matrix $Y(\varepsilon)$ is composed of the original admittance matrix, Y , in addition to elements of value, ε , imposed on all the diagonal entries of Y as equation (5.85).

$$Y(\varepsilon) = Y + \varepsilon I \quad (5.85)$$

where I is the identity matrix. After that, the modified admittance, $Y(\varepsilon)$, is not singular.

Linear algebra theories can be applied to find the inverse of $Y(\varepsilon)$. The final step is to push the limit of the parameter, ε , to reach zero. No divergent solutions are expected to happen, as the system should have a valid physical solution. However, because the admittance matrix, $Y(\varepsilon)$, is complex, valued, and symmetrical, then (5.86) is true.

$$Y^\dagger(\varepsilon) = Y^*(\varepsilon) \neq Y(\varepsilon) \quad (5.86)$$

where $Y^\dagger(\varepsilon)$ is the Hermitian conjugate of $Y(\varepsilon)$, and $Y^*(\varepsilon)$ is the complex conjugate of $Y(\varepsilon)$. Hence, due to the property of (5.86), $Y(\varepsilon)$ is a non-diagonalizable matrix. An alternative approach to find the eigenvalues and eigenvectors of the admittance matrix, $Y(\varepsilon)$, is by considering the matrix, $Y^\dagger(\varepsilon)Y(\varepsilon)$, which is diagonalizable (5.87).

$$Y^\dagger(\varepsilon)Y(\varepsilon)\psi_\alpha(\varepsilon) = \sigma_\alpha(\varepsilon)\psi_\alpha(\varepsilon), \sigma_\alpha \geq 0, \alpha = 1, 2, \dots, N \quad (5.87)$$

The first eigenvalue is $\sigma_1(\varepsilon) = \varepsilon^2$, and the first eigenvector is $\psi_1(\varepsilon) = [1, 1, \dots, 1]^T / \sqrt{N}$.

The eigenvalues, $\sigma_\alpha(\varepsilon)$, and eigenvectors, $\psi_\alpha(\varepsilon)$ of $Y^\dagger(\varepsilon)Y(\varepsilon)$ can be converted to eigenvalues and eigenvectors of the admittance matrix, $Y(\varepsilon)$, as (5.88).

$$Y(\varepsilon)u_\alpha(\varepsilon) = \sqrt{\sigma_\alpha(\varepsilon)}e^{j\theta_\alpha(\varepsilon)}u_\alpha^*(\varepsilon), \theta_\alpha(\varepsilon) = \text{Real}, \alpha = 1, 2, \dots, N \quad (5.88)$$

Therefore, $Y(\varepsilon)$ is diagonalizable by the transformation expressed in (5.89).

$$U^T(\varepsilon)Y(\varepsilon)U(\varepsilon) = \Delta(\varepsilon) \quad (5.89)$$

where $U(\varepsilon)$ is unitary matrix with columns consisting of $u_\alpha(\varepsilon)$, and $\Delta(\varepsilon)$ is diagonal matrix with diagonal entries of $\sqrt{\sigma_\alpha(\varepsilon)}e^{j\theta_\alpha(\varepsilon)}$. Therefore, the inverse of the admittance matrix $Y(\varepsilon)$ is as (5.90).

$$Y^{-1}(\varepsilon) = U(\varepsilon)\Delta^{-1}(\varepsilon)U^T(\varepsilon) \quad (5.90)$$

Finally, (5.83) is solved to obtain (5.84) by using (5.90) as (5.91).

$$Z_{pq} = \lim_{\varepsilon \rightarrow 0} \sum_{\alpha=1}^N \frac{(u_{\alpha p}(\varepsilon) - u_{\alpha q}(\varepsilon))^2}{\sqrt{\sigma_\alpha(\varepsilon)}e^{j\theta_\alpha(\varepsilon)}} \quad (5.91)$$

where $u_{\alpha p}(\varepsilon)$ is the p th component of eigenvector, $u_\alpha(\varepsilon)$.

5.7. Conclusion

The overall objective of this chapter is to realize an IDS for a multi-layer controlled PEDG to improve the situational awareness feature. This situational awareness enhancement results in improved cybersecurity against malicious set-points requests for the upper layer. Firstly, a mathematical theory is developed for deriving a safe operation region for multiple point of common coupling (PCC) buses. This mathematical theory extends the stability margins deduced from $P - V$ curves to generalized morphisms. Particularly, there are two morphisms for each PCC bus when operating in the safe

operation region: (*Morphism 1*) PCC bus voltage mapped to network set-points that is \mathbb{R} to \mathbb{R}^{2N} mapping, and (*Morphism 2*) network set-points mapped to the PCC bus voltage that is \mathbb{R}^{2N} to \mathbb{R} mapping. *Morphism 1* is used for anomaly detection originating from the secondary layer dispatched set-points manipulation. Explicitly, observation of a non-zero imaginary-part in the PCC voltage L_2 norm is evidence of an anomaly. *Morphism 2* is utilized for independent decision making at the primary layer of the DEG during cyber intrusion scenarios. In other words, *Morphism 2* is an alternative for the secondary layer when the dispatched set-points are not trusted. Finally, two scenarios were simulated illustrating the effectiveness of the proposed theory.

Chapter 6

6. Corrective Action Post Cyberattack Operation Based on Consensus Dynamics Control

6.1. Post-Attack Operation

This chapter presents an event-triggered consensus distributed control scheme for multiple grid-following inverters (GFLIs) in a power electronics-dominated grid (PEDG). The main objective is to address the voltage and frequency stability for network of GFLIs in stealthy-cyberattack scenarios on the grid configuration shown in Figure 6.1. Particularly, the considered stealthy-cyberattack scenario is when the centralized secondary control layer dispatched set-points are compromised. The objective of the proposed event-triggered consensus distributed control is to regain normal point of common coupling (PCC) voltage and frequency levels in the PEDG. This is accomplished through distributing the reactive and active power among the GFLIs to correct the frequency and the voltage of the network. This consensus distributed control is validated with 5 different scenarios (see Figure 6.2(a)-(e)) demonstrating that the GFLIs are capable to operate independent of the secondary control layer.

6.2. Background about Consensus Dynamics Control in Power Systems

The legacy power system is evolving progressively toward the PEDG paradigm [131]. In fact, the grid-edge network now, with the support of GFLIs, can generate power. It is

projected that the utilization of GFLIs will create phenomena with fast-time scale dynamics that previously were not observed in the power grid [177]. Consequently, more rigorous control schemes are developed to optimize the power exchange between the grid-edge assets and the upper grid. For instance, the multi-layer-controlled PEDG is a good candidate for operating the grid-edge network. In this control, the primary layer of the GFLI's receives optimally dispatched set-points from the centralized secondary control layer (see Figure 6.1). This centralized control layer sent optimized set-point obtained using forecasted data for optimal frequency and voltage profile operation [178].

Nevertheless, this futuristic grid layout is vulnerable to cyber-attacks as more dispersed energy generation are deployed. For instance, security violations in the cyber-layer have an instantaneous impact on the physical layer, which disturbs nominal operation. A stealthy cyberattack spreads slowly compromising the cyber-layer and may remain hidden from intrusion detection systems until a tipping point when the grid voltage and frequency restoration become infeasible. The scope of this chapter is to provide an alternative control that can operate the PEDG without relying on the centralized secondary control layer. This

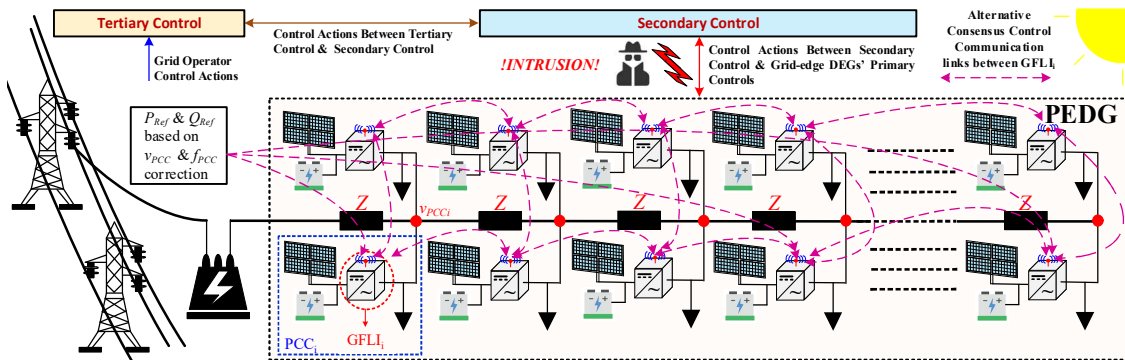


Figure 6.1. Multi-layered controlled PEDG with stealthy attacker compromising the secondary control layer and showing that the GFLIs are distributing the active and reactive power reference generated from correcting the main PEDG PCC bus voltage and frequency through a specific mesh graph.

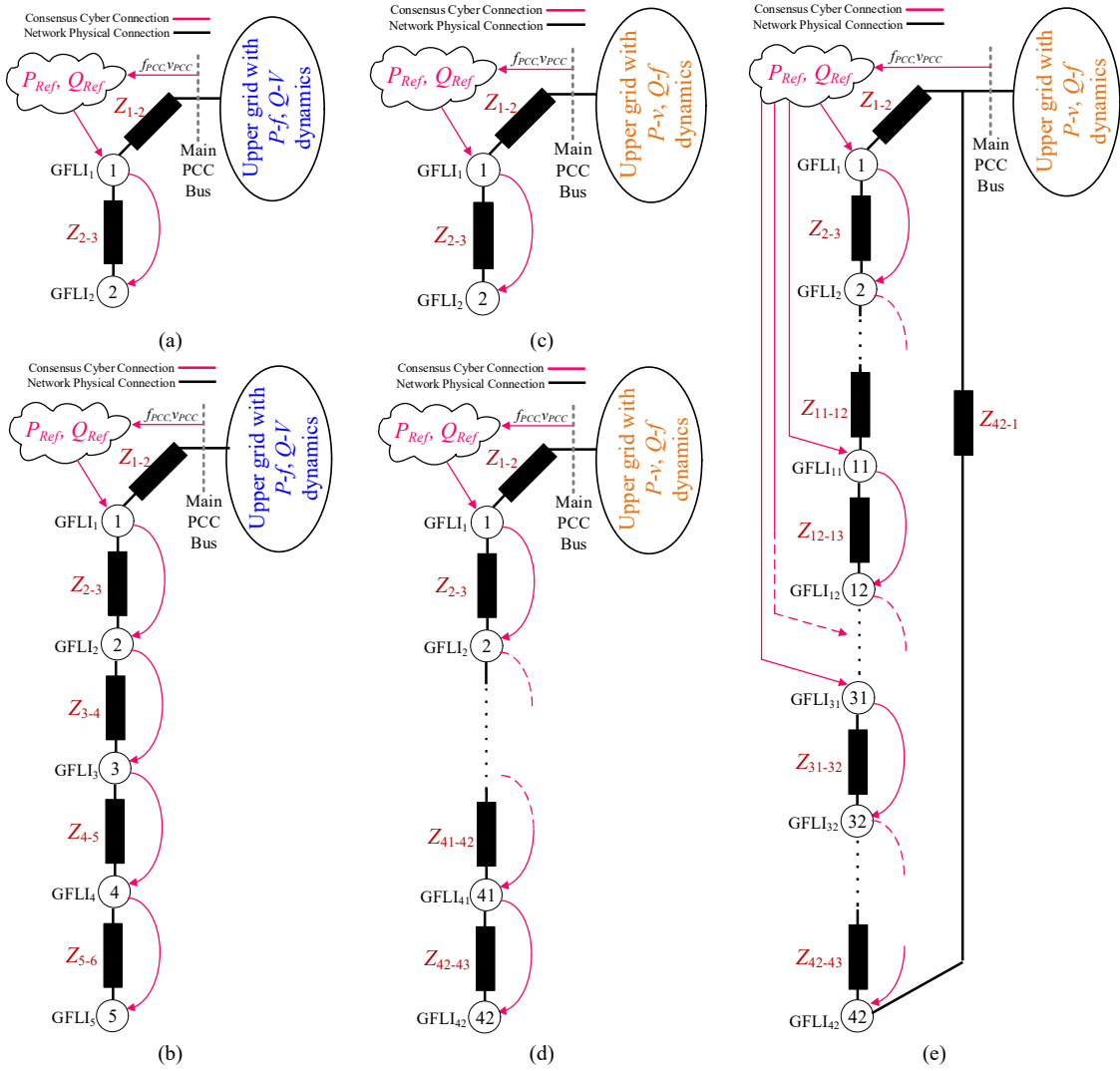


Figure 6.2. Consensus dynamics control cyber layers layout tested in this chapter: (a) scenario 1, (b) scenario 2, (c) scenario 3, (d) scenario 4, and (e) scenario 5.

alternative distributed control is based on consensus dynamics theory. Consensus control is an agreement control where all participating agents exchange information to reach a common specified target collectively. This theory is intersection of systems theory with graph theory. Mathematically, the consensus control is an unforced dynamical system that is governed by the interconnection topology and the initial condition for each participating agent. In power system, consensus control has been introduced in [179], for forcing

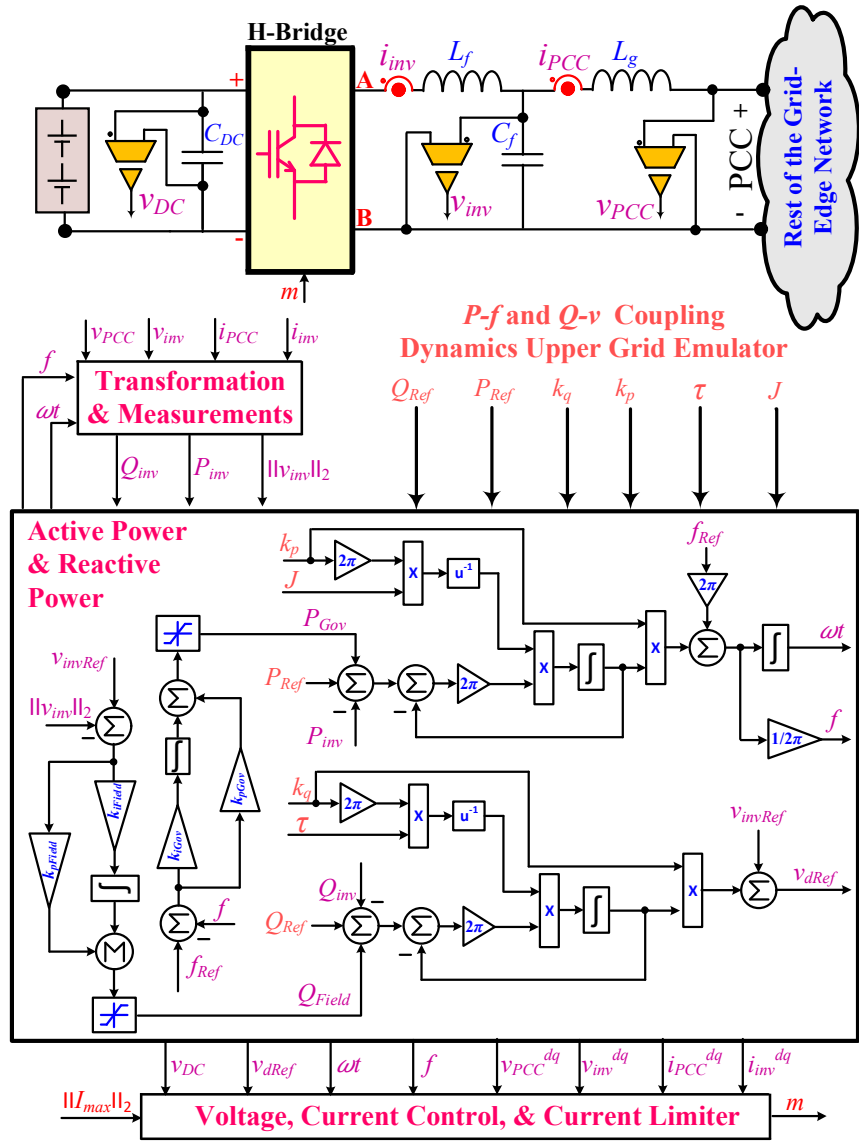


Figure 6.3. $P - f$ and $Q - v$ coupling dynamics upper grid modelling for the scenarios testing the consensus dynamics control.

multiple distributed energy resources to agree on the active power set-point requested at primary bus interconnecting the distribution system to the transmission system. Likewise, the same concept is utilized in [180] for distributing the reactive power requested by transmission system among distribution system distributed energy resources. These consensus controls are model free and have the benefit of no requirement of knowing the

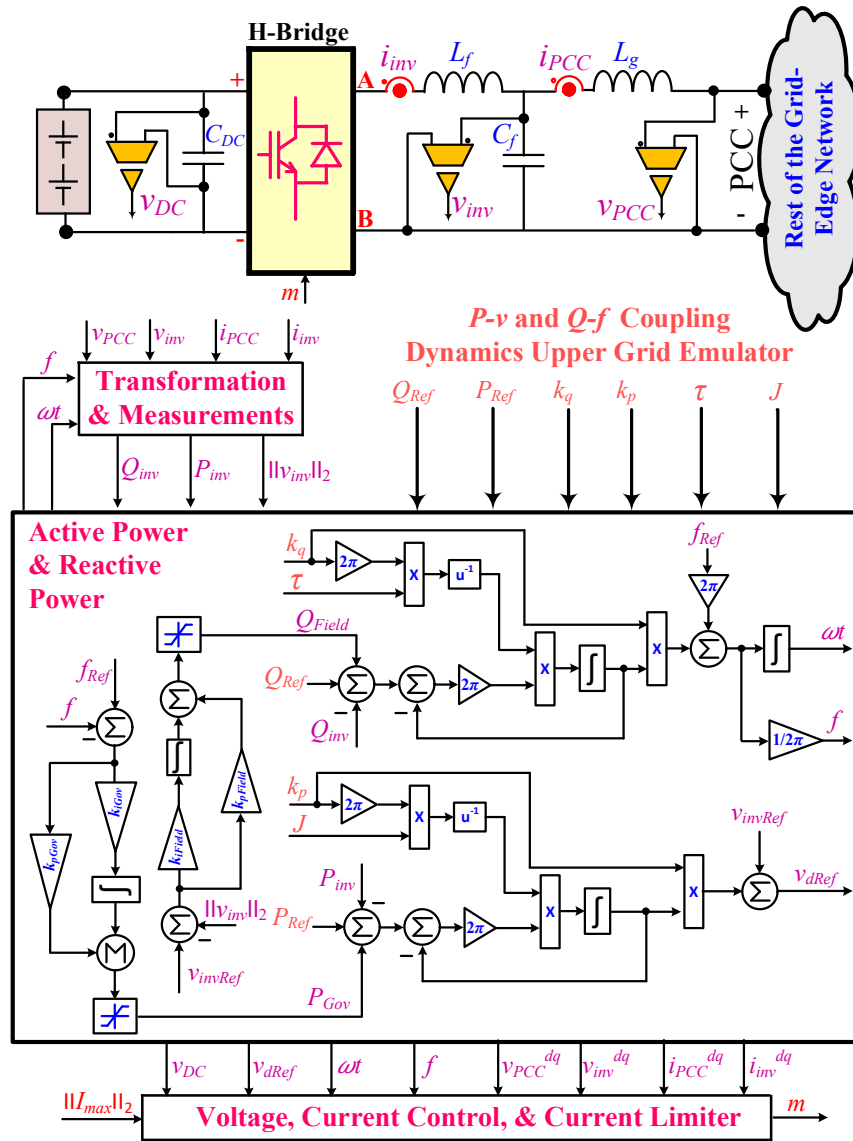


Figure 6.4. $P - v$ and $Q - f$ coupling dynamics upper grid modelling for the scenarios testing the consensus dynamics control.

detailed modeling of the distribution system. In fact, this control is based on simple integral control that is practical and acceptable in the industry [181]. This chapter is utilizing a similar concept; however, the consensus agents agree on forcing the PEDG main PCC bus to stay within acceptable frequency and voltage levels during different events independently of the secondary control layer.

6.3. Event-Triggered Consensus Distributed Control Scheme Formulation

Consider the PEDG Network depicted in Figure 6.1, during a stealthy-cyberattack scenarios the dispatched set-points of the centralized secondary control layer are disregarded. Then, the GFLIs operate in a way that the PCC bus regains normal frequency and voltage through an alternative secure communication link. This is achieved by the controller in (6.1).

$$\begin{bmatrix} \frac{dQ_{Ref}}{dt} \\ \frac{dP_{Ref}}{dt} \end{bmatrix} = \begin{bmatrix} k_f (f_{PCC}^{Ref} - \hat{f}_{PCC}) \\ k_v (v_{PCC}^{Ref} - \|\hat{v}_{PCC}\|_2) \end{bmatrix} \quad (6.1)$$

where k_f is the integral gain that corrects the frequency through reactive power control, k_v is the integral gain that corrects the voltage through active power control, f_{PCC}^{Ref} is the reference frequency, \hat{f}_{PCC} is the measured frequency, v_{PCC}^{Ref} is the reference voltage, $\|\hat{v}_{PCC}\|_2$ is the measured L_2 norm of the main PEDG main PCC bus voltage. Moreover, the GFLIs are communicating with each other through an undirected and connected graph of $\mathcal{G} = (\mathcal{V}, \mathcal{E})$, $\mathcal{V} = \{1, \dots, n\}$ with Laplacian matrix \mathcal{L} . The event-triggered consensus distributed post-attack control is described by (6.2) for $i = 1, \dots, n$.

$$\begin{bmatrix} \frac{dQ_{PCCi}}{dt} \\ \frac{dP_{PCCi}}{dt} \end{bmatrix} = \begin{bmatrix} k_Q \left(\gamma_i Q_{Ref} - \sum_{j \in \mathcal{N}_i} \mathcal{L}_{ij} (Q_{PCCj} - Q_{PCCi}) - \gamma_i Q_{PCCi} \right) \\ k_P \left(\mu_i P_{Ref} - \sum_{j \in \mathcal{N}_i} \mathcal{L}_{ij} (P_{PCCj} - P_{PCCi}) - \mu_i P_{PCCi} \right) \end{bmatrix} \quad (6.2)$$

The parameters γ_i and μ_i are vector whose value is all zero except for the GFLIs that are receiving direct communication of the vector $[Q_{Ref} \ P_{Ref}]^T$ (i.e., These GFLIs are the consensus control leading GFLIs and any other GFLI is considered as a nonleading GFLI).

produce frequency deviations, and for reactive load disturbances will cause voltage deviations. The second universal grid-forming inverter in Figure 6.4 has reverse dynamics as $P - v$ and $Q - f$. This grid-forming inverter under active load disturbances causes the voltage of the network to change, while, under reactive load disturbances the frequency of the network will be influenced. Regarding the primary current control of the GFLIs, the control is depicted in Figure 6.5. This control was developed in Chapter 2 which is PLL-less with adaptation feature to the frequency of the network.

6.4. Validations Scenario with Stability Analysis

6.4.1. Validation Scenario 1: Two GFLIs in Radial Network with Cyber Layer Layout of Figure 6.2(a)

Consider a radial network where the two integral controllers that corrects the frequency and the voltage in (6.1) and (6.2) are communicating with the PCC bus 1 GFLI₁ directly (see Figure 6.1(a)). Then, the GFLI₁ at PCC bus 1 is communicating with PCC bus 2 GFLI₂ (see Figure 6.2(a) for the cyber layer of this scenario). This system can be formulated with the following state-space in (6.3) utilizing (6.2).

$$\underbrace{\begin{bmatrix} \frac{dQ_{PCC1}}{dt} \\ \frac{dQ_{PCC2}}{dt} \\ \frac{dP_{PCC1}}{dt} \\ \frac{dP_{PCC2}}{dt} \end{bmatrix}}_{\frac{dx}{dt}} = \underbrace{\begin{bmatrix} -1-k_Q & 1 & 0 & 0 \\ 1 & -1 & 0 & 0 \\ 0 & 0 & -1-k_P & 1 \\ 0 & 0 & 1 & -1 \end{bmatrix}}_A \underbrace{\begin{bmatrix} Q_{PCC1} \\ Q_{PCC2} \\ P_{PCC1} \\ P_{PCC2} \end{bmatrix}}_x + \underbrace{\begin{bmatrix} 1 & 0 \\ 0 & 0 \\ 0 & 1 \\ 0 & 0 \end{bmatrix}}_B \underbrace{\begin{bmatrix} Q_{Ref} \\ P_{Ref} \end{bmatrix}}_u \quad (6.3)$$

The operation set-points decided by the distributed control for the GFLI₁ at PCC bus 1 are derived from the inputs of the state-space (6.3), as the following (6.4) and (6.5).

$$Q_{PCC1}(s) = \frac{s+1}{s^2 + (2+k_Q)s + k_Q} Q_{Ref}(s) \quad (6.4)$$

$$P_{PCC1}(s) = \frac{s+1}{s^2 + (2+k_P)s + k_P} P_{Ref}(s) \quad (6.5)$$

This is found from the selection of an appropriate C output matrix and utilizing $\frac{y(s)}{u(s)} = C(sI - A)^{-1}B$. Then, GFLI₂ at PCC bus 2 formulate its set-points from the operation set-points of the GFLI₁ at PCC bus 1 as (6.6) and (6.7).

$$Q_{PCC2}(s) = \frac{1}{s+1} Q_{PCC1}(s) \quad (6.6)$$

$$P_{PCC2}(s) = \frac{1}{s+1} P_{PCC1}(s) \quad (6.7)$$

The stability of the consensus dynamics control is investigated simply by checking the eigenvalues of the state space in (6.3). These eigenvalues provide evidence on the internal stability of the consensus control indicating the allowable range of the consensus control gains k_Q and k_P . Therefore, the eigenvalues of the consensus control produce a Hurwitz A matrix in (6.3) if the conditions below (6.8)-(6.11) are satisfied.

$$\text{Re} \left\{ -1 - \frac{k_Q}{2} + \sqrt{1 - \frac{k_Q^2}{4}} \right\} < 0 \quad (6.8)$$

$$\text{Re} \left\{ -1 - \frac{k_Q}{2} - \sqrt{1 - \frac{k_Q^2}{4}} \right\} < 0 \quad (6.9)$$

$$\text{Re} \left\{ -1 - \frac{k_P}{2} + \sqrt{1 - \frac{k_P^2}{4}} \right\} < 0 \quad (6.10)$$

$$\text{Re} \left\{ -1 - \frac{k_P}{2} - \sqrt{1 - \frac{k_P^2}{4}} \right\} < 0 \quad (6.11)$$

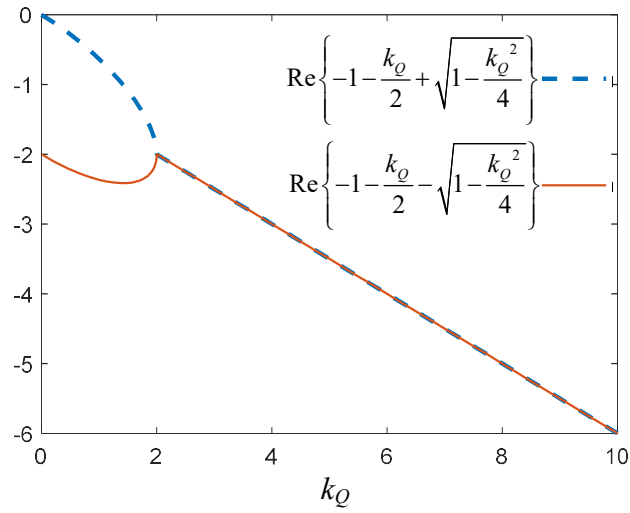


Figure 6.6. Range of consensus gain k_Q that guarantees BIBO stability

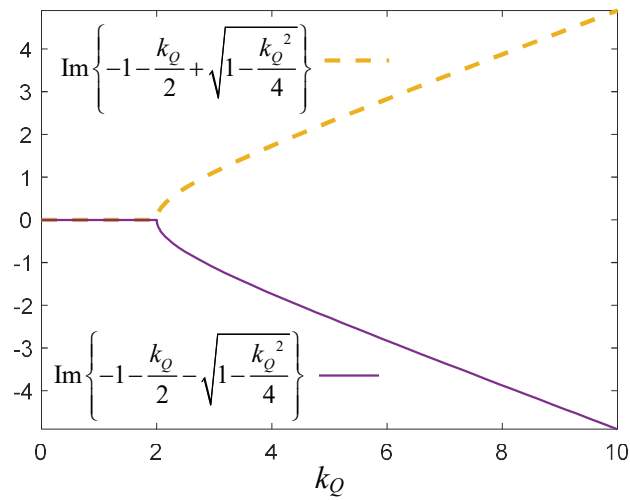


Figure 6.7. Range of consensus gain k_Q that guarantees BIBO stability that produce oscillatory behavior.

Furthermore, regarding the reachability of consensus dynamics nonleading GFLIs, firstly it can be seen that the gains that guarantees making the matrix A in (6.3) Hurwitz, is also the same eigenvalues of the leading GFLI consensus dynamics. However, for nonleading it can be deduced from (6.6) and (6.7) that both active and reactive power dynamics for the nonleading GFLI has a pole at -1. This conclude that the consensus control is stable in the

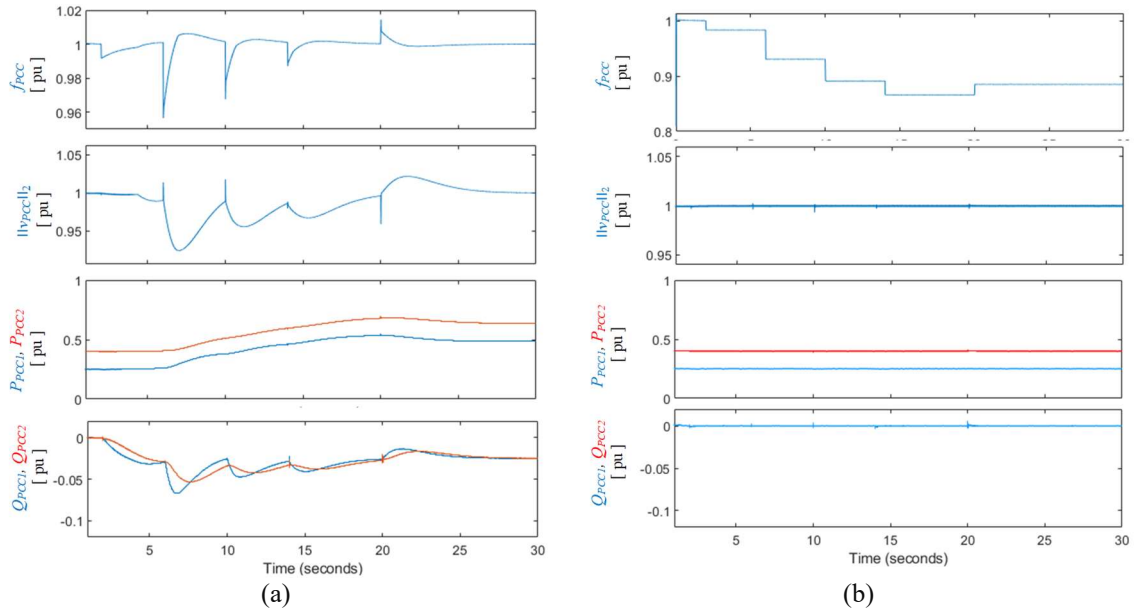


Figure 6.8. Scenario 1 the proposed distributed control performance under random disturbances in resistive radial PEDG with $GFLI_1$ at PCC bus 1 and $GFLI_2$ at PCC bus 2 with capacities of 20 kVA: (a) control is activated, and (b) control is deactivated. [frequency base is 60 Hz, voltage base is 171 V, active and reactive power base is 20 kVA]

sense of Bounded Input and Bounded Output (BIBO). In fact, assuring the Hurwitz stability property is sufficient to conclude BIBO stability. Furthermore, the example of the range of the consensus gain that produce a Hurwitz system with BIBO stability is plotted in Figure 6.6 for inequalities (6.8) and (6.9). Figure 6.6 depicts that for consensus gain k_Q in range $(0, 2]$ the response of the system is Hurwitz with no oscillatory sinusoidal behavior. However, the for consensus gain k_Q in range $[2, \infty)$ the response is Hurwitz but with an oscillatory sinusoidal behavior that is damped quickly if the consensus gain is high as evident in Figure 6.7. Note that, the conclusion regarding the gain of the active power dynamics consensus gain k_P is identical to k_Q due to the symmetry in the in the inequalities in (6.10) and (6.11) compared to (6.8) and (6.9).

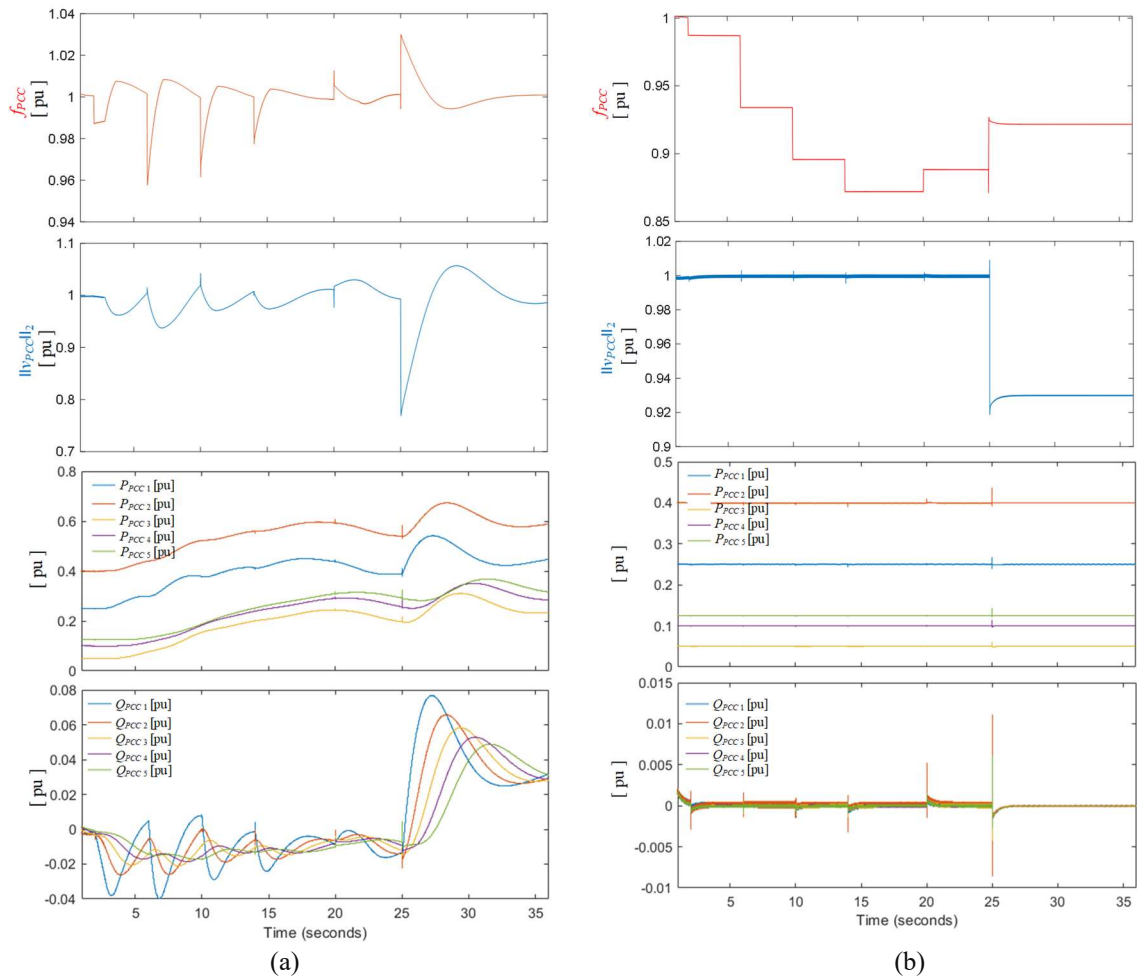


Figure 6.9. Scenario 2 the proposed distributed control performance under random disturbances in resistive radial PEDG with five GFLI with the capacities of 20 kVA: (a) control is activated, and (b) control is deactivated. [Frequency base is 60 Hz, voltage base is 171 V, active and reactive power base is 20 kVA]

This control is tested for operating the GFLIs independently from the upper layer in Figure 6.8. Particularly, in the scenario 1 shown in Figure 6.8(a), the network is operating independently of the upper layer control and the target is to maintain the main PEDG PCC bus frequency and voltage in the nominal level. It is evident in Figure 6.8(a) that the GFLIs are participating in correcting the main PCC bus voltage and frequency. In contrast, Figure 6.8(b) shows that when the event-triggered consensus distributed control is deactivated, the active load disturbances result in deviating the frequency. This example shows that the

proposed event-triggered consensus distributed control can successfully operate independently without relying on a secondary control layer.

6.4.2. Validation Scenario 2: Five GFLIs in Radial Network with Cyber Layer Layout

Figure 6.2(b)

In Figure 6.9, another example is considering for testing the proposed distributed control for a radial network with cyber layer layout as Figure 6.2(b). In this scenario, the network has five GFLIs. The integral control that corrects the frequency and voltage at the main PEDG PCC bus is communicating with GFLI at PCC bus 1, then PCC bus 1 is communicating with PCC bus 2, and PCC bus 2 with PCC bus 3, and so on (see Figure 6.2(b) for the cyber layer of this scenario). As shown in Figure 6.9 (a) the proposed control can adjust the active and reactive power injected by GFLIs with targeting correct frequency and voltage levels at the main PEDG PCC bus. In contrast, when the consensus control is

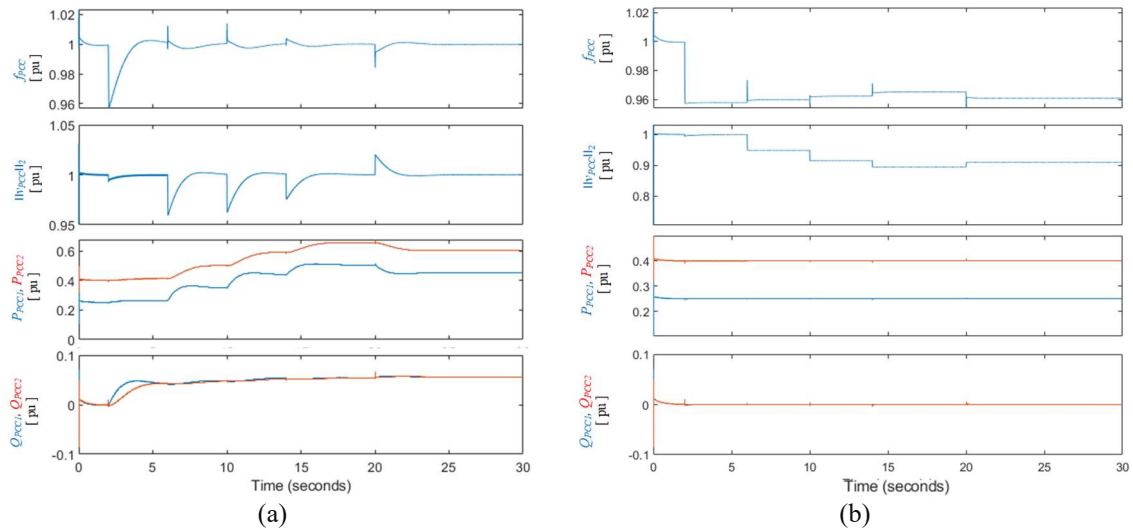


Figure 6.10. Scenario 3 the proposed distributed control performance under random disturbances in resistive radial PEDG reverse coupling dynamics $P - V$ and $Q - f$ with GFLI₁ at PCC bus 1 and GFLI₂ at PCC bus 2 with capacities of 20 kVA: (a) control is activated, and (b) control is deactivated. [frequency base is 60 Hz, voltage base is 171 V, active and reactive power base is 20 kVA]

deactivated in Figure 6.9(b) and with absence of the secondary control layer the frequency and voltage of the main PEDG PCC bus cannot be regulated. These results are evident that the proposed control can operate independently without the need for a secondary control layer when the upper layer is suspected to be compromised. Note that, in these scenarios the GFLI's primary control is adaptive to frequency and the upper grid dynamics are represented by a grid-forming inverter with virtual inertia and tau of $5.067 \times 10^{-3} \text{ kg/m}^2$. Furthermore, this grid-forming inverter has coupling dynamics as $P - f$ and $Q - v$. Moreover, regarding the stability of the consensus dynamics in this scenario, the leading GFLIs gains are described in (6.12)-(6.15).

$$\text{Re} \left\{ -1 - \frac{k_Q}{2} + \sqrt{1 - \frac{k_Q^2}{4}} \right\} < 0 \quad (6.12)$$

$$\text{Re} \left\{ -1 - \frac{k_Q}{2} - \sqrt{1 - \frac{k_Q^2}{4}} \right\} < 0 \quad (6.13)$$

$$\text{Re} \left\{ -1 - \frac{k_P}{2} + \sqrt{1 - \frac{k_P^2}{4}} \right\} < 0 \quad (6.14)$$

$$\text{Re} \left\{ -1 - \frac{k_P}{2} - \sqrt{1 - \frac{k_P^2}{4}} \right\} < 0 \quad (6.15)$$

(6.16) and (6.17) described how leading GFLIs deduce their set-points.

$$Q_{PCC_{Leading}}(s) = \frac{s+1}{s^2 + (2+k_Q)s + k_Q} Q_{Ref}(s) \quad (6.16)$$

$$P_{PCC_{Leading}}(s) = \frac{s+1}{s^2 + (2+k_P)s + k_P} P_{Ref}(s) \quad (6.17)$$

For nonleading GFLIs the dynamics are as follows.

$$Q_{PCC_{i+1}}(s) = \frac{1}{s+1} Q_{PCC_i}(s) \quad (6.18)$$

$$P_{PCC_{i+1}}(s) = \frac{1}{s+1} P_{PCC_i}(s) \quad (6.19)$$

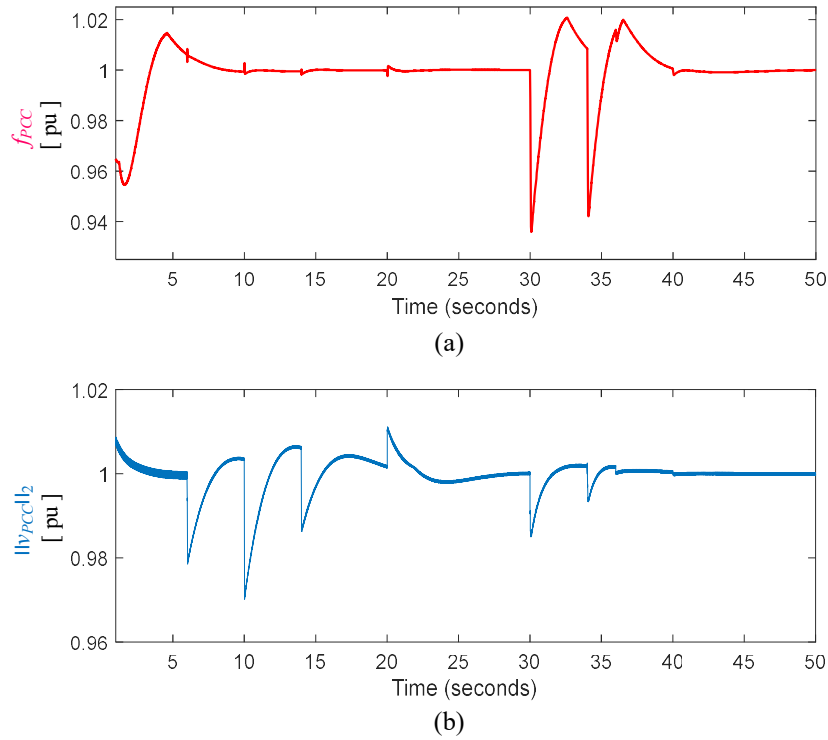


Figure 6.11. Scenario 4 the proposed distributed control performance under random disturbances in distribution feeder with 42 GFLIs in a reverse coupling dynamics $P - V$ and $Q - f$ with GFLI_{*i*} at PCC bus *i* and GFLI_{*i*+1} at PCC bus *i*+1 with capacities of 20 kVA: (a) frequency at main PCC bus, and (b) voltage of the main PCC bus. [frequency base is 60 Hz, voltage base is 171 V]

Meaning that, nonleading GFLIs has poles at -1. Concluding, that the consensus dynamics control in scenario 2 is BIBO stable.

6.4.3. Validation Scenario 3: Two GFLIs in Radial Network with Reverse Coupling Dynamics $P - V$ and $Q - f$ with Cyber Layer Layout Figure 6.2(c)

This scenario is testing the operation of the GFLIs independently from the upper layer in Figure 6.10 with reverse coupling dynamics $P - V$ and $Q - f$ with cyber layer layout as Figure 6.2(c)Figure 6.8. Particularly, in the scenario shown in Figure 6.10(a), the network is operating independently of the upper layer control and the target is to maintain the main PEDG PCC bus frequency and voltage in the nominal level. It is evident in Figure 6.10(a)

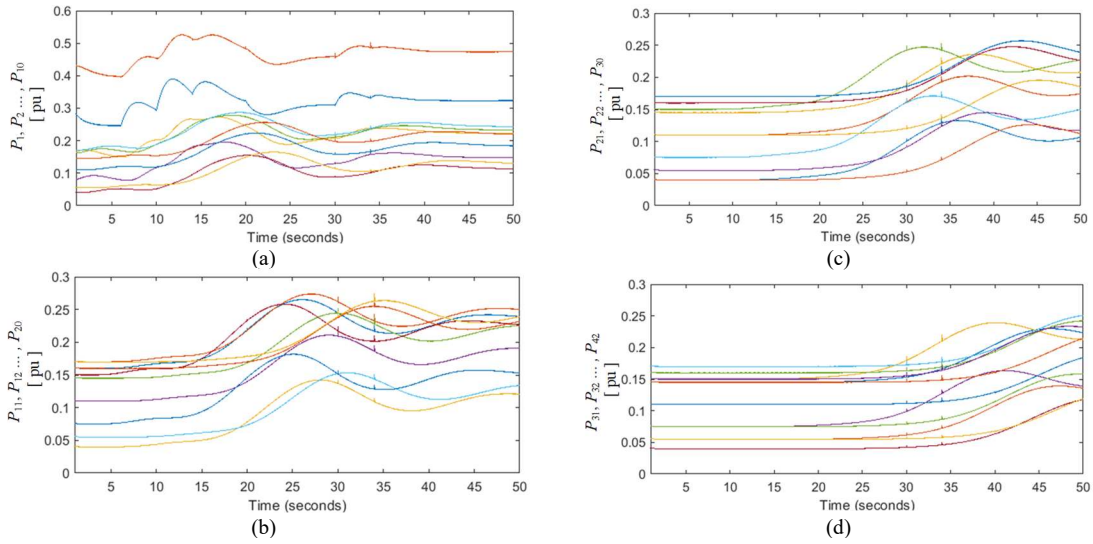


Figure 6.12. Scenario 4 the proposed distributed control performance under random disturbances in distribution feeder with 42 GFLIs in a reverse coupling dynamics such as $P - V$ and $Q - f$ with GFLI_{*i*} at PCC bus *i* and GFLI_{*i*+1} at PCC bus *i*+1 with capacities of 20 kVA: (a) internal PCC bus GFLI active power from bus number 1 to 10, and (b) internal PCC bus GFLI active power from bus number 11 to 20, (c) internal PCC bus GFLI active power from bus number 21 to 30, and (d) internal PCC bus GFLI active power from bus number 31 to 42. [Active power base is 20 kVA]

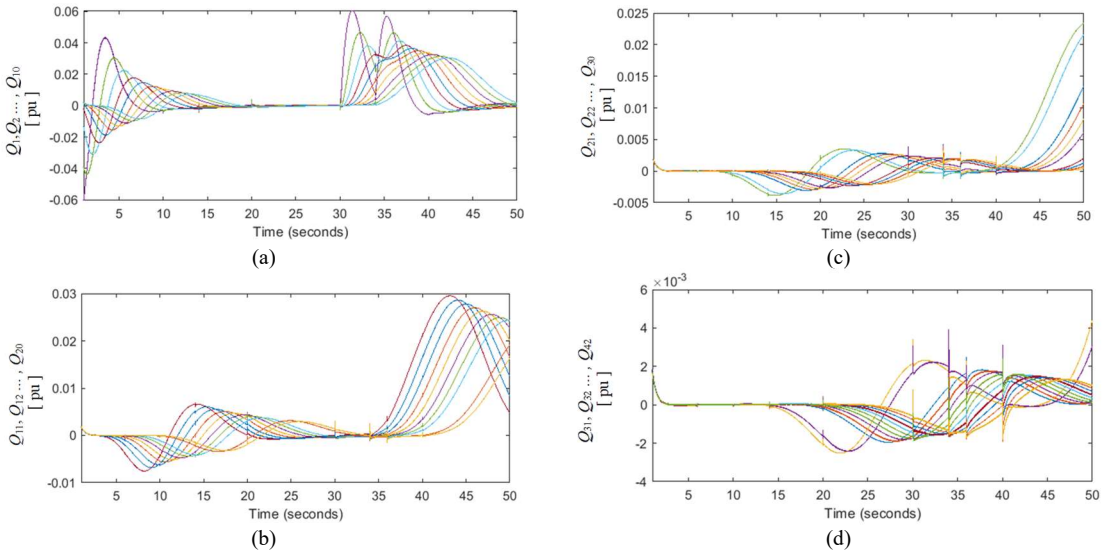


Figure 6.13. Scenario 4 the proposed distributed control performance under random disturbances in distribution feeder with 42 GFLIs in a reverse coupling dynamics such as $P - V$ and $Q - f$ with GFLI_{*i*} at PCC bus *i* and GFLI_{*i*+1} at PCC bus *i*+1 with capacities of 20 kVA: (a) internal PCC bus GFLI reactive power from bus number 1 to 10, and (b) internal PCC bus GFLI reactive power from bus number 11 to 20, (c) internal PCC bus GFLI reactive power from bus number 21 to 30, and (d) internal PCC bus GFLI reactive power from bus number 31 to 42. [Reactive power base is 20 kVA]

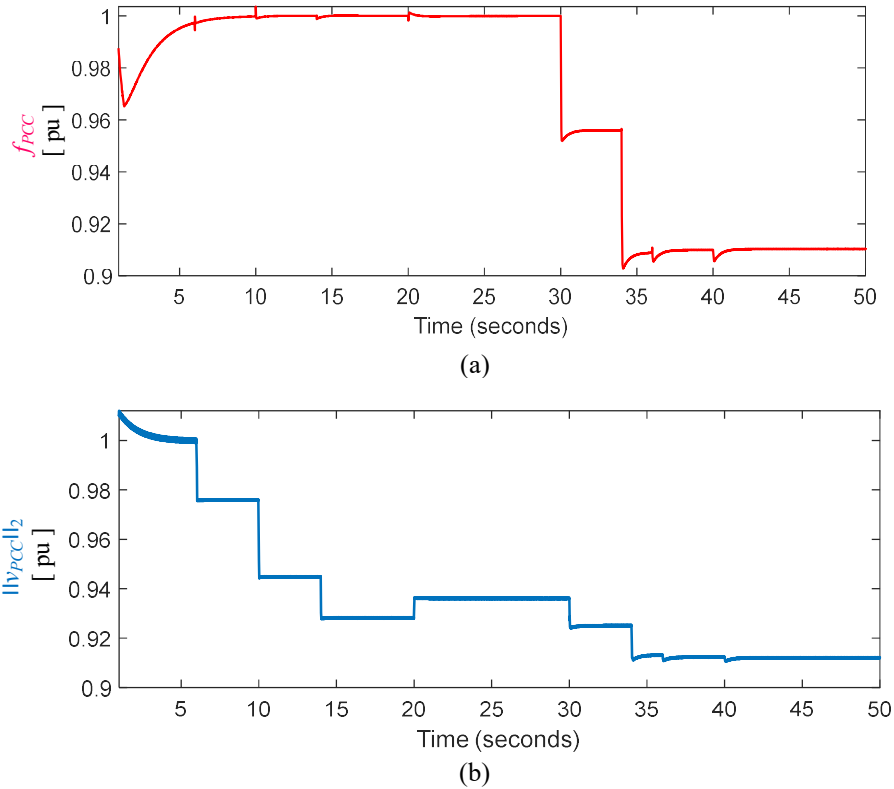


Figure 6.14. Scenario 4 the post-attack operation without the proposed distributed control performance under random disturbances in distribution feeder with 42 GFLIs in a reverse coupling dynamics $P - V$ and $Q - f$ network with GFLI_{*i*} at PCC bus *i* and GFLI_{*i*+1} at PCC bus *i*+1 with capacities of 20 kVA: (a) frequency at main PCC bus, and (b) voltage of the main PCC bus. [Frequency base is 60 Hz, voltage base is 171 V]

that the GFLIs are participating in correcting the main PCC bus voltage and frequency. In contrast, Figure 6.10(b) shows that when the event-triggered consensus distributed control is deactivated, the reactive and active load disturbances result in deviating the frequency and the voltage from nominal range. This shows that the proposed event-triggered consensus distributed control can operate independently without relying on an upper secondary control layer even in a network with reverse coupling dynamics $P - V$ and $Q - f$.

6.4.4. Validation Scenario 4: Distribution Feeder with 42 GFLIs in a Reverse Coupling Dynamics $P - V$ and $Q - f$ with Cyber Layer Layout Figure 6.2(d)

6.4.4.1. Post-Attack Operation with the Consensus Control

This scenario is application of the consensus dynamics control on a distribution feeder with 42 internal PCC buses with 42 GFLIs communicating with each nearby GFLI (see Figure 6.2(d) for the cyber layer of this scenario). This network is designed to have reverse coupling dynamics (i.e., $P - V$ and $Q - f$). In this scenario, random active and reactive loads disturbances occur to validate the capability of the GFLIs to collectively support the main PCC bus voltage and frequency. It is evident in Figure 6.11 (a) and (b) that the frequency and voltage are always restored to their nominal ranges by the support of the network GFLIs' set-points changes through consensus control. Specifically, it is evident that the GFLIs active power set-points are supporting the voltage of the main PCC bus as depicted in Figure 6.12(a)-(d). In contrast, the GFLIs reactive power set-point is supporting the frequency of the main PCC bus as seen in Figure 6.13(a)-(d). This scenario shows that the consensus dynamics distributed control can operate a network with high penetration of GFLIs independently without the need for an upper secondary control layer. In fact, as the network becomes highly penetrated by GFLIs the restoration of the main PCC bus frequency and the voltage to nominal range is faster and more aggressive. Similarly, if the consensus dynamics communication graph produces a Hurwitz consensus A matrix the system is always reachable in sense of BIBO stability even with high penetration of GFLIs.

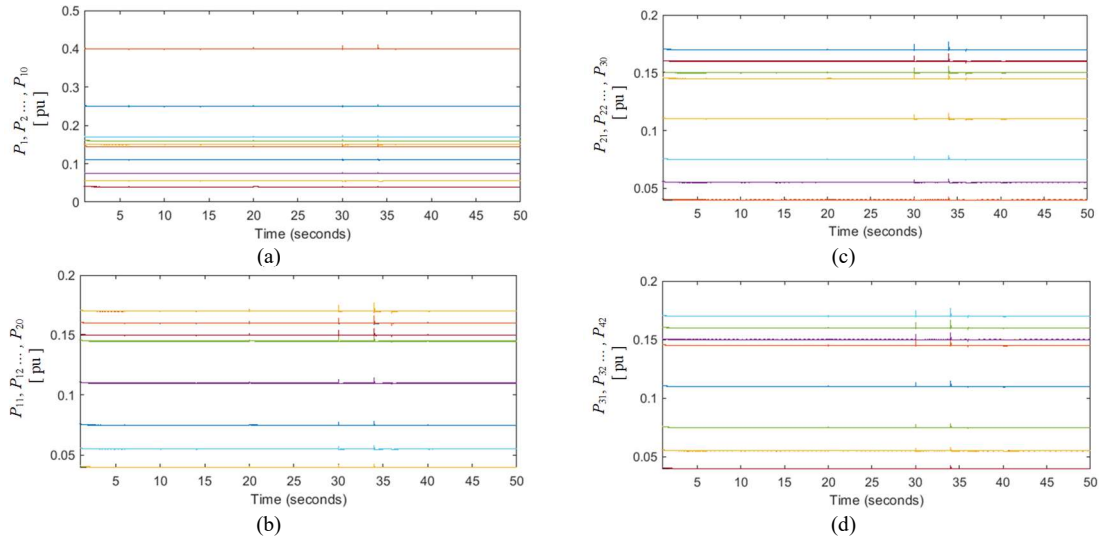


Figure 6.15. Scenario 4 the post-attack operation without the proposed distributed control performance under random disturbances in distribution feeder with 42 GFLIs in a reverse coupling dynamics such as $P - V$ and $Q - f$ with GFLI_{*i*} at PCC bus *i* and GFLI_{*i*+1} at PCC bus *i*+1 with capacities of 20 kVA: (a) internal PCC bus GFLI active power from bus number 1 to 10, and (b) internal PCC bus GFLI active power from bus number 11 to 20, (c) internal PCC bus GFLI active power from bus number 21 to 30, and (d) internal PCC bus GFLI active power from bus number 31 to 42. [Active power base is 20 kVA]

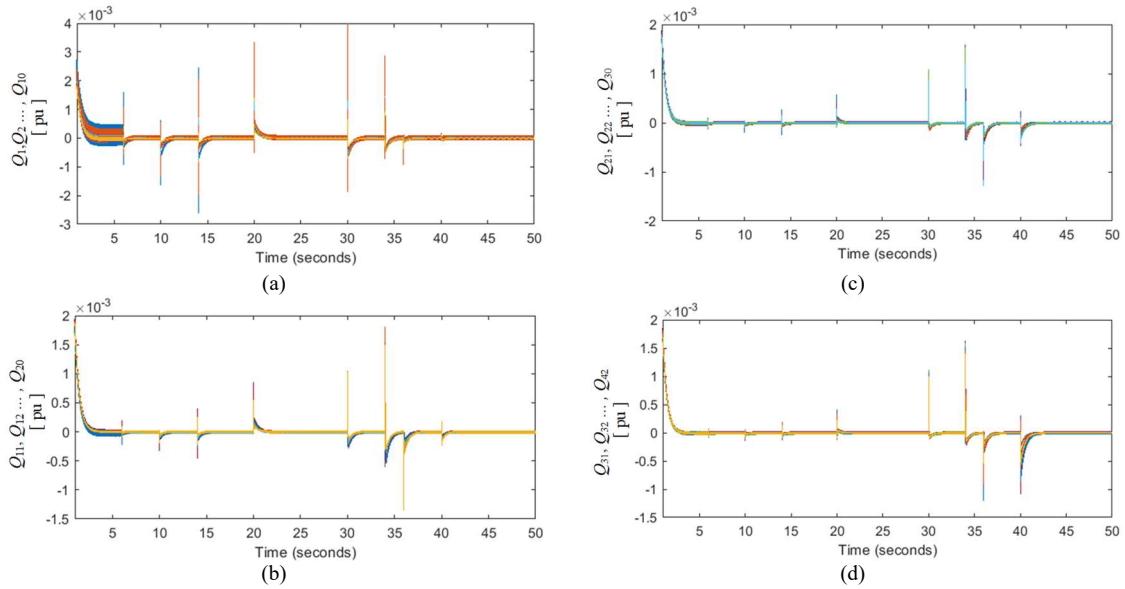


Figure 6.16. Scenario 4 the post-attack operation without the proposed distributed control performance under random disturbances in distribution feeder with 42 GFLIs in a reverse coupling dynamics such as $P - V$ and $Q - f$ with GFLI_{*i*} at PCC bus *i* and GFLI_{*i*+1} at PCC bus *i*+1 with capacities of 20 kVA: (a) internal PCC bus GFLI reactive power from bus number 1 to 10, and (b) internal PCC bus GFLI reactive power from bus number 11 to 20, (c) internal PCC bus GFLI reactive power from bus number 21 to 30, and (d) internal PCC bus GFLI reactive power from bus number 31 to 42. [Reactive power base is 20 kVA]

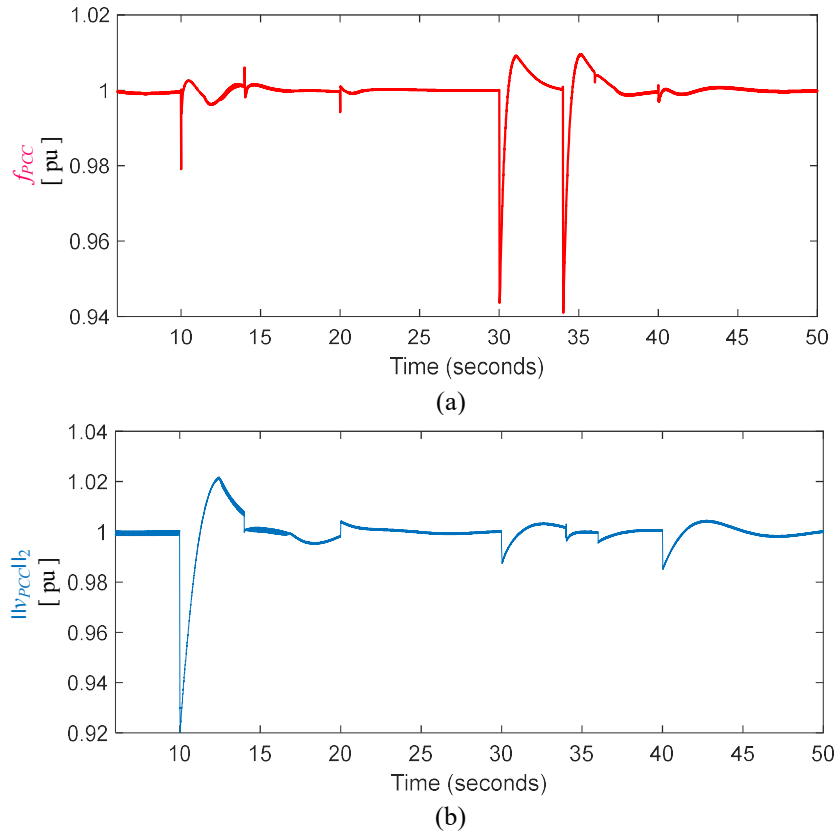


Figure 6.17. Scenario 5 the proposed distributed control performance under random disturbances in distribution network in ring configuration with 42 GFLIs in a reverse coupling dynamics $P - V$ and $Q - f$ network with GFLIs of 20 kVA and the cyber layer is as Figure 6.2(e): (a) frequency at main PCC bus, and (b) voltage of the main PCC bus. [frequency base is 60 Hz, voltage base is 171 V]

6.4.4.2. Post-Attack Operation without Consensus Control

The scenario in Figure 6.11, Figure 6.12, and Figure 6.13 is repeated but without activating the consensus dynamics control in Figure 6.14, Figure 6.15, and Figure 6.16. It is evident without activating the consensus control the main PCC bus voltage and frequency are not being restored to nominal values as seen in Figure 6.14 (a) and Figure 6.14(b). Note that, random active power disturbances cause drifting the voltage of the main PCC bus. While random reactive power disturbances influence the frequency of the main

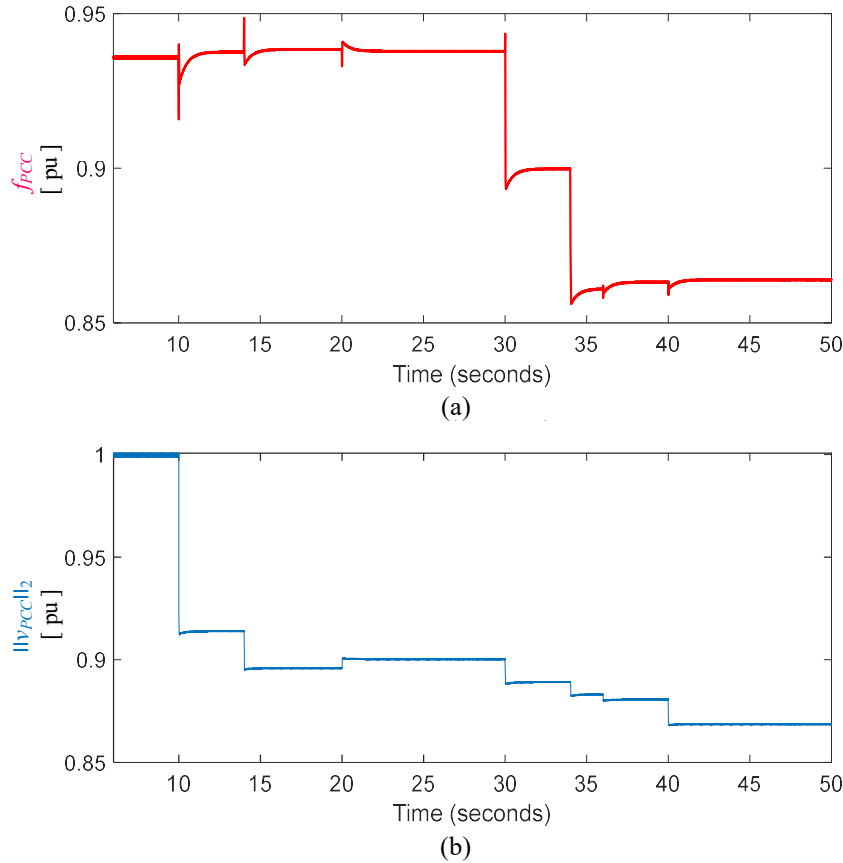


Figure 6.18. Scenario 5 the post-attack operation without the proposed distributed control performance under random disturbances in distribution network in ring configuration with 42 GFLIs in a reverse coupling dynamics $P - V$ and $Q - f$ network with GFLIs of 20 kVA and the cyber layer is as Figure 6.2(e): (a) frequency at main PCC bus, and (b) voltage of the main PCC bus. [frequency base is 60 Hz, voltage base is 171 V]

PCC bus. This is because this distribution feeder has reverse dynamic coupling (i.e., $P - V$ and $Q - f$). The deactivation of the consensus control is evident in the waveforms of the GFLIs' active and reactive power injection shown in Figure 6.15(a)-(d) for active power and Figure 6.16(a)-(d) for reactive power. This scenario shows the powerful contribution of the GFLIs in Figure 6.11, Figure 6.12, and Figure 6.13 in post-attack operation when the secondary upper layer control is lost compared to Figure 6.14, Figure 6.15, and Figure 6.16.

6.4.5. Validation Scenario 5: Distribution Network in Ring Configuration with 42 GFLIs in a Reverse Coupling Dynamics $P - V$ and $Q - f$ with Cyber Layer Layout of Figure 6.2(e)

6.4.5.1. Post-Attack Operation with the Consensus Control

This scenario the cyber layer layout is defined as Figure 6.2(e) for a distribution network in ring configuration layout and with reverse coupling dynamics $P - V$ and $Q - f$. Random active and reactive load disturbances occur in this scenario. The consensus dynamics control is able to maintain the main PCC bus voltage and frequency in their nominal range (see Figure 6.17(a) and (b)). This is done by the support of the 42 GFLIs that are cooperating among each other's through consensus dynamics control graph of Figure 6.2(e) by changing their active and reactive power set-points.

6.4.5.2. Post-Attack Operation without the Consensus Control

The same scenario Figure 6.17 is repeated without activating the consensus dynamics control in Figure 6.18. Note that, in this scenario initially the reactive load was intentionally unbalanced with the supply of reactive power. This is to show that the consensus control is able to balance the reactive power demand initially and indicates the coupling between the reactive power and the frequency dynamics. It is evident that the without the consensus control activation the frequency and voltage at the main PCC bus are not within the nominal range as seen in Figure 6.18(a) and (b) compared to Figure 6.17(a) and (c).

6.5. Conclusion

An event-triggered consensus distributed control for multiple grid-following inverters (GFLIs) in a power electronics-dominated grid (PEDG) is proposed in this Chapter. This control is a substitute control for the GFLIs in stealthy-cyberattack scenarios when the upper secondary control layer dispatched set-points are compromised. The objective of this control is to regain normal point of common coupling (PCC) voltage and frequency levels. This is accomplished through distributing the reactive and active power among the GFLIs to correct the frequency and the voltage of the network. In addition, stability analysis is done to establish that the consensus dynamics control gains that guarantee the consensus control system matrix is Hurwitz is sufficient to conclude BIBO stability. This consensus distributed control is validated with 5 different scenarios showing that the GFLIs are capable to operate independent of the centralized secondary control layer. This Chapter provided an alternative solution for the PEDG network to operate after the intrusion detection system designed in Chapter 5 decided that the upper control layer is compromised.

Chapter 7

7. Conclusions

In this dissertation, the stability aspects, vulnerabilities, and cybersecurity of the modern power grid that is heavily penetrated by power electronics-based power generation (i.e., power electronics-dominated grid (PEDG)) are discussed in Chapter 1. Then, in Chapter 2, the phase locked loop (PLL) issue related to grid-following inverter operation in futuristic power grids is discussed. Furthermore, chapter 2 develops a single loop decoupled direct active and reactive power control for grid-following single-phase inverters without PLL requirement with adaptation feature to the network frequency deviations. This developed control stability, and stability from the perspective of the upper network voltage is analyzed. Chapter 3, provides a solution for the issue of DC link failures that is expected to occur frequently in the futuristic PEDG. Firstly, a solution is developed with conventional grid-following control to describe the origin of the 2nd order harmonic that is associated with DC link failures. This solution stability, control design, system design, stabilization schemes are analyzed. After that, a solution is provided based on the developed grid-following control without PLL requirement with adaptive to network frequency and 2nd order harmonic ripple mitigations. Chapter 4, is theoretical backgrounds that links the voltage stability bounds to cybersecurity through the field of group theory. Chapter 5, designs an intrusion detection system based on the developed theory in Chapter 4. Chapter 6, is developing control in post-attack operation. Specifically, how consensus

dynamics control can be utilized to maintain a network of grid-following inverter operating correctly with absence of the upper layer secondary control. Chapter 7, is the conclusions.

8. APPENDIX

8.1. Permission from the IEEE website (RightsLink) regarding Thesis/Dissertation reuse

This appendix presents the copyright permissions for the articles, whose contents were utilized in my dissertation. The list of the articles includes several journal, conference, and workshop publications: IEEE Industrial Electronics Magazine, 2020, IEEE Energy Conversion Congress and Exposition (ECCE, 2020), IEEE Industrial Application Society Annual Meeting (IAS, 2021), IEEE Power & Energy Conference at Illinois (PECI, 2019), IEEE 12th International Symposium on Power Electronics for Distributed Generation Systems (PEDG, 2021), IEEE 22nd Workshop on Control and Modelling of Power Electronics (COMPEL, 2021), and IEEE CyberPELS, 2020.

The copyright permissions for reusing the published materials are presented in the Appendix.

APPENDIX (Continued)



On the Stability of the Power Electronics-Dominated Grid: A New Energy Paradigm

Author: Ahmad Khan
Publication: IEEE Industrial Electronics Magazine
Publisher: IEEE
Date: December 2020

Copyright © 2020, IEEE

Thesis / Dissertation Reuse

The IEEE does not require individuals working on a thesis to obtain a formal reuse license, however, you may print out this statement to be used as a permission grant:

Requirements to be followed when using any portion (e.g., figure, graph, table, or textual material) of an IEEE copyrighted paper in a thesis:

- 1) In the case of textual material (e.g., using short quotes or referring to the work within these papers) users must give full credit to the original source (author, paper, publication) followed by the IEEE copyright line © 2011 IEEE.
- 2) In the case of illustrations or tabular material, we require that the copyright line © [Year of original publication] IEEE appear prominently with each reprinted figure and/or table.
- 3) If a substantial portion of the original paper is to be used, and if you are not the senior author, also obtain the senior author's approval.

Requirements to be followed when using an entire IEEE copyrighted paper in a thesis:

- 1) The following IEEE copyright/ credit notice should be placed prominently in the references: © [year of original publication] IEEE. Reprinted, with permission, from [author names, paper title, IEEE publication title, and month/year of publication]
- 2) Only the accepted version of an IEEE copyrighted paper can be used when posting the paper or your thesis online.
- 3) In placing the thesis on the author's university website, please display the following message in a prominent place on the website: In reference to IEEE copyrighted material which is used with permission in this thesis, the IEEE does not endorse any of [university/educational entity's name goes here]'s products or services. Internal or personal use of this material is permitted. If interested in reprinting/republishing IEEE copyrighted material for advertising or promotional purposes or for creating new collective works for resale or redistribution, please go to http://www.ieee.org/publications_standards/publications/rights/rights_link.html to learn how to obtain a License from RightsLink.

If applicable, University Microfilms and/or ProQuest Library, or the Archives of Canada may supply single copies of the dissertation.

BACK

CLOSE WINDOW

APPENDIX (Continued)



PLL-less Active and Reactive Power Controller for Grid-Following Inverter

Conference Proceedings: 2020 IEEE Energy Conversion Congress and Exposition (ECCE)

Author: Ahmad Khan

Publisher: IEEE

Date: 11 October 2020

Copyright © 2020, IEEE

Thesis / Dissertation Reuse

The IEEE does not require individuals working on a thesis to obtain a formal reuse license, however, you may print out this statement to be used as a permission grant:

Requirements to be followed when using any portion (e.g., figure, graph, table, or textual material) of an IEEE copyrighted paper in a thesis:

- 1) In the case of textual material (e.g., using short quotes or referring to the work within these papers) users must give full credit to the original source (author, paper, publication) followed by the IEEE copyright line © 2011 IEEE.
- 2) In the case of illustrations or tabular material, we require that the copyright line © [Year of original publication] IEEE appear prominently with each reprinted figure and/or table.
- 3) If a substantial portion of the original paper is to be used, and if you are not the senior author, also obtain the senior author's approval.

Requirements to be followed when using an entire IEEE copyrighted paper in a thesis:

- 1) The following IEEE copyright/ credit notice should be placed prominently in the references: © [year of original publication] IEEE. Reprinted, with permission, from [author names, paper title, IEEE publication title, and month/year of publication]
- 2) Only the accepted version of an IEEE copyrighted paper can be used when posting the paper or your thesis online.
- 3) In placing the thesis on the author's university website, please display the following message in a prominent place on the website: In reference to IEEE copyrighted material which is used with permission in this thesis, the IEEE does not endorse any of [university/educational entity's name goes here]'s products or services. Internal or personal use of this material is permitted. If interested in reprinting/republishing IEEE copyrighted material for advertising or promotional purposes or for creating new collective works for resale or redistribution, please go to http://www.ieee.org/publications_standards/publications/rights/rights_link.html to learn how to obtain a License from RightsLink.

If applicable, University Microfilms and/or ProQuest Library, or the Archives of Canada may supply single copies of the dissertation.

BACK

CLOSE WINDOW

APPENDIX (Continued)



RightsLink



Home



Help ▾



Email Support



Sign in



Create Account



Active Power Decoupling Control for Rectifiers with Variable Frequency Supply for More Electric Aircraft

Conference Proceedings: 2021 IEEE Industry Applications Society Annual Meeting (IAS)

Author: Ahmad Khan

Publisher: IEEE

Date: 10 October 2021

Copyright © 2021, IEEE

Thesis / Dissertation Reuse

The IEEE does not require individuals working on a thesis to obtain a formal reuse license, however, you may print out this statement to be used as a permission grant:

Requirements to be followed when using any portion (e.g., figure, graph, table, or textual material) of an IEEE copyrighted paper in a thesis:

- 1) In the case of textual material (e.g., using short quotes or referring to the work within these papers) users must give full credit to the original source (author, paper, publication) followed by the IEEE copyright line © 2011 IEEE.
- 2) In the case of illustrations or tabular material, we require that the copyright line © [Year of original publication] IEEE appear prominently with each reprinted figure and/or table.
- 3) If a substantial portion of the original paper is to be used, and if you are not the senior author, also obtain the senior author's approval.

Requirements to be followed when using an entire IEEE copyrighted paper in a thesis:

- 1) The following IEEE copyright/ credit notice should be placed prominently in the references: © [year of original publication] IEEE. Reprinted, with permission, from [author names, paper title, IEEE publication title, and month/year of publication]
- 2) Only the accepted version of an IEEE copyrighted paper can be used when posting the paper or your thesis online.
- 3) In placing the thesis on the author's university website, please display the following message in a prominent place on the website: In reference to IEEE copyrighted material which is used with permission in this thesis, the IEEE does not endorse any of [university/educational entity's name goes here]'s products or services. Internal or personal use of this material is permitted. If interested in reprinting/republishing IEEE copyrighted material for advertising or promotional purposes or for creating new collective works for resale or redistribution, please go to http://www.ieee.org/publications_standards/publications/rights/rights_link.html to learn how to obtain a License from RightsLink.

If applicable, University Microfilms and/or ProQuest Library, or the Archives of Canada may supply single copies of the dissertation.

BACK

CLOSE WINDOW

APPENDIX (Continued)



Active Power Decoupling Control Scheme for Distorted Grids

Conference Proceedings: 2019 IEEE Power and Energy Conference at Illinois (PECI)

Author: Ahmad Khan

Publisher: IEEE

Date: February 2019

Copyright © 2019, IEEE

Thesis / Dissertation Reuse

The IEEE does not require individuals working on a thesis to obtain a formal reuse license, however, you may print out this statement to be used as a permission grant:

Requirements to be followed when using any portion (e.g., figure, graph, table, or textual material) of an IEEE copyrighted paper in a thesis:

- 1) In the case of textual material (e.g., using short quotes or referring to the work within these papers) users must give full credit to the original source (author, paper, publication) followed by the IEEE copyright line © 2011 IEEE.
- 2) In the case of illustrations or tabular material, we require that the copyright line © [Year of original publication] IEEE appear prominently with each reprinted figure and/or table.
- 3) If a substantial portion of the original paper is to be used, and if you are not the senior author, also obtain the senior author's approval.

Requirements to be followed when using an entire IEEE copyrighted paper in a thesis:

- 1) The following IEEE copyright/ credit notice should be placed prominently in the references: © [year of original publication] IEEE. Reprinted, with permission, from [author names, paper title, IEEE publication title, and month/year of publication]
- 2) Only the accepted version of an IEEE copyrighted paper can be used when posting the paper or your thesis online.
- 3) In placing the thesis on the author's university website, please display the following message in a prominent place on the website: In reference to IEEE copyrighted material which is used with permission in this thesis, the IEEE does not endorse any of [university/educational entity's name goes here]'s products or services. Internal or personal use of this material is permitted. If interested in reprinting/republishing IEEE copyrighted material for advertising or promotional purposes or for creating new collective works for resale or redistribution, please go to http://www.ieee.org/publications_standards/publications/rights/rights_link.html to learn how to obtain a License from RightsLink.

If applicable, University Microfilms and/or ProQuest Library, or the Archives of Canada may supply single copies of the dissertation.

BACK

CLOSE WINDOW

APPENDIX (Continued)



Home

Help ▾

Email Support

Sign in

Create Account



Decoupled Active and Reactive Power Control without PLL Requirement for Differential Buck Converter

Conference Proceedings: 2020 IEEE Energy Conversion Congress and Exposition (ECCE)

Author: Ahmad Khan

Publisher: IEEE

Date: 11 October 2020

Copyright © 2020, IEEE

Thesis / Dissertation Reuse

The IEEE does not require individuals working on a thesis to obtain a formal reuse license, however, you may print out this statement to be used as a permission grant:

Requirements to be followed when using any portion (e.g., figure, graph, table, or textual material) of an IEEE copyrighted paper in a thesis:

- 1) In the case of textual material (e.g., using short quotes or referring to the work within these papers) users must give full credit to the original source (author, paper, publication) followed by the IEEE copyright line © 2011 IEEE.
- 2) In the case of illustrations or tabular material, we require that the copyright line © [Year of original publication] IEEE appear prominently with each reprinted figure and/or table.
- 3) If a substantial portion of the original paper is to be used, and if you are not the senior author, also obtain the senior author's approval.

Requirements to be followed when using an entire IEEE copyrighted paper in a thesis:

- 1) The following IEEE copyright/ credit notice should be placed prominently in the references: © [year of original publication] IEEE. Reprinted, with permission, from [author names, paper title, IEEE publication title, and month/year of publication]
- 2) Only the accepted version of an IEEE copyrighted paper can be used when posting the paper or your thesis online.
- 3) In placing the thesis on the author's university website, please display the following message in a prominent place on the website: In reference to IEEE copyrighted material which is used with permission in this thesis, the IEEE does not endorse any of [university/educational entity's name goes here]'s products or services. Internal or personal use of this material is permitted. If interested in reprinting/republishing IEEE copyrighted material for advertising or promotional purposes or for creating new collective works for resale or redistribution, please go to http://www.ieee.org/publications_standards/publications/rights/rights_link.html to learn how to obtain a License from RightsLink.

If applicable, University Microfilms and/or ProQuest Library, or the Archives of Canada may supply single copies of the dissertation.

BACK

CLOSE WINDOW

APPENDIX (Continued)



Cybersecurity Analytics for Virtual Power Plants



Conference Proceedings:
2021 IEEE 12th International Symposium on Power Electronics for Distributed Generation Systems (PEDG)
Author: Ahmad Khan
Publisher: IEEE
Date: 28 June 2021

Copyright © 2021, IEEE

Thesis / Dissertation Reuse

The IEEE does not require individuals working on a thesis to obtain a formal reuse license, however, you may print out this statement to be used as a permission grant:

Requirements to be followed when using any portion (e.g., figure, graph, table, or textual material) of an IEEE copyrighted paper in a thesis:

- 1) In the case of textual material (e.g., using short quotes or referring to the work within these papers) users must give full credit to the original source (author, paper, publication) followed by the IEEE copyright line © 2011 IEEE.
- 2) In the case of illustrations or tabular material, we require that the copyright line © [Year of original publication] IEEE appear prominently with each reprinted figure and/or table.
- 3) If a substantial portion of the original paper is to be used, and if you are not the senior author, also obtain the senior author's approval.

Requirements to be followed when using an entire IEEE copyrighted paper in a thesis:

- 1) The following IEEE copyright/ credit notice should be placed prominently in the references: © [year of original publication] IEEE. Reprinted, with permission, from [author names, paper title, IEEE publication title, and month/year of publication]
- 2) Only the accepted version of an IEEE copyrighted paper can be used when posting the paper or your thesis online.
- 3) In placing the thesis on the author's university website, please display the following message in a prominent place on the website: In reference to IEEE copyrighted material which is used with permission in this thesis, the IEEE does not endorse any of [university/educational entity's name goes here]'s products or services. Internal or personal use of this material is permitted. If interested in reprinting/republishing IEEE copyrighted material for advertising or promotional purposes or for creating new collective works for resale or redistribution, please go to http://www.ieee.org/publications_standards/publications/rights/rights_link.html to learn how to obtain a License from RightsLink.

If applicable, University Microfilms and/or ProQuest Library, or the Archives of Canada may supply single copies of the dissertation.

BACK

CLOSE WINDOW

APPENDIX (Continued)



Real-Time Stability Boundary Identification of Prosumers PCC in a Virtual Power Plant



Conference Proceedings:
2021 IEEE 22nd Workshop on Control and Modelling of Power Electronics (COMPEL)
Author: Ahmad Khan
Publisher: IEEE
Date: 02 November 2021

Copyright © 2021, IEEE

Thesis / Dissertation Reuse

The IEEE does not require individuals working on a thesis to obtain a formal reuse license, however, you may print out this statement to be used as a permission grant:

Requirements to be followed when using any portion (e.g., figure, graph, table, or textual material) of an IEEE copyrighted paper in a thesis:

- 1) In the case of textual material (e.g., using short quotes or referring to the work within these papers) users must give full credit to the original source (author, paper, publication) followed by the IEEE copyright line © 2011 IEEE.
- 2) In the case of illustrations or tabular material, we require that the copyright line © [Year of original publication] IEEE appear prominently with each reprinted figure and/or table.
- 3) If a substantial portion of the original paper is to be used, and if you are not the senior author, also obtain the senior author's approval.

Requirements to be followed when using an entire IEEE copyrighted paper in a thesis:

- 1) The following IEEE copyright/ credit notice should be placed prominently in the references: © [year of original publication] IEEE. Reprinted, with permission, from [author names, paper title, IEEE publication title, and month/year of publication]
- 2) Only the accepted version of an IEEE copyrighted paper can be used when posting the paper or your thesis online.
- 3) In placing the thesis on the author's university website, please display the following message in a prominent place on the website: In reference to IEEE copyrighted material which is used with permission in this thesis, the IEEE does not endorse any of [university/educational entity's name goes here]'s products or services. Internal or personal use of this material is permitted. If interested in reprinting/republishing IEEE copyrighted material for advertising or promotional purposes or for creating new collective works for resale or redistribution, please go to http://www.ieee.org/publications_standards/publications/rights/rights_link.html to learn how to obtain a License from RightsLink.

If applicable, University Microfilms and/or ProQuest Library, or the Archives of Canada may supply single copies of the dissertation.

BACK

CLOSE WINDOW

APPENDIX (Continued)



Intrusion Detection for Cybersecurity of Power Electronics Dominated Grids: Inverters PQ Set-Points Manipulation

Conference Proceedings: 2020 IEEE CyberPELS (CyberPELS)

Author: Ahmad Khan

Publisher: IEEE

Date: 13 October 2020

Copyright © 2020, IEEE

Thesis / Dissertation Reuse

The IEEE does not require individuals working on a thesis to obtain a formal reuse license, however, you may print out this statement to be used as a permission grant:

Requirements to be followed when using any portion (e.g., figure, graph, table, or textual material) of an IEEE copyrighted paper in a thesis:

- 1) In the case of textual material (e.g., using short quotes or referring to the work within these papers) users must give full credit to the original source (author, paper, publication) followed by the IEEE copyright line © 2011 IEEE.
- 2) In the case of illustrations or tabular material, we require that the copyright line © [Year of original publication] IEEE appear prominently with each reprinted figure and/or table.
- 3) If a substantial portion of the original paper is to be used, and if you are not the senior author, also obtain the senior author's approval.

Requirements to be followed when using an entire IEEE copyrighted paper in a thesis:

- 1) The following IEEE copyright/ credit notice should be placed prominently in the references: © [year of original publication] IEEE. Reprinted, with permission, from [author names, paper title, IEEE publication title, and month/year of publication]
- 2) Only the accepted version of an IEEE copyrighted paper can be used when posting the paper or your thesis online.
- 3) In placing the thesis on the author's university website, please display the following message in a prominent place on the website: In reference to IEEE copyrighted material which is used with permission in this thesis, the IEEE does not endorse any of [university/educational entity's name goes here]'s products or services. Internal or personal use of this material is permitted. If interested in reprinting/republishing IEEE copyrighted material for advertising or promotional purposes or for creating new collective works for resale or redistribution, please go to http://www.ieee.org/publications_standards/publications/rights/rights_link.html to learn how to obtain a License from RightsLink.

If applicable, University Microfilms and/or ProQuest Library, or the Archives of Canada may supply single copies of the dissertation.

BACK

CLOSE WINDOW

9. REFERENCES

- [1] B. K. Bose, "Global Energy Scenario and Impact of Power Electronics in 21st Century," *IEEE Transactions on Industrial Electronics*, vol. 60, no. 7, pp. 2638-2651, 2013.
- [2] F. Blaabjerg and K. Ma, "Future on Power Electronics for Wind Turbine Systems," *IEEE Journal of Emerging and Selected Topics in Power Electronics*, vol. 1, no. 3, pp. 139-152, 2013.
- [3] O. Ellabban, H. Abu-Rub, and F. Blaabjerg, "Renewable energy resources: Current status, future prospects and their enabling technology," *Renewable and Sustainable Energy Reviews*, vol. 39, pp. 748-764, 2014/11/01/ 2014.
- [4] Y. Gui, X. Wang, F. Blaabjerg, and D. Pan, "Control of Grid-Connected Voltage-Source Converters: The Relationship Between Direct-Power Control and Vector-Current Control," *IEEE Industrial Electronics Magazine*, vol. 13, no. 2, pp. 31-40, 2019.
- [5] "Global market outlook for solar power 2019-2023," Solar Power Europe, Belgium 2019.
- [6] "New Energy Outlook 2019," BloombergNEF, USA 2019.
- [7] Q. Peng, Q. Jiang, Y. Yang, T. Liu, H. Wang, and F. Blaabjerg, "On the Stability of Power Electronics-Dominated Systems: Challenges and Potential Solutions," *IEEE Transactions on Industry Applications*, vol. 55, no. 6, pp. 7657-7670, 2019.
- [8] F. Blaabjerg, Y. Yang, D. Yang, and X. Wang, "Distributed Power-Generation Systems and Protection," *Proceedings of the IEEE*, vol. 105, no. 7, pp. 1311-1331, 2017.
- [9] A. Mohammed, S. S. Refaat, S. Bayhan, and H. Abu-Rub, "AC Microgrid Control and Management Strategies: Evaluation and Review," *IEEE Power Electronics Magazine*, vol. 6, no. 2, pp. 18-31, 2019.
- [10] X. Wang and F. Blaabjerg, "Harmonic Stability in Power Electronic-Based Power Systems: Concept, Modeling, and Analysis," *IEEE Transactions on Smart Grid*, vol. 10, no. 3, pp. 2858-2870, 2019.
- [11] J. Sun, G. Wang, X. Du, and H. Wang, "A Theory for Harmonics Created by Resonance in Converter-Grid Systems," *IEEE Transactions on Power Electronics*, vol. 34, no. 4, pp. 3025-3029, 2019.

REFERENCES (Continued)

- [12] M. M. Andrew DB Paice, "Rail network modeling and stability: The input admittance criterion," in *14th Int. Symp. Math. Theory Netw. Syst.*, France, 2000.
- [13] B. Wen, D. Dong, D. Boroyevich, R. Burgos, P. Mattavelli, and Z. Shen, "Impedance-Based Analysis of Grid-Synchronization Stability for Three-Phase Paralleled Converters," *IEEE Transactions on Power Electronics*, vol. 31, no. 1, pp. 26-38, 2016.
- [14] L. Harnefors, M. Bongiorno, and S. Lundberg, "Input-Admittance Calculation and Shaping for Controlled Voltage-Source Converters," *IEEE Transactions on Industrial Electronics*, vol. 54, no. 6, pp. 3323-3334, 2007.
- [15] F. Blaabjerg, R. Teodorescu, M. Liserre, and A. V. Timbus, "Overview of Control and Grid Synchronization for Distributed Power Generation Systems," *IEEE Transactions on Industrial Electronics*, vol. 53, no. 5, pp. 1398-1409, 2006.
- [16] H. Wu and X. Wang, "Design-Oriented Transient Stability Analysis of PLL-Synchronized Voltage-Source Converters," *IEEE Transactions on Power Electronics*, pp. 1-1, 2019.
- [17] N. Bottrell, M. Prodanovic, and T. C. Green, "Dynamic Stability of a Microgrid With an Active Load," *IEEE Transactions on Power Electronics*, vol. 28, no. 11, pp. 5107-5119, 2013.
- [18] *IEEE Guide for Design, Operation, and Integration of Distributed Resource Island Systems with Electric Power Systems*, *IEEE Std. 1547.4*, 2011.
- [19] T. S. Tran, D. T. Nguyen, and G. Fujita, "The Analysis of Technical Trend in Islanding Operation, Harmonic Distortion, Stabilizing Frequency, and Voltage of Islanded Entities," *Resources*, vol. 8, no. 1, p. 14, 2019.
- [20] J. Liu, Y. Miura, and T. Ise, "Comparison of Dynamic Characteristics Between Virtual Synchronous Generator and Droop Control in Inverter-Based Distributed Generators," *IEEE Transactions on Power Electronics*, vol. 31, no. 5, pp. 3600-3611, 2016.
- [21] Q. Zhong and G. Weiss, "Synchronverters: Inverters That Mimic Synchronous Generators," *IEEE Transactions on Industrial Electronics*, vol. 58, no. 4, pp. 1259-1267, 2011.
- [22] Q. Zhong, "Virtual Synchronous Machines: A unified interface for grid integration," *IEEE Power Electronics Magazine*, vol. 3, no. 4, pp. 18-27, 2016.

REFERENCES (Continued)

- [23] C. Li, S. K. Chaudhary, M. Savaghebi, J. C. Vasquez, and J. M. Guerrero, "Power Flow Analysis for Low-Voltage AC and DC Microgrids Considering Droop Control and Virtual Impedance," *IEEE Transactions on Smart Grid*, vol. 8, no. 6, pp. 2754-2764, 2017.
- [24] C. Yuen, A. Oudalov, and A. Timbus, "The Provision of Frequency Control Reserves From Multiple Microgrids," *IEEE Transactions on Industrial Electronics*, vol. 58, no. 1, pp. 173-183, 2011.
- [25] Q. Zhong and Z. Lyu, "Droop-Controlled Rectifiers That Continuously Take Part in Grid Regulation," *IEEE Transactions on Industrial Electronics*, vol. 66, no. 8, pp. 6516-6526, 2019.
- [26] R. S. Balog, M. Metry, and M. Shadmand, "The load as a controllable energy asset in dc microgrids," in *Energy Engineering, DC Distribution Systems and Microgrids: Institution of Engineering and Technology*, 2018, pp. 153-187. [Online]. Available.
- [27] H. Wang and F. Blaabjerg, "Reliability of Capacitors for DC-Link Applications in Power Electronic Converters—An Overview," *IEEE Transactions on Industry Applications*, vol. 50, no. 5, pp. 3569-3578, 2014.
- [28] D. Lu, X. Wang, and F. Blaabjerg, "Influence of Reactive Power Flow on the DC-Link Voltage Control in Voltage-Source Converters," in *2018 IEEE Energy Conversion Congress and Exposition (ECCE)*, 2018, pp. 2236-2241.
- [29] J. Zhou, F. Tang, Z. Xin, S. Huang, P. C. Loh, and J. Jiang, "Differences Between Continuous Single-Phase and Online Three-Phase Power-Decoupled Converters," *IEEE Transactions on Power Electronics*, vol. 34, no. 4, pp. 3487-3503, 2019.
- [30] D. Lu, X. Wang, and F. Blaabjerg, "Impedance-Based Analysis of DC-Link Voltage Dynamics in Voltage-Source Converters," *IEEE Transactions on Power Electronics*, vol. 34, no. 4, pp. 3973-3985, 2019.
- [31] Y. Huang, X. Zhai, J. Hu, D. Liu, and C. Lin, "Modeling and Stability Analysis of VSC Internal Voltage in DC-Link Voltage Control Timescale," *IEEE Journal of Emerging and Selected Topics in Power Electronics*, vol. 6, no. 1, pp. 16-28, 2018.
- [32] G. Delille, B. Francois, and G. Malarange, "Dynamic Frequency Control Support by Energy Storage to Reduce the Impact of Wind and Solar Generation on Isolated Power System's Inertia," *IEEE Transactions on Sustainable Energy*, vol. 3, no. 4, pp. 931-939, 2012.

REFERENCES (Continued)

- [33] N. Pogaku, M. Prodanovic, and T. C. Green, "Modeling, Analysis and Testing of Autonomous Operation of an Inverter-Based Microgrid," *IEEE Transactions on Power Electronics*, vol. 22, no. 2, pp. 613-625, 2007.
- [34] Y. Gui, X. Wang, H. Wu, and F. Blaabjerg, "Voltage-Modulated Direct Power Control for a Weak Grid-Connected Voltage Source Inverters," *IEEE Transactions on Power Electronics*, vol. 34, no. 11, pp. 11383-11395, 2019.
- [35] Y. Gui, C. Kim, C. C. Chung, J. M. Guerrero, Y. Guan, and J. C. Vasquez, "Improved Direct Power Control for Grid-Connected Voltage Source Converters," *IEEE Transactions on Industrial Electronics*, vol. 65, no. 10, pp. 8041-8051, 2018.
- [36] S. Harb, M. Kedia, H. Zhang, and R. S. Balog, "Microinverter and string inverter grid-connected photovoltaic system — A comprehensive study," in *2013 IEEE 39th Photovoltaic Specialists Conference (PVSC)*, 2013, pp. 2885-2890.
- [37] A. Tayyebi, D. Groß, A. Anta, F. Kupzog, and F. Dörfler, "Interactions of Grid-Forming Power Converters and Synchronous Machines--A Comparative Study," *arXiv preprint arXiv:1902.10750*, 2019.
- [38] I. Cvetkovic, D. Boroyevich, R. Burgos, C. Li, and P. Mattavelli, "Modeling and control of grid-connected voltage-source converters emulating isotropic and anisotropic synchronous machines," in *2015 IEEE 16th Workshop on Control and Modeling for Power Electronics (COMPEL)*, 2015, pp. 1-5.
- [39] J. W. Simpson-Porco, F. Dörfler, and F. Bullo, "Synchronization and power sharing for droop-controlled inverters in islanded microgrids," *Automatica*, vol. 49, no. 9, pp. 2603-2611, 2013/09/01/ 2013.
- [40] Q. Zhong, P. Nguyen, Z. Ma, and W. Sheng, "Self-Synchronized Synchronverters: Inverters Without a Dedicated Synchronization Unit," *IEEE Transactions on Power Electronics*, vol. 29, no. 2, pp. 617-630, 2014.
- [41] Q. Zhong, Y. Wang, and B. Ren, "Connecting the Home Grid to the Public Grid: Field Demonstration of Virtual Synchronous Machines," *IEEE Power Electronics Magazine*, vol. 6, no. 4, pp. 41-49, 2019.
- [42] S. D'Arco, J. A. Suul, and O. B. Fosso, "A Virtual Synchronous Machine implementation for distributed control of power converters in SmartGrids," *Electric Power Systems Research*, vol. 122, pp. 180-197, 2015/05/01/ 2015.

REFERENCES (Continued)

- [43] H. Bevrani, T. Ise, and Y. Miura, "Virtual synchronous generators: A survey and new perspectives," *International Journal of Electrical Power & Energy Systems*, vol. 54, pp. 244-254, 2014/01/01/ 2014.
- [44] B. B. Johnson, S. V. Dhople, J. L. Cale, A. O. Hamadeh, and P. T. Krein, "Oscillator-Based Inverter Control for Islanded Three-Phase Microgrids," *IEEE Journal of Photovoltaics*, vol. 4, no. 1, pp. 387-395, 2014.
- [45] M. Sinha, F. Dörfler, B. B. Johnson, and S. V. Dhople, "Uncovering Droop Control Laws Embedded Within the Nonlinear Dynamics of Van der Pol Oscillators," *IEEE Transactions on Control of Network Systems*, vol. 4, no. 2, pp. 347-358, 2017.
- [46] M. Colombino, D. Groß, J. Brouillon, and F. Dörfler, "Global Phase and Magnitude Synchronization of Coupled Oscillators With Application to the Control of Grid-Forming Power Inverters," *IEEE Transactions on Automatic Control*, vol. 64, no. 11, pp. 4496-4511, 2019.
- [47] B. Johnson, M. Rodriguez, M. Sinha, and S. Dhople, "Comparison of virtual oscillator and droop control," in *2017 IEEE 18th Workshop on Control and Modeling for Power Electronics (COMPEL)*, 2017, pp. 1-6.
- [48] L. Huang *et al.*, "A Virtual Synchronous Control for Voltage-Source Converters Utilizing Dynamics of DC-Link Capacitor to Realize Self-Synchronization," *IEEE Journal of Emerging and Selected Topics in Power Electronics*, vol. 5, no. 4, pp. 1565-1577, 2017.
- [49] C. Arghir, T. Jouini, and F. Dörfler, "Grid-forming control for power converters based on matching of synchronous machines," *Automatica*, vol. 95, pp. 273-282, 2018/09/01/ 2018.
- [50] S. Curi, D. Groß, and F. Dörfler, "Control of low-inertia power grids: A model reduction approach," in *2017 IEEE 56th Annual Conference on Decision and Control (CDC)*, 2017, pp. 5708-5713.
- [51] M. C. Chandorkar, D. M. Divan, and R. Adapa, "Control of parallel connected inverters in standalone AC supply systems," *IEEE Transactions on Industry Applications*, vol. 29, no. 1, pp. 136-143, 1993.
- [52] S. Sahoo, T. Dragičević, and F. Blaabjerg, "Cyber Security in Control of Grid-Tied Power Electronic Converters—Challenges and Vulnerabilities," *IEEE Journal of Emerging and Selected Topics in Power Electronics*, pp. 1-1, 2019.

REFERENCES (Continued)

- [53] F. Pasqualetti, F. Dörfler, and F. Bullo, "Attack Detection and Identification in Cyber-Physical Systems," *IEEE Transactions on Automatic Control*, vol. 58, no. 11, pp. 2715-2729, 2013.
- [54] Y. Mo *et al.*, "Cyber-Physical Security of a Smart Grid Infrastructure," *Proceedings of the IEEE*, vol. 100, no. 1, pp. 195-209, 2012.
- [55] P. J. Hart, R. H. Lasseter, and T. M. Jahns, "Enforcing coherency in droop-controlled inverter networks through use of advanced voltage regulation and virtual impedance," in *2017 IEEE Energy Conversion Congress and Exposition (ECCE)*, 2017, pp. 3367-3374.
- [56] P. J. Hart, R. H. Lasseter, and T. M. Jahns, "Coherency Identification and Aggregation in Grid-Forming Droop-Controlled Inverter Networks," *IEEE Transactions on Industry Applications*, vol. 55, no. 3, pp. 2219-2231, 2019.
- [57] J. Fang, H. Li, Y. Tang, and F. Blaabjerg, "On the Inertia of Future More-Electronics Power Systems," *IEEE Journal of Emerging and Selected Topics in Power Electronics*, vol. 7, no. 4, pp. 2130-2146, 2019.
- [58] J. Fang, H. Li, Y. Tang, and F. Blaabjerg, "Distributed Power System Virtual Inertia Implemented by Grid-Connected Power Converters," *IEEE Transactions on Power Electronics*, vol. 33, no. 10, pp. 8488-8499, 2018.
- [59] H. Wu *et al.*, "Small-Signal Modeling and Parameters Design for Virtual Synchronous Generators," *IEEE Transactions on Industrial Electronics*, vol. 63, no. 7, pp. 4292-4303, 2016.
- [60] Q. C. Zhong, "Cyber synchronous machine (cybersync machine)," 2019.
- [61] Q. Zhong and D. Boroyevich, "Structural Resemblance Between Droop Controllers and Phase-Locked Loops," *IEEE Access*, vol. 4, pp. 5733-5741, 2016.
- [62] F. Sadeque, J. Benzaquen, A. Adib, and B. Mirafzal, "Direct Phase-Angle Detection for Three-Phase Inverters in Asymmetrical Power Grids," *IEEE Journal of Emerging and Selected Topics in Power Electronics*, pp. 1-1, 2020.
- [63] Q. Zhong, W. Ming, and Y. Zeng, "Self-Synchronized Universal Droop Controller," *IEEE Access*, vol. 4, pp. 7145-7153, 2016.
- [64] M. Farrokhabadi *et al.*, "Microgrid Stability Definitions, Analysis, and Examples," *IEEE Transactions on Power Systems*, pp. 1-1, 2019.

REFERENCES (Continued)

- [65] X. Wang, L. Harnefors, and F. Blaabjerg, "Unified Impedance Model of Grid-Connected Voltage-Source Converters," *IEEE Transactions on Power Electronics*, vol. 33, no. 2, pp. 1775-1787, 2018.
- [66] G. C. Konstantopoulos, Q. Zhong, and W. Ming, "PLL-Less Nonlinear Current-Limiting Controller for Single-Phase Grid-Tied Inverters: Design, Stability Analysis, and Operation Under Grid Faults," *IEEE Transactions on Industrial Electronics*, vol. 63, no. 9, pp. 5582-5591, 2016.
- [67] Y. Gui, C. Kim, and C. C. Chung, "Grid voltage modulated direct power control for grid connected voltage source inverters," in *2017 American Control Conference (ACC)*, 2017, pp. 2078-2084.
- [68] M. Hosseinzadehtaher, A. Khan, M. W. Baker, and M. B. Shadmand, "Model Predictive Self-healing Control Scheme for Dual Active Bridge Converter," in *2019 2nd International Conference on Smart Grid and Renewable Energy (SGRE)*, 2019, pp. 1-6.
- [69] M. F. Umar, A. Khan, and M. B. Shadmand, "A Stabilizer based Predictive Control Scheme for Smart Inverters in Weak Grid," in *2020 IEEE Texas Power and Energy Conference (TPEC)*, 2020, pp. 1-6.
- [70] A. Khan, A. Gastli, and L. Ben-Brahim, "Modeling and control for new LLCL filter based grid-tied PV inverters with active power decoupling and active resonance damping capabilities," *Electric Power Systems Research*, vol. 155, pp. 307-319, 2018.
- [71] M. Ciobotaru, R. Teodorescu, and F. Blaabjerg, "A new single-phase PLL structure based on second order generalized integrator," in *2006 37th IEEE Power Electronics Specialists Conference*, 2006, pp. 1-6.
- [72] M. Easley, M. Hosseinzadehtaher, A. Y. Fard, M. B. Shadmand, and H. Abu-Rub, "Computationally-efficient Hierarchical Optimal Controller for Grid-tied Cascaded Multilevel Inverters," in *2019 IEEE Energy Conversion Congress and Exposition (ECCE)*, 2019, pp. 219-224.
- [73] M. Easley, M. Baker, A. Khan, M. B. Shadmand, and H. Abu-Rub, "Self-healing Model Predictive Controlled Cascaded Multilevel Inverter," in *2019 IEEE Energy Conversion Congress and Exposition (ECCE)*, 2019, pp. 239-244.

REFERENCES (Continued)

- [74] M. Stecca, L. R. Elizondo, T. B. Soeiro, P. Bauer, and P. Palensky, "A Comprehensive Review of the Integration of Battery Energy Storage Systems into Distribution Networks," *IEEE Open Journal of the Industrial Electronics Society*, vol. 1, pp. 46-65, 2020.
- [75] M. E. Baran and N. R. Mahajan, "DC distribution for industrial systems: opportunities and challenges," *IEEE Transactions on Industry Applications*, vol. 39, no. 6, pp. 1596-1601, 2003.
- [76] R. Abdollahi, "Multi-Phase Shifting Autotransformer Based Rectifier," *IEEE Open Journal of the Industrial Electronics Society*, vol. 1, pp. 38-45, 2020.
- [77] F. Chen, R. Burgos, D. Boroyevich, and X. Zhang, "Low-Frequency Common-Mode Voltage Control for Systems Interconnected With Power Converters," *IEEE Transactions on Industrial Electronics*, vol. 64, no. 1, pp. 873-882, 2017.
- [78] G. Zhu, H. Wang, B. Liang, S. Tan, and J. Jiang, "Enhanced Single-Phase Full-Bridge Inverter With Minimal Low-Frequency Current Ripple," *IEEE Transactions on Industrial Electronics*, vol. 63, no. 2, pp. 937-943, 2016.
- [79] B. Ge *et al.*, "An Active Filter Method to Eliminate DC-Side Low-Frequency Power for a Single-Phase Quasi-Z-Source Inverter," *IEEE Transactions on Industrial Electronics*, vol. 63, no. 8, pp. 4838-4848, 2016.
- [80] L. Zhang, X. Ruan, and X. Ren, "Second-Harmonic Current Reduction and Dynamic Performance Improvement in the Two-Stage Inverters: An Output Impedance Perspective," *IEEE Transactions on Industrial Electronics*, vol. 62, no. 1, pp. 394-404, 2015.
- [81] G. Liu and *e. al.*, "Suppression of Second-Order Harmonic Current for Droop-Controlled Distributed Energy Resource Converters in DC Microgrids," *IEEE Transactions on Industrial Electronics*, pp. 1-1, 2019.
- [82] X. Li and *e. al.*, "Power Management Unit With Its Control for a Three-Phase Fuel Cell Power System Without Large Electrolytic Capacitors," *IEEE Transactions on Power Electronics*, vol. 26, no. 12, pp. 3766-3777, 2011.
- [83] R. Wai and C. Lin, "Dual Active Low-Frequency Ripple Control for Clean-Energy Power-Conditioning Mechanism," *IEEE Transactions on Industrial Electronics*, vol. 58, no. 11, pp. 5172-5185, 2011.

REFERENCES (Continued)

- [84] R. Wai and C. Lin, "Active Low-Frequency Ripple Control for Clean-Energy Power-Conditioning Mechanism," *IEEE Transactions on Industrial Electronics*, vol. 57, no. 11, pp. 3780-3792, 2010.
- [85] M. E. Schenck, L. Jih-Sheng, and K. Stanton, "Fuel cell and power conditioning system interactions," in *Twentieth Annual IEEE Applied Power Electronics Conference and Exposition, 2005. APEC 2005.*, 2005, vol. 1, pp. 114-120 Vol. 1.
- [86] S. Harb and R. S. Balog, "Reliability of Candidate Photovoltaic Module-Integrated-Inverter (PV-MII) Topologies—A Usage Model Approach," *IEEE Transactions on Power Electronics*, vol. 28, no. 6, pp. 3019-3027, 2013.
- [87] H. Wang *et al.*, "Transitioning to Physics-of-Failure as a Reliability Driver in Power Electronics," *IEEE Journal of Emerging and Selected Topics in Power Electronics*, vol. 2, no. 1, pp. 97-114, 2014.
- [88] Y. Sun and *e. al.*, "Review of Active Power Decoupling Topologies in Single-Phase Systems," *IEEE Transactions on Power Electronics*, vol. 31, no. 7, pp. 4778-4794, 2016.
- [89] H. Li and *e. al.*, "Active Power Decoupling for High-Power Single-Phase PWM Rectifiers," *IEEE Transactions on Power Electronics*, vol. 28, no. 3, pp. 1308-1319, 2013.
- [90] Z. Qin and *e. al.*, "Benchmark of AC and DC Active Power Decoupling Circuits for Second-Order Harmonic Mitigation in Kilowatt-Scale Single-Phase Inverters," *IEEE Journal of Emerging and Selected Topics in Power Electronics*, vol. 4, no. 1, pp. 15-25, 2016.
- [91] M. A. Vitorino and *e. al.*, "Low-Frequency Power Decoupling in Single-Phase Applications: A Comprehensive Overview," *IEEE Transactions on Power Electronics*, vol. 32, no. 4, pp. 2892-2912, 2017.
- [92] H. Zhang and *e. al.*, "Capacitance, dc Voltage Utilization, and Current Stress: Comparison of Double-Line Frequency Ripple Power Decoupling for Single-Phase Systems," *IEEE Industrial Electronics Magazine*, vol. 11, no. 3, pp. 37-49, 2017.
- [93] H. Yuan, S. Li, W. Qi, S. Tan, and S. Hui, "On Nonlinear Control of Single-Phase Converters With Active Power Decoupling Function," *IEEE Transactions on Power Electronics*, vol. 34, no. 6, pp. 5903-5915, 2019.

REFERENCES (Continued)

- [94] D. Neumayr, D. Bortis, and J. W. Kolar, "Ultra-compact Power Pulsation Buffer for single-phase DC/AC converter systems," in *2016 IEEE 8th International Power Electronics and Motion Control Conference (IPEMC-ECCE Asia)*, 2016, pp. 2732-2741.
- [95] S. Harb, H. Zhang, and R. S. Balog, "AC-link, single-phase, photovoltaic Module Integrated Inverter," in *2013 Twenty-Eighth Annual IEEE Applied Power Electronics Conference and Exposition (APEC)*, 2013, pp. 177-182.
- [96] J. Itoh and F. Hayashi, "Ripple Current Reduction of a Fuel Cell for a Single-Phase Isolated Converter Using a DC Active Filter With a Center Tap," *IEEE Transactions on Power Electronics*, vol. 25, no. 3, pp. 550-556, 2010.
- [97] H. Wang, H. S. Chung, and W. Liu, "Use of a Series Voltage Compensator for Reduction of the DC-Link Capacitance in a Capacitor-Supported System," *IEEE Transactions on Power Electronics*, vol. 29, no. 3, pp. 1163-1175, 2014.
- [98] B. Gu, J. Dominic, J. Zhang, L. Zhang, B. Chen, and J. Lai, "Control of electrolyte-free microinverter with improved MPPT performance and grid current quality," in *2014 IEEE Applied Power Electronics Conference and Exposition - APEC 2014*, 2014, pp. 1788-1792.
- [99] R. Wang *et al.*, "A High Power Density Single-Phase PWM Rectifier With Active Ripple Energy Storage," *IEEE Transactions on Power Electronics*, vol. 26, no. 5, pp. 1430-1443, 2011.
- [100] A. C. Kyritsis, N. P. Papanikolaou, and E. C. Tatakis, "A novel Parallel Active Filter for Current Pulsation Smoothing on single stage grid-connected AC-PV modules," in *2007 European Conference on Power Electronics and Applications*, 2007, pp. 1-10.
- [101] Y. Tang, Z. Qin, F. Blaabjerg, and P. C. Loh, "DQ reference frame modeling and control of single-phase active power decoupling circuits," in *2015 IEEE Applied Power Electronics Conference and Exposition (APEC)*, 2015, pp. 2725-2732.
- [102] B. Ge, H. Abu-Rub, Y. Liu, and R. S. Balog, "An active filter method to eliminate dc-side low-frequency power for single-phase quasi-Z source inverter," in *2015 IEEE Applied Power Electronics Conference and Exposition (APEC)*, 2015, pp. 827-832.
- [103] W. Qi, H. Wang, X. Tan, G. Wang, and K. D. T. Ngo, "A novel active power decoupling single-phase PWM rectifier topology," in *2014 IEEE Applied Power Electronics Conference and Exposition - APEC 2014*, 2014, pp. 89-95.

REFERENCES (Continued)

- [104] Y. Tang, F. Blaabjerg, and P. C. Loh, "Decoupling of fluctuating power in single-phase systems through a symmetrical half-bridge circuit," in *2014 IEEE Applied Power Electronics Conference and Exposition - APEC 2014*, 2014, pp. 96-102.
- [105] H. Li, K. Zhang, H. Zhao, S. Fan, and J. Xiong, "Active Power Decoupling for High-Power Single-Phase PWM Rectifiers," *IEEE Transactions on Power Electronics*, vol. 28, no. 3, pp. 1308-1319, 2013.
- [106] M. A. Vitorino, L. V. Hartmann, D. A. Fernandes, E. L. Silva, and M. B. R. Corrêa, "Single-phase current source converter with new modulation approach and power decoupling," in *2014 IEEE Applied Power Electronics Conference and Exposition - APEC 2014*, 2014, pp. 2200-2207.
- [107] Y. Tang, W. Yao, P. C. Loh, and F. Blaabjerg, "Highly Reliable Transformerless Photovoltaic Inverters With Leakage Current and Pulsating Power Elimination," *IEEE Transactions on Industrial Electronics*, vol. 63, no. 2, pp. 1016-1026, 2016.
- [108] S. Li, W. Qi, S. Tan, and S. Y. Hui, "Integration of an Active Filter and a Single-Phase AC/DC Converter With Reduced Capacitance Requirement and Component Count," *IEEE Transactions on Power Electronics*, vol. 31, no. 6, pp. 4121-4137, 2016.
- [109] I. Serban, "Power Decoupling Method for Single-Phase H-Bridge Inverters With No Additional Power Electronics," *IEEE Transactions on Industrial Electronics*, vol. 62, no. 8, pp. 4805-4813, 2015.
- [110] Y. Tang and F. Blaabjerg, "A Component-Minimized Single-Phase Active Power Decoupling Circuit With Reduced Current Stress to Semiconductor Switches," *IEEE Transactions on Power Electronics*, vol. 30, no. 6, pp. 2905-2910, 2015.
- [111] D. E. Olivares and *e. al.*, "Trends in Microgrid Control," *IEEE Transactions on Smart Grid*, vol. 5, no. 4, pp. 1905-1919, 2014.
- [112] A. Bidram and A. Davoudi, "Hierarchical Structure of Microgrids Control System," *IEEE Transactions on Smart Grid*, vol. 3, no. 4, pp. 1963-1976, 2012.
- [113] L. Xu and D. Chen, "Control and Operation of a DC Microgrid With Variable Generation and Energy Storage," *IEEE Transactions on Power Delivery*, vol. 26, no. 4, pp. 2513-2522, 2011.
- [114] D. Chen, L. Xu, and L. Yao, "DC Voltage Variation Based Autonomous Control of DC Microgrids," *IEEE Transactions on Power Delivery*, vol. 28, no. 2, pp. 637-648, 2013.

REFERENCES (Continued)

- [115] A. Khorsandi, M. Ashourloo, and H. Mokhtari, "A Decentralized Control Method for a Low-Voltage DC Microgrid," *IEEE Transactions on Energy Conversion*, vol. 29, no. 4, pp. 793-801, 2014.
- [116] P. Wang, L. Goel, X. Liu, and F. H. Choo, "Harmonizing AC and DC: A Hybrid AC/DC Future Grid Solution," *IEEE Power and Energy Magazine*, vol. 11, no. 3, pp. 76-83, 2013.
- [117] B. Banerjee and W. W. Weaver, "Generalized Geometric Control Manifolds of Power Converters in a DC Microgrid," *IEEE Transactions on Energy Conversion*, vol. 29, no. 4, pp. 904-912, 2014.
- [118] B. Tamyurek, "A High-Performance SPWM Controller for Three-Phase UPS Systems Operating Under Highly Nonlinear Loads," *IEEE Transactions on Power Electronics*, vol. 28, no. 8, pp. 3689-3701, 2013.
- [119] M. Liserre, F. Blaabjerg, and S. Hansen, "Design and control of an LCL-filter-based three-phase active rectifier," *IEEE Transactions on Industry Applications*, vol. 41, no. 5, pp. 1281-1291, 2005.
- [120] A. Reznik and *e. al.*, "LCL Filter Design and Performance Analysis for Grid-Interconnected Systems," *IEEE Transactions on Industry Applications*, vol. 50, no. 2, pp. 1225-1232, 2014.
- [121] A. Khan, M. Houchati, J. Ur-Rehman, L. Ben-Brahim, and A. Gastli, "Switchless Power Decoupling and Switchless Leakage Current Elimination in Grid-Tied Inverters," in *2017 9th IEEE-GCC Conference and Exhibition (GCCCE)*, 2017, pp. 1-6.
- [122] J. Roy, Y. Xia, and R. Ayyanar, "High Step-Up Transformerless Inverter for AC Module Applications With Active Power Decoupling," *IEEE Transactions on Industrial Electronics*, vol. 66, no. 5, pp. 3891-3901, 2019.
- [123] J. Roy, Y. Xia, and R. Ayyanar, "Half-Bridge Voltage Swing Inverter With Active Power Decoupling for Single-Phase PV Systems Supporting Wide Power Factor Range," *IEEE Transactions on Power Electronics*, vol. 34, no. 8, pp. 7450-7461, 2019.
- [124] Y. Sun, Y. Liu, M. Su, W. Xiong, and J. Yang, "Review of Active Power Decoupling Topologies in Single-Phase Systems," *IEEE Transactions on Power Electronics*, vol. 31, no. 7, pp. 4778-4794, 2016.

REFERENCES (Continued)

- [125] Z. Qin, Y. Tang, P. C. Loh, and F. Blaabjerg, "Benchmark of AC and DC Active Power Decoupling Circuits for Second-Order Harmonic Mitigation in Kilowatt-Scale Single-Phase Inverters," *IEEE Journal of Emerging and Selected Topics in Power Electronics*, vol. 4, no. 1, pp. 15-25, 2016.
- [126] W. Yao, X. Wang, X. Zhang, Y. Tang, P. C. Loh, and F. Blaabjerg, "A unified active damping control for single-phase differential mode buck inverter with LCL-filter," in *2015 IEEE 6th International Symposium on Power Electronics for Distributed Generation Systems (PEDG)*, 2015, pp. 1-8.
- [127] W. Yao, X. Wang, P. C. Loh, X. Zhang, and F. Blaabjerg, "Improved Power Decoupling Scheme for a Single-Phase Grid-Connected Differential Inverter With Realistic Mismatch in Storage Capacitances," *IEEE Transactions on Power Electronics*, vol. 32, no. 1, pp. 186-199, 2017.
- [128] W. Yao, Y. Xu, Y. Tang, P. C. Loh, X. Zhang, and F. Blaabjerg, "Generalized Power Decoupling Control for Single-Phase Differential Inverters With Nonlinear Loads," *IEEE Journal of Emerging and Selected Topics in Power Electronics*, vol. 7, no. 2, pp. 1137-1151, 2019.
- [129] A. Khan, M. B. Shadmand, and H. Abu-Rub, "Active Power Decoupling Control Scheme for Distorted Grids," in *2019 IEEE Power and Energy Conference at Illinois (PECI)*, 2019, pp. 1-7.
- [130] P. D. F. Ferreira, P. M. S. Carvalho, L. A. F. M. Ferreira, and M. D. Ilic, "Distributed Energy Resources Integration Challenges in Low-Voltage Networks: Voltage Control Limitations and Risk of Cascading," *IEEE Transactions on Sustainable Energy*, vol. 4, no. 1, pp. 82-88, 2013.
- [131] A. Khan, M. Hosseinzadehtaher, M. B. Shadmand, S. Bayhan, and H. Abu-Rub, "On the Stability of the Power Electronics-Dominated Grid: A New Energy Paradigm," *IEEE Industrial Electronics Magazine*, vol. 14, no. 4, pp. 65-78, 2020.
- [132] S. D. Silva, M. Shadmand, S. Bayhan, and H. Abu-Rub, "Towards Grid of Microgrids: Seamless Transition between Grid-Connected and Islanded Modes of Operation," *IEEE Open Journal of the Industrial Electronics Society*, vol. 1, pp. 66-81, 2020.
- [133] S. Y. Hadush and L. Meeus, "DSO-TSO cooperation issues and solutions for distribution grid congestion management," *Energy Policy*, vol. 120, pp. 610-621, 2018.

REFERENCES (Continued)

- [134] J. Ye *et al.*, "A Review of Cyber-Physical Security for Photovoltaic Systems," *IEEE Journal of Emerging and Selected Topics in Power Electronics*, pp. 1-1, 2021.
- [135] Z. Tan, H. Zhong, Q. Xia, C. Kang, X. S. Wang, and H. Tang, "Estimating the Robust P-Q Capability of a Technical Virtual Power Plant Under Uncertainties," *IEEE Transactions on Power Systems*, vol. 35, no. 6, pp. 4285-4296, 2020.
- [136] N. Ruiz, I. Cobelo, and J. Oyarzabal, "A Direct Load Control Model for Virtual Power Plant Management," *IEEE Transactions on Power Systems*, vol. 24, no. 2, pp. 959-966, 2009.
- [137] X. Liu, A. M. Cramer, and Y. Liao, "Reactive power control methods for photovoltaic inverters to mitigate short-term voltage magnitude fluctuations," *Electric Power Systems Research*, vol. 127, pp. 213-220, 2015.
- [138] Y. Gui, C. C. Chung, F. Blaabjerg, and M. G. Taul, "Dynamic Extension Algorithm-Based Tracking Control of STATCOM Via Port-Controlled Hamiltonian System," *IEEE Transactions on Industrial Informatics*, vol. 16, no. 8, pp. 5076-5087, 2020.
- [139] M. Xie, M. M. Gulzar, H. Tehreem, M. Y. Javed, and S. T. H. Rizvi, "Automatic Voltage Regulation of Grid Connected Photovoltaic System Using Lyapunov Based Sliding Mode Controller: A Finite — Time Approach," *International Journal of Control, Automation and Systems*, vol. 18, no. 6, pp. 1550-1560, 2020.
- [140] A. Khan, M. Easley, M. Hosseinzadehtaher, M. B. Shadmand, H. Abu-Rub, and P. Fajri, "PLL-less Active and Reactive Power Controller for Grid-Following Inverter," in *2020 IEEE Energy Conversion Congress and Exposition (ECCE)*, 2020, pp. 4322-4328.
- [141] S. K. Mazumder, "Energy Storage: A Power Electronics System View," *IEEE Power Electronics Magazine*, vol. 6, no. 4, pp. 36-38, 2019.
- [142] A. Khan, M. Hosseinzadehtaher, M. B. Shadmand, and S. K. Mazumder, "Cybersecurity Analytics for Virtual Power Plants," in *2021 IEEE 12th International Symposium on Power Electronics for Distributed Generation Systems (PEDG)*, 2021, pp. 1-5.
- [143] J. Rotman, "The Fundamental Theorem of Galois Theory," in *Galois Theory*, J. Rotman, Ed. New York, NY: Springer US, 1990, pp. 48-50.

REFERENCES (Continued)

- [144] O. H. Abu-Rub, A. Y. Fard, M. F. Umar, M. Hosseinzadehtaher, and M. B. Shadmands, "Towards Intelligent Power Electronics-Dominated Grid via Machine Learning Techniques," *IEEE Power Electronics Magazine*, vol. 8, no. 1, pp. 28-38, 2021.
- [145] S. N. Vukosavic and A. M. Stankovic, "Non-Intrusive Estimation of Single-Port Thevenin Equivalents in AC Grids," *IEEE Transactions on Power Delivery*, pp. 1-1, 2020.
- [146] D. Pattabiraman, R. H. Lasseter, and T. M. Jahns, "Comparison of Grid Following and Grid Forming Control for a High Inverter Penetration Power System," in *2018 IEEE Power & Energy Society General Meeting (PESGM)*, 2018, pp. 1-5.
- [147] B. Mirafzal and A. Adib, "On Grid-Interactive Smart Inverters: Features and Advancements," *IEEE Access*, vol. 8, pp. 160526-160536, 2020.
- [148] M. Hosseinzadehtaher, A. Khan, M. B. Shadmand, and H. Abu-Rub, "Anomaly Detection in Distribution Power System based on a Condition Monitoring Vector and Ultra- Short Demand Forecasting," in *2020 IEEE CyberPELS (CyberPELS)*, 2020, pp. 1-6.
- [149] A. Khan, M. Hosseinzadehtaher, M. B. Shadmand, D. Saleem, and H. Abu-Rub, "Intrusion Detection for Cybersecurity of Power Electronics Dominated Grids: Inverters PQ Set-Points Manipulation," in *2020 IEEE CyberPELS (CyberPELS)*, 2020, pp. 1-8.
- [150] A. Y. Fard, M. Easley, G. T. Amariuca, M. B. Shadmand, and H. Abu-Rub, "Cybersecurity Analytics using Smart Inverters in Power Distribution System: Proactive Intrusion Detection and Corrective Control Framework," in *2019 IEEE International Symposium on Technologies for Homeland Security (HST)*, 2019, pp. 1-6.
- [151] Z. Zhang, M. Easley, M. Hosseinzadehtaher, G. Amariuca, M. B. Shadmand, and H. Abu-Rub, "An Observer Based Intrusion Detection Framework for Smart Inverters at the Grid-Edge," in *2020 IEEE Energy Conversion Congress and Exposition (ECCE)*, 2020, pp. 1957-1962.
- [152] A. Y. Fard and M. B. Shadmand, "Multitimescale Three-Tiered Voltage Control Framework for Dispersed Smart Inverters at the Grid Edge," *IEEE Transactions on Industry Applications*, 2021.

REFERENCES (Continued)

- [153] Q. Ai, S. Fan, and L. Piao, "Optimal scheduling strategy for virtual power plants based on credibility theory," *Protection and Control of Modern Power Systems*, vol. 1, no. 1, p. 3, 2016.
- [154] C. Kieny, B. Berseneff, N. Hadjsaid, Y. Besanger, and J. Maire, "On the concept and the interest of virtual power plant: Some results from the European project Fenix," in *2009 IEEE Power & Energy Society General Meeting*, 2009, pp. 1-6.
- [155] "CFCL BlueGen units for virtual power plant project in Netherlands," *Fuel Cells Bulletin*, vol. 2012, no. 7, p. 3, 2012.
- [156] T. Hossen, F. Sadeque, M. Gursoy, and B. Mirafzal, "Self-Secure Inverters Against Malicious Setpoints," in *2020 IEEE Electric Power and Energy Conference (EPEC)*, 2020, pp. 1-6.
- [157] A. Y. Fard, M. B. Shadmand, and S. K. Mazumder, "Holistic Multi-timescale Attack Resilient Control Framework for Power Electronics Dominated Grid," in *2020 Resilience Week (RWS)*, 2020, pp. 167-173.
- [158] S. Harshbarger, M. Hosseinzadehtaher, B. Natarajan, E. Vasserman, M. Shadmand, and G. Amariuca, "(A Little) Ignorance is Bliss: The Effect of Imperfect Model Information on Stealthy Attacks in Power Grids," in *2020 IEEE Kansas Power and Energy Conference (KPEC)*, 2020, pp. 1-6.
- [159] M. Mola, N. Meskin, K. Khorasani, and A. Massoud, "Distributed Event-Triggered Consensus-Based Control of DC Microgrids in Presence of DoS Cyber Attacks," *IEEE Access*, vol. 9, pp. 54009-54021, 2021.
- [160] C. Xu, F. C. Huff, and P. Francino, "Optimal load dispatch based on generator reactive capability curve," in *2006 IEEE Power Engineering Society General Meeting*, 2006, p. 6 pp.
- [161] D. Pudjianto, C. Ramsay, and G. Strbac, "Virtual power plant and system integration of distributed energy resources," *IET Renewable Power Generation*, vol. 1, no. 1, pp. 10-16
- [162] N. Xue *et al.*, "Dynamic Security Optimization for N-1 Secure Operation of Hawai'i Island System with 100% Inverter-Based Resources," *IEEE Transactions on Smart Grid*, 2021.
- [163] T. Zhang *et al.*, "KPI-based Real-time Situational Awareness for Power Systems with a High Proportion of Renewable Energy Sources," *CSEE Journal of Power and Energy Systems*, vol. 8, no. 4, pp. 1060-1073, 2022.

REFERENCES (Continued)

- [164] B. Kroposki *et al.*, "Achieving a 100% Renewable Grid: Operating Electric Power Systems with Extremely High Levels of Variable Renewable Energy," *IEEE Power and Energy Magazine*, vol. 15, no. 2, pp. 61-73, 2017.
- [165] Q. Hou, E. Du, N. Zhang, and C. Kang, "Impact of High Renewable Penetration on the Power System Operation Mode: A Data-Driven Approach," *IEEE Transactions on Power Systems*, vol. 35, no. 1, pp. 731-741, 2020.
- [166] V. Telukunta, J. Pradhan, A. Agrawal, M. Singh, and S. G. Srivani, "Protection challenges under bulk penetration of renewable energy resources in power systems: A review," *CSEE Journal of Power and Energy Systems*, vol. 3, no. 4, pp. 365-379, 2017.
- [167] S. Liu *et al.*, "Robust System Separation Strategy Considering Online Wide-Area Coherency Identification and Uncertainties of Renewable Energy Sources," *IEEE Transactions on Power Systems*, vol. 35, no. 5, pp. 3574-3587, 2020.
- [168] A. Halbouni, T. S. Gunawan, M. H. Habaebi, M. Halbouni, M. Kartiwi, and R. Ahmad, "Machine Learning and Deep Learning Approaches for CyberSecurity: A Review," *IEEE Access*, vol. 10, pp. 19572-19585, 2022.
- [169] M. R. Endsley and E. S. Connors, "Situation awareness: State of the art," in *2008 IEEE Power and Energy Society General Meeting - Conversion and Delivery of Electrical Energy in the 21st Century*, 2008, pp. 1-4.
- [170] Y. Wang, C. Chen, J. Wang, and R. Baldick, "Research on Resilience of Power Systems Under Natural Disasters—A Review," *IEEE Transactions on Power Systems*, vol. 31, no. 2, pp. 1604-1613, 2016.
- [171] P. Cuffe, P. Smith, and A. Keane, "Capability Chart for Distributed Reactive Power Resources," *IEEE Transactions on Power Systems*, vol. 29, no. 1, pp. 15-22, 2014.
- [172] A. V. Jayawardena, L. G. Meegahapola, D. A. Robinson, and S. Perera, "Capability chart: A new tool for grid-tied microgrid operation," in *2014 IEEE PES T&D Conference and Exposition*, 2014, pp. 1-5.
- [173] F. L. Müller, J. Szabó, O. Sundström, and J. Lygeros, "Aggregation and Disaggregation of Energetic Flexibility From Distributed Energy Resources," *IEEE Transactions on Smart Grid*, vol. 10, no. 2, pp. 1205-1214, 2019.
- [174] J. W. Simpson-Porco, "Lossy DC Power Flow," *IEEE Transactions on Power Systems*, vol. 33, no. 3, pp. 2477-2485, 2018.

REFERENCES (Continued)

- [175] W. J. Tzeng and F. Y. Wu, "Theory of impedance networks: the two-point impedance and LC resonances," *Journal of Physics A: Mathematical and General*, vol. 39, no. 27, pp. 8579-8591, 2006/06/21 2006.
- [176] F. Y. Wu, "Theory of resistor networks: The two-point resistance," *J. Phys. A: Math. Gen.*, vol. 37, no. 26, p. 6653, 2004.
- [177] Y. Ji, W. He, S. Cheng, J. Kurths, and M. Zhan, "Dynamic Network Characteristics of Power-electronics-based Power Systems," *Scientific Reports*, vol. 10, no. 1, p. 9946, 2020/06/19 2020.
- [178] K. Ahmed, M. Seyedmahmoudian, S. Mekhilef, N. M. Mubarak, and A. Stojcevski, "A Review on Primary and Secondary Controls of Inverter-interfaced Microgrid," *Journal of Modern Power Systems and Clean Energy*, vol. 9, no. 5, pp. 969-985, 2021.
- [179] H. Xin, Z. Qu, J. Seuss, and A. Maknouninejad, "A Self-Organizing Strategy for Power Flow Control of Photovoltaic Generators in a Distribution Network," *IEEE Transactions on Power Systems*, vol. 26, no. 3, pp. 1462-1473, 2011.
- [180] A. Maknouninejad and Z. Qu, "Realizing Unified Microgrid Voltage Profile and Loss Minimization: A Cooperative Distributed Optimization and Control Approach," *IEEE Transactions on Smart Grid*, vol. 5, no. 4, pp. 1621-1630, 2014.
- [181] N. Xue, U. Muenz, Z. Qu, and W. Sun, "Stability Quantification for Consensus-Based Power Flow Control between Transmission and Distribution Power Systems," in *2021 60th IEEE Conference on Decision and Control (CDC)*, 2021, pp. 3501-3506.

VITA

NAME: Ahmad Mir Dad Khan

EDUCATION: B.Sc. Electrical Engineering, Qatar University, Doha, Qatar 2014.

M.Sc. Electrical Engineering, Qatar University, Doha, Qatar 2017.

Ph.D. Electrical and Computer Engineering, University of Illinois at Chicago, Chicago, IL, USA, 2023.

PROFESSIONAL EXPERIENCE: R&D Engineer, Siemens Technology, Princeton, NJ, USA, June 2021- Jan 2022.

Senior Engineer, Quanta Technology, Lombard, IL, USA, Jan 2023.

Technical Chair of IEEE Kansas Power & Energy Conference (KPEC 2020), Manhattan, KS, USA, 2020.

HONOURS AND AWARDS: Best Paper Award from the 2019 IEEE Conference on Smart Grid and Renewable Energy

Best Paper Award from the 2018 IEEE 12th International Conference on Compatibility, Power Electronics and Power Engineering.

Outstanding M.Sc. Thesis Award from Qatar University, 2017

IEEE 2019 IAS Myron Zucker Student Faculty Grant, for the project "Compact, Reliable, and Robust GaN-based Active Rectifiers for More Electric Aircraft".

IEEE 2019 IAS Outstanding Branch Chapter Award, Kansas State University IAS branch chapter.

IEEE ECCE 2019 Travel Award.

IEEE TEPC 2020 Travel Award.

IEEE IES Student & Young Professionals Award (SYPA) in CPE-POWERENG 2018

MEMBERSHIP IEEE

VITA (Continued)

IEEE IAS

IEEE PES

IEEE IES

IEEE PELS

REVIEWER:

IEEE Transactions on Industrial Electronics

IEEE Transactions on Power Electronics

Renewable Sustainable Energy Reviews

IAS Renewable and Sustainable Energy Conversion System

IEEE IAS Power System Engineering

IET Renewable Power Generation

Elsevier Energy for Sustainable Development

IEEE Applied Power Electronics Conference & Exposition (APEC 2019)

IEEE CPE-POWERENG-2018

IEEE IECON-2018

IEEE ECCE-2019

IEEE ECCE-2020

IEEE 2nd SGRE-2019

JOURNALS:

M. Hosseinzadehtaher, A. Zare, A. Khan, M. F. Umar, S. D'silva, and M. B. Shadmand, "Towards More Resilient Low Inertia Power Electronic Dominated-Grid: Grid-Following Inverters' Maximum Capability Utilization", *IEEE Transactions on Industrial Electronics*, Submitted.

A. Khan, M. Hosseinzadehtaher, M. Shadmand, S. Bayhan, H. Abu-Rub. "On the Stability of the Power Electronics-Dominated Grid: A New Energy Paradigm" *IEEE Industrial Electronics Magazine*, vol. 14, no. 4, pp. 65-78, December 2020

VITA (Continued)

M. Hosseinzadahtaher, A. Khan, M. Shadmand, P. Fajri. "Self-healing Predictive Control of Battery System in Naval Power System with Pulsed Power Loads" *IEEE Transactions on Energy Conversion.*, vol. 36, no. 2, pp. 1056-1069, June 2021

A. Khan, S. D'Silva, A. Fard, M. B. Shadmand, H. Abu-Rub, "On Stability of PV Clusters with Distributed Power Reserve Capability", *IEEE Transactions on Industrial Electronics*, vol. 68, no. 5, pp. 3928-3938, May 2021

A. Khan, A. Gastli, L. Ben-Brahim, "Modeling and control for new LLCL filter based grid- tied pv inverters with active power decoupling and active resonance damping capabilities", *Electric Power Systems Research*, vol. 155, pp. 307-319, Feb. 2018.

A. Khan, L. Ben-Brahim, A. Gastli, M. Benammar, "Review and simulation of leakage current in transformerless microinverters for PV applications", *Renewable and Sustainable Energy Reviews*, vol. 74, pp. 1240-1256, July 2017.

F. Jarraya, A. Khan, A. Gastli, L. Ben-Brahim, R. Hamaila, "Design Considerations, Modeling and Control of Dual Active Full Bridge for Electric Vehicles Charging Applications" *IET the Journal of Engineering*, Vol. 2019, Issue 12, December 2019.

A. Khan, M. B. Shadmand, S. Bayhan and H. Abu-Rub, "A Power Ripple Compensator for DC Nanogrids via a Solid-State Converter," *IEEE Open Journal of the Industrial Electronics Society*, vol. 1, pp. 311-325, 2020

A. Khan, M. B. Shadmand, S. K. Mazumder, "Intrusion Detection System for Multi-Layer-Controlled Power Electronics-Dominated Grid" *IEEE Access*, 2022.

M. F. Ummar, M. Easley, B. Nun, A. Khan, M. B. Shadmand, S. Bayhan, H. Abu-Rub, ""Grid-Interactive Inverter with Resonance Suppression based on Adaptive Predictive Control in Weak Grid Condition" *IEEE Journal of Emerging and Selected Topics in Industrial Electronics*, 2021.

VITA (Continued)

- CONFERENCE: A. Khan, M. Hosseinzadahtaher, M. Shadmand, “Single Stage PLL-less Decoupled Active and Reactive Power Control for Single Phase Weak Grid-Connected Inverters”, *21st IFAC World Congress, 2020 (IFAC 2020)*, Berlin, Germany, 2020, pp 1-6.
- M. F. Ummar, A. Khan, M. Shadmand, “A Stabilizer based Predictive Control Scheme for Smart Inverters in Weak Grid”, *2020 IEEE Texas Power and Energy Conference (2020 TEPC)*, pp 1-6, Texas, USA, 2020.
- M. Hosseinzadahtaher, A. Khan, M. W. Baker, M. Shadmand, “Model Predictive Self-healing Control Scheme for Dual Active Bridge Converter”, *IEEE 2nd International Conference on Smart Grid and Renewable Energy (SGRE)*, pp 1-6, Doha, Qatar, 2019, “Best paper award.”
- M. Easley, M. W. Baker, A. Khan, M. Shadmand, H. Abu-Rub “Self-healing Model Predictive Controlled Cascaded Multilevel Inverter”, *IEEE Energy Conversion Congress and Exposition (ECCE)*, pp 1-8, Baltimore, MD, USA, 2019
- A. Khan, M. B. Shadmand, H. Abu-Rub “Active Power Decoupling Control Scheme for Distorted Grids”, *IEEE Power and Energy Conference at Illinois (PECI)*, Champaign, IL, USA, pp. 1-7, 2019
- A. Khan, S. D’silva, M. Hosseinzadehtaher, M. B. Shadmand, H. Abu-Rub “Differential and Common Mode Active Resonance Damping Control for Shunt-less LCL Filter Based Grid-Connected PV Inverters”, *IEEE Power and Energy Conference at Illinois (PECI)*, Champaign, IL, USA, pp. 1-8, 2019.
- A. Khan, A. Iqbal, M. B. Shadmand, “Novel LCL Filter for Non-Isolated Photovoltaic Inverters with CM Current Trapping Capability for Weak Grids”, *IEEE 44th Annual Conference of the IEEE Industrial Electronics Society (IECON)*, Washington D.C., USA, pp. 6128-6132, 2018.
- A. Khan, M. B. Shadmand, S. K. Mazumder, ” On The Voltage Stability of The Power Electronics- Dominated Grid: Mathematical Derivation of The Stability Margin “*2023 IEEE PES GM*, 2023

VITA (Continued)

A. Khan, F. Blaabjerg, “Novel Shunt-less Filter for Grid-Connected Transformerless Photovoltaic Applications”, *IEEE 12th International Conference on Compatibility, Power Electronics and Power Engineering (CPE-POWERENG)*, Doha, Qatar, pp. 1-6, 2018. “Best paper award.”

A. Khan, F. Blaabjerg, “Modified Dual Buck Inverter with Improved Lifetime for PV Applications”, *IEEE International Reliability Physics Symposium (IRPS)*, Burlingame, California, USA, pp. 6C.2-1-6C.2-6, 2018.

A. Khan, L. Ben-Brahim, A. Gastli, N. El-Emadi “Electrolytic Capacitor-less Dual Buck Inverter with CM and DM Active Resonance Damping Control for Non-isolated Grid-Tied Photovoltaic Applications”, *IEEE 12th International Conference on Compatibility, Power Electronics and Power Engineering (CPE-POWERENG)*, Doha, Qatar, pp. 1-6, 2018.

A. Khan, F. Jarraya, A. Gastli, L. Ben-Brahim, R. Hamaila, K. Rajashekara, “Dual Active Full Bridge Implementation on Typhoon HIL for G2V and V2G Applications” *IEEE Vehicle Power and Propulsion Conference (VPPC)*, Belfort, France, pp. 1-6. 2017

A. Khan, M. Hosseinzadahtaher, D. Saleem ,M. Shadmand, H. Abu-Rub, “Intrusion Detection for Cybersecurity of Power Electronics Dominated Grids: Inverters PQ Set-Points Manipulation”, *IEEE Cyber PELS Conference*, pp 1-6. 2020.

M. Hosseinzadahtaher, A. Khan, M. Shadmand, H. Abu-Rub, “Anomaly Detection in Distribution Power System based on a Condition Monitoring Vector and Ultra- Short Demand Forecasting.” *IEEE Cyber PELS Conference*, pp 1-6, 2020.

A. Khan, L. Ben-Brahim, A. Gastli , “Switchless Power Decoupling and Switchless Leakage Current Elimination in Grid-Tied Inverters” *9th IEEE-GCC Conference and Exhibition (GCCCE)*, Manama, Bahrain, pp. 1-6, 2017

A. Khan, L. Ben-Brahim, A. Gastli, “Microinverters & String inverters: A Techno-Economic Study,” *Proc. GCC Power 2016 Conference Cigre* , Doha , Qatar, 2016

VITA (Continued)

A. Khan, M. Hosseinzadehtaher, M. Easley, M. B. Shadmand and H. Abu-Rub, "Decoupled Active and Reactive Power Control without PLL Requirement for Differential Buck Converter," *2020 IEEE Energy Conversion Congress and Exposition (ECCE)*, Detroit, MI, USA, 2020, pp. 4994-4999

M. F. Umar, A. Khan, M. Easley, S. D'Silva, B. Nun and M. B. Shadmand, "Resonance Suppression based on Predictive Control of Grid-following Inverters with LCL Filter in Weak Grid Condition," *2020 IEEE Energy Conversion Congress and Exposition (ECCE)*, Detroit, MI, USA, 2020, pp. 4742-4748.

A. Khan, M. Easley, M. Hosseinzadehtaher, M. B. Shadmand, H. Abu-Rub and P. Fajri, "PLL-less Active and Reactive Power Controller for Grid-Following Inverter," *2020 IEEE Energy Conversion Congress and Exposition (ECCE)*, Detroit, MI, USA, 2020, pp. 4322-4328

S. D'silva, A. Khan, M. F. Umar, M. B. Shadmand and H. Abu-Rub, "On Stability of Hybrid Power Ramp Rate Control for High Photovoltaic Penetrated Grid," *2020 IEEE Energy Conversion Congress and Exposition (ECCE)*, Detroit, MI, USA, 2020, pp. 2806-2813.

A. Khan, M. Hosseinzadehtaher, M. B. Shadmand, S. K. Mazumder, "Proactive Intrusion Detection System for Virtual Power Plants based on Real-Time Normal Operation Regions Identification" *2021 IEEE 12th International Symposium on Power Electronics for Distributed Generation Systems (PEDG 2021)*, 2021.

A. Khan, M. Hosseinzadehtaher, A. Y. Fard, M. B. Shadmand, "Active Power Decoupling Control for Rectifiers with Variable Frequency Supply for More Electric Aircraft" *2021 IEEE IAS General Meeting*, 2021.

A. Khan, M. B. Shadmand, "Real-Time Stability Boundary Identification of Prosumers PCC in a Virtual Power Plant", *2021 IEEE COMPEL*, 2021